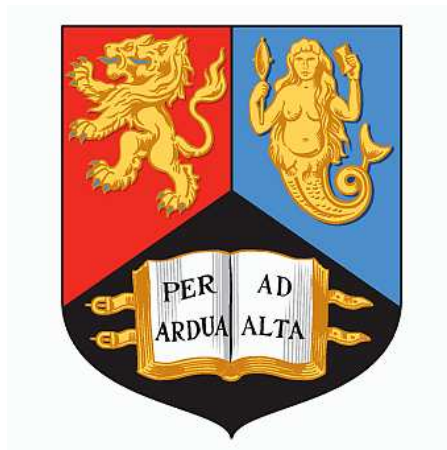


COMMISSIONING OF THE LEVEL-I CALORIMETER  
TRIGGER PHASE-I UPGRADE AND SEARCHES FOR  
HIGH-MASS HEAVY NEUTRAL LEPTONS IN THE  
ATLAS EXPERIMENT AT THE LHC

**Gareth Bird**

*Thesis submitted for the degree of  
Doctor of Philosophy*



Particle Physics Group,  
School of Physics and Astronomy,  
University of Birmingham.





---

## ABSTRACT

---

The ATLAS experiment is capable of measuring consistent proton collisions at the highest energies to date with  $\sqrt{s} = 13.6$  TeV. This allows many previously impossible measurements of standard model physics and searches for new physics. This thesis is split into two major parts. The phase one upgrade of the level one calorimeter trigger is outlined. This discusses the author's contributions to installation of the eFEX system, allowing the rate of single electron triggers in run 3 to be reduced by 5kHz or about 20% for the same level of performance. Then an analysis of Heavy Neutral Leptons (HNLs) produced in a t-channel VBS-like topology is outlined. This leads to the first limits on HNL mass-mixing up to masses of 20 TeV alongside the CMS experiment.

---

## DECLARATION OF AUTHORS CONTRIBUTION

---

This work would have been impossible without the work of generations of scientists spanning over a century. Very little work on the LHC can be considered purely the work of the thesis writer and this is reflected in the LHC experiment paper author lists being several thousand people long. Here we distinguish necessary motivations from others' work and the author's work.

Chapter 2 is a necessary contextual summary of the LHC and ATLAS detector. This is needed to discuss the Trigger and Data Acquisition system and upgrade in Chapter 3 which the author did not design. However, section 3.3 and beyond is a mixed summary of the author's work in the final software, firmware and commissioning work for the upgrade. This would have been impossible without the guidance and work of the L1Calo community as a whole. The early performance plots shown are public results that the author did not directly create.

Chapter 4 is the minimum theory needed to interpret the search paper that comprises the remainder of the thesis. This is not the author's work aside from the HNL s-channel LNC/LNV interpretations (figure 4.5), which had already been considered in the context of similar experiments by theorists.

The remainder of the thesis is a summary of the work of a medium-sized analysis team ( $\sim 20$  people with varying institutional affiliations) in which several theses will be written. Aside from various small tasks that enabled the main analysis strategy<sup>1</sup>, the author's main tasks discussed in this thesis were rare photon background studies (section 6.3) and running and interpreting the statistical fitting framework prior to and after unblinding (section 5.5 and chapter 7).

---

<sup>1</sup>i.e. debugging object selections and creating the platform for UK users to work the analysis from 2022 onwards

The event displays and photos in the thesis are the author's own.

---

## ACKNOWLEDGEMENTS

---

Firstly, I have to thank STFC for making this PhD possible financially and providing me with the opportunity to complete a PhD in conjunction with Rutherford Appleton Laboratory.

Now, I would like to thank the many people who made this thesis possible over the last fun but overly complicated 4 years over various locations which Quarter Horse Coffee ship to.

I'd like to thank everyone who have made the L1Calo world such a friendly space at Birmingham, RAL and CERN. Notably, I'd like especially like to thank Juraj, Steve, Will and Rhys for tolerating my many questions.

My time on LTA in Geneva was more complicated than most. I'd like to thank the post-COVID LTA community for making working through a major health crisis extremely entertaining. Special thanks to Charlotte and Clara for getting up at ungodly hours to take me to the HUG.

The second half of the thesis would have been impossible without the relentless efforts of a small, seemingly ever-changing team of people. I would especially like to thank my publication crunch team of Ben, Jonas, Matthias and Krisztian for getting this cool search paper across the finish line.

This thesis would not have been of the quality it is without me throwing 5 months of questions at the Birmingham ATLAS PhD office. Will deserves several nice beers for the sheer number of statistics and theory problems I threw at him.

When I returned to Birmingham to finish the analysis and write a thesis in 12 months,

I wasn't expecting to have so much fun. For this I can only thank Ala.

I'd like to thank my supervisors Dave, Alan and Monika for going well out of their way to make sure I had what I needed to make this PhD happen and how to sell myself.

Finally, I'd like to thank my parents for their unending support, without them this career path would have been completely impossible.



*I love deadlines. I like the whooshing sound they make as they fly by.*

Douglas Adams



# Contents

1	Introduction	1
2	The Large Hadron Collider and the ATLAS Experiment	3
2.1	The LHC	3
2.2	The ATLAS Experiment	7
2.3	Preliminary Definitions	8
2.4	Tracking Detector	10
2.5	Transition Radiation Tracker	11
2.6	Calorimetry	12
2.7	Muon spectroscopy	15
2.8	Combined Performance	16
3	L1Calo Phase-I Upgrade	20
3.1	The Level 1 Calorimeter Trigger	20
3.1.1	Trigger and Data Acquisition at ATLAS and The LHC	21
3.1.2	L1Calo System And Upgrade Overview	24
3.1.3	Physics Aims of L1Calo	25
3.1.4	Run 1 and 2 System	26
3.1.5	Phase-I Upgrade	27
3.2	Hardware Enabling Improved Electromagnetic Clustering Algorithms	30
3.2.1	LTDB & LATOME	30
3.2.2	The eFEX	31
3.2.3	Topological Combination and Readout	32
3.2.4	The FTM	33
3.3	Software for L1Calo	34
3.4	LATOME to eFEX Channel Mappings	34
3.4.1	Hardware Description	35
3.4.2	Software Capabilities	38
3.5	Firmware Development	39
3.6	Example Commissioning jobs	41
3.6.1	FTM Loopback	42
3.6.2	Installation and Cabling	44
3.6.3	Align Frame Capture	46
3.7	Preliminary Run 3 data checks	46
3.8	Early Performance Results	48

---

4	The Standard Model, Heavy Neutral Leptons and The Weinberg Operator	52
4.1	Preliminaries: Fields, Chirality and Masses in the Standard Model	53
4.2	Majorana Construction	56
4.3	Type-I Seesaw Mechanism	57
4.4	ATLAS and CMS HNL Signal Models	58
4.5	The Higgs Mechanism From The Perspective of Fermion Masses	60
4.6	The Weinberg Operator	63
4.7	Suppression of Lepton Number Violation in HNL models	65
4.8	Limitations and Naturalness of Collider HNLs	67
5	Searching for high mass HNLs at ATLAS	69
5.1	Motivation and Signal Topology	70
5.2	Object Definitions	71
5.2.1	Electrons	73
5.2.2	Muons	74
5.2.3	Jets	76
5.2.4	Missing Transverse Momentum	77
5.2.5	Heavy Hadron Tagging	78
5.2.6	Overlap Removal	79
5.3	Samples	79
5.3.1	Data	80
5.3.2	Monte Carlo Generators	81
5.3.2.1	Heavy Neutral Leptons	83
5.3.2.2	Weinberg	84
5.3.2.3	Same Sign WW Production	84
5.3.3	WZ Production	85
5.3.4	Other Samples	86
5.4	Event Selection	87
5.4.1	Region Design	87
5.4.1.1	Signal Region	88
5.4.1.2	ssWW Control Region	90
5.4.1.3	WZ Control Region	93
5.5	Statistical Methods	95
5.5.1	Fitting Methodology	95
5.5.2	Background Only Fit	96
5.5.3	Signal and Background Fit	101
5.5.4	Systematic Uncertainties	106
5.5.4.1	Under-Constraints and Smoothing	113
5.6	Conclusions	114
6	Rare Background Estimation Studies for HNLs at ATLAS	117
6.1	Monte-Carlo Truth Studies	118
6.2	Hadronic Fake Estimates	122
6.3	Photon Fake Estimates	128
6.4	Muon Charge Misidentification	136

6.5	Co-Incidental and Double Parton W production . . . . .	<b>136</b>
6.6	Conclusions . . . . .	<b>138</b>
<b>7</b>	<b>Results</b>	<b>139</b>
7.1	Unblinded Fit . . . . .	<b>139</b>
7.1.1	Unblinded Signal Region Data . . . . .	<b>139</b>
7.1.2	Control Regions and Systematic Pulls . . . . .	<b>141</b>
7.2	Hypothesis Testing and Confidence Limits . . . . .	<b>148</b>
7.3	Conclusions . . . . .	<b>151</b>
<b>8</b>	<b>Conclusions</b>	<b>152</b>
<b>A</b>	<b>Supplementary Statistical Modelling Plots</b>	<b>167</b>
A.1	Extra Unblinded Background-Only Fit Plots . . . . .	<b>167</b>
A.2	Signal Fit on Unblinded Data . . . . .	<b>171</b>
A.3	Blinded Weinberg Fit . . . . .	<b>175</b>
<b>B</b>	<b>Supplementary Images</b>	<b>179</b>
<b>C</b>	<b>Systematics Quantification Summary</b>	<b>181</b>
C.1	Experimental Systematics . . . . .	<b>181</b>
C.2	Theoretical Systematic Variations . . . . .	<b>182</b>

# List of Tables

4.1	Electroweak Charges of the Standard Model. . . . .	55
5.1	Baseline electron selection criteria. . . . .	73
5.2	Signal electron selection criteria (additional cuts with respect to the baseline selection) . . . . .	73
5.3	Baseline muon selection criteria. . . . .	74
5.4	Signal muon selection criteria. . . . .	74
5.5	Additional cuts above baseline muons to define anti-ID muons. . . . .	75
5.6	Baseline jet reconstruction criteria . . . . .	76
5.7	Signal jet reconstruction criteria (additional cuts with respect to baseline). . . . .	77
5.8	Heavy flavour, b-tag selection criteria. . . . .	78
5.9	The overlap removal procedure for the analysis. . . . .	78
5.10	The single muon HLT trigger chains used in the analysis. . . . .	80
5.11	Total Luminosity Of Each Year of Data . . . . .	80
5.12	A summary of our generators used for the analysis. . . . .	82
5.13	Summary of all the region cuts after preselection, the validation regions not included in the fit are written in grey. . . . .	88
5.14	Results of the Signal Region Scan . . . . .	90
5.15	Injected asimov values . . . . .	101
6.1	Breakdown off IFF Classifier codes. . . . .	118
6.2	Cutflow for the di-jet enriched hadronic fake control region after preselection, with the motivations. . . . .	123
6.3	$ee + (e/\mu)$ channel cutflow for the ZGammaCR in section 6.3. . . . .	131
6.4	$mm + (e/\mu)$ channel cutflow for the ZGammaCR in section 6.3. . . . .	132
7.1	Yield Table of Signal and Control Regions . . . . .	141
C.1	Summary of the experimental systematic uncertainties considered in the analysis. . . . .	183

# List of Figures

2.1	A schematic of the entire Conseil Européen pour la Recherche Nucléaire (CERN) accelerator complex which acts in part to inject protons/ions into the Large Hadron Collider (LHC) . . . . .	4
2.2	The projected luminosity and energy profile for the LHC between 2010 and 2040. . . . .	6
2.3	The ATLAS Detector cut-away diagram. . . . .	7
2.4	A rough cross section schematic for how different particle travel through and interact with the A Toroidal LHC Apparatus (ATLAS) detector. . . . .	8
2.5	A schematic of the inner detector with the small, more spatially precise silicon pixels clustered around the centre. . . . .	9
2.6	A schematic of the accordion geometry ECAL for the ATLAS experiment.	13
2.7	The bipolar response of the LAr detector compared to the real analogue signal directly from the calorimeter cells. . . . .	14
2.8	The layout of the muon-spectrometer surrounding the rest of the detector. . . . .	16
2.9	The run 2 identification efficiency as a function of rapidity and $p_T$ . .	18
2.10	Mean of a Gaussian fit of $\frac{E_{T, reco}}{E_{T, truth}}$ as a function of truth rapidity and energy on a collection of di-jets. . . . .	19
3.1	The ‘frontier’ Level 1 Hardware trigger read-out for different LHC experiments. Ultimately, a compromise must be found between event data size and acceptance rate as we are limited by read out and storage costs. . . . .	22
3.2	A rough overview of the Phase-I TDAQ system plan. The trigger path is on the left side and the readout to storage path is on the right. . .	23
3.3	A simplified L1Calo algorithm path from LAr and L1Muon data. From left to right, the input data is combined and summed into different sized cells, scanned with algorithms to meet specific physics targets before events of desired topology are accepted. . . . .	25
3.4	The increased granular data from ECAL for the Phase-I Upgrade of the LHC, with increased $\eta$ segmentation and additional depth information allowing improved probing of shower shapes. These are known as supercells and have dimensions of either $(\eta \times \phi)$ 0.1x0.1 or 0.025x0.1.	27

---

3.5	The predicted single electron efficiency ‘turn on’ curve for L1Calo in run 3 using simulated events. It can be seen that once the new Phase-I upgrade is applied, we anticipate a sharper efficiency turn on at a much lower L1 rate. This is especially true once an $\eta$ dependent energy calibration is applied. . . . .	29
3.6	The eFEX seedfinder algorithm. . . . .	30
3.7	A schematic of the MiniPODs physical position into the FPGA . . .	33
3.8	The channel mapping tables required to convert to and from global/local algorithmic information to hardware specific description of a supercell.	37
3.9	The procedures needed for generating the mapping tables in figure 3.8 in their entirety. . . . .	38
3.10	The class structure for accessing mapping information within online software. All the Phase-I related parts of the diagram were written/significantly altered by the author aside from the ‘EfexSim’ Package.	39
3.11	The four packets sent and parsed to assign an IP address. The FPGA firmware acts as the client. . . . .	40
3.12	The full packet structure for DHCP DISCOVER . . . . .	42
3.13	The FTM loopback setup at the University of Birmingham. . . . .	43
3.14	Installation of eFEX fibres . . . . .	45
3.15	The RAW LAr supercell energy output given to eFEX. Even with the system in its early form, the spread of data (Root Mean Square or RMS) can be seen to have different noise levels depending on the layer depth and rapidity of the cell. Depth is labeled in the form (P,M,F,B) standing for (Pre-Sampler,Middle,Front,Back) with separate colours. These can be seen to have similar shapes by cell. The RAW code has a zero value corresponding to 32 due to a subtlety of the analogue to digital conversion giving negative values. . . . .	47
3.16	Early attempts to match CPM (legacy) and eFEX (Phase-I) ROI (matching the leading ROI in each event) information together when a full set of eFEXs were not yet available (note the gap in $\phi$ coverage). Some kinematic correlations can be seen which directs debugging of the system. . . . .	49
3.17	The $e/\gamma$ L1 efficiency of the eFEX(eEM26) vs the CPM (EM22). As can be seen in conjunction with figure 3.18 this gives an improved maximum efficiency threshold at lower rates. This is derived on $Z \rightarrow ee$ events with a tag and probe method. VHI and M are isolation and calibration codes for the trigger devices. . . . .	50
3.18	The Level 1 rate on the day of removing the CPM based triggers from the menu. We see an immediate 5 kHz saving. . . . .	51
4.1	The Standard Model of particle physics. All fermions have observed left and right-handed interacting chiral parts with the exception of the neutrino. Hence, Heavy Neutral Leptons (HNLs) break this mass chiral symmetry with various resulting properties. . . . .	54
4.2	A simplified overview of HNL parameter exclusion space (red) with future developments in blue. This doesn’t include neutrino experiments.	59

4.3	The resonant and non-resonant HNL production probed at ATLAS [1].	61
4.4	Weinberg Model LHC production [1]	64
4.5	The tri-leptonic signal model for HNL prompt analysis. These final states are heavily suppressed in Standard Model processes due to the outgoing lepton number ( $L_{e/\mu} = -2$ ) being different to the incoming value ( $L_{e/\mu} = 0$ ). (a) is the previously probed signal whereas (b) is an example of what could be probed if flavour mixing is allowed for HNLs. This allows a way to circumvent LNV suppression.	66
5.1	Sub-Leading Lepton $p_T$ distributions of the Signal and background. It is clear this is the main discriminator of signal over background.	71
5.2	An example EW ssWW process. Here, the EW process with vertices totalling $\alpha^6$ dominates as it has the same back-to-back topology due to the colour charge.	85
5.3	An example QCD + EW WZ boson production process digram mediated with a gluon exchange. This is the main background with total coupling $\alpha^4\alpha_s^2$ .	86
5.4	Observables distribution used for Signal Region Design targeted cut removed	91
5.5	Shape and Monte Carlo Data agreement between the ssWW CR and SR.	92
5.6	Shape and MC Data agreement between the WZ CR and the SR.	94
5.7	Normalisation factors derived in the background only fit with Asimov data in the Signal Region (SR).	97
5.8	Pre-and postfit Distributions in SR and WZCR	98
5.9	Pre-and postfit Distributions in SR and WZCR	99
5.10	Summary plot of the regions before (a) and after (b) the blinded background-only fit.	100
5.11	Normalisation Factors derived in the $m_N = 1$ TeV fit.	102
5.12	Pre-and post-fit Distributions in SR and WZCR	103
5.13	Pre-and post-fit Distributions in CRs and VRs for $m_N = 1$ TeV	104
5.14	Summary plot of the regions before (a) and after (b) the $m_N = 1$ TeV fit.	105
5.15	Pruning plot for the blinded background-only fit. This shows which of the systematic variations are used in the profiled likelihood as they have quantifiably large impact on bin-by-bin event counts. This keeps the numerical minimisation of the likelihood stable. The individual systematic variations are outlined in chapter 6 and appendix C.	108
5.16	Gammas in the background-only fit.	109
5.17	Correlation matrix for the background-only fit, correlations smaller than 2% are not shown.	110
5.18	Pull plot of all nuisance parameters blinded background only fit	111
5.19	Ranking Plots	112
5.20	The smoothed systematic variations	115
5.21	An Illustration Of asimov-data discrepancy leads to under-constrained pulls	116

---

6.1	The background sample IFF Classification Scores (table 6.1) of the lepton pairs at pre-selection and in the Signal Region, this show that most of our non prompt background is from heavy hadronic sources. . . . .	120
6.2	Projections of figure 6.1 by sub-leading lepton. . . . .	121
6.3	Distributions of the ID (top) and Anti-ID (bottom) lepton $p_T$ for HLT_mu14 (left) and HLT_mu50 (right) in events with $n(b\text{-jet}) > 0$ . By taking the excesses of data in these distributions, we derive a fake factor. . . . .	124
6.4	The derived fake factor with binning such the distributions from various systematics variations can be compared. . . . .	126
6.5	Visualisation of functional form fits for smoothing hadronic fake estimates. . . . .	127
6.6	The tri-lepton mass distributions ( $m_{Zg}$ or $m_{\ell\ell}$ in the description) of the 4 validation regions. It can be seen from the peak at 90GeV in the data we are successfully selecting Zs with mis-reconstructed electrons and muons. The scale factor $\alpha$ is derived from the mismatch, aiming to rescale the Z+jets/ $\gamma$ MC. . . . .	133
6.7	IFF Class of third leptons in ZgammaCR, as can be seen it is much more successful at selecting electron fakes than muon fakes. The codes are listed in table 6.1. . . . .	134
6.8	Fake lepton $\eta$ distributions filtered to the desired IFF Class, which demonstrates the difference between $\gamma \rightarrow e$ and $\gamma^* \rightarrow \mu$ . The data is not included as we have filtered by the MC truth record which is impossible in data. . . . .	135
7.1	The pre- and post-, background-only fit signal region distributions, of which many features of statistical interpretations can be read off by eye. Most notably are the slight excesses in bins 1,2 and 5. . . . .	140
7.2	An event display of a candidate event in the final (high $p_T$ and HNL signal-like) bin in the signal region. The missing $E_T$ is 75GeV with significance of 1.1. The muons are the long outgoing tracks and the jets are in grey. . . . .	142
7.3	Pre-and post-fit distributions in same-sign WW (ssWW) and WZ CR	144
7.4	Pre-and post-fit Distributions in VRs . . . . .	145
7.5	The normalisation factors derived ( $\hat{\mu}$ s) in the background-only fit to the unblinded data. . . . .	146
7.6	Pull plot of all Nuisance Parameters . . . . .	146
7.7	The $\pm 1\sigma$ variations in the SR and Control Regions (CRs) of FF_FitModel that lead to an under constraint. The flip in up-down variations in the first two bins in figure 7.7a alongside the underestimate in these bins post-fit is the main cause. . . . .	147
7.8	The $CL_S$ limits for the analysis . . . . .	150
A.1	Pruning plot for the unblinded background-only fit. . . . .	168
A.2	Gammas in the unblinded background-only fit. . . . .	169
A.3	Correlation matrix for the unblinded background-only fit. . . . .	170

A.4	Pre-and post-fit Distributions in SR and WZCR for the unblinded $m_N = 1$ TeV fit. . . . .	172
A.5	Pre-and post-fit Distributions in ssWW CRs and VRs for $m_N = 1$ TeV unblinded fit . . . . .	173
A.6	Summary plot of the regions Pre-Fit (a) and Post-Fit (b) the $m_N = 1$ TeV fit. . . . .	174
A.7	Pre-and post-fit Distributions in SR and WZCR for the blinded Weinberg fit . . . . .	176
A.8	Pre-and post-fit Distributions in ssWW CRs and VRs for the blinded Weinberg fit . . . . .	177
A.9	Summary plot of the regions pre-fit (a) and post-fit (b) for the blinded Weinberg fit. . . . .	178
B.1	Candidate event in the penultimate bin ( $p_T^{\mu_2}$ between 100 and 120 GeV) in the signal region . . . . .	180

---

## DEFINITIONS OF ACRONYMS

---

**ALICE** A Large Ion Collider Experiment

**ASIC** Application-Specific Integrated Circuit

**ATLAS** A Toroidal LHC Apparatus

**BOOTP** Bootstrap Protocol

**CB** ComBined

**CERN** Conseil Européen pour la Recherche Nucléaire

**CMS** Compact Muon Solenoid

**CPM** Cluster Processor Module

**CPU** Central Processing Unit  
the conventional modern calculation component of a computer

**CP** Combined Performance

**CR** Control Region

**CT** Calorimeter-Tagged

**CTP** Central Trigger Processor

**DHCP** Dynamic Host Configuration Protocol

**EFT** Effective Field Theory

- EM** Electro Magnetic  
Refers to either classical electromagnetic phenomena or to particle showers (as opposed to hadronic)
- EW** ElectroWeak
- FEX** Feature EXtractor
- FPGA** Field Programmable Gate Array
- FTM** FEX Test Module
- GPU** Graphics Processing Unit
- HLT** High Level Trigger
- HNL** Heavy Neutral Lepton
- ID** Inner Detector
- IO** Inside-Out combined
- IP** Internet Protocol
- JEM** Jet/Energy processor Module
- JVT** Jet Vertex Tagger
- L1A** Level 1 Accept
- L1Calo** Level 1 Calorimeter trigger
- L1Muon** Level 1 Muon trigger
- L1Topo** Level 1 Topological processor
- LATOME** Liquid Argon Trigger prOcessing MEzzanines
- LAr** Liquid Argon  
The Name and Unique Material of the ATLAS EM Calorimetetry
- LHCb** LHC-beauty
- LHC** Large Hadron Collider  
Superconducting collider occupying the 27 km ring at CERN.
- LNC** Lepton Number Conservating
- LNV** Lepton Number Violating
- LTDB** LAr Digital Processing Blade
- LO** Leading Order

**MC** Monte Carlo  
Integration and broad term used for signal and background modelling

**ME** Muon-spectrometer Extrapolated

**MGT** Multi Gigabit Transceiver

**NLO** Next-to Leading Order

**PDF** Parton Distribution Function

**PMNS** Pontecorvo–Maki–Nakagawa–Sakata matrix  
the phenomenological mass matrix for neutrino oscillations

**PPM** Pre-Processor Module

**QCD** Quantum ChromoDynamics

**QFT** Quantum Field Theory

**RAM** Random Access Memory

**RARP** Reverse Address Resolution Protocol

**RF** Radio Frequency

**ROI** Regions Of Interest

**RTM** Rear Transmission Modules

**SCT** ATLAS SemiConductor Tracker

**SR** Signal Region

**ST** Segment-Tagged

**TDAQ** Trigger and Data AcQuisition

**TOB** Trigger OBject

**TRT** Transition Radiation Tracker

**VBS** Vector Boson Scattering

**VHDL** Very high speed integrated circuit Hardware Description Language

**VR** Validation Region

**UDP/IP** User Datagram Protocol/Internet Protocol

**csv** comma separated variable

**eFEX** electron FEX

**gFEX** global FEX

**jFEX** jet FEX

**ssWW** same-sign WW



# CHAPTER 1

---

## Introduction

---

Physicists have used scattering experiments to probe the nature of reality since the 1900s and the discovery of the Rutherford model of the atom [2]. A century on, we precisely design experiments that can probe Quantum Field Theory within the Standard Model framework to derive precise observations about how these phenomena behave. As such, we can generate precise simulations of hypothesized Beyond the Standard Model phenomena and test our understanding of the world.

The apparatus and techniques required to capture these collisions and test these hypotheses have immeasurably increased in complexity. This is to such an extent that it is impossible to design, build, run and analyse data from these experiments without the support of thousands of people. This thesis outlining one of the thousands of ATLAS analysis papers is standing on the shoulders of giants.

In this thesis, the author's two main contributions to the ATLAS collaboration

between 2019 and 2023 are outlined. Chapter 2 gives a basic overview of the LHC and ATLAS. Then in chapter 3, this thesis contextualises and outlines the ongoing work of upgrading the Level 1 Calorimeter Trigger through various software, firmware and hardware tasks. The second half of the thesis is on Heavy Neutral Leptons and mass mechanisms for neutrinos. Chapter 4 gives an experimentalist's take on the theory of these models. Chapters 5 to 7 takes this theory to describe a high mass di-muon HNL search from signal simulation through to unblinded results.

---

# The Large Hadron Collider and the ATLAS Experiment

---

## 2.1 The LHC

The LHC is the world's largest particle accelerator to date [3]. It is capable of colliding protons and heavy ions together at higher energies than ever before. This allows us to probe deeper into high-energy and rare physics processes. As transverse beam size becomes reduced when the beam energy is increased, it is typical for cost reasons to 'inject' from smaller pre-existing accelerators to larger ones. As a result, the LHC uses previous accelerators at CERN in a chain (see figure 2.1). The accelerator complex must be built underground to shield the detectors from cosmic background radiation alongside protecting the outside world from ionising radiation from the LHC.

The LHC is a synchrotron, which is a circular design of accelerator. The key first

parts to design such a machine are dipole magnets and Radio Frequency (RF) cavities. The dipole magnets bend and create a nominal trajectory for the charged particles to traverse. The RF cavities are waveguides that provide an oscillating Electro Magnetic (EM) field in the direction of the beam. By adding the particles to the beam in bunches (RF buckets) and carefully managing timings, we can ensure that particles get boosted forward every time they pass through the cavity. Furthermore, particles different from the nominal energy can get corrected by having late particles experience a stronger E field and vice versa [4]. The period of these bunches is 25ns.

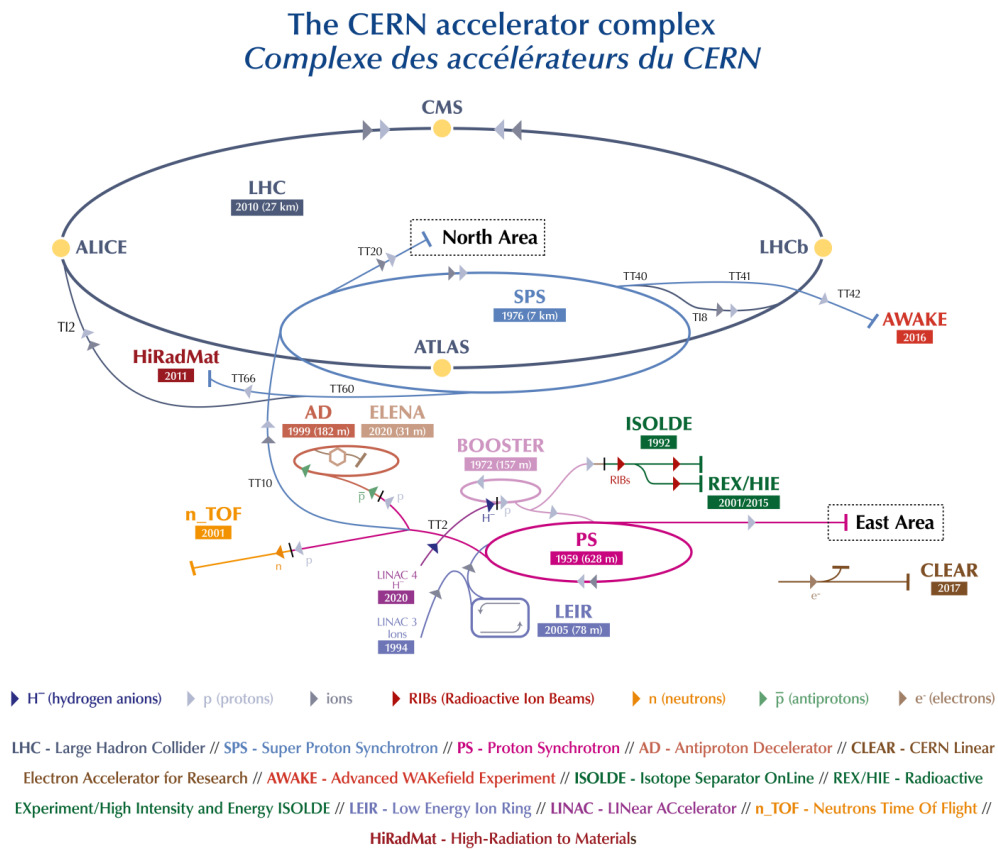


Figure 2.1: A schematic of the whole CERN accelerator complex which acts in part to inject protons/ions into the LHC [5].

To have the highest energy beam possible for proton collisions, we are primarily driven by tunnel building costs and the strength of the dipole magnets to hold the beam. As a result, this means we require cutting edge scalable magnet technology. This is done through superconducting magnets that require a large array of cryogenic

equipment across the ring.

Alongside acceleration and steering, accelerators use quadrupole magnets to focus the beam to a smaller size in a very similar way to a set of lenses to first order. Even higher order corrections are made in the magnetic field to avoid instabilities driven by subtle effects of resonant trajectories (tune) [4, 6].

Then, once a beam is stabilised, it must be understood and characterised to know how many physics collision events we expect in a given collision. The standard metric is luminosity ( $\mathcal{L}$ ). This can be shown to be a function of the beam geometry and proportional to the number of protons present in the bunches. Given a theoretical cross-section of a particular process from Quantum Field Theory (QFT) ( $\sigma$ ), we can combine to get a rate (equation (2.1)).

$$\text{Event rate} = \mathcal{L} \times \sigma \tag{2.1}$$

Luminosity is typically precisely calibrated through Van der Meer scans [7]. By sweeping the beams gradually across one another at the interaction point and using well-known rate events as a baseline, it is possible to deduce the instantaneous luminosity. From careful bookkeeping, we can as a result know how many events we expect to see in our outgoing data. The total number of events is found by integrating luminosity over time. Given a particular signal in data we can also perform this procedure in reverse to deduce a cross section.

As part of the LHC's physics programme, the energy and luminosity of the beam are being ramped up. This is shown in detail in figure 2.2. Run 1 was between 2010 and 2012 with energies at 7 and 8 TeV at 75% target instantaneous luminosity. In Run 2 (2015-2018) the energy reached 13 TeV and luminosity ramped to double. During the research undertaken in this thesis, Run 3 started. During this, the LHC reached 13.6 TeV. In the upcoming LHC runs, the experiment approaches the High Luminosity frontier (HL-LHC). This has a variety of detector technology challenges

due to higher backgrounds; the parts relevant to the ATLAS trigger are discussed in chapter 3.

Obviously, the upgraded performance of the LHC has benefit for the experiments that use the beamline. The LHC has a large variety of experiments surrounding the LHC collision points. ATLAS and the Compact Muon Solenoid (CMS) are the two general purpose detectors that were created with one of the main purposes being the Higgs discovery [9, 10, 11, 12]. Since the success of the 2012 discovery, work is being done to precisely pin down the Higgs boson's properties alongside many other tests of the Standard Model including probing previously unexamined exotic model parameter space. This will be done from the HL-LHC alongside theoretical and experimental progress. Similar developments are taking place with precision flavour physics at LHC-beauty (LHCb) and A Large Ion Collider Experiment (ALICE), which uses heavy ion runs to probe quark gluon plasma and the strong force.[13, 14]

The remainder of this thesis focuses on ATLAS' part in these developments.

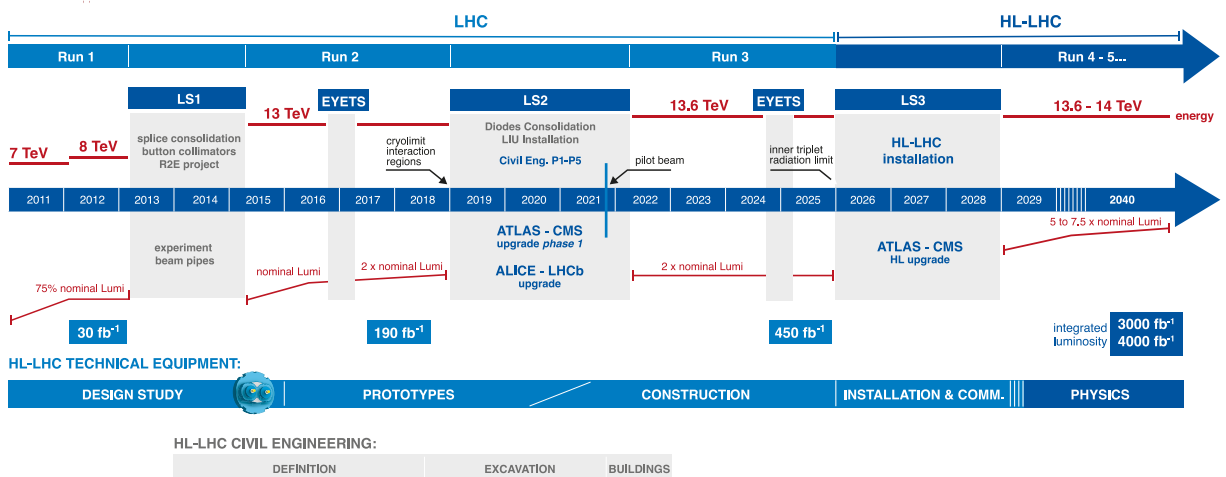


Figure 2.2: The projected luminosity and energy profile for the LHC between 2010 and 2040 [8].

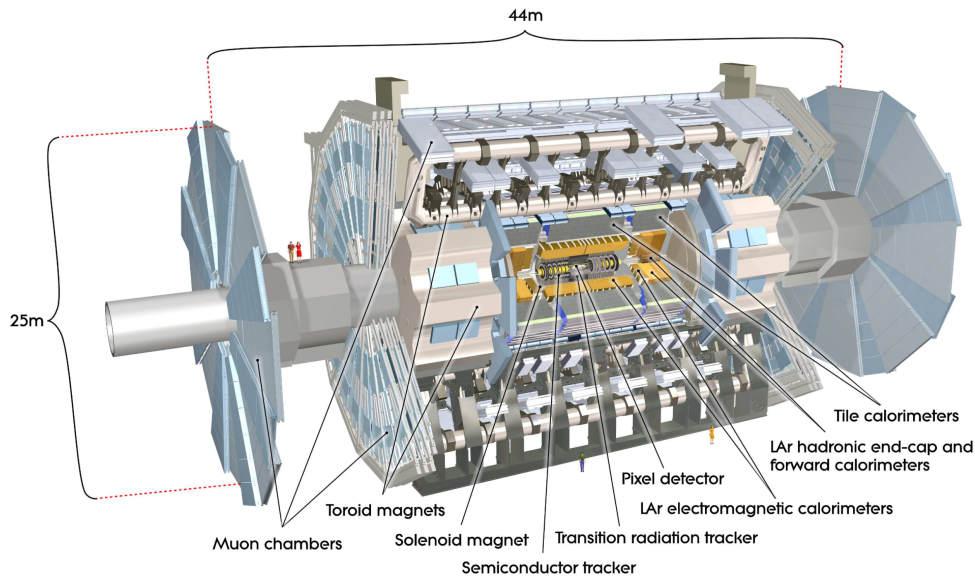


Figure 2.3: The ATLAS Detector cut-away diagram. [9].

## 2.2 The ATLAS Experiment

The ATLAS experiment (figure 2.3) is a cylindrical general purpose detector with hardware built to distinguish rare processes from proton collisions and to precisely measure the kinematic quantities of the outgoing states [9]. From the interaction point outwards we broadly have four methods to extract information from the event:

1. Tracking, which allows reconstruction of the charged particle trajectories through the detector as well as the measurement of the transverse momenta deduced from the bending in a magnetic field.
2. Transition radiation measurement, which provides additional means of identifying electrons and rejecting light hadrons alongside space points that improve momentum resolution.
3. Calorimetry, which measures energy deposits and shapes through inducing showers.
4. Muon Spectroscopy, which uses a secondary magnetic field to identify and measure muons that travel through the detector with minimal scattering.

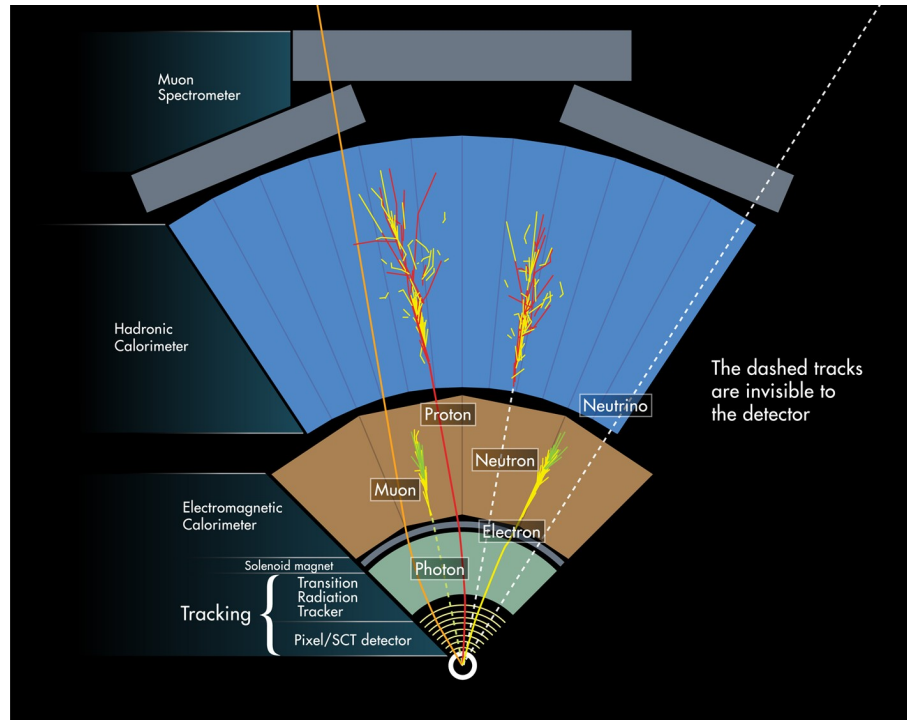


Figure 2.4: A rough cross section schematic for how different particle travel through and interact with the ATLAS detector [15].

These layers are visualised in figure 2.4 for different outgoing particles from a collision. Some of the specific designs within the detector are now discussed before explaining some of the work that is done to combine the data together for physics analysis.

## 2.3 Preliminary Definitions

The ATLAS experiment itself follows a coordinate system common to most collider experiments where the  $xy$  plane is placed perpendicularly to the beam direction. The  $x$  axis points towards the center of the LHC ring and the  $y$  axis points vertically. The origin is in the geometric center. Then, by construction, the  $z$  axis points anti-clockwise with respect to the LHC. The ATLAS experiment uses the standard physics convention of spherical coordinates. To easily construct Lorentz  $z$  boost invariant observables the following definitions are used. Here we use the standard four-momentum notation  $(E, p_x, p_y, p_z)$  with the speed of light  $c = 1$ .

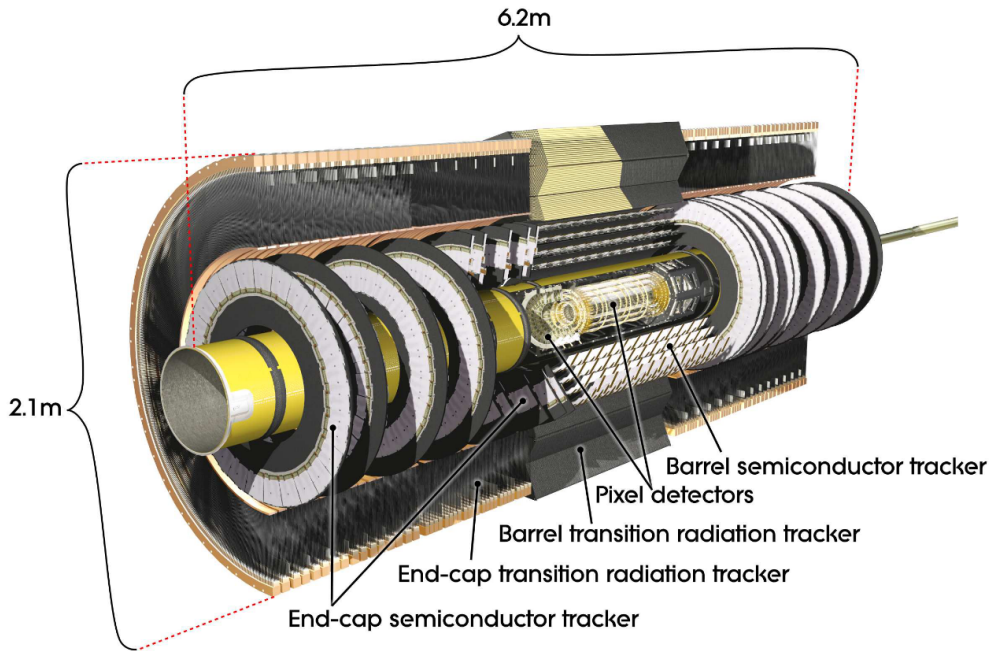


Figure 2.5: A schematic of the inner detector with the small, more spatially precise silicon pixels clustered around the centre [16].

- Transverse Momenta  $p_T$ : the three momenta projected into the  $xy$  plane of the detector
- Rapidity and Pseudo Rapidity: the rapidity  $y$  is formally given by equation (2.2). This has the property that  $y_1 - y_2$  is boost invariant in the  $z$  direction [17].

$$y \equiv \frac{1}{2} \ln \left( \frac{E + p_z}{E - p_z} \right) \quad (2.2)$$

A more experimentally realisable variable is the pseudo rapidity  $\eta$  (often called rapidity as well) which is the ultra-relativistic limit of rapidity which only depends on  $\theta$  (the angle with respect to the  $z$  axis).

$$\eta = -\ln \tan(\theta/2) \quad (2.3)$$

- The azimuthal angle  $\phi$ , which is already boost invariant.
- The transverse calorimeter energy deposits  $E_T$ , are a summed vector quantity in the  $xy$  plane, will also be relevant later.

Hence for an ultra-relativistic particle (as most outgoing detectable particles are to first order) we can write the four momentum as  $(E, p) = (p_T \cosh \eta, p_T \cos \phi, p_T \sin \phi, p_T \sinh \eta)$ .

## 2.4 Tracking Detector

The ATLAS Silicon Tracker is the closest part of the detector to the interaction point. This consists of silicon devices built to detect the path of high-energy charged particles through ATLAS's 2T solenoidal magnetic field [16]. By exploiting the band structure of silicon, we can build devices that generate electron hole pairs ( $\sim 25000$  per junction) that create a detectable current when high-energy charged particles pass through. To make this current visible over leakage currents and have fast enough response for a high event rate, doped p-n diode junctions must be used with a reverse bias voltage applied [18].

These sensors have the geometric layout shown in figure 2.5. Towards the interaction point geometric precision is key, and therefore, small pixel sensors are used. However, at larger radii this becomes cost ineffective. Moreover, you do not see the same performance improvement as the particles are already spread out from the interaction point. Hence cheaper silicon strips are used with larger dimensions. These cover phase space up to  $|\eta| < 2.5$ . The devices output binary 'hits' that are reconstructed into curved tracks. The radii ( $R$ ) of these curved charged ( $q$ ) tracks in the magnetic field tells us the transverse momenta given by the approximate form given in equation (2.4). In reality, the magnetic field varies with the displacement and a numerical solution must be derived.

$$p_T \approx 0.6qR \text{ [GeV] with a magnetic field of 2 T} \quad (2.4)$$

When reconstructing events, extensive computational power is devoted to tracking due to the sheer number of sensors and the combinatorial logic required. The many

tracks formed are described by following the convention given in the form (2.5).  $d_0$  and  $z_0$  are the transverse and longitudinal distances of closest approach from the primary collision point<sup>1</sup> and  $q/p$  is the charge/momentum fraction the tracker is sensitive to. The significance  $d_0/\sigma(d_0)$  of a given track compared to its resolution is a key parameter in tagging b-hadron decays.

$$(d_0, z_0, \theta, \phi, q/p) \tag{2.5}$$

As each LHC collision in nominal running conditions contains many scattering events with a positional spread ( $\sigma_z \sim 30\text{mm}$  and  $\sigma_{xy} \sim 10\mu\text{m}$ ), these tracks must be assigned to a scattering event at a given ‘vertex’. When looking for energetic processes, we typically have primary and secondary vertices [19]. Primary vertices are used to find the original collision point. Secondary vertices are found by looking for additional vertices using only tracks within the jet<sup>2</sup>.

To target c- and b-hadron decays which have detectable decay length, additional reconstruction is done to search for these secondary vertices alongside the incompatibility of some tracks with the primary vertex (IP3D) [20]. This type of information is combined for different physics cases (see section 5.2.5).

## 2.5 Transition Radiation Tracker

The outermost layer of the inner detector ( $0.5\text{m} < \text{Radius} < 1\text{m}$ ) has a dual functionality. The Transition Radiation Tracker (TRT) contains an array of gas-filled (70% Xenon, 27% CO<sub>2</sub> and 3% Oxygen) cylinders with a small gold-plated tungsten wire in the centre. If a voltage is applied between the cylinder and the wire, a current is generated when a charged particle passes through (similar to the ATLAS SemiConductor Tracker (SCT)) [21]. Additionally, with the aid of polymer fibres and foils in these regions we can generate transition radiation. This is caused by

---

<sup>1</sup>The point/vertex with the highest summed  $|p_T|^2$  of tracks associated with it.

<sup>2</sup>section 2.6 introduces the notion of a jet

charged particles travelling through the boundary of two dielectric media. These photons cause greatly amplified signals from the Xenon in the tubes.

The amount of transition radiation strongly depends on how ultra-relativistic the particle is. This is described by the gamma factor  $\gamma = \frac{E}{m}$ . An important part of the physics performance of ATLAS is to distinguish pion signatures from electron signatures. Due to pions being  $\sim 300$  times heavier, we greatly improve our ability to distinguish between the objects over large energy ranges. The tracking itself, only provides radial and angular tracking information but no longitudinal resolution beyond the sign of  $\eta$ . The combined silicon and transition radiation tracker is known as the Inner Detector (ID).

## 2.6 Calorimetry

Calorimeter design is broadly split into two regimes: electromagnetic and hadronic. The goal for both is to measure total energy and shapes (for identification) from the outgoing high-energy particles from the collisions. After having a reduced interacting material budget in the tracker, the calorimeters are designed so that most particles will fragment. This generates a measurable electrical signal that can be calibrated to an energy. This process is known as a shower or jet which is where a high-energy particle from the collision scatters off material, producing more particles (i.e. for EM showers: Bremsstrahlung, pair production and multiple scattering). These, in turn, scatter, forming a cascade. This stops most of the particles before they leave the detector. Showers formed by hadronic and electromagnetic particles have distinct scattering phenomena, which lead to different amounts of signal generated for the same incoming energy. Due to this and the fact that hadronic showers penetrate deeper, we construct electromagnetic and hadronic calorimetry to optimise for both types. This can be seen visually in figure 2.4.

This presents a wide variety of technological and theoretical challenges. Shower

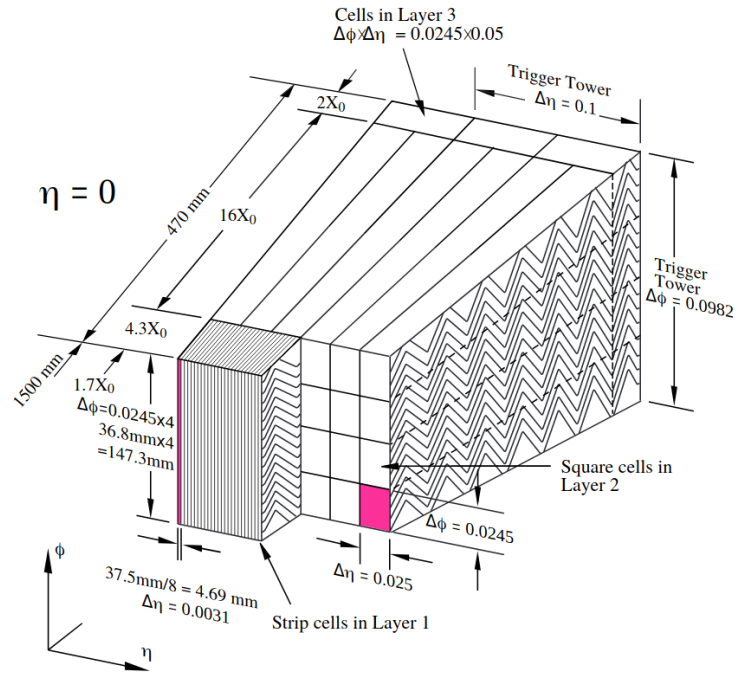


Figure 2.6: A schematic of the accordion geometry ECAL for the ATLAS experiment [23].

formation is reasonably stochastic and requires theoretical approximations to generate [18, 22]. Moreover, hadronic showers have significant energy deposits that cannot be captured as a signal.

For the electromagnetic calorimetry at ATLAS, a sandwich calorimeter of lead and Liquid Argon (LAr) is used. The passive lead induces more showers whilst the active LAr generates ionisation currents that form a signal. These currents induce a signal in the electrodes following the accordion geometry of the cells (figure 2.6). This allows for the construction of a self-supporting structure (no dead space) that can be easily segmented into the desired lateral and longitudinal cells [18]. This does not significantly affect resolution due to the fact that the Compton and photoelectric effect showers are produced uniformly in angular space [22].

The geometry of the ECAL leads to precision shower information up to  $|\eta| < 3.2$ . There is additional forward calorimetry using LAr technology up to  $|\eta| < 4.9$ , which is optimised for higher backgrounds from soft scattering. At  $|\eta| < 1.8$  there is an

additional ‘pre-sampler’ layer of LAr to correct energies of photons and electrons showering upstream of the detector.

An extensive amount of research was spent in converting the analogue current response to the energy of the cells of the calorimeter with a response time of  $\sim 600\text{ns}$  into a digital energy signal for trigger and readout. It is paramount to the performance of the detector as a whole that the cell’s output represents the right energy from the right bunch crossing. This is achieved through bipolar pulse shape electronics, which purely rely on the large initial increase in current and ignore the slow decaying tail (figure 2.7).

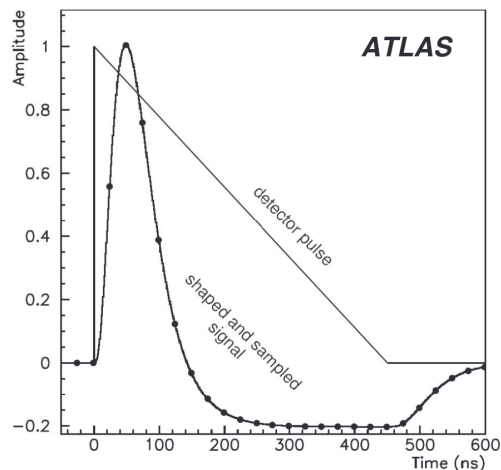


Figure 2.7: The bipolar response of the LAr detector (curved and dotted line) compared to the original analogue signal directly from the calorimeter cells (triangle waveform) [23]. This captures the energy deposit with a faster response time that can still be reconstructed to the correct bunch crossing with frequent collisions.

The hadronic calorimetry for the central region of the detector is provided by the Tile Calorimeter ( $|\eta| < 1.7$ ). For extended rapidity, the hadronic calorimetry is provided through the hadronic end cap ( $1.7 < |\eta| < 3.2$ ) provided by LAr. The Tile Calorimeter uses different material selections to optimise the hadronic response for its sandwich calorimetry. It uses steel plates as the passive layer and scintillation tiles with wavelength-shifting fibres to be read out by photomultipliers. It also has a dual purpose of being the flux return for the solenoid for the tracker.

## 2.7 Muon spectroscopy

The final layer of the ATLAS detector is the muon-spectrometer (visualised in figures 2.4 and 2.8) [24]. Muons have a relatively small interaction cross-section with matter and a long decay length, so they pass through the rest of the detector mostly unhindered. Using sets of toroidal magnetic fields and similar signal production mechanisms to the TRT, the muon spectrometer provides additional identification and  $p_T$  reconstruction power. There are four kinds of detectors within the muon system with different use cases:

- Thin gap and resistive plate chambers in the end cap and barrel respectively provide the fast reconstruction needed for triggering.
- The monitored drift tubes (barrel) and cathode strip chambers (endcap) respectively provide the higher precision measurement for offline reconstruction.

This provides coverage up to  $|\eta| < 2.7$ .

Using this dedicated hardware alongside the ID and calorimetry, muon objects are reconstructed through various classifications [26]. Muon tracks can be reconstructed purely by the spectrometer through a local hough transform [27] of various smaller sectors before a global  $\chi^2$  fit is applied. Muon tracks can also be flagged in the ID and through the minimally interacting calorimeter deposit shape.

These are then formed into higher level reconstruction objects. ComBined (CB) muons take the spectrometer tracks and complete a global fit with matched ID tracks. Inside-Out combined (IO) objects search for muon hits from ID tracks, then use a global fit. Muon tracks with no matchable tracks in the ID are called Muon-spectrometer Extrapolated (ME) (compensating for the lack of ID for  $2.5 < |\eta| < 2.7$ ). Segment-Tagged (ST) muons are ID muons with angular matching requirements to the muon spectrometer, but uses only ID to determine the kinematics and vertexing. Finally, Calorimeter-Tagged (CT) muons take ID tracks and add look for energy

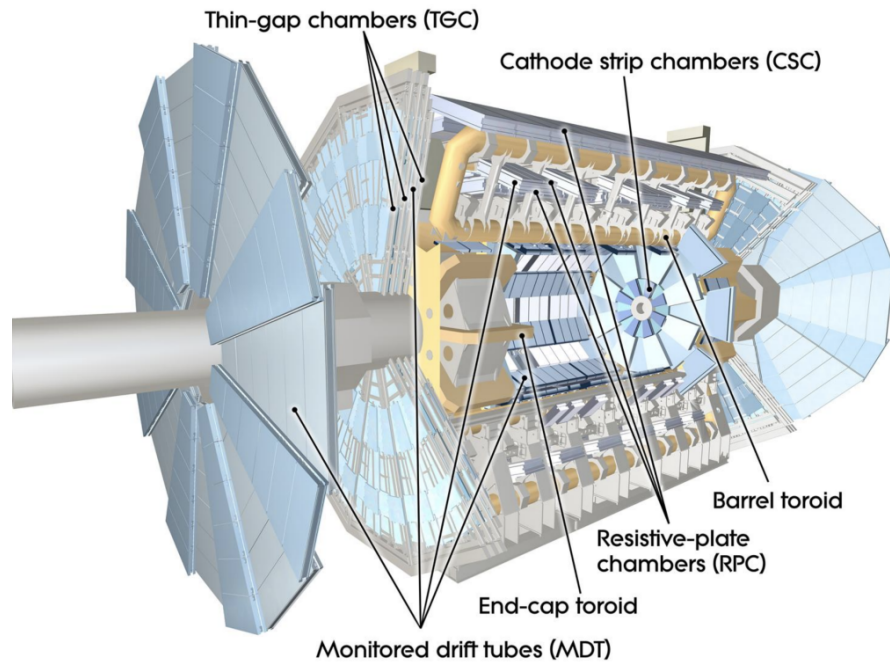


Figure 2.8: The layout of the muon spectrometer surrounding the rest of the detector [25].

deposits consistent with a minimally-ionising particle. These help fill a gap in rapidity coverage at  $|\eta| < 0.1$ .

## 2.8 Combined Performance

As is clear, the experiment has a large number of complex working parts alongside huge theoretical frameworks to simulate events and detector responses<sup>3</sup>. As a result, it is key to have dedicated groups with the objective to optimise the performance of selecting and measuring key physics objects in data and calibrating the corresponding kinematic information. These are known as Combined Performance (CP) groups. There are six of these groups:

- $e/\gamma$ : Electron and photon identification performance
- Flavour tagging: Identification of heavy flavoured quark content in jets

<sup>3</sup>Particulars of the simulation are discussed in section 5.3.

- Jet &  $E_T$ : Encompasses a lot of features, including jet clustering and ‘missing’ energy lost through neutrinos or Beyond Standard Model (BSM) non-interacting particles.
- $\mu$ : Muon identification and measurement
- $\tau$ : Tau identification and measurement
- Inner Tracking: Performance of the inner tracker

A major output of these groups is sets of ‘working points’. These are parameter sets that give a known efficiency and background rejection, optimised to identify particles in offline data. In principle, the job of reconstructing particles can be abstracted away from an analysis user. In reality, a user needs a reasonably good knowledge of the experiment to understand the data with respect to detector performance.

For later discussions in chapter 5, it is useful to discuss the muon and jet performance output from these groups.

For muons, the various objects defined in section 2.7 are used to generate the working points of isolation and efficiency. These are discussed in depth in [26]. For this thesis, the relevant working points are Medium and Loose. Medium only accepts CB and IO muons<sup>4</sup> with ME for  $2.5 < |\eta| < 2.7$ . Loose contains all Medium muons but also allows CT and ST for the gap at  $|\eta| < 0.1$  alongside less relevant low  $p_T$  corrections. The resulting efficiencies estimated on simulation are given in figure 2.9.

There exist many performance measures for jets to calibrate the reconstructed energy to be as close to the true value of the outgoing particle as possible. The most recent summary of these calibrations is given in [28]. An example of a performance metric is the mean of the Gaussian ratio between  $E_{T,\text{reco}}$  and  $E_{T,\text{truth}}$  on di-jet events (figure 2.10). These studies are used in systematics (appendix C). What can be seen is that the data-simulation agreement is poorer at high- $\eta$  and energies. This is what the analysis in chapter 5 targets, so it is relevant in our later statistical studies.

---

<sup>4</sup>98% of events in the standard  $t\bar{t}$  metric sample are CB

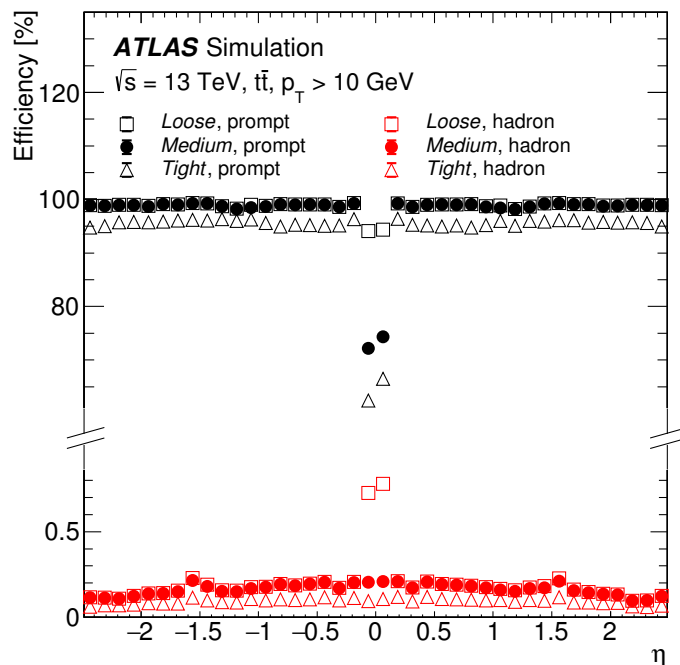
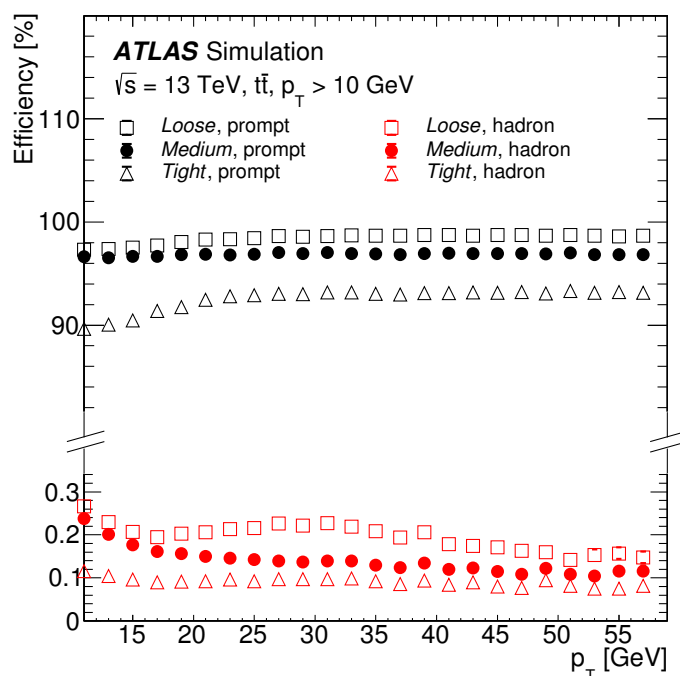
(a) Efficiency in  $\eta$ (b) Efficiency in  $p_T$ 

Figure 2.9: The run 2 prompt muon identification efficiency (with respect to simulation truth information) as a function of  $\eta$  and  $p_T$  for the Loose, Medium and Tight working points. The prompt muons are in black and the non-prompt heavy hadronic decays are in red [26].

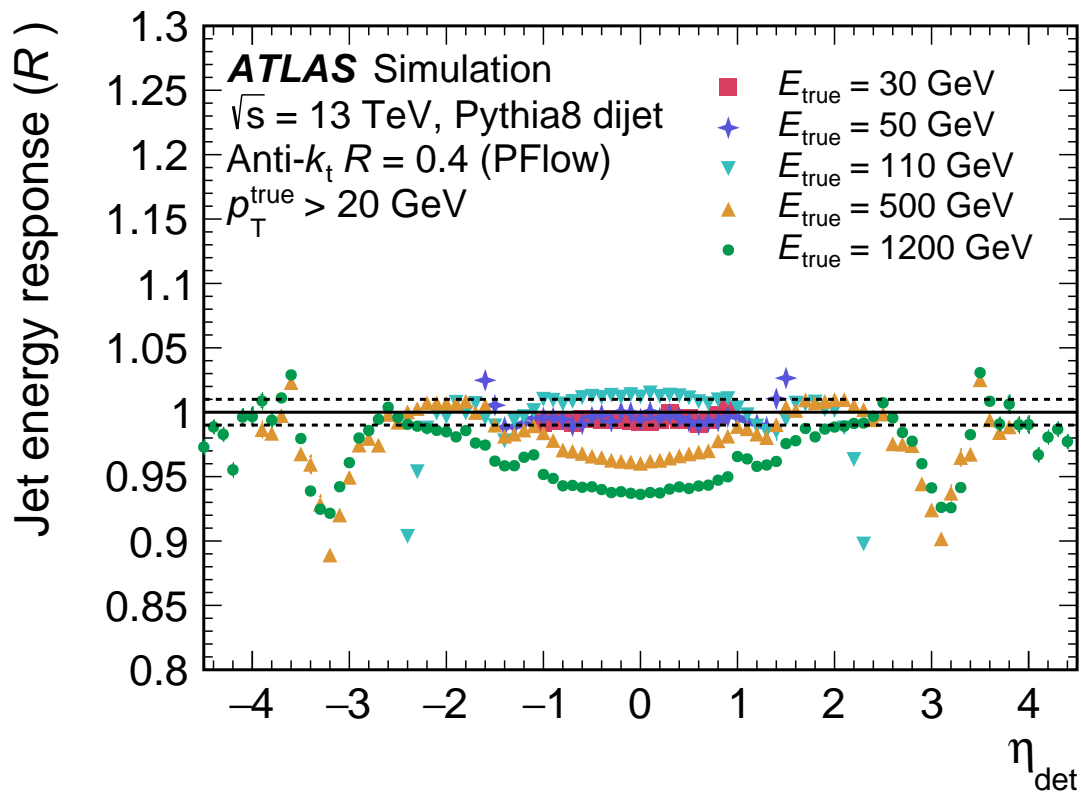


Figure 2.10: Mean of a Gaussian fit of  $\frac{E_{T,\text{reco}}}{E_{T,\text{truth}}}$  as a function of truth rapidity and energy on a collection of simulated di-jets [28]. It can be seen that the performance is better for low energy central jets and weaker for high-energy forward jets.

---

### L1Calo Phase-I Upgrade

---

#### 3.1 The Level 1 Calorimeter Trigger

This section of the thesis discusses the details of the author's work in online software/firmware for the Level 1 Calorimeter trigger (L1Calo) upgrade. To do so, the general context and challenges of Trigger and Data Acquisition (TDAQ) in particle physics are described before discussing ATLAS's Calorimeter trigger. How and why it is currently being upgraded for the next run of the LHC is outlined before the hardware and software needs for this new system are explained. This includes the need for a well-documented and optimised mapping of the data from the calorimeter to trigger hardware alongside gradually more complex dataflow tests. More tasks prior to the start of run 3 of the LHC, including an example of firmware development, are shown. Finally, some early performance results from ATLAS run 3 are presented.

### 3.1.1 Trigger and Data Acquisition at ATLAS and The LHC

Particle physics has always been at the forefront of what has been possible to collect large volumes of data from a single piece of apparatus. Naturally, for a complex experiment such as a LHC detector, very high-speed electronics are required to process and read out data. Moreover, there is a cost and technology limit on how much data we can store permanently on disks and tape. Currently, in most contexts, this is significantly less than what is required to store information about every collision. Furthermore, the detector components themselves cannot read out every event.

Hence, experiments must rely on triggers to pick which events are interesting to store. The events required to test the Standard Model beyond our current understanding are rare (fractions ranging from  $10^{-3}$  to  $10^{-9}$  are commonplace in the field). Triggers are optimised to pick out signal features that have minimal overlap with commonplace background events.

There exist numerous metrics to measure TDAQ quality. A few useful ones for contextualising ATLAS's system are as follows. Event rate (typically measured in Hz) gives the number of events inputted and outputted from algorithms per second. This can be combined with the event size ( $\sim$ GB) to give a bandwidth. Latency is the total time for a part of the trigger to decide whether to accept an event to pass to the next trigger or storage. This is critical because the longer the decision takes, the more intermediate data buffers are needed to keep data temporarily before a decision is made. This can be very costly for large systems. Finally, dead time may need to be considered if a detector takes a considerable amount of time to retrieve detailed data for analysis. More modern TDAQ systems make this effect is smaller and more mitigable.

As the physics case and detection methodology for experiments can be very different, the choice of these parameters varies. This is illustrated through figure 3.1. If you are probing more complex events with lower rarity, you may choose a system with a large

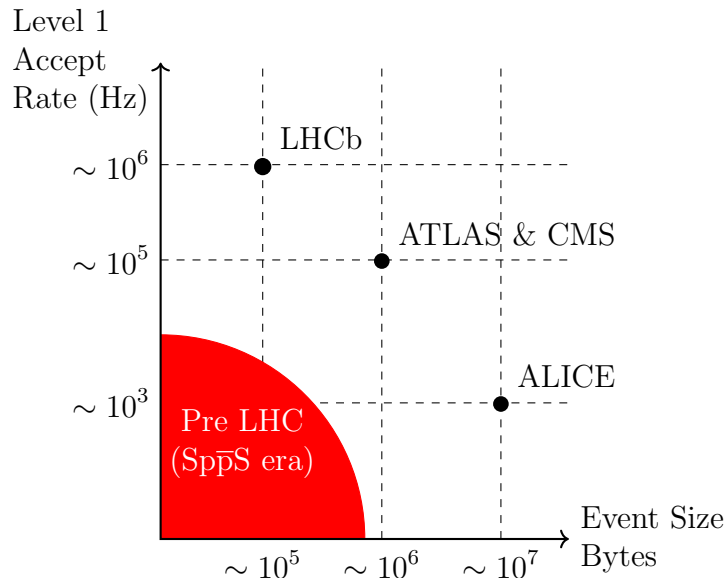


Figure 3.1: The ‘frontier’ Level 1 Hardware trigger read-out for different LHC experiments. Ultimately, a compromise must be found between event data size and acceptance rate as we are limited by read out and storage costs (inspired by [29]).

event data size (such as ALICE, a heavy ion experiment) and a lower rate. However, if events are rarer and large statistics are required (i.e. flavour physics/LHCb), then a smaller event size can be chosen to accept more events in hardware triggers.

General purpose detectors (ATLAS and CMS) occupy somewhat of a middle ground, primarily searching for rare ElectroWeak (EW) processes. For ATLAS, a two-level trigger system is used (figure 3.2). The first level takes data directly from the detector and uses dedicated fixed latency hardware to reduce the event rate from 40MHz to 100kHz using Calorimeter and Muon data (L1Calo and Level 1 Muon trigger (L1Muon)). This has at most a  $2.5\mu\text{s}$  latency. Events that pass these selections trigger Level 1 Accepts (L1As). The second level is done by the High Level Trigger (HLT) with more conventional hardware (commercial CPUs) and has a significant amount of flexibility, both algorithmically and in terms of latency. The HLT aims to put events to storage at roughly 1kHz. The HLT also manages the broader task of generating various categories of reconstructed object combinations and the various physics and instrumentation cases for them. These are known as chains and streams, which together form the ‘menu’. For example, a muon chain

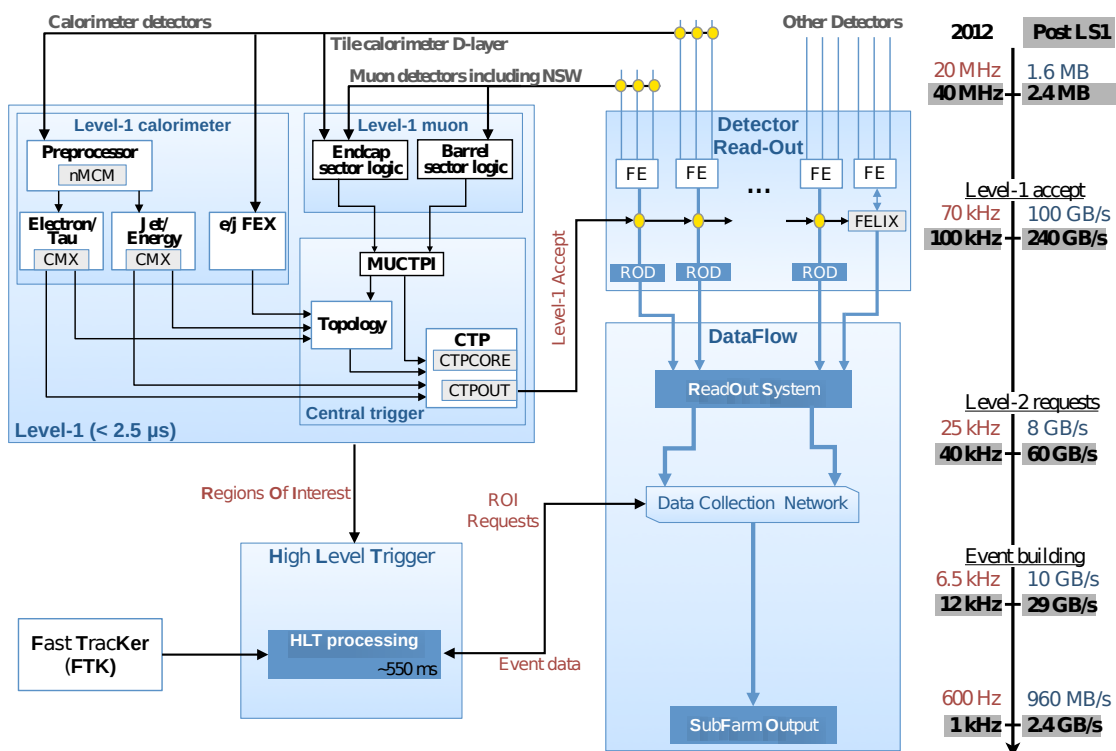


Figure 3.2: A rough overview of the planned Phase-I TDAQ system. The trigger path is on the left side and the readout to storage path is on the right [30]. A simplified L1Calo only diagram is given in figure 3.3. gFEX (discussed later) was previously considered an optional extra and was not included in the diagram. The FTK was dropped from the plan.

could be denoted HLT\_2mu14\_L12MU10 (A HLT chain with 2 muons at threshold 14 and 2 L1 muons at threshold 10 which *very* roughly corresponds to  $p_T$  in GeV). The streams are classified into many categories, most notably “physics main” for physics analysis. Many other streams exist for different calibrations, debugging and types of LHC run.

This structure also allows for ‘prescaling’, where a trigger only accepts a predefined fraction of events to have a manageable read-out rate in the HLT. This process is also applied at L1 (see section 3.2.3).

### 3.1.2 L1Calo System And Upgrade Overview

To make the 2.5  $\mu$ s decision, L1Calo consists of a chain of fixed latency boards connected with high-speed optical fibres, resulting in a L1A. An overview of the algorithm path is given in figure 3.3. Data is received from calorimeters by the fixed latency algorithm modules. These identify local object signatures and measure global event properties (discussed in detail in section 3.1.3). The results are then sent to the Level 1 Topological processor (L1Topo) with L1Muon data. This checks if the algorithm outputs pass thresholds to be triggered on and counts objects that pass each threshold. It also combines different types of objects based on their energies and angular separation to form more complex L1 menu items. L1Topo sends the multiplicities and combinations to the Central Trigger Processor (CTP). The CTP then generates the L1A decision. How the relative rate and threshold of menu items is decided is a highly complex one weighing the priorities of all users.

Between run 2 and run 3, L1Calo performed the Phase-I upgrade, which introduced improvements to the calorimeter data and to the algorithm boards. This will be motivated and elaborated in section 3.1.5 and beyond.

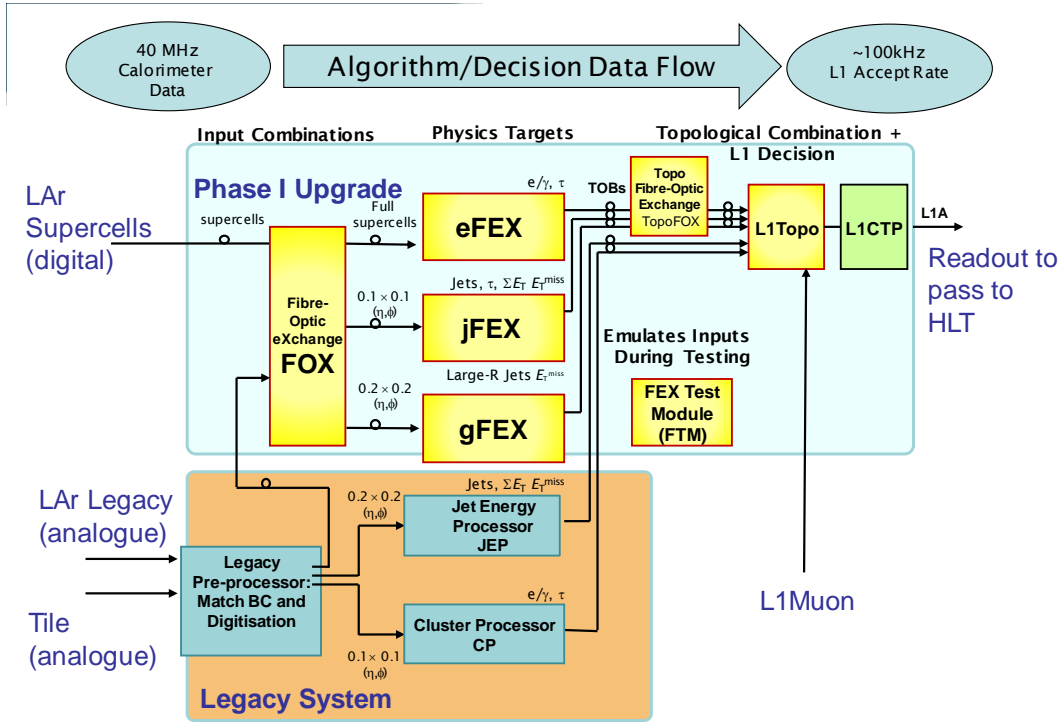


Figure 3.3: A simplified L1Calo algorithm path from LAr and L1Muon data. From left to right, the input data is combined and summed into different sized cells, scanned with algorithms to meet specific physics targets before events of desired topology are accepted. Adapted from [31]

### 3.1.3 Physics Aims of L1Calo

L1Calo represents the set of hardware electronics that analyse the signals from the calorimeters and generates the physics items desired to create ‘accepts’ for Read Out buffers and the HLT.

This is split into 5 categories:

1.  $e/\gamma$ : Here we target selecting electromagnetic showers, which are typically narrower than their hadronic counterparts (see section 3.2.2 for more depth).
2.  $\tau$ : Similarly targeting hadronic tau decay signatures, these use similarly motivated algorithms to  $e/\gamma$ . Due to the lost energy through neutrino productions and more similar topology to the jet background, the truth energy threshold is

higher.

3. Jets: Selecting the most interesting high- $p_T$  events that originate from strong force QCD interactions, partially based on the number of jets. Jets at L1 come in two sizes in  $\eta, \phi$ : denoted small and large. Small-radius jets target individual particles. Large-radius jets form larger clusters targetting collimated heavy decays such as boosted Higgs decays into b-quarks.
4. Missing transverse energy: using missing momentum to indicate a weakly interacting particle has been produced.
5. Total transverse energy: ensuring any sufficiently rare high energy deposit is accepted as it is likely to be of interest.

The performance of these various targeted processes is typically described by efficiency versus  $E_T$  or  $p_T$  (e.g. figure 3.5). The efficiency in this context is the fraction of real objects within the acceptance of the detector correctly passing the trigger threshold. Metrics of purity are also considered.

### 3.1.4 Run 1 and 2 System

For the first two runs of the LHC, L1Calo had a successful and mostly constant system for processing calorimeter data. This consisted of three key modules.

The Pre-Processor Module (PPM) converts the analogue calorimeter signals into a digital one alongside attaching each calorimeter signal to the correct bunch crossing (compensating for system propagation time). These are then passed to two modules that identify the physics signatures. The Cluster Processor Module (CPM) is used to identify showers seeded by electrons, photons and taus ( $e/\gamma$  and  $\tau$ ). The Jet/Energy processor Module (JEM) looks for large-scale features such as jets structures and missing transverse energy [32, 33]. These are then combined in L1Topo and passed to the CTP. Due to the design of this system being as early as the late 90s, the

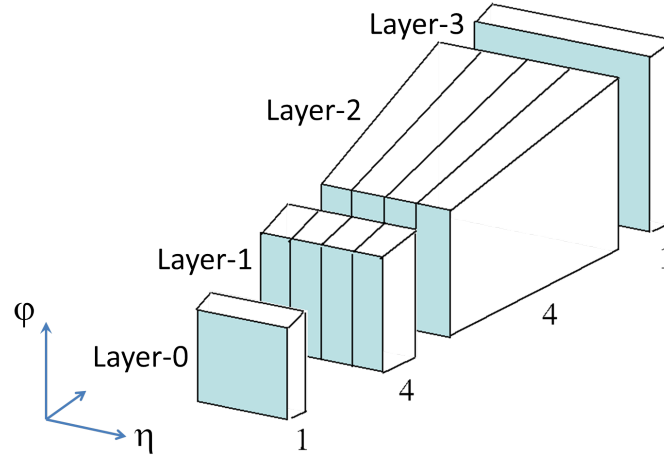


Figure 3.4: The increased granular data from ECAL for the Phase-I Upgrade of the LHC, with increased  $\eta$  segmentation and additional depth information allowing improved probing of shower shapes. These are known as supercells and have dimensions of either  $(\eta \times \phi)$   $0.1 \times 0.1$  or  $0.025 \times 0.1$ .

algorithmic capability of these designs in this latency window is very limited. The CPM uses  $0.1 \times 0.1$  ( $\eta \times \phi$ ) summed EM and Hadronic cells and the JEM uses  $0.2 \times 0.2$ .

### 3.1.5 Phase-I Upgrade

With each new run of the LHC, the plan is to continue to increase the luminosity and, hence, the number of collision events per bunch crossing. This comes at the cost of pile-up, typically low- $p_T$  strong force events with limited interesting physics use that contaminate our rare, interesting physics events. L1Calo, as a result, must improve efficiency in selecting physics objects while keeping good background rejection. Notably relevant to our discussion is the ability to accept as many low- $p_T$  EW event signals as possible without overwhelming the HLT. As a result, it is crucial to broadly improve background rejection at L1. Otherwise, the only way to take data stably will be to increase thresholds such as  $p_T$  on a menu item and significantly worsen our physics sensitivity for some analyses. L1Calo will use more sophisticated algorithms and more granular input data to do this. Figure 3.4 shows the new ‘supercell’ input from LAr with  $0.025 \times 0.1$  ( $\eta \times \phi$ ) depth-segmented cells. This takes

full advantage of the 15 years of technological advancements since the original trigger was put in place.

A new menu of trigger thresholds is implemented by three new Feature EXtractor (FEX) modules (visualised in figure 3.3) [30, 34].

1. **eFEX**: generates  $e/\gamma$  and  $\tau$  candidates using  $0.025 \times 0.1$  ( $\eta, \phi$ ) input granularity with improved selection variables compared to the  $0.1 \times 0.1$  used by the CPM module.
2. **jFEX**: generates small-**jet**,  $E_T^{\text{miss}}$  and  $\tau$  candidates using  $0.1 \times 0.1$  input granularity compared to  $0.2 \times 0.2$  in runs 1 and 2.
3. **gFEX**: generates ‘**global**’ large-jet and  $E_T^{\text{miss}}$  candidates using larger  $0.2 \times 0.2$  summed input data allowing whole calorimeter comparisons within the same algorithm block.

Each of these boards produces Trigger OBjects (TOBs) data packets containing information about the location, energy and type of target physics object.

These are then topologically combined together to give more rejection power and flexibility over object choice through the L1Topo.

During run 3, both the legacy system and the Phase-I upgrade are being run in parallel until the new algorithms are verified. The legacy system will then be switched off.

The most granular data used by this system is used by the eFEX, which receives ‘supercells’ in the form given in figure 3.4. This exploits the fact that EM showers are narrower and deposit their energy over a shorter length than a hadronic jet with the same incoming energy. Additional segmentation is chosen in the  $\eta$  direction to allow for photon conversions being separated in  $\phi$  by the magnetic field. The rotational symmetry of this effect about the axis of the shower is broken by the immersed magnetic field, and hence, the performance is better with this choice of granularity.

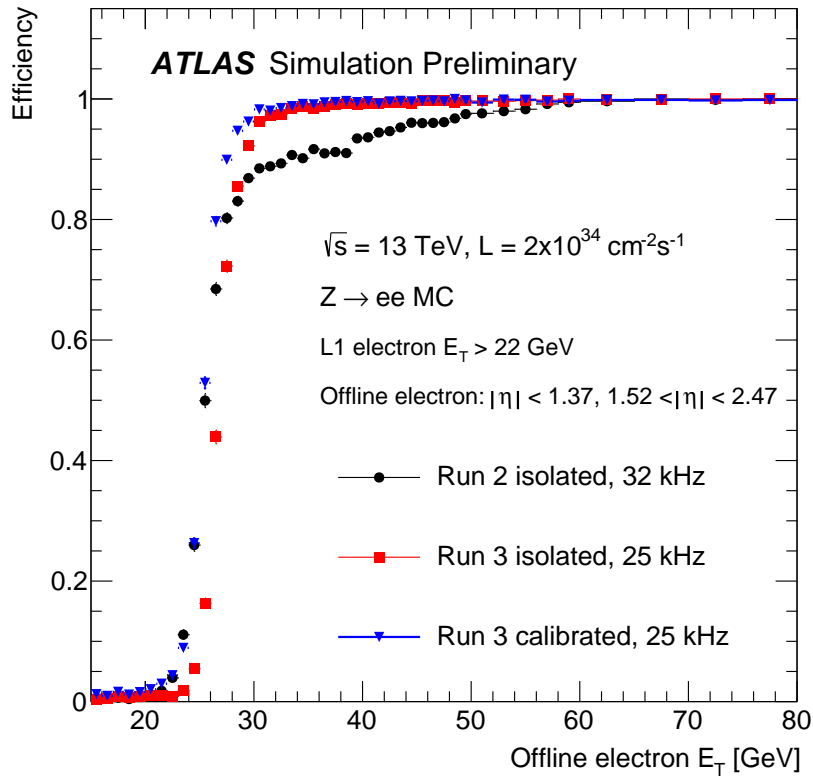


Figure 3.5: The predicted single electron efficiency ‘turn on’ curve for L1Calo in run 3 using simulated events. It can be seen that once the new Phase-I upgrade is applied, a sharper efficiency turn on at a much lower L1 rate (labelled in the legend) was anticipated. This is especially true once an  $\eta$  dependent energy calibration is applied [35].

These more granular, depth-segmented cells allow for types of measurement of showers at L1 which was not possible in the legacy system. For example, in an eFEX with the full supercell data, it is possible to select clusters of candidate  $e/\gamma$  in smaller steps of  $\eta$  compared to the CPM (0.025 vs 0.1). This allows narrower  $\eta \times \phi$  candidate ranges to encapsulate a  $e/\gamma$  shower, leading to better jet rejection. Moreover, the increased granularity and algorithmic capacity allow for metrics of EM versus hadronic distinction that you do not have the resolution and computational ability to do in the CPM. When combined, these features result in the improved performance seen in figure 3.5, by capturing the edge cases that limit the efficiency plateauing to one and also significantly reduce the rate required.

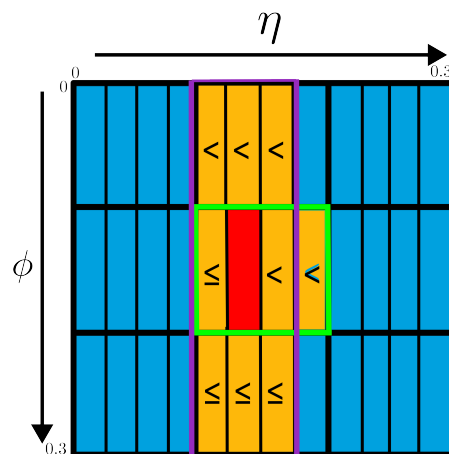


Figure 3.6: The electron FEX (eFEX) seedfinder algorithm. The seed (red) must be the largest supercell  $E_T$  value within its  $0.1 \times 0.1$  algorithm block (green). It also must be the largest value of all its adjacent neighbours (purple). The varied use of strictly less than is to ensure if two cells have identical values, only one TOB is produced. These comparisons are done in parallel only on the 2nd depth layer of supercells in figure 3.4. (Adapted from [37]).

## 3.2 Hardware Enabling Improved Electromagnetic Clustering Algorithms

### 3.2.1 LTDB & LATOME

To enable the L1Calo Phase-I upgrade, LAr has improved its read-out capabilities for triggering [36]. This is done through the addition of two new electronics boards directly connected to the analogue outputs of cells. The LAr Digital Processing Blades (LTDBs) first convert the signal from analogue to digital, then the Liquid Argon Trigger prOcessing MEzzaniness (LATOMEs) assign the signal to the correct bunch crossing and serialise various sums of cells into signals to be sent along optical fibres to the FEX boards. This replaces the PPM from runs 1 and 2.

### 3.2.2 The eFEX

A single eFEX module covers an area in  $(\eta, \phi)$  of  $1.6 \times \pi/4$  and for each  $0.1 \times 0.1$  algorithm block (see figure 3.6 in green) looks for a ‘seed’: a local maximum over an extended  $0.3 \times 0.3$  region to avoid several triggers of the same candidate. For each seed found it produces a TOB containing the coordinates, object  $E_T$  and results of isolation algorithms inspired by HLT measurement quantities using the seed coordinates. These quantities probe the showering profile of a particle. EM showers are narrower and less deeply penetrating than their hadronic counterparts for the same  $E_T$ , so ratios that quantify this are used. This is done through 5 Xilinx Virtex-7 Field Programmable Gate Arrays (FPGAs). Two shelves of 12 eFEXs then cover a region up to  $|\eta| < 2.5$ .

FPGAs are commonly used components for high-speed, fixed latency signal processing. These consist of logic gates (containing sequential and combinatorial logic), Look Up Tables and Random Access Memory (RAM) (allowing for small settings changeable at runtime and I/O testing).

Unlike standard Central Processing Units (CPUs), they cannot run arbitrary tasks quickly. However, this style of digital electronics design allows for much lower latencies. The connections between components are made through a process known as synthesis, which reprograms the FPGA. This takes considerable time and cannot be changed during a run. They are reprogrammable at a slight expense of computation speed compared to an Application-Specific Integrated Circuit (ASIC), which aids smaller scale iterative development<sup>1</sup>. To describe these connections, we use the hardware description language, Very high speed integrated circuit Hardware Description Language (VHDL) [38]. This is a low-level programming language built to design highly parallelised digital electronics (although as devices become larger, there has been a slow shift to using high-level languages).

The conditions and comparisons needed in each algorithm block to define a seed in

---

<sup>1</sup>Small ASICs are often used in modern FPGA design

firmware are illustrated in figure 3.6. This seed is then used to calculate threshold values that can be used to trigger. For example, an important variable is  $R_\eta$  for  $e/\gamma$  triggering, which quantifies narrowness in the middle LAr EM layer (layer 2 in figure 3.4). Equation (3.1) uses the notation  $E_{T,\eta\times\phi}^{(layer)}$ , where  $\eta \times \phi$  defines the area used by the seed.

$$R_\eta = \frac{E_{T,0.075\times 0.2}^{(2)}}{E_{T,0.175\times 0.3}^{(2)}} \geq R_{Thresh} \quad (3.1)$$

Each module splits  $\eta$  space further between four ‘processor’ FPGAs (pFPGA) that primarily generate the information to create a TOB. Alongside this, there is a ‘control’ FPGA (cFPGA) which is responsible for connections to registers in the other FPGAs and read out.

To enable the high-speed (1.4 GB/s) inputs into each FPGA link, equally high-speed components are required to convert the input optical fibre data into a compatible digital signal for the FPGA. This is done through external components. MiniPODs<sup>TM</sup> (figure 3.7) convert the optical signal to an electrical signal before inputting it into the FPGA through Multi Gigabit Transceivers (MGTs). Four MGTs share some control hardware and are organised into Quads.

### 3.2.3 Topological Combination and Readout

To generate a ‘trigger bit’ for the CTP, the L1Topo system accumulates all the TOBs from the FEXs systems, along with L1Muon data, for a specific bunch crossing. The CTP then applies the L1 equivalent to the trigger menu (see section 3.1.1) to generate a L1A to trigger read-out and Regions Of Interest (ROI) to point the HLT to where reconstruction should be targeted to pick up the interesting physics objects. This also implements the pre-scaling and dead time algorithms to limit the readout requests to what is possible within the various detector components outlined in

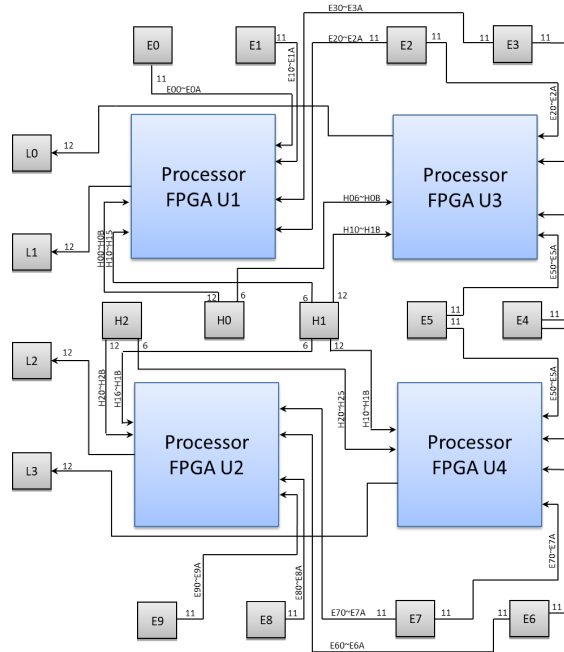


Figure 3.7: A schematic of the MiniPODs (grey) physical position into the FPGA (blue) [39].

chapter 2.

### 3.2.4 The FTM

In addition to the modules installed in the ATLAS cavern, we require dedicated high-speed hardware capable of testing the firmware of high-speed electronics at various institutes. The FEX Test Module (FTM) is purely designed for these ongoing commissioning activities [30]. It contains 3 FPGAs with RAMs loadable from software. These produce dummy data patterns that emulate input from other boards (source RAM). They can also read in and compare these to the simulated expected outputs (spy RAM and ref RAM, respectively). This is useful because we can emulate boards that may not be present for particular tests. Due to the speed and cutting-edge nature of these boards, no commercial solutions exist. It has been used in acceptance testing of L1Calo modules, system-level tests (where it has been invaluable) and commissioning.

### 3.3 Software for L1Calo

Alongside the firmware development for the various FPGAs used by L1Calo, an extensive suite of software must be created in parallel. This is needed to ensure that we can control, monitor, and test the physics performance of the hardware trigger. Resultantly, the software is split into three groups.

1. **Online Software.** Configures, calibrates and runs boards at test rigs and in the real system. It is built with the ATLAS run control system so all operations to manage the system can be contained with machine states including ‘Configure’ and ‘Run’.
2. **Offline Software.** For use in ATLAS’s event reconstruction and simulation software packages. Optimised to be fast and multi-threaded, yet exactly encapsulates the FPGA’s operations (bitwise).
3. **Performance Software.** Written prior to hardware production and firmware to direct the physics needs for the hardware trigger. Roughly emulates a potential hardware trigger’s behaviour. May take shortcuts for optimisation.

The remainder of this section discusses this author’s contribution to online software. A significant amount of effort during the build up to run 3 was put into building new tests and commissioning tools for the Phase-I upgrade within online software.

### 3.4 LATOME to eFEX Channel Mappings

The online software set-up for L1Calo consists of many packages that simulate, test and control the system during LHC runs alongside specific institutional test set-ups. As a result, it is key that this system has a shared understanding of where calorimeter data ‘goes’ into eFEX hardware exactly.

With the increased granularity supercells (figure 3.4) from the calorimeter, the input data has additional complexity in terms of variable  $(\eta, \phi)$  widths and depth information. Each of these must be *mapped* to an exact set of corresponding points in eFEX hardware.

This is a deceptively challenging task due to the sheer number of channels and subtleties within the system. There is no uniform naming convention between the upstream boards from the eFEX and great care must be taken to ensure that the methods used in the description are both usable and coherent. They should also be set up, so that if a correction has to be made during development, it can be propagated to all users.

This section details how the mapping is parsed from several hardware descriptions and then discusses how this information is accessed within online software.

### 3.4.1 Hardware Description

For a complete mapping of every word, fibre and optical link into the eFEX hardware description, the following hardware information needs to be combined:

1. LATOMES's data packing scheme for a fibre signal
2. The data packing scheme for a fibre from the Tile Calorimeter's digitiser (TREX)
3. FOX (Fibre Optic eXchange) which maps the calorimeter fibres to the individual FEXs
4. Internal information about eFEX hardware

Resultantly, the following tables were proposed (given in figure 3.8). To avoid miscommunication and improve maintainability, the code that generates these tables

directly parses time-stamped versions of firmware/simulation software and combines them to give a master table, before reducing it to a smaller set of tables. In detail, figure 3.8 describes the steps between LAr’s incoming digital summed supercells (‘Tower’) and the abstract ‘algorithm inputs’ into an eFEX FPGA (Table 1 in figure 3.8). To do this for online software, it is necessary also to trace through and append hardware information in the input data path (Tables 2 through 5). The procedure of tracing through and combining various pieces of hardware documentation is described in figure 3.9.

To allow for iterative development and to self-document the run-once procedure needed to create these tables, a Jupyter notebook is used. The outputted tables are then imported into the online software repository for L1Calo through simple comma separated variable (csv) files.

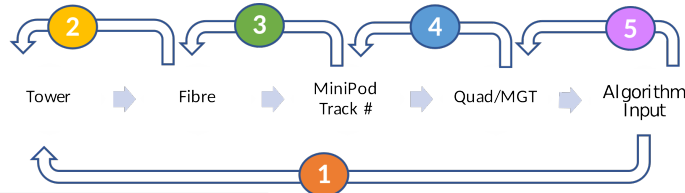


**TABLE 1 - Algorithm Input -> Tower**

eFEX	FPGA	(Algorithm)		Layer	Tower		
		$\eta$	$\phi$		$\eta$	$\phi$	Layer
[A1:C8]	[0:3]	[0:5]	[0:9]	[0x0:0xa]	[-25:24]	[0:63]	[0x0:0xa]

**TABLE 2 - Fibre->Tower**

eFEX	Input Connector #	Fibre# Within Connector	Data Word	Tower		
				$\eta$	$\phi$	Layer
[A1:C8]	[0:3]	[0:47]	[0:19]	[-25:24]	[0:63]	[0:a]

**TABLE 3 - MiniPod Track #-> Fibre**

eFEX	MiniPod Track #	Input Connector #	Fibre# Within

**TABLE 4 - MGT #-> MiniPod Track #**

eFEX	FPGA	Quad	MGT	MiniPod Track #

**TABLE 5 - Algorithm Input -> MGT #**

eFEX	FPGA	(Algorithm)		Layer	Quad	MGT	Data Word
		$\eta$	$\phi$				
[A1:C8]	[0:3]	[0:5]	[0:9]	[0x0:0xa]	[0:19]	[0:3]	[0:19]

Figure 3.8: The channel mapping tables required to go to and from a given FPGA’s local algorithmic input information to a LAr supercell [40]. Table 1 describes the link between the LAr cell description and any associated eFEX algorithm inputs (Describing the board and FPGA followed by the calorimeter cell in firmware’s coordinate system for algorithms). [down:up] gives the range of values possible. Layer counts supercells (figure 3.4) in hex going outwards and increasing in  $|\eta|$  or  $\eta$  depending on LAr or L1Calo conventions, respectively.

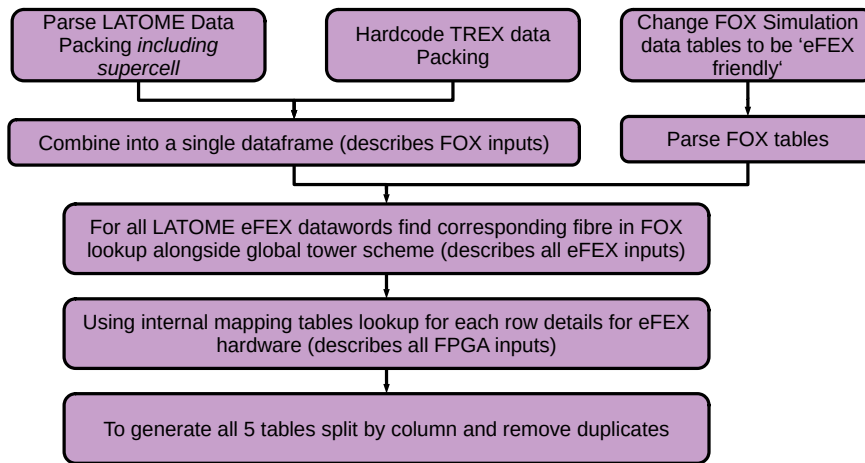


Figure 3.9: The procedures needed for generating the mapping tables in figure 3.8 in their entirety.

### 3.4.2 Software Capabilities

The generated tables must then be used in an efficient and maintainable way that can be reused for several cases within the C++ online software repository as a utility. The software is broadly split into three parts (shown through the coding structure in figure 3.10):

1. An optimised (for memory and CPU time) access and search method for the 5 csv tables.
2. A class to abstract away the specific searches within the tables needed to extract all possible information for the end user.
3. Return objects that allow for description of the eFEX hardware and calorimeter cell geometry. Also allows for several naming convention outputs where appropriate.

The main use case for this is to allow online software to simulate and control the whole eFEX system for validation, testing and running. Hence, mapping is used indirectly in a lot of contexts. Originally, it was used in firmware testing, but

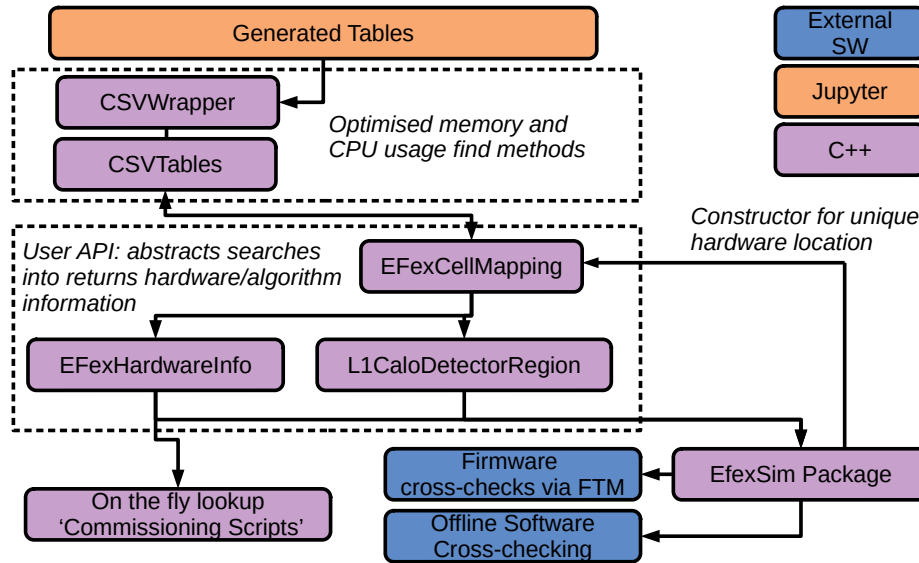


Figure 3.10: The class structure for accessing mapping information within online software. All the Phase-I related parts of the diagram were written/significantly altered by the author aside from the ‘EfexSim’ Package.

it inevitably became more critical as larger-scale tests were completed with the electronics included in the real DAQ path. During commissioning, this software needed a reasonable amount of maintenance and debugging as minor errors were found in firmware and software. This remains a core component in the software for operations and system monitoring during runs.

The class structure and methods generated by the author were sufficiently robust and documented that they were used for the g/jFEXs system’s commissioning purposes. For example, online software generates displays of L1A rate against  $\eta, \phi$  for live monitoring/debugging (usually to identify if a calorimeter cell produces dissatisfactory data). This needs to know what hardware to interact with for each point in phase space.

### 3.5 Firmware Development

Alongside direct firmware development for the FTM and eFEX, L1Calo UK contributes to the development of IPbus. This is a repository of firmware and software.

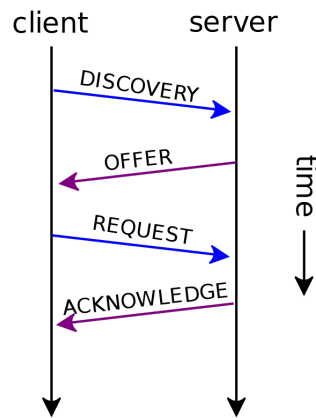


Figure 3.11: The four packets sent and parsed to assign an Internet Protocol (IP) address. The FPGA firmware acts as the client [41].

Together, they allow for reliable high-speed communication and read-write access to registers on a FPGA. This is used by a large number of high energy physics experiments [42].

A critical part of IPbus’s functionality is assigning an IP address to each board. Hardcoding an IP address in the firmware is possible, but this does not scale to large systems (i.e. the ATLAS detector). The alternative is to use a client-server architecture to manage the address assignment. The original implementation in IPBus used the Reverse Address Resolution Protocol (RARP), which runs on raw Ethernet. This only works on a limited number of set-ups<sup>2</sup>. This protocol has long since been rendered obsolete by first the Bootstrap Protocol (BOOTP) and more recently Dynamic Host Configuration Protocol (DHCP), which runs on the higher level User Datagram Protocol/Internet Protocol (UDP/IP) and supports a much greater feature set than RARP. This has been a requested feature by users for some time and a long-term desire of the IPbus team.

The DHCP protocol is the exchange of packets through UDP/IP (figure 3.11). To complete this task logistically, the packets of data must be set on the Ethernet RAM and a ‘write’ command sent. In VHDL, this kind of logic is split into components

<sup>2</sup>A server needs to be on every Ethernet segment, which is now rare and is deprecated by most operating systems/kernels

that generate output digital signals given a set of input signals. The behaviour of these components can then be built upwards and tested in software.

In figure 3.12 an example packet for DHCP discovery is given. The majority of the packet is fixed and does not depend on specific hardware details or time. As a result, it can be statically written in the firmware. However, in a part of the packet called the IPv4 Header we have a checksum within it which depends on the MAC address (the unique ID of the hardware). This has the potential to be resource-heavy to implement in logic. However, there is some redundancy in the header (transaction ID and lower half of IP address) where the value does not matter because it will be ignored by the server. As a result, it is possible to cancel these two parts in the checksum calculation. The checksum is a one's compliment sum [43]. This is a simple binary addition with a wraparound overflow bit. Hence, by setting redundant bits in to cancel out exactly with the MAC address (a bitwise NOT) we have a fixed checksum. This trick significantly reduces both the logic and code complexity of the firmware.

Once such considerations on optimally constructing packets are made, we can begin to write VHDL components that generate and parse these packets. With minor adjustments, these can be built into the same firmware as the RARP protocol components. We then synthesise this firmware onto an FPGA and see if it communicates with a server successfully. This has now been added to the new releases of IPbus and is used throughout the High Energy Physics community. This includes the eFEX and LATOME projects (hundreds of boards).

## 3.6 Example Commissioning jobs

This section outlines various key short tasks connected to the installation of Phase-I electronics at CERN and the University of Birmingham. It follows a chronological discussion of tasks to validate the data path from LAr to eFEX and its readout.

```

-- dhcp packet structure:
-- ETHERNET
-- Ethernet DST_MAC(6) discover -> broadcast (FFFFFFFFFFFF) ,
-- SRC_MAC(6) = MAC_addr
-- Ether_Type IPv4 = x"0800"
-- IP header length = x"45"
-- IPV4
-- 'Differentiated services' set to: x"00"
-- IPv4 Packet Length 272 (DHCPDISCOVER) or 284 (DHCPCREQUEST) = x"0110" or x"011c"
-- Identification: MAC address bits
-- Flags: x"4000" (Don't fragment)
-- Time to live ~64s x"40"
-- UDP protocol = x"11" (17)
-- Checksum: Fixed by source IP and ID
-- Source IP (on discover) 0.0.0.0 = x 192.168 & NOT MAC addr
-- Dest IP (broadcast on discover) 255.255.255.255 = x"FFFFFFFF"
-- UDP
-- Ports (68->67) x"00440043"
-- UDP Packet Length 252 or 264 = x"00fc" or x"0108"
-- Checksum empty =x"0000"
-- Bootstrap Discover Packet
-- Boot request x"01"
-- Ethernet x"01"
-- (HW) Address length x"06" (in octets/bytes)
-- hops x"00"
-- trans ID MAC_addr(31 downto 0) fudge as only 1 XID
-- secs elapsed sec_count defined through sec_counter
-- bootpflag x"8000" broadcast
-- 4 empty IPs x"00000000" * 4
-- MAC address
-- 192 empty bytes (!)
-- DHCP magic cookie (x"63825363")
-- Options
-- DHCPDISCOVER x"350101" or DHCPCREQUEST x"350103"
-- DHCPCREQUEST Server Identifier x"3604" & Server_IP_addr
-- DHCPCREQUEST Requested IP Address x"3204" & My_IP_addr
-- End x"FF"

```

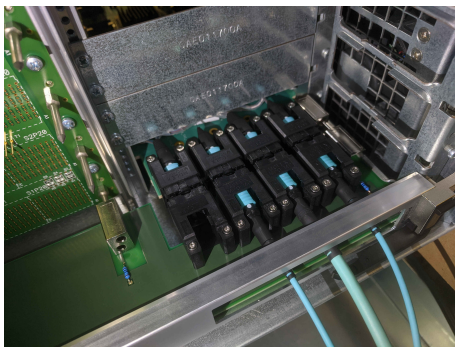
Figure 3.12: The full packet structure for DHCP DISCOVER [44].

### 3.6.1 FTM Loopback

As a very early test of functionality at the test rig at the University of Birmingham, the FTMs had the output data connected back into itself with a simple counting up pattern. This had a twofold benefit:

- Make sure the online software and hardware behave on the test rig setup.
- Measure and verify the latency of the FTM path.

The data pattern of the input and output RAMs alongside the cabling is shown in figure 3.13. By making 40 MHz signals in the source RAM that counts up (1,2,3,4) and reading in the sink RAM synchronously, the latency of the fibre can be measured (7×25 ns bunches). This test worked as anticipated and became the foundation for the online software operating larger-scale tests.



(a) The fibres plugged into the back of FTM in a crate to enable fibre loopback (two output cables merging to one input cable).

FTM0-DSS1 MGT_Source_Ram		FTM0-DSS1 MGT_Sink_Ram Sink00	
00000000	bc	00000000	0
00000001	1	00000001	0
00000002	2	00000002	0
00000003	3	00000003	0
00000004	4	00000004	0
00000005	5	00000005	0
00000006	6	00000006	bc
00000007	7	00000007	1
00000008	0	00000008	2
00000009	0	00000009	3
0000000a	0	0000000a	4
0000000b	0	0000000b	5
0000000c	0	0000000c	6
0000000d	0	0000000d	7

(b) Sink and spy registers/RAM in a FTM loopback test manually read using online software (serendip). Each column is the data sent/received in a 40MHz pulse over time (y axis of the table). By generating a counting up pattern in RAM (Source\_Ram) and recording the returned signal (Sink\_RAM), the latency of the fibres is clearly visible ( $7 \times 25$  ns).

Figure 3.13: The FTM loopback setup at the University of Birmingham.

### 3.6.2 Installation and Cabling

Once the eFEXs were transported to CERN, they had to be carefully installed. This involves visual inspection of the boards for faults before installation with anti-static gear into the test rig in the Surface Test Facility separate from the cavern at CERN. Light functionality is then tested on the boards (connectivity to the network and reading of basic registers through IPbus).

These were then transferred to their final position in the cavern. Some images of the process and cabling are shown in figure 3.14. When doing so, the back of the boards must be connected to the outputs of the LATOMEs. The shelves allow for the swapping of modules without powering off the shelf or disconnecting the fibres through the Rear Transmission Modules (RTM). This is a deceptively technical job due to the following caveats:

- High-speed fibre optic cables are extremely fragile and can break even if they only bear their own weight.
- The cables are extremely hard to connect into the RTMs.
- 48 of these cables must be connected into a dense grid at the back of the shelves.

To mediate this, the following steps were taken:

- Shelves were built on the backs of the racks to bear the weight of the cable bundles.
- Cables must be connected in a specific order to avoid over torsioning and making some cables very hard to place into the RTM due to the placement of other cables.



(a) Installed cable routing shelf

(b) Installed fibres sorted into  $\eta$  (yellow) and  $\phi$  (red) segmentation



(c) Front panels and output fibres



(d) Insertion of an eFEX into a shelf

Figure 3.14: Installation of a shelf of eFEXs at CERN.

### 3.6.3 Align Frame Capture

As part of the commissioning process, LATOMEs have the functionality to generate packets of data in unused bunch crossings by the LHC. This transmits data that uniquely describes each output board and fibre from the LATOME. These are called ‘Align Frames’.

Capturing align frame data to compare to expectation in the eFEXs was an important early step in eFEX installation at Point 1 in the cavern. This was done to ensure that one can distinguish algorithm bugs instead of the missending of data. For example, this style of test determined if the firmware and simulation design did not match or if the boards were not cabled up correctly. Setting up a procedure to do these checks when they were attempted posed additional challenges, as the standard readout path for the final system did not yet work. Resultantly, an online software procedure was needed to capture data.

The eFEX’s firmware design contains accessible RAMs that allow for capture and short-term storage of input data from LATOME on a readout request (L1A). Hence, if you pulse a L1A on the correct bunch crossing, you will store the desired align frame to be read by software. The software designed within this also needed to run the comparisons between online simulation and read values of the align frame structure relevant for eFEX and provide readable error reports.

After significant debugging, the connections were validated using these tools. Also, simply in setting up these tests, several other bugs were found and fixed.

## 3.7 Preliminary Run 3 data checks

Before the complete set of eFEXs were installed in the cavern, run 3 of the LHC had already begun. This section describes a few of the early checks of the data the

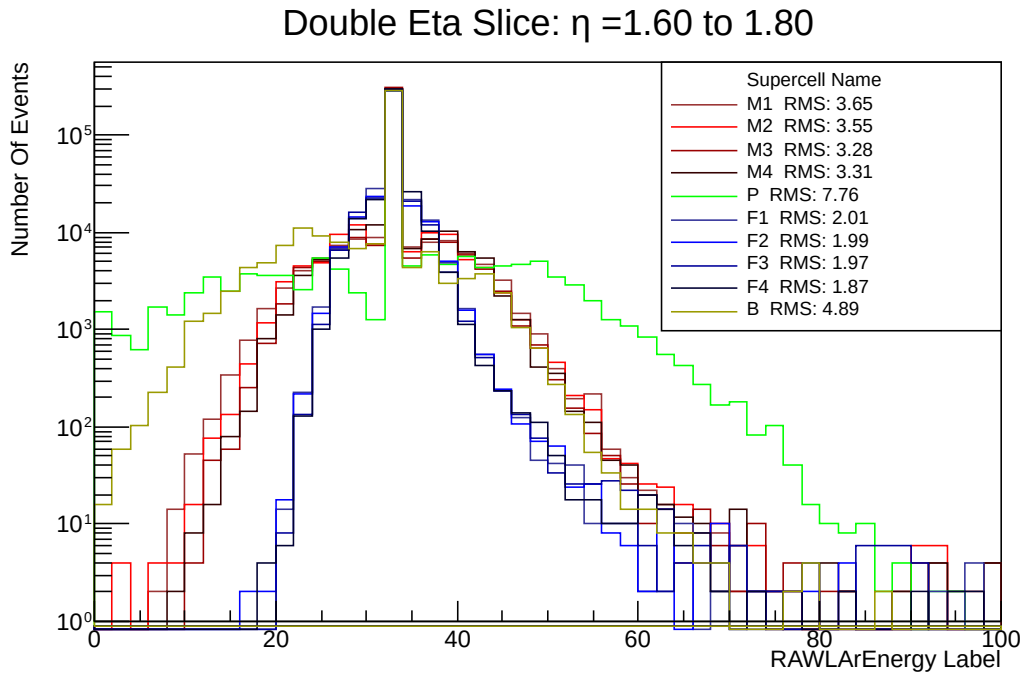
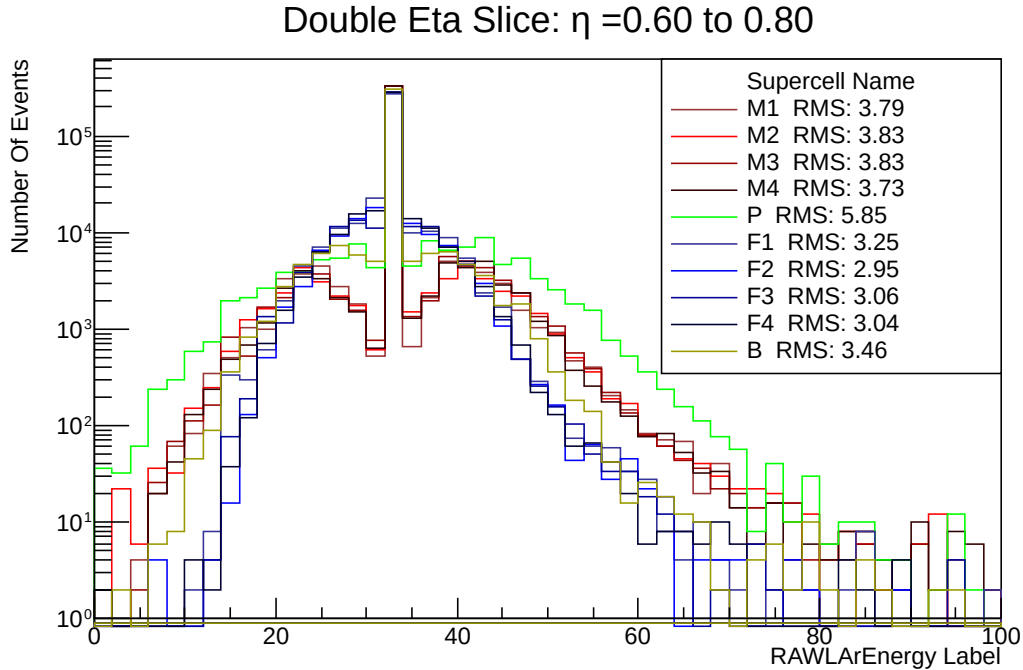


Figure 3.15: The RAW LAr supercell energy output given to eFEX. Even with the system in its early form, the spread of data (Root Mean Square or RMS) can be seen to have different noise levels depending on the layer depth and rapidity of the cell. Depth is labeled in the form (P,M,F,B) standing for (Pre-Sampler,Middle,Front,Back) with separate colours. These can be seen to have similar shapes by cell. The RAW code has a zero value corresponding to 32 due to a subtlety of the analogue to digital conversion giving negative values.

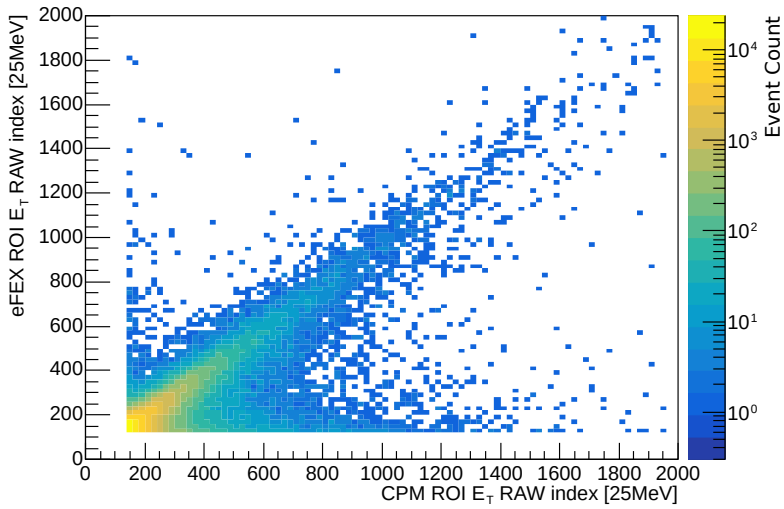
author contributed to commissioning. During this early stage of commissioning in the ATLAS cavern, the eFEXs were capable of reading out the LATOME supercell output/eFEX input. This enabled the cross-validation of algorithms alongside validating the quality of data received from LAr, including the first inspection of supercells in the readout path. Some of these distributions are found in figure 3.15.

This supercell data was unverified, but some common features can be seen between the different samples. It can be seen the spread of energy deposits depends on the supercell layer depth (grouped by colour). After some filtering, the LAr cells generating noisy unphysical data could be found.

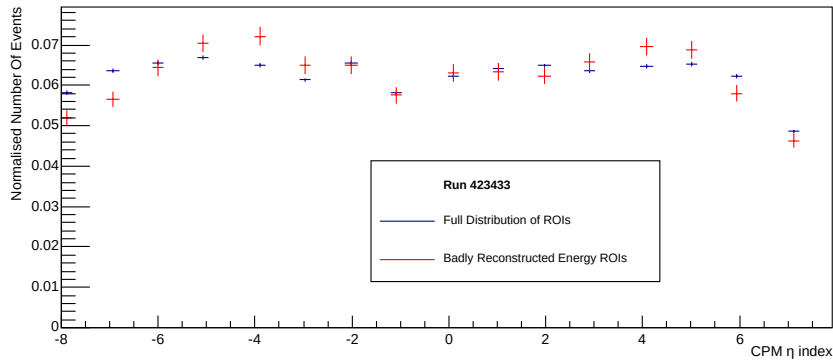
Later, work was completed to select CPM and eFEX Regions Of Interest (ROI) and the kinematic distributions of the energy mismatch outliers were observed. Similar, but not identical, responses are expected from each system. Some early plots are shown in figure 3.16. Energies between the Legacy and Phase-I system broadly match as hoped; however, when filtering out events for which the energies match poorly (difference of 2.5 GeV or more), the normalised kinematic distributions were not entirely flat in  $\phi$ , indicating a systematic issue to monitor during commissioning. These checks became part of the many steps required to validate the system.

## 3.8 Early Performance Results

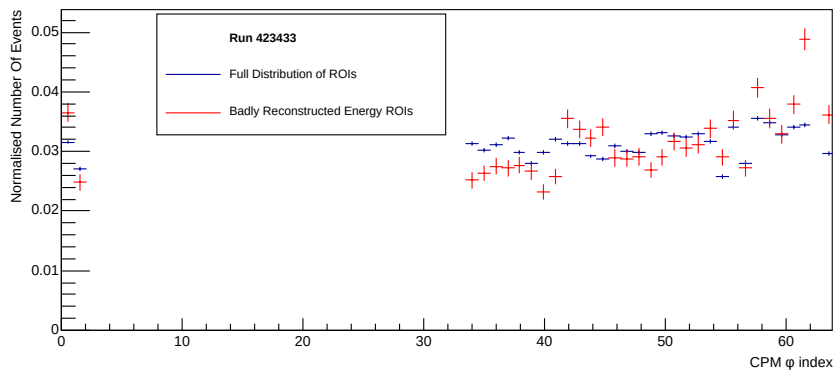
As run 3 progresses whilst this thesis is being written, the FEXs were further debugged, calibrated and validated. The eFEX is already at the point where it is outperforming the predecessor CPM as anticipated. A recent public efficiency plot demonstrates this in figure 3.17. This shows the efficiency of L1  $e/\gamma$  triggers approaching one with  $p_T$  faster at a similar threshold compared to the legacy system on real data. Recently, the eFEX was deemed ready for being the sole way of deriving L1  $e/\gamma$  triggers. Figure 3.18 shows that turning off the CPM input to  $e/\gamma$  HLT inputs reduced the rate by  $\sim 5\text{kHz}$  of the total rate into the CTP of  $\sim 100\text{kHz}$ .



(a) The transverse energies reported by the CPM and eFEX in ROIs. Strong correlation is broadly seen. Badly reconstructed ROIs (red in the figures below) are taken for events where there is at least a 2500 MeV difference ( $\sim 5\%$  of events).



(b) Normalised  $\eta$  distributions for badly reconstructed energies.



(c) Normalised  $\phi$  distributions for badly reconstructed energies. Here a significant deviation can be seen between the full ROI distribution and the badly reconstructed ROIs.

Figure 3.16: Early attempts to match CPM (legacy) and eFEX (Phase-I) ROI (matching the leading ROI in each event) information together when a full set of eFEXs were not yet available (note the gap in  $\phi$  coverage). Some kinematic correlations can be seen which directs debugging of the system.

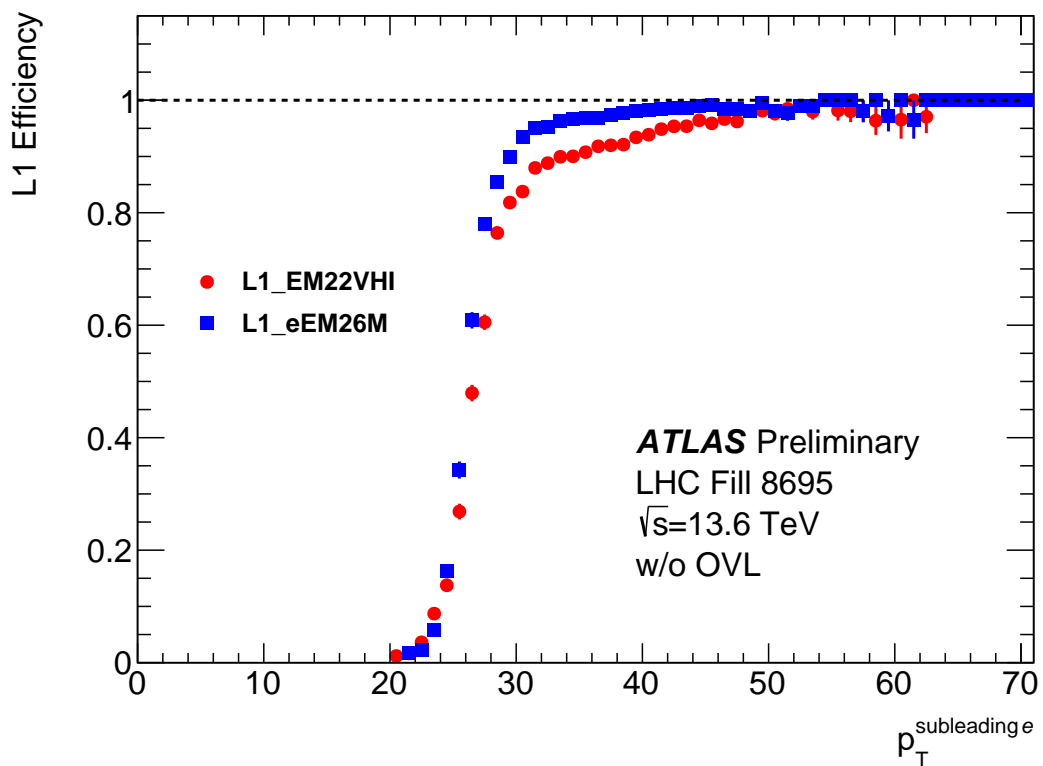


Figure 3.17: The  $e/\gamma$  L1 efficiency of the eFEX(eEM26) vs the CPM (EM22). As can be seen in conjunction with figure 3.18 this gives up an improved maximum efficiency threshold at lower rates. This is derived on  $Z \rightarrow ee$  events with a tag and probe method. VHI and M are isolation and calibration codes for the trigger devices [45].

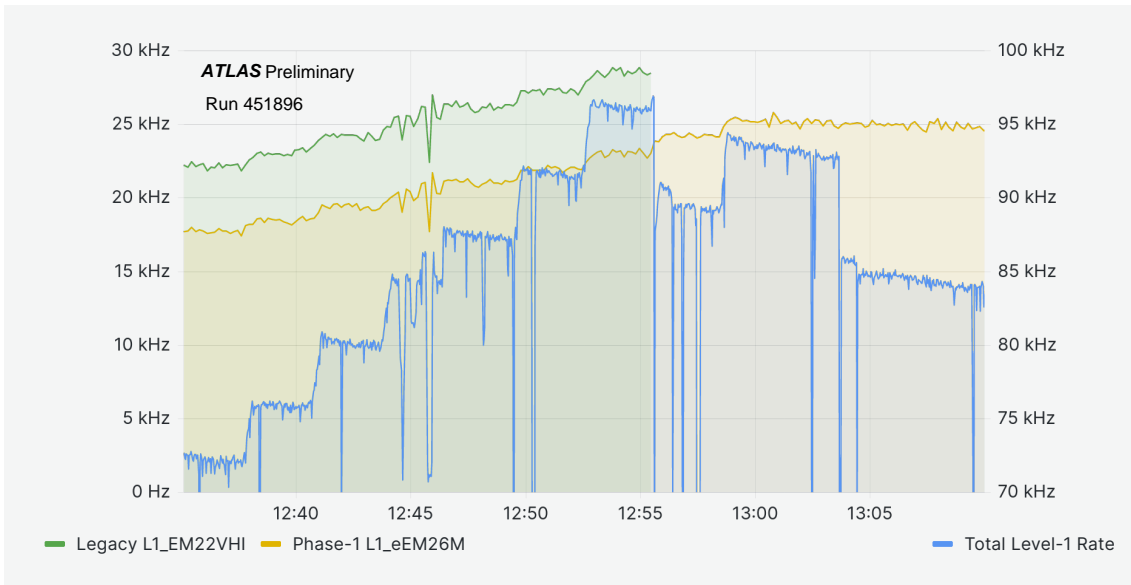


Figure 3.18: The Level 1 rate on the day of removing the CPM based triggers from the menu. We see an immediate 5 kHz saving [45]. The rates of the individual L1A items use the left  $y$  axis labels. The total CTP L1A Rate is the right  $y$  axis labels.

This is a testament to the continued work of  $\sim 50$  people over the course of a decade. This chapter provides a case study of the true scale of effort required to upgrade even a small part of a LHC detector.

## CHAPTER 4

---

# The Standard Model, Heavy Neutral Leptons and The Weinberg Operator

---

Due to infrequent interactions with other matter, neutrinos are the least well-understood part of the Standard Model. All attempts to measure their mass directly have been unsuccessful to date. However, due to the phenomenology of neutrino oscillations, we can measure the difference of the squares of the masses. As a result, there remain simple models for masses and interactions that remain untested. This chapter aims to summarise these from an ATLAS experimentalist's perspective.

Heavy Neutral Leptons (HNLs) are the particles proposed originally as a means to explain the very small masses of neutrinos by making use of the Majorana neutrino hypothesis. These three hypothetical particles, given observation with the correct mass ranges, could be a Dark Matter Candidate (keV mass scales) and could be the origin of Leptogenesis (ATLAS detectable mass range of  $\sim 10$  GeV) [46].

The notion of HNLs and Majorana neutrinos is included in many beyond the Standard Model theories. In this section, two minimal perturbations in the Standard Model are derived and motivated. Firstly, the construction of a Majorana spinor is motivated. Then using a Type-I see-saw model, the notion of HNL is derived and how this can be measured using a  $W$  branching fraction. These are then used to motivate ATLAS's search strategies. Finally, without using HNLs, a Weinberg model is derived as an alternative model for the high-mass ATLAS search outlined in chapters 5 to 7. This involves a brief discussion of Effective Field Theories (EFTs) and the Higgs mechanism. A minimal approach is taken throughout this chapter to only discuss the theory related to the masses and  $W$  currents to which the analysis is sensitive. Natural units ( $\hbar = c = 1$ ) is assumed throughout.

As an interesting aside, some of the author's older work with theorists is discussed for the s-channel. This involves looking at the potential suppression of HNL Lepton Number Violating (LNV) currents probed for the s-channel analysis and how it is possible to re-interpret an excess as a Lepton Number Conserving (LNC) current with mass mixing. This is not used in subsequent chapters.

## 4.1 Preliminaries: Fields, Chirality and Masses in the Standard Model

The Standard Model of particle physics contains three generations of quarks and leptons (figure 4.1). These (with the exception of neutrinos) have been proven to be spin- $\frac{1}{2}$  Dirac fields. This means in the absence of interactions from gauge fields, we have objects satisfying the Dirac equation canonically used to make Quantum Mechanics consistent with special relativity (equation (4.1))[17].  $\psi$  is our spin half particle field and  $\gamma^\mu$  are the indexed Dirac matrices ( $\gamma^{0-3}$ ), which describe the algebraic properties needed for the solution to represent the field.  $m$  is mass and  $\partial_\mu$

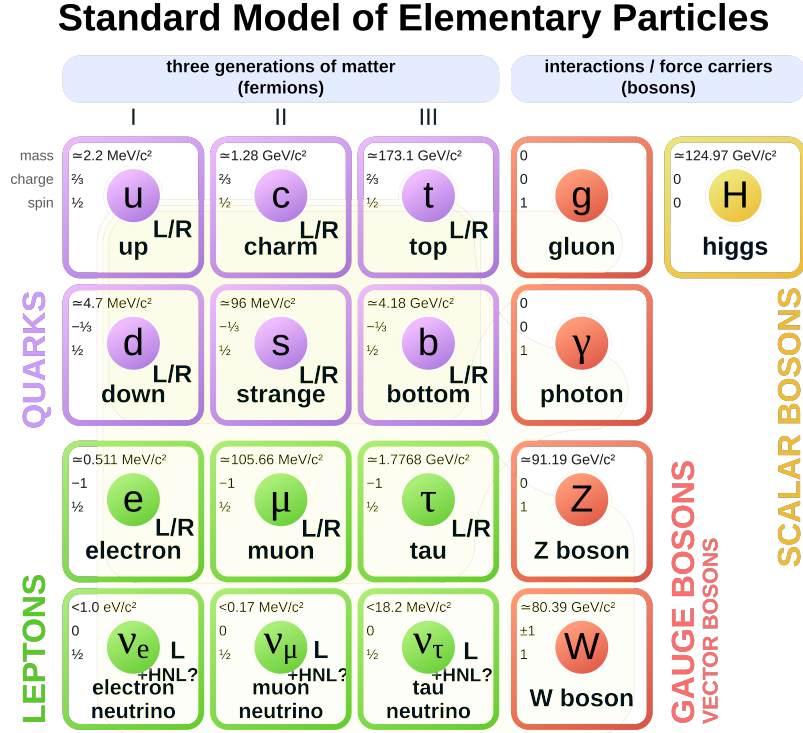


Figure 4.1: The Standard Model of particle physics. All fermions have observed left and right-handed interacting chiral parts with the exception of the neutrino. Hence, HNLs break this mass chiral symmetry with various resulting properties. Adapted from [47].

is 4 vector derivative.

$$i\gamma^\mu \partial_\mu \psi = m\psi \quad (4.1)$$

In order to introduce the neutrino masses and the Type-I seesaw mechanism, Lagrangian densities are also introduced. These are a generalisation of a classical Lagrangian such that  $L_{\text{classical}} = \int d^3x \mathcal{L}$ . By defining an analogous action (equation (4.2)) and minimising it with respect to fields, equations of motion like equation (4.1) can be obtained.

$$\mathcal{L}_{\text{Dirac}} = \underbrace{\bar{\psi} i \gamma^\mu \psi}_{\text{'Kinetic Term'}} - \underbrace{m \bar{\psi} \psi}_{\text{'Mass term'}} \quad (4.2)$$

Another key concept in particle physics is chirality. It is formally the eigenvalues ( $\pm 1$ ) of  $\gamma^5 \stackrel{\text{def}}{=} i\gamma^0 \gamma^1 \gamma^2 \gamma^3$ . More intuitively, it is the direction of complex phase advance

Lepton $\ell \in (e, \mu, \tau)$	$I_W$	$I_{W,3}$	$Y$	$Q$	Quarks	$I_W$	$I_{W,3}$	$Y$	$Q$
$\nu_{\ell,L}$	$\frac{1}{2}$	$\frac{1}{2}$	-1	0	$(u/c/t)_L$	$\frac{1}{2}$	$\frac{1}{2}$	$\frac{1}{3}$	$\frac{2}{3}$
$\nu_{\ell,R}$ (sterile)	0	0	0	0	$(u/c/t)_R$	0	0	$\frac{4}{3}$	$\frac{2}{3}$
$\ell_L$	$\frac{1}{2}$	$-\frac{1}{2}$	-1	-1	$(d'/s'/b')_L$	$\frac{1}{2}$	$-\frac{1}{2}$	$\frac{1}{3}$	$-\frac{1}{3}$
$\ell_R$	0	0	-2	-1	$(d'/s'/b')_R$	0	0	$-\frac{2}{3}$	$-\frac{1}{3}$

Bosons	$I_W$	$I_{W,3}$	$Y$	$Q$
$W^\pm$	$\pm 1$	$\pm 1$	0	$\pm 1$
$Z/\gamma/g$	0	0	0	0
$\Phi = \begin{pmatrix} \phi^+ \\ \phi^0 \end{pmatrix}$	$\begin{pmatrix} \frac{1}{2} \\ \frac{1}{2} \end{pmatrix}$	$\begin{pmatrix} \frac{1}{2} \\ -\frac{1}{2} \end{pmatrix}$	$\begin{pmatrix} 1 \\ 1 \end{pmatrix}$	$\begin{pmatrix} 1 \\ 0 \end{pmatrix}$

Table 4.1: Weak isospin ( $I_W, I_{W,3}$ ), Hypercharge ( $Y$ ) and Charge ( $Q$ ) of the Standard Model and the hypothesised sterile neutrino sector.

under rotations and hence is right or left-handed ( $R$  or  $L$ ). In the ultra-relativistic limit, chirality is identical to helicity, the projection of spin onto 3-momentum. It is very important because it has been observed that charged weak currents via  $W^\pm$  only interact with left-handed particles and right-handed antiparticles (known as V-A coupling), which is used to construct the Standard Model. The relative  $W$  couplings are given by isospin, as outlined by table 4.1 (The Higgs doublet  $\Phi$  is introduced in section 4.6). Consequently, it is instructive to show that projecting Dirac spinors in right and left-handed parts gives equation (4.3).

$$\mathcal{L}_{\text{Dirac,mass}} = -m (\overline{\psi}_L \psi_R + \overline{\psi}_R \psi_L) \quad (4.3)$$

The important part to note is that the Dirac mass terms contain left and right-handed chiral fields coupled together. This leads to a potential uncertainty in the Standard Model. Under the Standard Model construction, the only interaction between neutrinos and the rest of the Standard Model is via  $W$  and  $Z$  bosons and both of these only couple to one chiral part of a neutrino. As a result, without any Beyond Standard Model constructions, there is an unobservable chiral part referred to as ‘sterile’. Alternatively, one can claim this is a ‘missing piece’ in the Standard Model and construct theories using this current unknown. In our context, the Type-I seesaw mechanism uses the possibility that neutrinos are Majorana and that the right and left-handed neutrino fields are coupled together [48]. This will now be

discussed in more detail.

## 4.2 Majorana Construction

As neutrinos interact through one chiral part, a common hypothesis is that neutrinos are Majorana rather than Dirac [49]. This exploits the fact that it is only possible to observe one chiral part of neutrinos. To motivate this, it is instructive to split the Dirac equation (equation (4.1)) into its chiral parts (equation (4.4)).

$$i\gamma^\mu \partial_\mu \psi_L = m\psi_R \quad (4.4a)$$

$$i\gamma^\mu \partial_\mu \psi_R = m\psi_L \quad (4.4b)$$

Minimal coupling from electromagnetism is used to deduce a charge conjugation operator (i.e transforming a neutrino into an anti-neutrino)  $\hat{C}\psi = i\gamma^2\gamma^0(\psi)^*$ . By applying  $\hat{C}$  and using the relevant anti-commutator algebras, equation (4.5) is obtained from equation (4.4b).

$$i\gamma^\mu \partial_\mu \underbrace{\left[ \hat{C} \bar{\psi}_R^T \right]}_{i\gamma^2\gamma^0} = m \left[ \hat{C} \bar{\psi}_L^T \right] \left( \stackrel{def}{=} m\psi_L^c \right) \quad (4.5)$$

It is then quick to deduce that  $\psi_L^c$  has right-handed chirality. As a result, it is possible to construct from one chiral part of the Dirac equation an opposite chiral part that also satisfies the Dirac equation (equation (4.5)). Combining these gives a Majorana spinor with different degeneracies and transformation properties. Canonically, a Majorana spinor is then written as equation (4.6).

$$\chi_L \stackrel{def}{=} \psi_L + \psi_L^c \text{ with } \chi_L^c = \chi_L \quad (4.6)$$

This form is given because from here, it is possible to get an intuition of how LNV is obtained later. However, in the next section to construct the Lagrangians these parts are then written separately ( $\nu_L \neq \nu_L^c$ ).

### 4.3 Type-I Seesaw Mechanism

This is now the point where one can define a HNL. For simplicity, a case with one lepton generation is used, but the model generalises easily to three.

Analogous to equation (4.3), the most generic Majorana mass Lagrangian that can be written down with 2 separate fields  $\nu_L, \nu_R$  is equation (4.7). In this context  $\nu_L$  is analogous to a Standard Model left-chiral charge eigenstate (i.e.  $\nu_e, \nu_\mu$  or  $\nu_\tau$ ) [50].  $\nu_R$  is the sterile field.

$$\begin{aligned}
 2\mathcal{L}_{D+M} = & - \underbrace{m_D \bar{\nu}_R \nu_L - m_D \bar{\nu}_L^c \nu_R^c}_{\text{Dirac mass terms}} \\
 & - \underbrace{m_L \bar{\nu}_L^c \nu_L - m_R \bar{\nu}_R^c \nu_R}_{\text{Majorana mass terms}} + h.c.
 \end{aligned} \tag{4.7}$$

By the constraints of ElectroWeak (EW) local gauge invariance  $m_L = 0$ .<sup>1</sup> Consequently, the Lagrangian can be written in a matrix form (equation (4.8)).

$$(\bar{\nu}_L^c, \bar{\nu}_R) \begin{pmatrix} 0 & m_D \\ m_D & m_R \end{pmatrix} \begin{pmatrix} \nu_L \\ \nu_R^c \end{pmatrix} + h.c. \tag{4.8}$$

This is then trivially diagonalised to change from a weak eigenstate to mass/propagation ( $\nu$  and  $N$ ) eigenstates given by equations (4.9) and (4.10). This uses that  $m_R \gg m_D$ .

$$m_{N,\nu} = \frac{1}{2} \left[ m_R \pm \sqrt{m_R^2 + 4m_D^2} \right] \approx m_R, \frac{m_D^2}{m_R} \tag{4.9}$$

$$\nu \sim (\nu_L + \nu_L^c) - \frac{m_D}{m_R^2} (\nu_R + \nu_R^c) \tag{4.10a}$$

$$N \sim (\nu_R + \nu_R^c) + \frac{m_D}{m_R^2} (\nu_L + \nu_L^c) \tag{4.10b}$$

---

<sup>1</sup>The weak charges of this term are  $T_3 = 1, Y = -2$  and, hence, cannot be made locally gauge invariant. This is critical to make the Standard Model renormalisable.

Now, given the correct mass scales of  $m_D$  and  $m_R$  the mass of the Standard Model neutrino  $\nu$  is suppressed (hence the term seesaw). It also predicts a massive resonance due to  $N$  which is a HNL. This construction of HNL is generated by several models used within the theory community.

## 4.4 ATLAS and CMS HNL Signal Models

To generate ATLAS sensitive signal processes, a  $W$  branching fraction and a more generalisable form of the mass eigenstates must be considered. To construct these Feynman diagrams one can use two bases:

1. Using the diagonalised mass states given in equation (4.10) can give direct branching from  $W$ s into HNLs (section 4.4). This can be seen by considering the effect of the small perturbation ( $\sim \frac{m_D}{m_R}$ ) on  $W^\pm$  currents in the Standard Model. This convention is taken as it leads to a more intuitive origin of mass resonances and allows for a simpler general model.
2. Using lepton number weak eigenstates without diagonalising for mass leads to identical behaviour provided all possible diagrams are considered.

Hence, three generations of neutrino and HNL are used in the Lagrangian. No assumption about the flavour mass matrix being diagonal are made. Inverting this generalisation to equation (4.10) gives a interaction state of the form in equation (4.11) [51, 52].

$$\nu_{L,\ell} = \sum_{\text{mass},i} U_{i,\ell} \nu_i + \sum_{\text{mass},j} V_{\ell,j} N_j \quad (4.11)$$

This is an equivalent extension to the Pontecorvo–Maki–Nakagawa–Sakata matrix (PMNS) [53]. Consequently, there is a unitarity condition such that  $UU^\dagger + VV^\dagger = 1$ . Using this in the  $W \rightarrow \ell\nu$  coupling terms for the Standard Model Lagrangian gives equation (4.12).  $P_{L/R}$  are the left and right-handed chiral projection operators

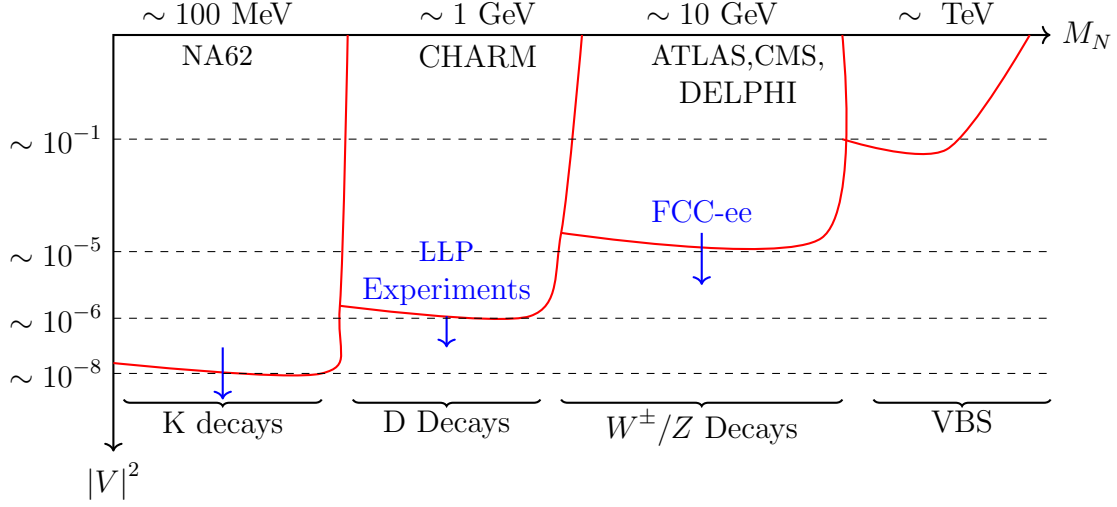


Figure 4.2: A simplified overview of HNL parameter exclusion space (red) with future developments in blue. This does not include neutrino experiments. (inspired by [54])

respectively.

$$\Delta\mathcal{L} = -\frac{g_W}{\sqrt{2}}W_\mu^+ \sum_{\text{HNL},k'} \sum_{\ell} [\bar{N}_{k'}V_{\ell k'}^* \gamma^\mu P_L \ell] + \text{h.c.} \quad (4.12)$$

This is enough to construct diagrams with the vertex  $W \rightarrow \ell N$  which will scale with  $|V|^2$  for each vertex in the cross-section. At this point it is now possible to consider and construct sensitive Feynman diagrams at EW scales. Figure 4.2 gives a simplified overview of parameter space for collider/fixed target searches.

For ATLAS-CMS sensitivity, two sensitive diagrams are used for searches: resonant and non-resonant W decays ( $m_N < m_W$ ) and non-resonant VBS scattering. These are shown in figure 4.3. By adding together the number of leptons ( $\ell^-$ ,  $\nu_\ell$ ) and anti-leptons ( $\ell^+$ ,  $\bar{\nu}_\ell$ ) of a particular flavour (for example,  $\ell = e$ ) in the outgoing final states a non-zero value is obtained. As the incoming state of  $pp$  has no leptons, this conservation property has been violated. This is known as Lepton Number Violating (LNV). This kind of process is negligible in the Standard Model, and hence, there will be minimal background for this kind of signal.

For resonant production there are two regimes. For small HNL masses below 10 GeV, ATLAS exploits a displaced signature [55]. This is where the HNL has a finite

lifetime and decays within the detector.<sup>2</sup> This requires special tracking reconstruction code to be run in order to reconstruct a displaced vertex deeper into the ID than standard reconstruction. Further, a LNC current can also be probed with final states such as  $e^+e^-\mu^+$ . For larger masses, the decay length becomes too short to observe, so a *prompt* signature is used. This relies on observing the LNV current only.

For non-resonant production either diagram shown in figure 4.3 can be used. Vector Boson Scattering (VBS) production (figure 4.3b) has a larger sensitivity to much higher mass HNLs [52]. This is due to high masses and energies being more kinematically accessible. This leads to the first direct probing of HNLs up to scales of 20 TeV.

To create exclusion plots for this theory, a standard minimal model is typically used for reinterpretation. This includes a single PNMS/CKM mixing angle with one lepton flavour  $|V_{l,N}|$  alongside a single massive neutrino  $m_N$ . This can be seen as the parameter that dictates the number of events you expect as  $N_{events} \propto |V_{l,N}|^4$ . This construction is dubbed the neutrino Minimal Standard Model extension or  $\nu$ MSM [56].

For the remaining chapters of this thesis, only the  $\mu\mu$  VBS style scattering is discussed. A more detailed discussion of the kinematic properties of this channel is given in section 5.3.2.1.

## 4.5 The Higgs Mechanism From The Perspective of Fermion Masses

In the previous sections of this thesis, a slightly incomplete form of the Standard Model masses is given. Mass terms of the form in equation (4.3) are not locally

---

<sup>2</sup>A typical propagator for a QFT calculation would not be valid over macroscopic distances due to quantum decoherence. Back-of-the-envelope calculations can show decoherence effects on HNLs to be negligible [51].

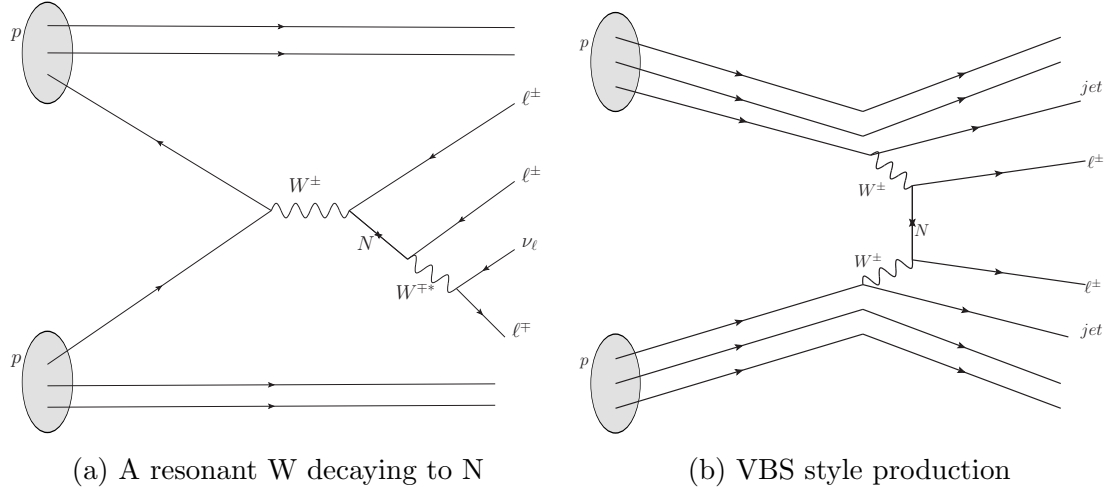


Figure 4.3: The resonant and non-resonant HNL production probed at ATLAS [1].

gauge invariant under  $SU(2)_L \times U(1)_Y$ . This symmetry group describes the EW interaction. Without this invariance, a theory cannot be re-normalisable and leads to divergences in the model's predictions [17].

This, alongside other diverging cross-sections and the massive nature of W and Z bosons, motivates the need for the Higgs mechanism. This was treated as 'the missing piece' of the Standard Model until 2012.

As a very brief summary, the Higgs mechanism is outlined as follows. An additional pair of complex scalar fields  $\Phi$  inspired by the Landau model of superconductivity are added to the Standard Model Lagrangian [57]. These are placed in a weak isospin interaction doublet (equation (4.13) and table 4.1) with a Mexican hat potential and Lagrangian (equations (4.14) and (4.15)).

$$\Phi = \begin{pmatrix} \phi^+ \\ \phi^0 \end{pmatrix} \quad (4.13)$$

$$V(\Phi) = -\mu^2 \Phi^\dagger \Phi + \lambda (\Phi^\dagger \Phi)^2 \quad (4.14)$$

$$\mathcal{L}_{\text{Higgs}} = (\partial_\mu \Phi)^\dagger (\partial^\mu \Phi) - V(\Phi) \quad (4.15)$$

As can be intuitively seen,  $\Phi$  has a non-zero minimum ground state at  $\Phi^\dagger \Phi = \frac{\mu^2}{2\lambda}$  with three degrees of freedom in which this is invariant. By expanding out from

this minimum and choosing a unitary gauge that ‘absorbs’ the unphysical Goldstone modes along the ground state<sup>3</sup>, a vacuum expectation value  $v = \sqrt{\frac{\mu^2}{\lambda}}$  can be perturbed by a real scalar field  $h(x)$ . This is the Higgs boson which is used within the QFT framework of the Standard Model. This results in equation (4.16).

$$\Phi = \frac{1}{\sqrt{2}} \begin{pmatrix} 0 \\ v + h(x) \end{pmatrix} \quad (4.16)$$

Putting this formula back into the Higgs doublet Lagrangian with the covariant derivative of  $SU(2)_L \times U(1)_Y$  gives many properties:

- The mechanism for EW symmetry breaking and the gauge invariant masses of  $W$  and  $Z$  bosons.
- The Higgs boson and its coupling to the  $W$  and  $Z$  bosons.
- A prescription for gauge invariant fermion masses.

The important detail to fall out of this framework for this thesis is equation (4.16) and the gauge invariant mass terms it can be used to generate. By using  $\Phi$  or  $\Phi_c \stackrel{def}{=} -i\sigma_2\Phi^*$ , one can write down what is known as a Yukawa coupling term of leptons<sup>4</sup> in the form of equation (4.17).

$$\mathcal{L}_\ell = -g_\ell \left( \bar{L}\Phi R + \bar{R}\Phi^\dagger L \right) \text{ or } \mathcal{L}_\nu = -g_\ell \left( \bar{L}\Phi_c R + \bar{R}\Phi_c^\dagger L \right) \quad (4.17)$$

$L = (\nu_{\ell,L}, \ell_L)$  and  $R = \ell_R$  or  $(\nu_{\ell,R}, \ell_R)$  depending the existence of sterile neutrinos (hence this treatment is also valid for HNLs).

$$\mathcal{L}_\nu = -\frac{g_\nu}{\sqrt{2}} v (\bar{\nu}_L \nu_R + \bar{\nu}_R \nu_L) - \frac{g_\nu}{\sqrt{2}} h (\bar{\nu}_L \nu_R + \bar{\nu}_R \nu_L). \quad (4.18)$$

<sup>3</sup>These can be shown to correspond to W and Z longitudinal modes.

<sup>4</sup>The approach for quarks is identical

This combination of terms is gauge invariant. Comparing terms with equation (4.7) gives  $m_D = \frac{1}{\sqrt{2}}vg_\nu$  which is used in the Type-I seesaw model. Using  $\Phi$  to construct the Lagrangian also allows generating a different mass term in the next section.

## 4.6 The Weinberg Operator

An alternative model for the t-channel analysis is the Weinberg operator model. This model is typically used for neutrinoless double beta decay [52].

Here, the notion that neutrinos are Majorana particles is taken from section 4.2 but without hypothesising any sterile parts ( $\nu_R$ ). Instead of through Yukawa coupling, neutrino masses are generated using a higher-order Lagrangian. Across theoretical physics, a common practice is to write down a general Lagrangian density with all terms allowed by symmetry and assume higher order terms only occur at higher corresponding energy scales and can be neglected [58]. In particle physics, we call this an Effective Field Theory (EFT). For local gauge symmetry at dimension five, the only gauge-invariant term possible is of the form of equation (4.19) [52, 59]. Here, all our definitions match those in section 4.5. This includes using the Higgs field.

$$\mathcal{L}_5 = \sum_{\ell, \ell'} \sum_{e, \mu, \tau} \frac{C_5^{\ell\ell'}}{\Lambda} [\Phi \cdot \bar{L}_\ell^c] [L_{\ell'} \cdot \Phi] + \text{h.c.} \quad (4.19)$$

The scaling of the Lagrangian density is determined by  $\frac{C_5^{\ell\ell'}}{\Lambda}$ .  $C_5^{\ell\ell'}$  is the EFT Wilson coefficient, which can contain a complex phase which varies according to which lepton flavour it couples to.  $\Lambda$  is the shared energy scale between terms of  $C_5^{\ell\ell'}$ . Due to the resulting interaction being very off-shell and only probing one channel, the analysis is only sensitive to this normalisation.

By taking a unitary gauge and using the Standard Model vacuum expectation, a

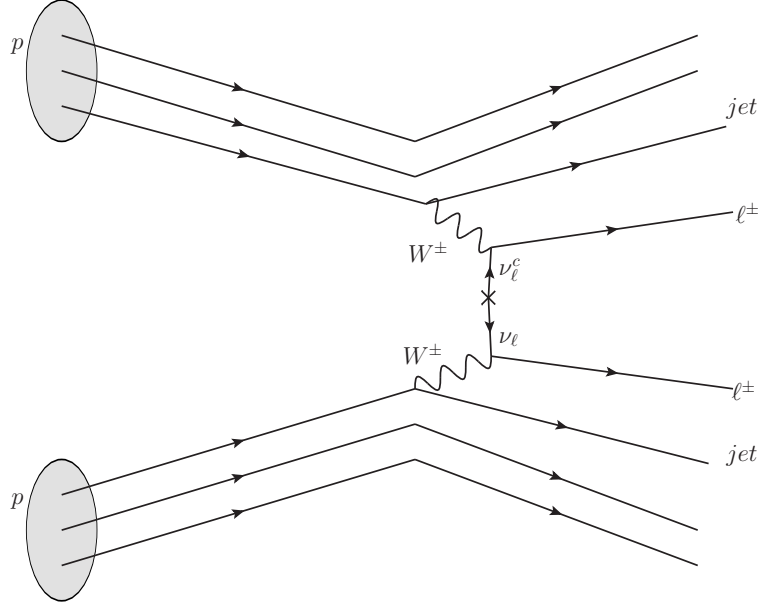


Figure 4.4: Weinberg Model LHC production [1]

three-term expansion is obtained [52].

$$\mathcal{L}_{5,\nu} = \sum_{\ell,\ell'}^{e,\mu,\tau} \underbrace{-\frac{C_5^{\ell\ell'}}{2\Lambda} hh \bar{\nu}_\ell^c \nu_{\ell'} - \frac{C_5^{\ell\ell'} v}{\Lambda} h \bar{\nu}_\ell^c \nu_{\ell'}}_{\text{Higgs Boson Couplings}} \quad (4.20a)$$

$$- \underbrace{\frac{C_5^{\ell\ell'} v^2}{2\Lambda} \bar{\nu}_\ell^c \nu_{\ell'}}_{\text{Mass Term and Signal Model}} + \text{h.c.} \quad (4.20b)$$

Using equation (4.20b) can also relate these to an effective Majorana matrix equivalently to neutrinoless double beta decay searches (equation (4.21)). This is then used to construct a Feynman diagram (figure 4.4) that mimics the topology of our HNL search. Using that momentum carried by the Weinberg current ( $\sim m_W$ ) is much larger than the effective mass, a perturbative Lagrangian equivalent to an unphysical HNL is obtained. The final modelling assumption is a simplified scheme where only one flavour as a benchmark is used [52].

$$m_{\ell\ell'} = C_5^{\ell\ell'} v^2 / \Lambda \quad (4.21)$$

With this construction probing  $m_{\mu\mu} \sim 10$  GeV, it is an interaction with a muon  $p_T$  distribution much more similar to our Standard Model background (see appendix A.3).

Moreover, the kinematic distributions in this limit change negligibly, so instead, the process is probed by scaling the normalisation  $\mu$  which is intuitively proportional to  $|\frac{C_5^{\ell\ell'}}{\Lambda}|^2$ . However, the no-outgoing neutrino same-sign same-flavour final state makes it feasible to re-use the same analysis strategy from the HNL search.

## 4.7 Suppression of Lepton Number Violation in HNL models

In some HNL models, one expects the LNV currents probed by a prompt signature to be suppressed. The phenomenology is relatively trivial, but the origin/naturalness of such a mechanism is still contentious. This appears to be especially true with respect to cosmological models. The phenomenology is discussed briefly here.

For this suppression, two of the three HNL particles are nearly degenerate in mass. This is known as a quasi-Dirac current. In this context, when constructing branching ratios/decay lengths it is needed to consider the interference between these diagrams. This is given by equation (4.22) [50].  $\Gamma^{\pm\pm}$  is the LFV case and gives  $(1 - \cos(\delta m_N \tau))$  on the RHS.  $\Gamma^{\pm\mp}$  is the LNC case and gives  $(1 + \cos(\delta m_N \tau))$  on the RHS.  $\alpha$  and  $\beta$  are the lepton flavours off of the HNL vertices and  $\tau$  is the decay length<sup>5</sup>.

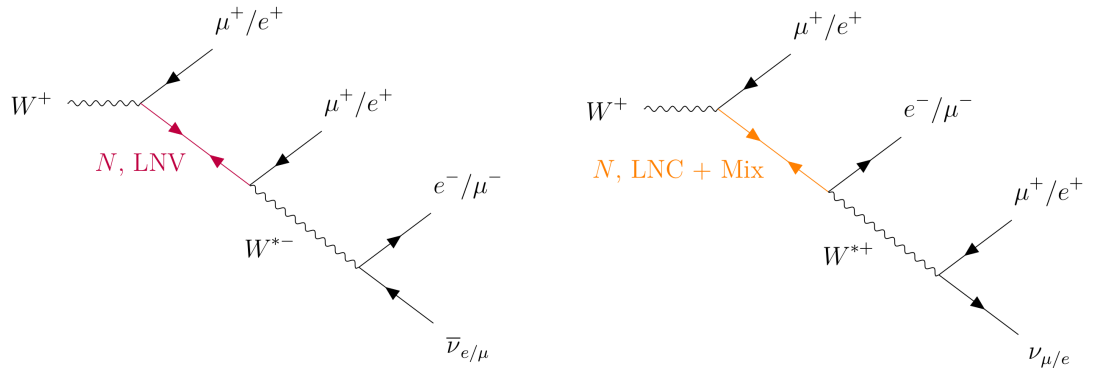
$$d\Gamma_{\alpha\beta}^{\pm\pm}(\tau) \sim |V_{\alpha 1}|^2 |V_{\beta 1}|^2 (1 \pm \cos(\delta m_N \tau)) e^{-\Gamma\tau} d\hat{\Gamma}_{\alpha\beta}^{\pm\pm} \quad (4.22)$$

The key point is that for LNV currents  $\delta m_N \tau \rightarrow 0$  gives  $(1 - \cos(\delta m_N \tau)) \rightarrow 0$  leading to suppression of prompt signatures. For ATLAS prompt signatures ( $\tau \sim 1mm$ ) this gives  $\delta m_N \lesssim 1$  eV. This is very small and arguably fine-tuned, making the setup unlikely in the eyes of some theorists and is discussed further in section 4.8.

Even if this is true, high-mass LNV suppressed HNLs are probeable. Recent experimental discussions have been exploring that HNLs could have large off-diagonal mixing terms as in in the SM neutrino sector. This extension to the  $\nu$ MSM makes contributions from diagrams including figure 4.5(b) possible. This means one flavour

---

<sup>5</sup>natural units are used here



(a)  $\nu$ MSM, no mixing between flavours and LNV current (b) Mixing between flavours permitted, allowing for a similar outgoing signal but for a LNC current, avoiding LNV suppression.

Figure 4.5: The tri-leptonic signal model for HNL prompt analysis. These final states are heavily suppressed in Standard Model processes due to the outgoing lepton number ( $L_{e/\mu} = -2$ ) being different to the incoming value ( $L_{e/\mu} = 0$ ). (a) is the previously probed signal whereas (b) is an example of what could be probed if flavour mixing is allowed for HNLs. This allows a way to circumvent LNV suppression.

of HNL could be generated by an electron and then decay into a muon via a  $W$  or vice versa. This allows two ways to get the same tri-leptonic same-sign same-flavour  $e$  or  $\mu$  state. Furthermore, if one does the non-trivial task of considering the Majorana spin correlations of both the diagrams in figure 4.5, then this changes the kinematics, and the two different types might be distinguishable in the analysis.<sup>6</sup>

These spin correlation effects were not included in the partial run 2 HNL  $s$ -channel analysis in the simulation of the signal [60]. As a result, the signal vs background rejection was likely not optimised properly.

This means that, in principle, if a signal was found with adequate statistics, we would be able to extract the probabilities for each of these hypotheses. The more likely scenario is that this extends the existing confidence limits but with a LNC+Mixing exclusion alongside the LNV exclusion. Theorists have reinterpreted the partial run 2 analysis with a model that uses relative mixing angles from a combined fit of neutrino oscillation experiments. This weakens the limits by up to a factor of 10 [61].

<sup>6</sup>There is a significant irreducible overlap of detectable phase space even at particle level

## 4.8 Limitations and Naturalness of Collider HNLs

As with all beyond Standard Model theories, there is much scrutiny and debate as to whether a model is consistent with current experimental results, self-consistent or ‘natural’. For HNLs, there are a few common points of discussion.

On the one hand, HNLs resolve some unexplained astrophysical phenomena without introducing new gauge symmetries and many particles like supersymmetry or technicolour. It also is an interesting model from an experimental standpoint due to being a detectable particle within precision data from both flavour and general-purpose collider experiments. However, especially in the higher mass ranges the collider experiment probe are too large to be a driver of baryon asymmetry [54].

However, this model is not without criticism. As discussed in section 4.3, the Type-I seesaw model does not resolve the suppression of neutrino masses in detectable phase space. For this, one would require a collider with much greater energies. Although there are no new particles, the effective addition of another PNMS-style matrix still adds many new parameters to our model, which would make it easy to overfit an astrophysical model or anomaly in a neutrino experiment. This is partially why the  $\nu$ MSM exists.

Furthermore, the LNV suppression mechanisms discussed here are extremely model-dependent. Such a small difference in masses opens up more criticisms about fine-tuning and stability against radiative corrections. Models to describe these phenomena typically add a larger group of particles or hidden sectors. Moreover, the Majorana neutrino hypothesis is one of the longest-standing open questions in particle physics and has never been proven. There exist claimed natural abstract mathematical routes of a Majorana spinor, but this brings in some philosophy and personal taste too [62].

The model can also lead to further fine-tuning issues. If the mass of the HNL is in our detectable phase space ( $M_N \gtrsim 5$  GeV), loop corrections to the light neutrino

generations become sizeable and fine-tuning of parameters is needed to cancel out these terms [63].

## CHAPTER 5

---

### Searching for high mass HNLs at ATLAS

---

This chapter outlines the specific steps on how to go from a large ATLAS dataset to a small subset of the data to deduce the presence of HNLs.

To do this, we first precisely define the models used and ATLAS data we run over. Then, we discuss the sensitive observable quantities in data we can use to create enriched regions for our signal and contaminating backgrounds from Standard Model  $W$  and  $Z$  boson scattering. Finally, we discuss our statistical modelling to test our data. In doing so, we demonstrate its capability to fit a signal or lack thereof on simulated Signal Region (SR) data. Unblinded plots and the corresponding hypothesis testing methodology are discussed in chapter 7.

## 5.1 Motivation and Signal Topology

A previously unprobed model in ATLAS data before this analysis is looking for type-I seesaw HNLs in a VBS-like WW scattering type topology. Given the recent success in measuring VBS ssWW scattering [64, 65], the exotic re-interpretations of this topology were considered [53]. For this analysis, the production diagram equivalent to neutrinoless double beta nuclear decay (figure 4.3b) is targeted. Decays, where the two outgoing lepton flavours are not electrons, are kinematically inaccessible by experiments targeting this process. Because of this, these are of particular interest to theorists because they have been probed less. ATLAS and CMS are uniquely placed to probe these channels due to the energy scales they access. Equivalently, we have unique direct sensitivity to a Weinberg model operator in the muon channel, and hence, to  $C_5^{\mu\mu}$  [52].

The VBS diagram allows for unique signal features. It can be shown that the scattering amplitude is proportional to the di-jet mass [66]. This is given simply by equation (5.1). This also implies the signal favours large rapidity gap hard jets with a back-to-back topology.

$$m_{jj}^2 \approx 2p_T^{j_1} p_T^{j_2} [\cosh(\eta_{j_1} - \eta_{j_2}) - \cos(\phi_{j_1} - \phi_{j_2})] \quad (5.1)$$

When the two incoming quarks have no gluon exchange, there is a suppression of additional central hadronic activity due to colour flow.<sup>1</sup> This makes the back-to-back topology more pronounced than the WW and WZ scattering with gluon exchange (section 5.3).

Due to the HNL being off-shell in t-channel for this analysis, the combined system has a less strong correlation between the signal mass and the kinematics than the

---

<sup>1</sup>Collinear emissions of a gluon need to be considered with the equivalent exchange between quarks to prevent infrared divergences. However, this gluon exchange changes the colour flow and so does not interfere with the original diagram of interest [66]. This argument also holds for ssWW EW but not EW+QCD

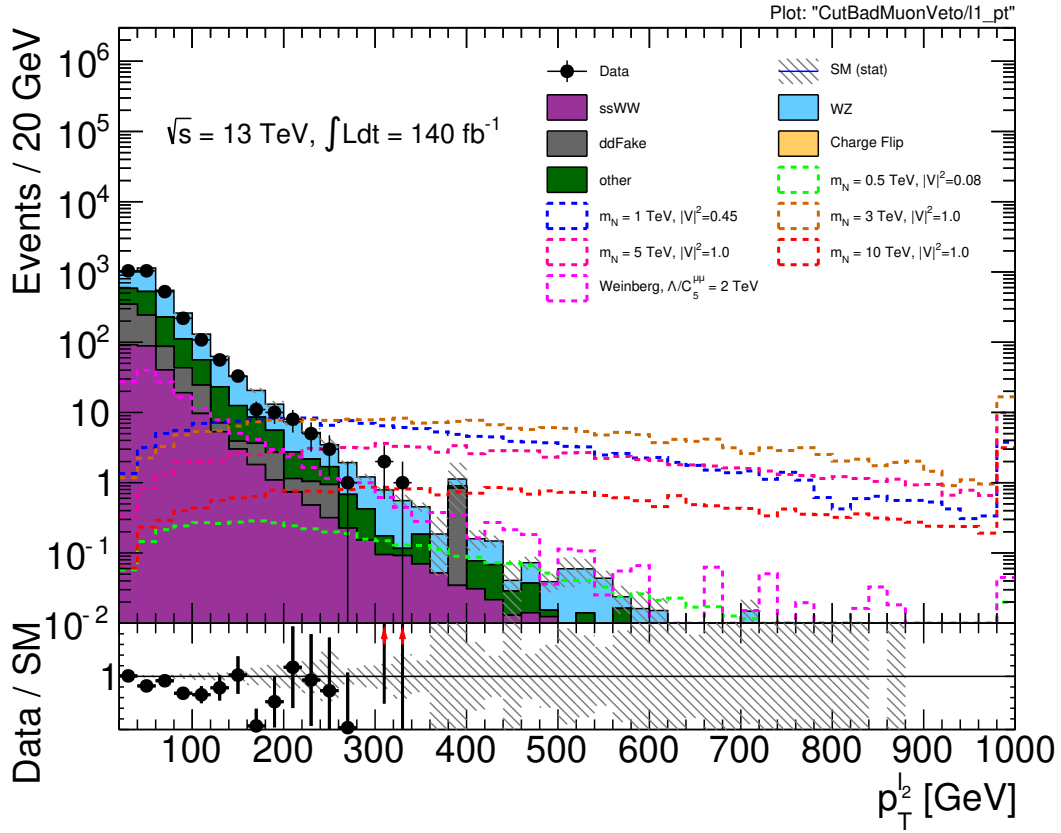


Figure 5.1: Sub-Leading Lepton  $p_T$  distributions of the Signal and background. It is clear this is the main discriminator of signal over background.

resonant case. However, the fact the outgoing leptonic activity is much broader kinematically (mostly lepton  $p_T$ ) than the Standard Model backgrounds (for WZ and WW  $p_T \sim 40\text{-}50$  GeV) remains the main selector for HNL signals. This can be seen well by plotting the signal and background distributions by sub-leading lepton  $p_T$ . Sub-leading  $p_T$  provides better signal vs background rejection compared to the leading lepton (figure 5.1). For the remainder of the thesis, every histogram's final bin includes all values exceeding the range. For example, the final bin of figure 5.1 includes  $p_T^l$  within  $[975, \infty]$  GeV.

## 5.2 Object Definitions

In this analysis, five reconstruction objects are used:

1. Electrons
2. Muons
3. Jets
4. Missing Energy  $E_T^{\text{miss}}$
5. Jet b-tagging

Taus and photons are not considered throughout the study.

Additionally for this analysis, we use three terms for the sub-collections of leptons and jets.

- **Baseline:** minimal selection matching skimming requirements; ‘overlap removal’ ( applied to prevent double counting objects outlined in section 5.2.6) and  $E_T^{\text{miss}}$  requirements.
- **Signal:** Tighter collection used for defining our final analysis signal and control regions.
- **Anti-ID Leptons:** baseline objects that fail a subset of the signal selection used in hadronic fake estimation (chapter 6).

These are discussed to be used to define our analysis selections.

At this stage, it is useful to introduce ‘Identification’ and ‘Isolation’ working points provided by the CP groups. Identification provides a known benchmark of efficiency, indicating the proportion of particles that are successfully selected. This can be determined through either simulation or data. Isolation, in the context of this thesis, provides rejection of leptons produced by heavy hadronic decays over the targeted process (see chapter 6).

Feature	Criterion
Pseudorapidity range cut $E_T$ cut	$ \eta  < 2.47$ $> 4.5 \text{ GeV}$
Object quality	Not from a known bad calorimeter cluster Remove clusters from regions with LAr bad high voltage (2016 data only)
Track to vertex association	$ d_0/\sigma(d_0)  < 5$ $ z_0 \sin \theta  < 0.5 \text{ mm}$
Identification Isolation	<b>Loose LH</b> <b>none</b>

Table 5.1: Baseline electron selection criteria [68, 67].

Feature	Criterion
Pseudorapidity range cut $E_T$ Cut	$( \eta  < 1.37) \quad    \quad (1.52 <  \eta  < 2.47)$ $> 10.0 \text{ GeV}$
Identification Isolation Overlap Removal	<b>Tight LH</b> <b>Gradient</b> applied, default behaviour

Table 5.2: Signal electron selection criteria (additional cuts with respect to the baseline selection). [68, 67]

### 5.2.1 Electrons

In this analysis, electrons are mostly used as a rejection or background estimation tool. The common working points are fully outlined in [67]. These are reconstructed by targeting EM shower shapes with a matching track.

Baseline electrons are required to be within  $|\eta| < 2.47$  and have a minimum transverse energy of 4.5 GeV. There are additional constraints on how prompt the lepton is from track reconstruction, alongside identification and isolation quantities derived from many tracking and calorimeter inputs (table 5.1). A small number of objects from 2016 are rejected due to bad calorimeter data in some phase space.

On top of this, signal electrons have tighter  $E_T$ , identification and isolation requirements table 5.2. Finally, crack electrons ( $1.37 < |\eta| < 1.52$ ) are rejected where there is a gap in calorimeter coverage with weaker reconstruction efficiency.

Feature	Criterion
Identification working point	<b>Loose</b>
Isolation working point	<b>none</b>
$p_T$ cut	$> 3.0$ GeV
Pseudorapidity range cut	$ \eta  < 2.7$
Cut	$< 15.0$
$ z_0 \sin \theta $ cut	$< 1.5$ mm

Table 5.3: Baseline muon selection criteria [26, 68].

Feature	Criterion
Identification working point	<b>Medium</b>
Isolation working point	<b>FixedCutPflowTight</b>
$p_T$ cut	$> 10.0$ GeV
Pseudorapidity range cut	$ \eta  < 2.5$
$d_0/\sigma(d_0)$ cut	$< 3.0$
$ z_0 \sin \theta $ cut	$< 0.5$ mm
Overlap Removal	applied, default behaviour

Table 5.4: Signal muon selection criteria (additional cuts with respect to the baseline selection) [26, 68].

### 5.2.2 Muons

Baseline muons have a minimum  $p_T$  of 3 GeV and  $|\eta| < 2.7$  alongside the loose object identification (see section 2.8) requirements and minimal track reconstruction quality for promptness from the collision point (table 5.3). The reconstruction steps are detailed in sections 2.7 and 2.8 with further depth in [69]. For a signal muon (table 5.4), stricter muon identification criteria are applied, in addition to requirements on how isolated the muon is [26].

In this analysis, we adopt the particle-flow muon metrics of isolation (denoted **Pflow**). This uses the combined calorimetry and tracking information nearby the muon object to search for charged and neutral hadronic activity. This loosely looks at what energy ratios are associated with the  $p_T$  of the muon track versus other activity. The actual observables/cuts are fully defined in [26].

Feature	Criterion
Fail Signal Selection	True
Identification working point	Medium
Isolation working point	FixedCutPflowLoose
$p_T$ cut	$> 10.0$ GeV
Pseudorapidity range cut	$ \eta  < 2.5$
$d_0/\sigma(d_0)$ cut	$< 10.0$
$ z_0 \sin \theta $ cut	$< 0.5$ mm

Table 5.5: Additional cuts above baseline muons to define anti-ID muons [68, 69]. The looser, inverted cuts with respect to signal key to background estimation are highlighted blue.

Feature	definition
Algorithm	anti- $k_t$
$R$ -parameter	0.4
Selection requirements	
Observable	Requirement
$p_T$	$> 20.0$ GeV
$ \eta $	$< 4.5$
JVT	$> 0.5$ for $p_T < 60$ GeV, $ \eta  < 2.4$
fJVT	$< 0.5$ , $ timing  < 10$ ns for $p_T < 60$ GeV, $2.5 <  \eta  < 4.5$

Table 5.6: Baseline jet reconstruction criteria [68, 71].

### 5.2.3 Jets

Jets are the hadronised final states of the outgoing quarks of our scattering process and are clustered according to the anti- $k_t$  clustering algorithm [70]. The baseline jet object is defined in table 5.6. For this analysis, we have the cluster algorithm  $R$  value set to 0.4, referred to as ‘small R jets’. This aims to pick hadronising light quarks originating from the targets scattering event. The inputs and calibration procedures are given in [71]. These algorithms are reasonably fixed in design due to the need to be provably stable against QCD divergences. This is discussed further in section 5.3.2. Many data-driven factors are then used to calibrate the energy, for example the jet area. The same particle-flow techniques are used as section 5.2.2 to form combined objects from tracks and calorimeter deposits [72].

A Jet Vertex Tagger (JVT) variable is then used to reject pile-up events from the target hard scatter event. This uses tracking quantities to attribute a quality of a jet being from the primary vertex instead of soft QCD pile-up [73]. A forward JVT (fJVT) provides pile-up rejection beyond the range of the tracker by attempting to tag vertices with missing momenta to forward jets [74].

To be a signal jet, a simple  $p_T > 25$  GeV requirement is applied alongside overlap removal (table 5.7).

Selection requirements	
Observable	Requirement
$p_T$	$> 25.0 \text{ GeV}$

Table 5.7: Signal jet reconstruction criteria (additional cuts with respect to baseline) [68, 71].

## 5.2.4 Missing Transverse Momentum

Missing transverse momentum measures how much energy is lost from the detector and not reconstructed, either through mismeasurement or from a real undetectable particle such as a neutrino. This is a negative vector sum of observed energy deposits. This is a valuable discriminator for the analysis because the signal model produces no neutrinos in the final outgoing state, whereas leptonically decaying W bosons result in a real neutrino.

For this analysis, the electrons, muons and jets are used as inputs for this calculation (equation (5.2)) [75]. Alongside this, we have a ‘soft term,’ which is any energy not assigned to an object. A tight working point is used, which corresponds to rejecting forward jets ( $|\eta| > 2.5$ ) with  $p_T$  under 30 GeV from being used in the calculation.

$$E_T^{\text{miss}} = -E_T^\mu - E_T^e - E_T^{\text{jets}} - E_T^{\text{soft}} \quad (\text{Vector Sum}) \quad (5.2)$$

For this analysis, it has been demonstrated that the  $E_T^{\text{miss}}$  significance is a more powerful discriminator. This variable is based on the proxy likelihood notion of significance against a  $E_T^{\text{miss}}=0$  truth value. This uses the detector resolution of the individual objects, giving more object-specific inputs to the calculation that can better discriminate poor resolution from real physics missing momenta [76].

### 5.2.5 Heavy Hadron Tagging

For this analysis, b- and c-quark productions may contaminate our signal region (discussed at length in chapter 6). Here, the work of the ATLAS experiment on b-tagging for Higgs measurements is a powerful starting point [77]. The DL1r algorithm uses an extensive list of information from the low-level tracking algorithms as input for a deep neural net to classify heavy hadron decays using the tracks alongside a separate b-tagger neural net. For example, the impact parameters (equation (2.5)), numbers of tracks attached to primary/secondary vertices. This decision is applied to a narrower jet collection outlined in table 5.8.

Here we use a 85% b acceptance tagger to reject b-jets in our regions (see section 5.4.1). This gives an expected rejection factor of 40 for light jets and 2.9 for charm quarks [77, 78, 79].

Feature	Criterion
	EM PFlow jets
Jet collection	<code>AntiKt4EMPFlowJets</code>
Jet selection	$p_T > 20$ GeV $ \eta  < 2.5$ JVT cut if applicable
Algorithm	<code>DL1r</code>
Operating point	Fixed Efficiency = 85 %

Table 5.8: Heavy flavour b-tag selection criteria [68, 77].

Reject	Against	Criteria
Electron	Electron	shared track, $\Delta\eta = 0.075$ , $\Delta\phi = 0.125$ , $p_{T,1} < p_{T,2}$
Muon	Electron	is Muon identified in the calorimeter and shared ID track
Electron	Muon	shared ID track
Jet	Electron	$\Delta R < 0.2$ and, if the electron satisfies $E_T < 100.0$ GeV, the jet is not a b-jet
Electron	Jet	$\Delta R < 0.4$
Jet	Muon	special cleaning procedure for fake PFlow jets
Jet	Muon	not a b-jet, <code>NumTrack</code> < 3 and (ghost-associated [80] or $\Delta R < 0.2$ )
Muon	Jet	$\Delta R < 0.4$

Table 5.9: The overlap removal procedure for the analysis [68].

### 5.2.6 Overlap Removal

For this analysis, we use the common ATLAS utilities and procedures to remove object identifications that use the same energy deposits. This is done with the baseline objects in the recommended way for b-jets. This is outlined in table 5.9.

## 5.3 Samples

To determine whether there are any observed phenomena beyond the Standard Model based on ATLAS data, it is necessary to extensively model the signal and background distributions. As a first step, Monte Carlo simulations of QFT processes<sup>2</sup> (known as generators) are used then fed into detector simulation (ATLFastII and GEANT 4) [81, 82]. Both simulated detector response and data are put through the same chain of CP reconstruction.

For a search with an unusually high  $p_T$  charge violating signal topology, the number of events in the signal, control and validation regions are very low ( $\sim 100$  Events in 4 years of data). Hence, the kind of processes that lead to contamination in our signal region may be detector effects that are not well-modelled or understood by the ATLAS collaboration. This leads to some backgrounds such as charge misidentification and QCD hadronic activity faking leptons being evaluated for the analysis ‘without’ simulation. This is done through ‘data-driven’ techniques. These are discussed in depth in chapter 6.

This section outlines how to precisely select the data and generate the modelling of background physics processes alongside the potential HNL or Weinberg signal. This is done through Monte Carlo (MC) integration. Alongside the software and parameter set choices for different generators, some intuitions for signal topologies are developed.

---

<sup>2</sup>Monte Carlo generation is numerically integrating differential cross-sections using random sampling. This term is used colloquially in physics to mean simulated data.

Trigger chain names	2015	2016	2017	2018
HLT_mu20_loose_L1MU15	✓			
HLT_mu26_ivarmedium		✓	✓	✓
HLT_mu50	✓	✓	✓	✓

Table 5.10: The single muon HLT trigger chains used in the analysis [68].

Year	$\mathcal{L}$ [ $\text{fb}^{-1}$ ]
2015	3.24
2016	33.4
2017	44.6
2018	58.8
total	140

Table 5.11: Total Luminosity Of Each Year of Data [84].

One advantage of this analysis is the topological similarity with the Standard Model same-sign WW processes. This means some of the methodologies can be taken from the respective Standard Model group analysis.

### 5.3.1 Data

After an event has been accepted by the HLT (see chapter 3), it is stored at various facilities. Running over every event ever accepted/simulated by ATLAS would be impossibly resource-intensive for individual analysis use. Hence, high-level ‘derivations’ (data selections) are used to filter events with the topology desired (skimming) and with reduced object information (pruning) [83]. The data used by this analysis is fired by single muon HLT chains shown in table 5.10.

The analysis is performed with the full ATLAS-Run 2  $pp$  collision data sample recorded at  $\sqrt{s} = 13$  TeV (table 5.11), i.e. combining data collected during the years 2015, 2016, 2017 and 2018. The analysis uses two derivations.

1. STDM3: The derivation used by the STanDard Model ssWW analysis requiring dilepton ( $ee, \mu\mu$  and  $e\mu$ ) events selected by the dilepton HLT triggers or by offline reconstruction. Used by the main analysis code as it provides a manageably

small but complete dataset for analysis work.

2. STDM4: Single lepton triggers used for data-driven hadronic fake estimation (see chapter 6.)

To not bias the analysis during its development, a blinding scheme is used. This is where, until the design of the analysis is finalised, we do not look at the data in areas we are sensitive to new models. The data was ‘blinded’ by the not looking at data matching the following cuts. This was guided by our signal MC.

- Same-sign  $ee$  or  $\mu\mu$  pair passing tight quality requirements,
- $E_T^{\text{miss}}$  less than 80 GeV,
- At least two jets with  $m_{jj} > 200$  GeV or  $\Delta y_{jj} > 2$ .

One exception is possible for 2015+2016 data only if the following two criteria are met:

- $E_T^{\text{miss}}$  larger than 30 GeV,
- No tight lepton or jet  $p_T$  cuts applied with respect to preselection.

This region of phase space was unblinded already in the context of the ATLAS same-sign WW analysis [85].

### 5.3.2 Monte Carlo Generators

As part of an ATLAS search style analysis, an exhaustive set of possible Standard Model contributions to data is used to estimate background alongside signal. For this, ATLAS maintains a list of recommended samples driven by theorists and

Sample	Generator	Parton Showering and Hadronisation
HNL	MadGraph	Pythia
Weinberg	MadGraph	Pythia
Same Sign WW	MadGraph	Pythia
Other Di-Boson		Sherpa
Tri-Boson		Sherpa
$t\bar{t}V$	MadGraph	Pythia
$t\bar{t}$	POWHEG	Pythia
Single $t$	POWHEG	Pythia
Other + $t$		Sherpa
$W$ or $Z$ + jets		Sherpa
$W$ or $Z$ + $\gamma$ (Mixed EW and QCD)	MadGraph	Pythia
$W$ or $Z$ + $\gamma$ (EW)		Sherpa
Multijet		Pythia

Table 5.12: A summary of our generators used for the analysis. The colour scheme represents the colours and groupings of samples used throughout this thesis in histograms (with the exception of our background estimation, chapter 6). Any uncoloured rows were used for completeness during development and background subtraction for hadronic fake estimation.

experimentalists. Here, these samples are summarised, and where relevant, how the topology leads to a sizeable contribution to the signal region is shown. Some backgrounds are not modelled well by these generators, and this is discussed further in chapter 6. Table 5.12 gives a broad overview of the software used to generate the samples. This is typically split into two key components. Firstly, the *generator* software takes a theoretical scattering matrix element calculation similar to those taken from a perturbative Leading Order (LO) calculation as seen throughout chapter 4. This typically will be modified by higher-order correction diagrams interfering with the LO diagrams. This is referred to as Next-to Leading Order (NLO) and the NNLO for the next highest order and so on. These calculations are done in this analysis by *generators* and are called the hard-scattering process.

Then, additional software is used to deal with the non-perturbativity of Quantum ChromoDynamics (QCD) [18]. At EW scales of energy, the strong coupling constant  $\alpha_s$  is perturbative ( $\sim 0.1$ ). This means the sum of diagrams with increasingly more QCD vertices converges, and we can calculate cross-sections for LHC  $pp$  collisions. However, this assumption fails for the resulting decaying objects, which form bound colour charge singlet states as the particles fragment [86]. In this context, it becomes

necessary to take empirical models. Two features of this field are relevant to this section:

1. A phenomenological approach is necessary to connect the perturbative high-energy quarks and gluons in the outgoing states of Feynman diagrams to an observable collection of hadronic activity. This is because of the divergent properties of QCD. This is called showering due to the emission of quarks/gluons down to energies  $\sim 1$  GeV. This modelling is typically done by separate software for the hard scattering process.
2. The internal structure of protons that scatter in the event is extremely non-trivial. Hence, for a given event, a parton model with two incoming quarks/gluons with 4-momenta fractions of the proton  $x_1, x_2$  and energy scale  $Q^2$  is considered. This leads to a probability/Parton Distribution Function (PDF)  $f_a$ , which is then integrated to obtain a total cross-section  $\sigma$  from the bare parton cross-section  $\hat{\sigma}$ . This is given by equation (5.3). These functions are found using phenomenological parameter fits [87].

$$\sigma = \sum_{\text{partons } a,b} \int_0^1 \int_0^1 dx_1 dx_2 f_a(x_1, Q^2) \overbrace{f_b(x_2, Q^2)}^{\text{PDF for parton b}} \times \hat{\sigma}(\text{targetted process}) \quad (5.3)$$

Finally, as part of the simulation process, it is necessary to overlay each event with a pile-up simulation from soft QCD. It also required to simulate the remaining outgoing proton partons that do not participate in the target scattering event. This is nominally done using Pythia 8 [88] and is known as the ‘underlying event’. Aside from Sherpa production, c- and b-quark decays are handled by the EvtGen package [89].

### 5.3.2.1 Heavy Neutral Leptons

The signal generator for HNLS is based off a phenomenology paper involving theorists tied to the analysis [53].

For the hard, parton-level scattering processes at the next-to-leading order (NLO) in QCD, the scattering matrix is generated with MadGraph5\_aMC@NLO v2.7.2 [90]. All the events are interfaced to Pythia 8.243 [88] using the A14 tune<sup>3</sup> [91] and the NNPDF2.3nlo [87] PDF set.

For the optimisation of the analysis, 5 mass points were generated with unity mixing  $V_{\mu N} = 1$ :  $m_N = 500$  GeV,  $m_N = 1$  TeV,  $m_N = 3$  TeV,  $m_N = 5$  TeV and  $m_N = 10$  TeV. For the final unblinded limit setting, more signal samples were generated to construct more detailed contours. The mixing parameter  $V_{\mu N}$  only impacts the total cross-section,  $\sigma \sim |V_{\mu N}|^4$ .

### 5.3.2.2 Weinberg

The Weinberg model is generated by the same theorists [52], and hence, uses a similar framework. From a generation standpoint, it can be considered an off-shell low-mass HNL. The generator used is MadGraph5\_aMC@NLO v2.9.3 [90] at NLO in QCD. The NNPDF3.1luxQED [87] PDF is used. All SMWeinberg events are interfaced to Pythia 8.245 [88] using the A14 tune [91].

### 5.3.2.3 Same Sign WW Production

The most topologically similar Standard Model process is same-sign WW production  $jj\mu^\pm\mu^\pm\nu_\mu\nu_\mu$  (figure 5.2). This has the same detectable topology as our HNL signal but has a significantly different kinematic distribution to the signal due to the two undetectable neutrinos and softer muon  $p_T$  spectra (see figure 5.1). It has modes with QCD+EW (vertices  $\alpha_s^2\alpha^4$ ) and EW production (vertices  $\alpha^6$ ) alongside the interference term ( $\alpha_s\alpha^5$ ).

For this analysis, the EW diagram dominates the total contribution to the analysis regions. This is due to the QCD colour connection between the EW+QCD scattering

<sup>3</sup>The standard set of phenomenological values needed for Pythia modelling of showers.

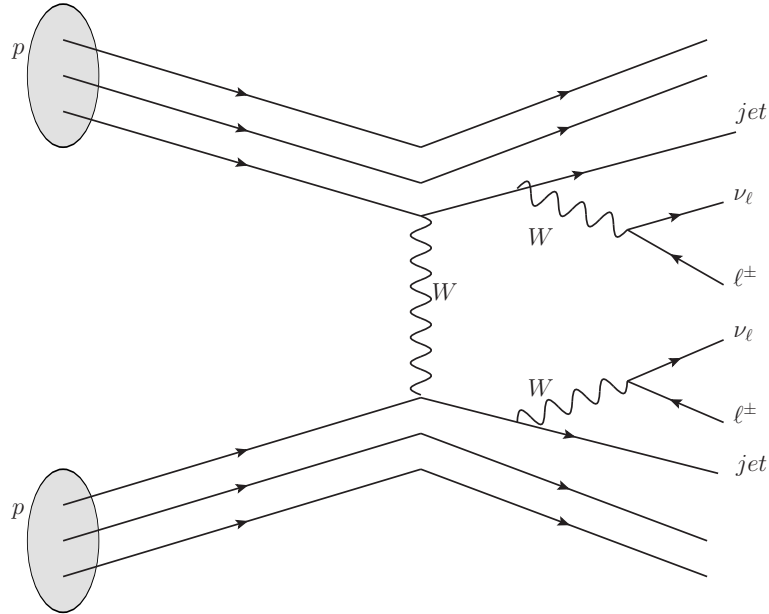


Figure 5.2: An example EW ssWW process. Here, the EW process with vertices totalling  $\alpha^6$  dominates as it has the same back-to-back topology due to the colour charge. [1]

diagrams, reducing the VBS back-to-back topology which this analysis selects for.

To simulate this, the same sequence of MadGraph5\_aMC@NLO v.2.6.7 and Pythia 8.244 with A14 and NNPDF3.0nlo PDF is used.

### 5.3.3 WZ Production

The other major background for this analysis is WZ production with the final state of  $jj\mu^\pm\mu^\pm\nu_\mu(+\mu^\mp \text{ lost})$ . The lost lepton is usually outside the detector's acceptance or does not pass our signal object requirements.

We have equivalent order QCD+EW mix diagrams as the ssWW background, but instead, the mixed QCD diagram is the dominant contribution (figure 5.3).

For this process, the entire production is done using Sherpa 2.1.2 with a mixture of NLO and LO depending on the additional number of outgoing partons [92].

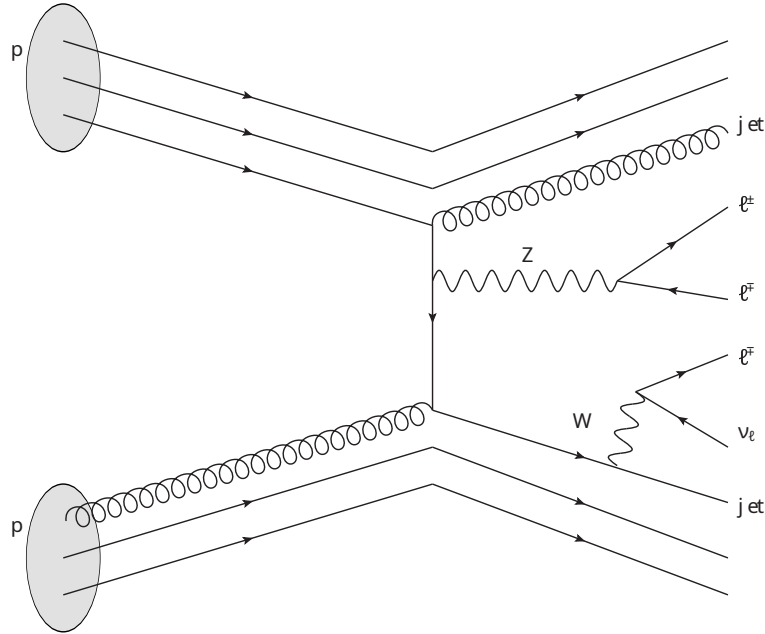


Figure 5.3: An example QCD + EW WZ boson production process digram mediated with a gluon exchange. This is the main background with total coupling  $\alpha^4 \alpha_s^2$  [1].

### 5.3.4 Other Samples

The remaining samples only provide sub-leading contributions to this analysis, so they are summarised more briefly. These contribute more to our validation regions and background estimations.

Three generated samples are used for single boson production of ( $W$  or  $Z$ )+jets, with or without photon radiation. The overlap between them is then removed with a dedicated tool. This results in stronger statistics for the photon production channel. Sherpa v2.2.11 is used with NNPDF3.0nnlo PDF set for ‘+jets’ and ‘+ $\gamma$ ’ EW and QCD higher order channels. For EW ‘+ $\gamma$ ’ production MadGraph5\_aMC@NLO v2.3.3 is used at LO with Pythia 8.212, A14 tune and NNPDF3nlo PDF set. To quantify our systemic uncertainties in a data-driven estimate, it becomes useful to have an alternative  $W$ +jets sample. This uses purely MadGraph5\_aMC@NLOv2.2.2 for all  $W$  or  $Z$  productions with NNPDF3lo interfaced to Pythia 8.186 with the A14 tune.

For the top samples  $t\bar{t}V$ ,  $t\bar{t}WW$ ,  $tZq$  and  $tWZ$  we use MadGraph5\_aMC@NLO v2.3.3 [90] at NLO with A14 tune. For single-top and  $t\bar{t}$  PowhegBox v2 [93, 94, 95, 96]

at NLO in QCD is used with Pythia 8.230 for showering.

Finally, we have multi-jet and  $\gamma + \text{jets}$ . Sherpa v2.2 is used for  $\gamma + \text{jets}$ , whereas the standard full Pythia 8.230 approach with NNPDF2.3lo is used for the multi-jet background.

Throughout the next three chapters, we have a data-driven sample labelled either `ddfake` or `ffFakeL`. This is a data-driven background which will be explained in depth in chapter 6.

## 5.4 Event Selection

### 5.4.1 Region Design

A significant aspect of particle physics analysis involves designing regions that allow for hypothesis testing in the most statistically powerful manner. This typically uses signal, control and validation regions. The SR provides our most signal-enriched region to test signal (where the data is all blinded in this context). The CRs ensure we have modelled our prompt backgrounds (`ssWW` and `WZ`) well with similar object selections by picking orthogonal cuts to the SR. The Validation Region (VR) regions are similar but are not aiming to be used in the fit (section 5.5.1), primarily due to too high signal contamination. They are still insightful for validating the fit. Hence, the two main adjacent Standard Model processes have control regions similar to the signal region.

Some basic topological and cleaning requirements are shared amongst these regions. This is called our preselection:

- **Triggers passed and matched**, i.e. the objects used in the trigger are the same ones as used at reconstruction.

Observable	SR	ssWW VR	ssWW CR (highpT VR)	WZ CR
$m_{jj}$	> 300 GeV	> 300 GeV	> 300 GeV (—)	> 300 GeV
$\Delta y_{jj}$	> 4	> 4	> 4 (—)	> 4
third lepton	= 0 (baseline)	= 0 (baseline)	= 0 (baseline)	= 1 (signal)
Z cand. (OSSF only)	—	—	—	✓
$E_T^{\text{miss}}$ sign.	< 4.5	∈ [4.5, 5.8]	> 5.8	< 4.5
$m_{ll}$	—	—	—	> 100 GeV
$p_T^{\mu 2}$	—	< 120	< 120 (> 120) GeV	—

Table 5.13: Summary of all the region cuts after preselection, the validation regions not included in the fit are written in grey [68, 97].

- $\geq 2$  same-sign signal muons with  $p_T^{l_{1,2}} > 27$  GeV, so that the triggers are at full efficiency, which has very little loss to our signal region due to searching mostly for very high  $p_T$  objects.
- $\geq 2$  signal jets, the hardest jet must have  $p_T \geq 30$  GeV for pile-up suppression purposes.
- $m_{jj} > 150$  GeV, selecting VBS style events.

Truth filtering of the Monte Carlo is done at this stage so that data-driven estimations are not double-counted. Specifically, any truth class of hadronic activity faking electrons or muons (IFF Class > 8 in section 6.1) is excluded. The cuts used after these preselections are summarised in table 5.13 and motivated in the following subsections.

#### 5.4.1.1 Signal Region

For a search-style analysis, an important task is to maximise the sensitivity of the data to identify a signal over the background. This trade-off involves three factors. First, the statistical significance is influenced by the raw number of signal and background events, denoted as  $n_s$  and  $n_b$ , respectively. Additionally, we aim to minimise the uncertainties associated with our background estimation, represented by  $\sigma_b$ . For this, the following figure of merit is recommended by ATLAS [98]. This is an extended form of the Poissonian significance,  $Z = \frac{n_s}{\sqrt{n_b}}$ , which compensates for

the background uncertainty.

$$Z = \sqrt{2((n_s + n_b) \ln \left( \frac{(n_s + n_b)(n_b + \sigma_b^2)}{n_b^2 + (n_s + n_b)\sigma_b^2} \right) - \frac{n_b^2}{\sigma_b^2} \ln \left( 1 + \frac{\sigma_b^2 n_s}{n_b(n_b + \sigma_b^2)} \right))} \quad (5.4)$$

For this analysis, when optimising  $Z$ , we find that we have adequately rare processes that mean alongside mismodelling effects (see chapter 6) that the statistics on our background estimate are poor enough and we do not have smooth background distributions in our SR selection. This was fixed later for our final fits. Thus, when optimising  $Z$  across mass points, the best cuts on VBS topology are not that stable. This can be seen in table 5.14 and the SR optimisation plots (figure 5.4) for the analysis. However, the exact choice of cut isn't that critical, so picking values that offer good significance across our mass range is adequate.

For this analysis, we optimise the following physics-motivated sensitive parameters.

- $E_T^{\text{miss}}$  Significance: This is a key cut because it discriminates between the ssWW background and the signal and allows us to define our control regions.
- $m_{jj}$ : The mass of the two signal jets. This is correlated with VBS topology events and the mass of the HNL in the case of the signal model.
- $\Delta Y_{jj}$ : The rapidity gap between the two jets. A large value is also correlated with a VBS topology.
- $p_T^{l_2}$ : The sub-leading lepton momentum.

In addition, the following filters are applied to the SR and CRs to reduce the hadronic fakes (chapter 6).

- $n_{b \text{ jet}} = 0$ : Rejecting an event if they are any b-jet candidates (section 5.2.5).

$m_N$ [TeV]	$p_T^{l_2}$ [GeV]	$m_{jj}$ [GeV]	$\Delta Y_{jj}$	$Z$
0.5	> 210	> 250	> 4	61.3
1.0	> 220	> 100	> 4	61.4
3.0	> 300	> 500	> 4.4	34.5
5.0	> 330	> 150	> 4.4	23.0
10.0	> 470	> 475	> 4.4	11.4

Table 5.14: Cuts maximizing the significance for each mass point starting from the preselection. Unity mixing parameters ( $\mu = V_{\mu N} = 1$ ) are considered here. The cause of instability in the  $m_{jj}$  cut can then be seen in figure 5.4a.

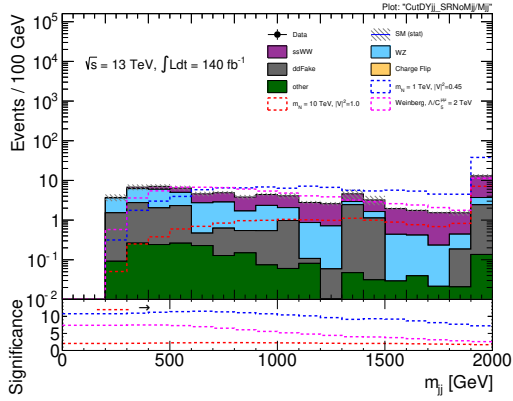
- $n_{\text{Extra Baseline Lep}} = 0$ , removing any events with extra leptons significantly reduces our SM background in our SR as well. This is lifted for the WZ CR.

By sweeping these parameters and finding  $Z$  using equation (5.4), we obtain the optimal cut values as a function of our signal input masses given in table 5.14. From this the cuts  $E_T^{\text{miss}}$  significance  $< 4.5$ ,  $m_{jj} > 300$  GeV and  $\Delta Y_{jj} > 4$  are chosen. This roughly optimises  $Z$  across all the targeted mass points.  $p_T^{l_2}$  is binned in the fit to use with the softer Weinberg model. The full set of (N-1) distributions is given in figure 5.4. These are the plots where the SR distribution in a variable is shown with the corresponding variable cut removed (i.e. a  $m_{jj}$  plot of the SR without applying  $m_{jj} > 300$  GeV).

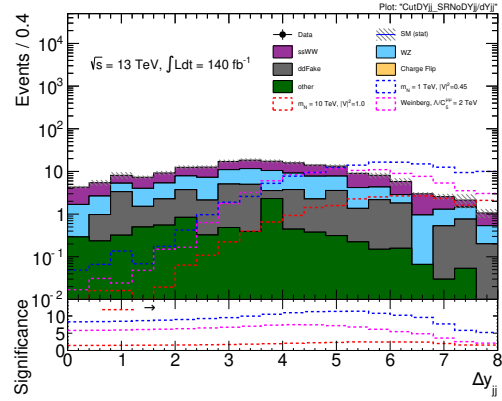
#### 5.4.1.2 ssWW Control Region

The design of the ssWW control region is made to deduce the normalisation of the ssWW Monte Carlo during the fit. To be topologically similar to the SR, we apply the same cuts except for inverting the  $E_T^{\text{miss}}$  significance due to the neutrinos generated by this process.

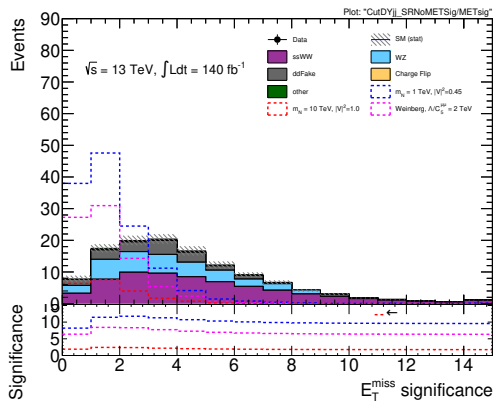
However, due to there still being significant signal contamination just above the  $E_T^{\text{miss}}$  significance threshold of  $< 4.5$  and for large  $p_T^{l_2}$  values, we instead cut at  $> 5.8$  and  $< 120$  GeV, respectively. In this selection, it was also essential to keep the data-driven background estimate due to its large statistical uncertainty in high  $p_T$



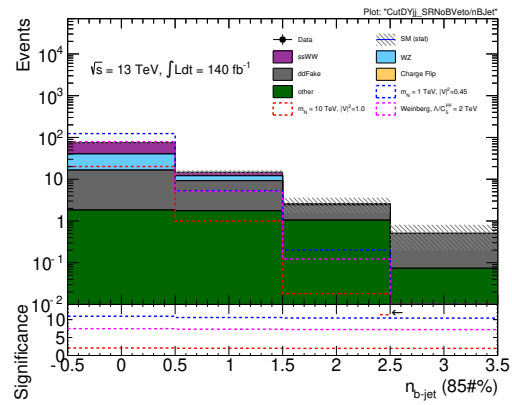
(a)  $m_{jj}$  with visible bumpiness in the back-ground estimation.



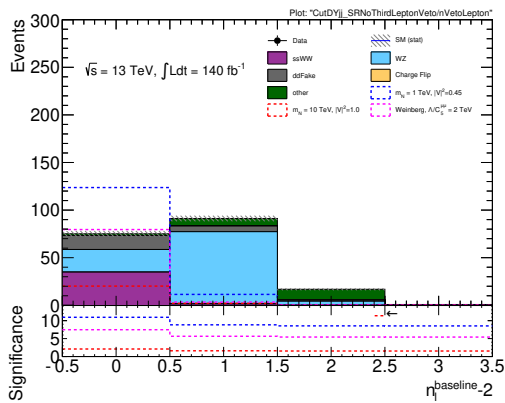
(b)  $\Delta Y_{jj}$ .



(c)  $E_T^{\text{miss}}$  Significance.

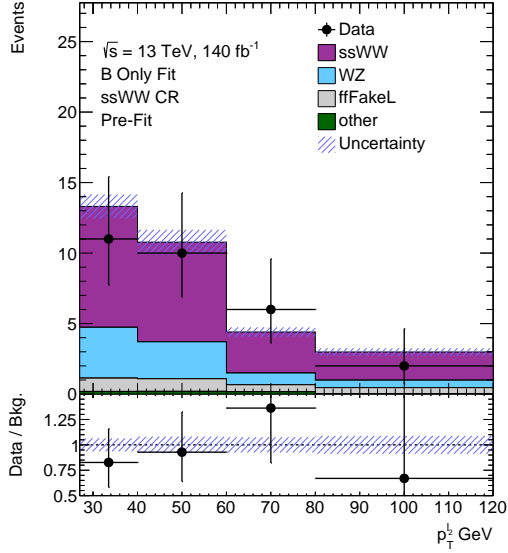


(d) Number of b-jets.

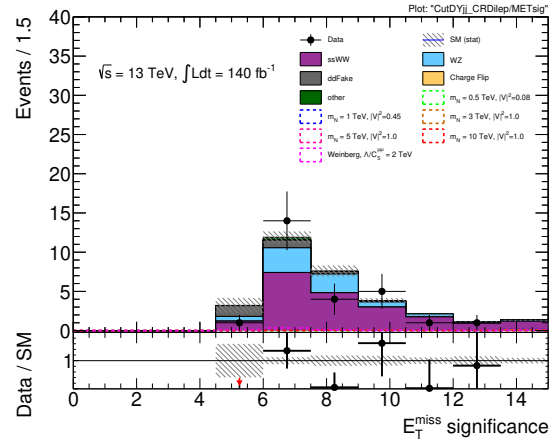


(e) Extra baseline leptons.

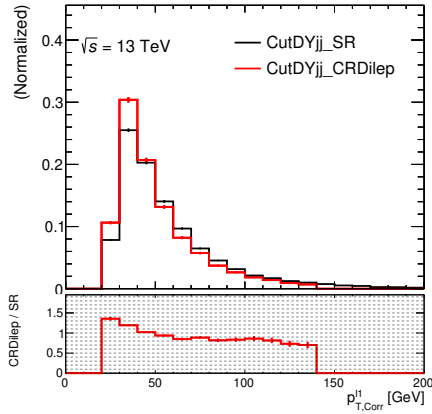
Figure 5.4: The N-1 plots of the SR cutflow. This visualises the significance (equation (5.4)) of each of the signal region cuts in the direction indicated and justifies the cuts shown in table 5.14. These plots were blinded at the time of study.



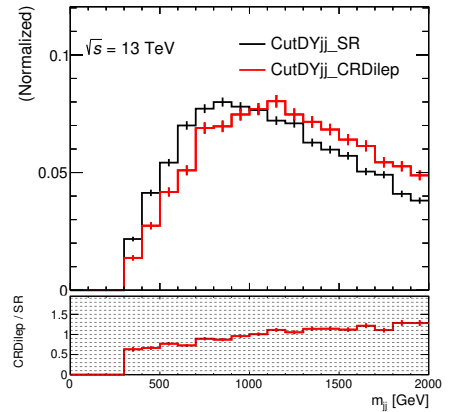
(a) The input for the statistical framework binned in subleading lepton  $p_T$ .



(b) The  $E_T^{\text{miss}}$  Significance distribution.



(c) The normalised shapes of the ssWW CR and SR in leading muon  $p_T$ , noting the correlated 120 GeV sub-leading muon  $p_T$  cut applied to just the CR.



(d) The di-jet mass normalised distributions of the ssWW CR and SR.

Figure 5.5: Shape and MC Data agreement plots for the ssWW CR. Here, it can be seen that there is good agreement between the MC and data and also reasonably similar MC kinematics between the signal and control regions.

phase space. The intermediate  $E_T^{\text{miss}}$  significance values are used as VR to cross-check the validity of using a single transfer factor between two different regions of phase space (section 5.5). This is labelled ssWW VR.

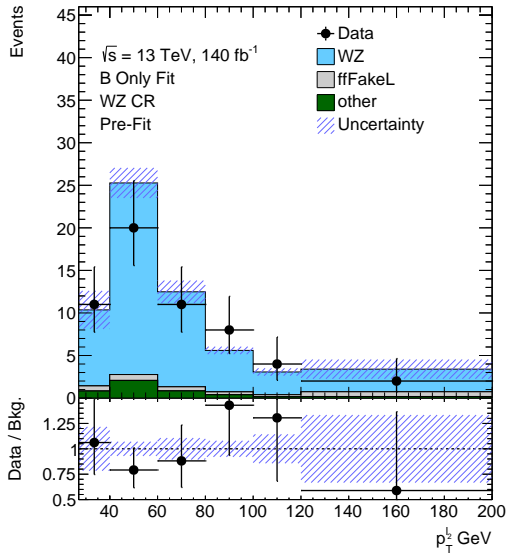
It was deemed vital that we have a ssWW enriched region at high  $p_T$  to validate the background estimate there. This was originally a CR in the fit but was changed to a VR (see section 5.5.4.1). To achieve this with a signal contamination that is not too high (as to not unblind), the VBS style cuts of  $m_{jj}$  and  $\Delta Y_{jj}$  are removed. This is denoted by the high- $p_T$  VR.

This results in the CR fit inputs shown in figures 5.5a and 5.5b. This has the desired levels of purity ( $\gtrsim 50\%$ ) and good matching between data and MC. It can also be seen in figures 5.5c and 5.5d that the kinematic distributions between the SR and CR agree adequately well.

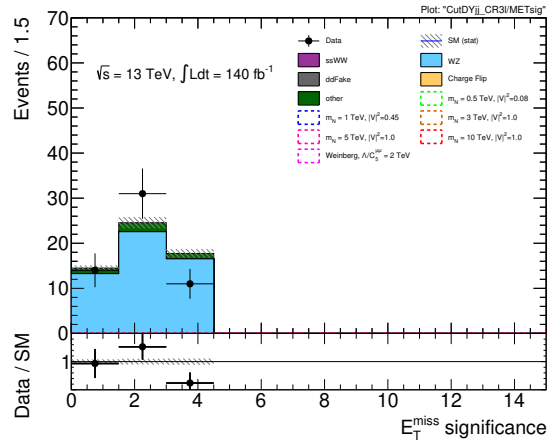
#### 5.4.1.3 WZ Control Region

To create a CR enriched in WZ, we require exactly one more signal quality lepton and no baseline leptons beyond this (reducing ZZ background). This selects WZ without a lost lepton. A tri-leptonic mass cut  $m_{ll} > 100$  GeV is made to ensure orthogonality to the photon fake CR (section 6.3). Otherwise, the cuts are identical to the SR.

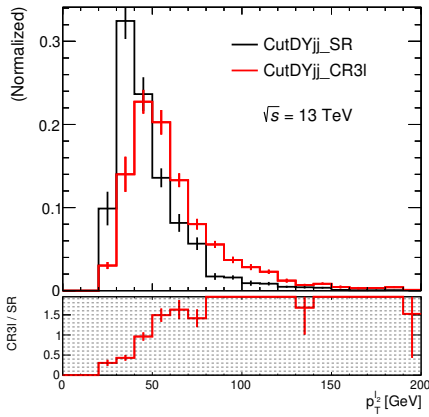
Good shape agreement and data-MC agreement is found in this region. This can be seen in figure 5.6.



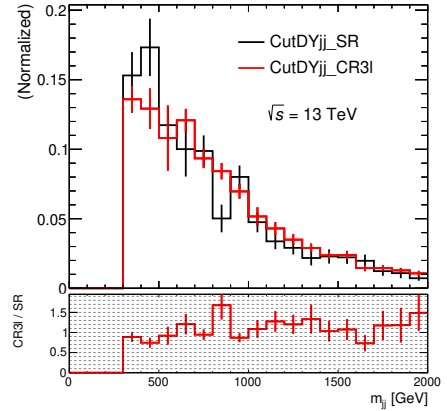
(a) The input for the statistical framework binned in subleading lepton  $p_T$ .



(b) The  $E_T^{\text{miss}}$  Significance distribution.



(c) The normalised shapes of the WZ CR and SR in leading muon  $p_T$ .



(d) The di-jet mass normalised distributions of the WZ CR and SR.

Figure 5.6: Shape and MC Data agreement plots for the WZ CR. Here it can be seen that there is good agreement between the MC and data and also reasonably similar MC kinematics between the signal and control regions.

## 5.5 Statistical Methods

This section aims to show how a fitting framework is set up to estimate the presence of signal and the correct modelling of our backgrounds. First, we briefly outline how a profile likelihood fit works. Then, we show how it behaves in our analysis regions. Finally, we outline how the systematic uncertainties are profiled and the resulting impact on our final fit values is shown.

### 5.5.1 Fitting Methodology

To formally deduce and hypothesis test on data, a fitting procedure is run on the signal and control regions. This involves maximising a likelihood function with the normalisation of the signal ( $\mu$ ) and the normalisation of the backgrounds enriched by our control regions ( $\mu_{WZ}, \mu_{ssWW}$ ). Alongside this, nuisance parameters are used to encapsulate systematic errors ( $\theta$ ) due to instrumentation, modelling and simulation effects (section 5.5.4). The normalisation of the signal is related to the mixing parameter  $\mu = |V|^4$ . This fit gives a maximum value of the likelihood (equation (5.5)), which is the estimator for the true value of all of these parameters denoted  $(\hat{\mu}, \hat{\theta})$ . For our binned analysis, our likelihood function (equation (5.5)) can be written as the probability of observing a data value ( $n_i$ ) given the expected Poissonian data estimate in each bin  $v_i = n_{s,i}(\mu, \theta) + n_{b,i}(\mu_{WZ}, \mu_{ssWW}, \theta)$  alongside constraints on the nuisance parameters derived from external sources  $C_j(\theta_j)$ . This is usually of a Gaussian form and is normalised such that  $\sigma = 1$ . The statistical uncertainty from Monte Carlo modelling is carried in ‘gammas’, which are given as additional systematic variations [99, 100].

$$L(\boldsymbol{\mu}, \boldsymbol{\theta}) = \prod_i \text{Poisson}(n_i | v_i(\boldsymbol{\mu}, \boldsymbol{\theta})) \cdot \prod_j C_j(\theta_j) \quad [99] \quad (5.5)$$

Alongside finding the likelihood maxima, the n-dimensional parameter space maximum is profiled to measure uncertainties. This is both in the normalisation measures

of signal and background ( $\mu$ ) and to see if the systematic nuisance parameters ( $\theta$ ) are constrained or pulled away from their central value by the provided data. Assuming a quadratic likelihood form near the measured value, the correlations between the  $\mu$  values and systematic variations can be deduced and interpreted.

To test that the fit behaviour and results are satisfactory for various hypotheses before unblinding, we construct several fits with various amounts of Asimov data with different hypotheses. Asimov data is where we simulate data from our MC background-only or signal-plus-background hypothesis such that maximising  $L$  gives us the central nominal value for each parameter.

The results shown in the main body of this section (sections 5.5.2 and 5.5.3) are completed with Asimov data in the blinded signal region and data everywhere else.

All the fitting and corresponding output plots are generated by the internal tool TRExFitter, which interacts with HistFactory [101] to run the fit in ROOStats [102].

### 5.5.2 Background Only Fit

Pre-fit and post-fit plots for the SR, the WZ-CR, the ssWW-CR and the ssWW-VR are shown in figure 5.8 and figure 5.9, respectively, as well as the summary plot showing the inclusive analysis bins in figure 5.10. The fitted normalisation factors are given in figure 5.7. Pre-fit is the raw histogram input into the fitting framework with a signal normalisation set to  $\mu = 1$ . Post-fit is where the best-fit values for normalisation and nuisance parameters are used ( $\hat{\mu}, \hat{\theta}$ ). The data/MC agreement pre-fit is already good and slightly improves post-fit. The uncertainty band increases, but this is a known artefact due to the fact that normalisation uncertainties are not included pre-fit. Due to the statistically limited nature of this analysis, this is a visible effect.

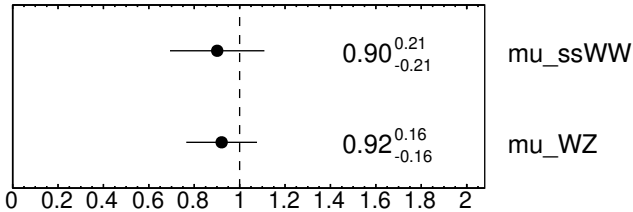


Figure 5.7: Normalisation factors derived in the background only fit with Asimov data in the SR.

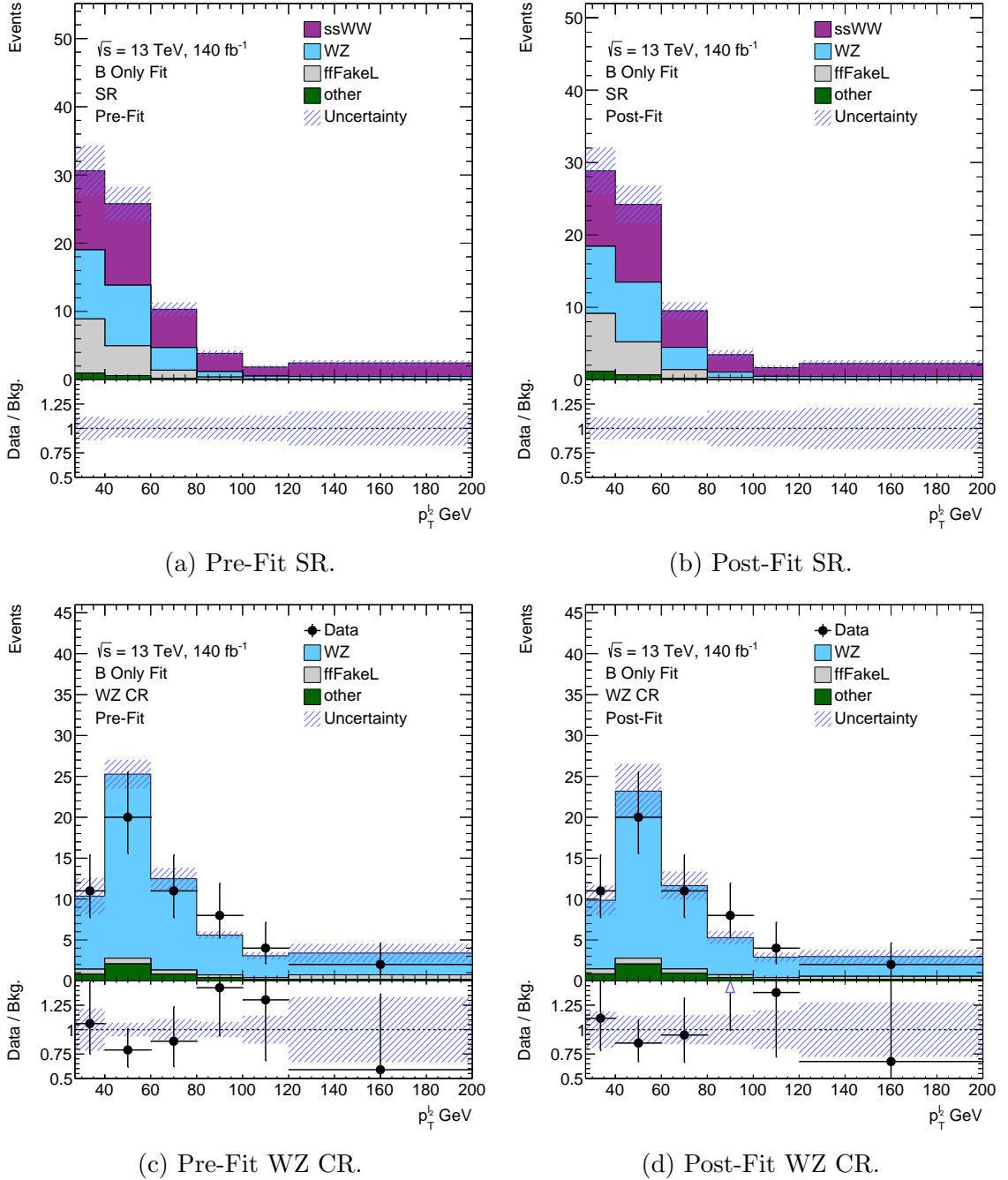


Figure 5.8: Pre- (a, c) and post-fit (b, d) distributions in the signal region (a, b) and WZ control region (c, d) for the background-only fit. The shaded area is the combined statistical and systematic uncertainty in the background estimate.

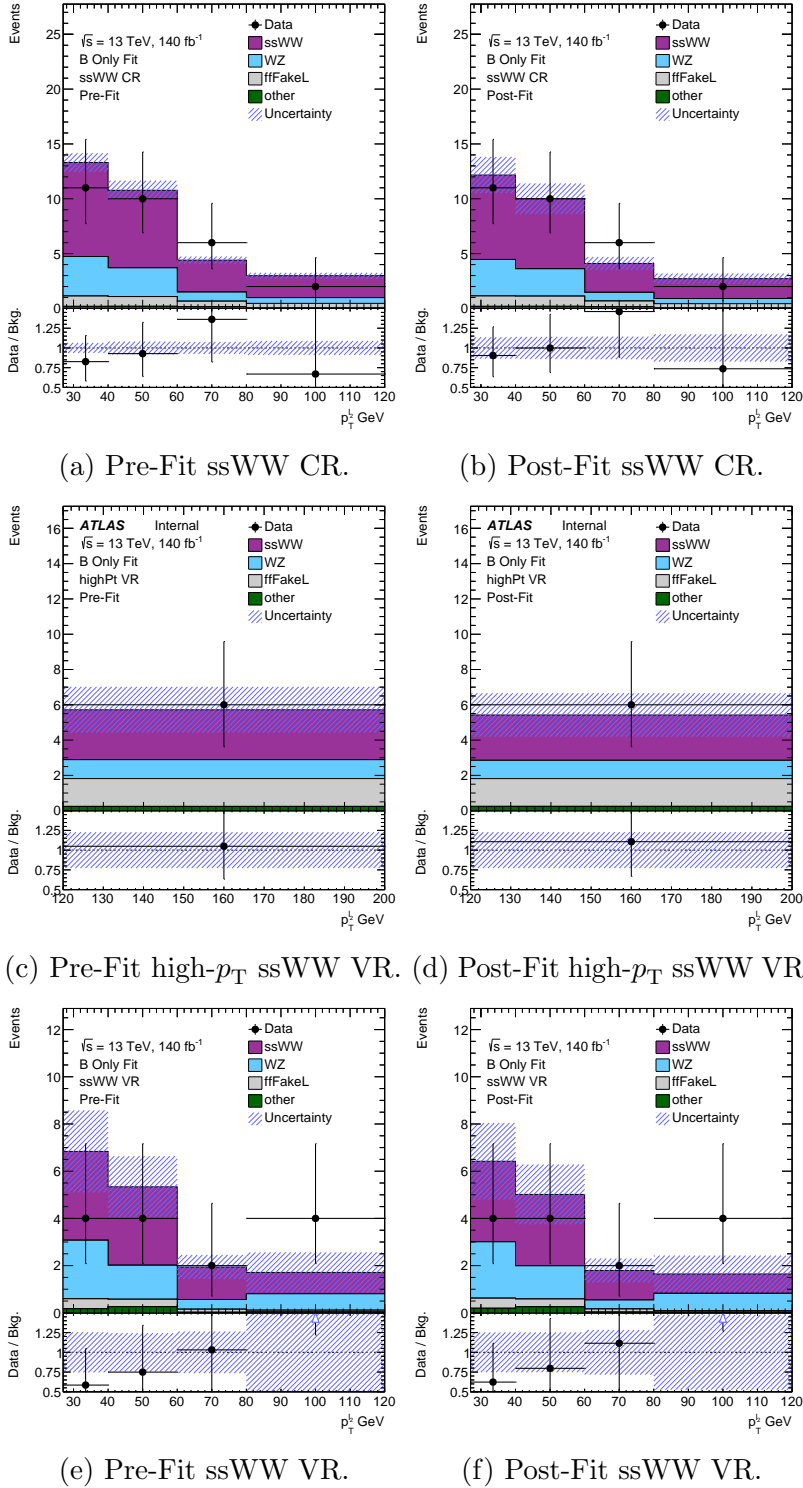
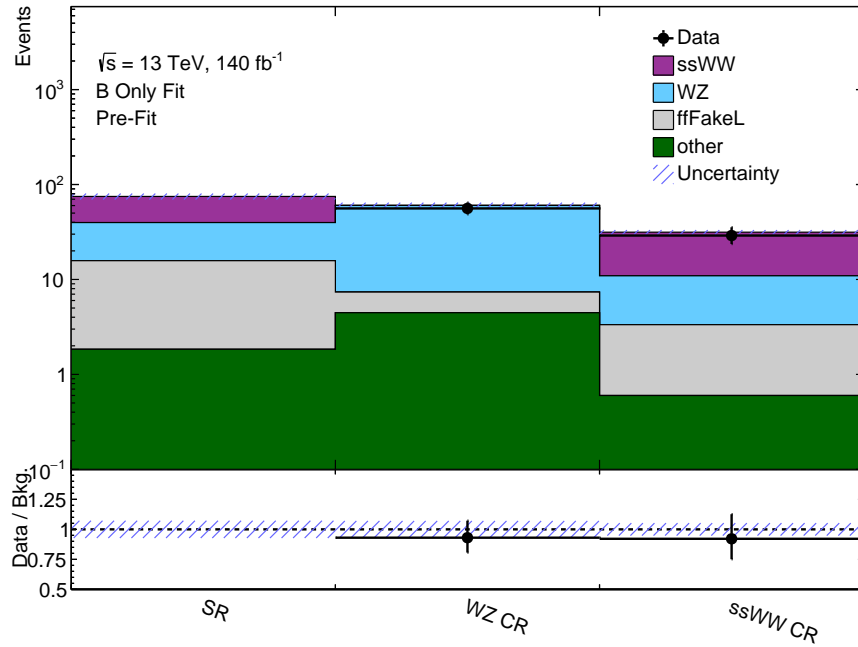
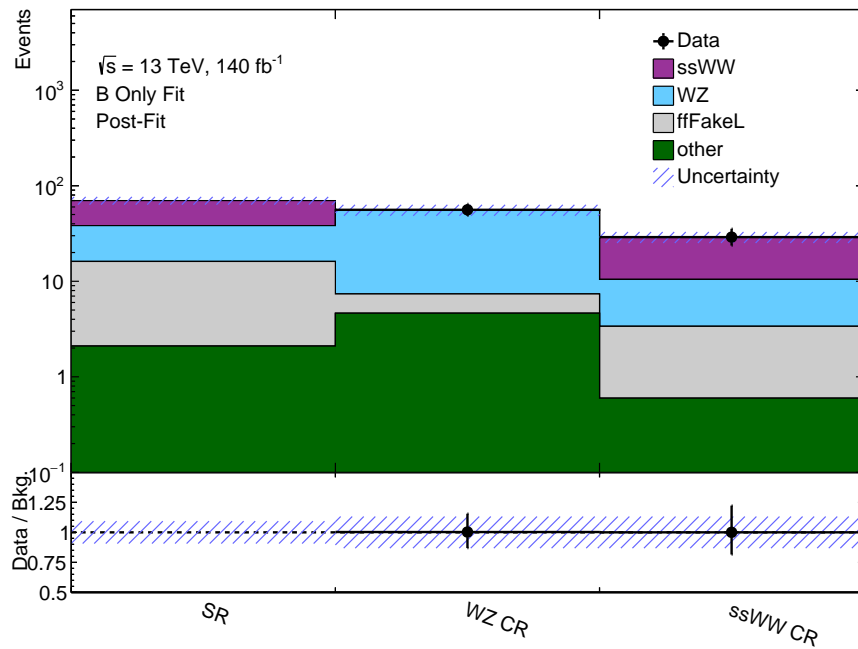


Figure 5.9: Pre- (a, c, e) and post-fit (b, f, d) distributions in the ssWW control (a, b) and validation region (c, d, e, f).



(a)



(b)

Figure 5.10: Summary plot of the regions before (a) and after (b) the blinded background-only fit.

### 5.5.3 Signal and Background Fit

In this section, the Asimov SR considered includes additional signal injection of our HNL/Weinberg model in the fit. A signal model normalisation is then allowed to float to match this. This is our blinded signal + background fit.

To avoid under-constrained and over-ranked systematic variations due to using the unrealistic, already excluded  $V = \mu = 1$  contaminating the high  $p_T$  CR<sup>4</sup>, we instead scale down our scale factor according to table 5.15.

A caveat of the TRExFitter package is that for pre-fit plots, the signal is plotted with  $\mu = 1$ ; for the post-fit plots, it is scaled correctly.

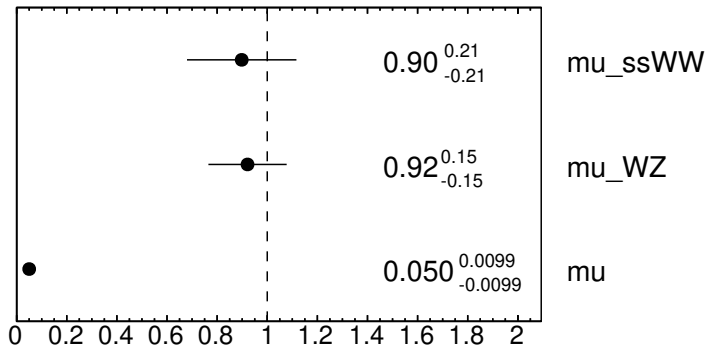
Here, we show the fit results for the signal+background fit with a HNL sample with  $m_N = 1$  TeV,  $\mu = 0.05$ . Overall, the fit behaves well and converges at sensible values for the data (figures 5.11 to 5.14).

$m_N$	Injected Asimov $\mu$
500 GeV	0.0064
1 TeV	0.05
3 TeV	0.5
5 GeV	0.5
10 TeV	1

Table 5.15: Injected Asimov signal normalisation values.

---

<sup>4</sup>This was later made a VR to mitigate this problem entirely.

Figure 5.11: Normalisation Factors derived in the  $m_N = 1$  TeV fit.

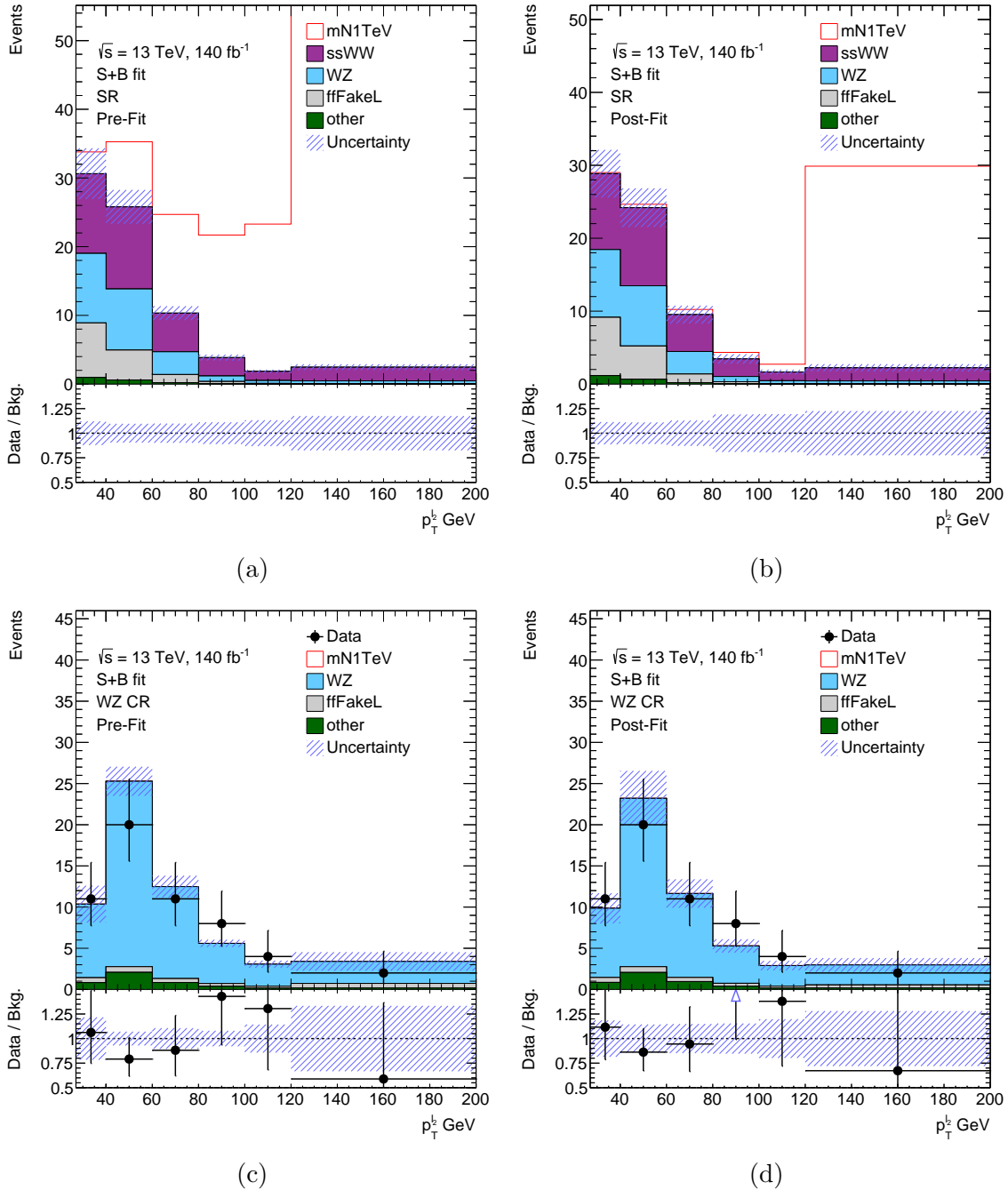


Figure 5.12: Pre- (a, c) and post-fit (b, d) distributions in the signal region (a, b) and WZ control region (c, d) Around 550 events are in the final SR bin pre-fit with  $\mu = 1$ .

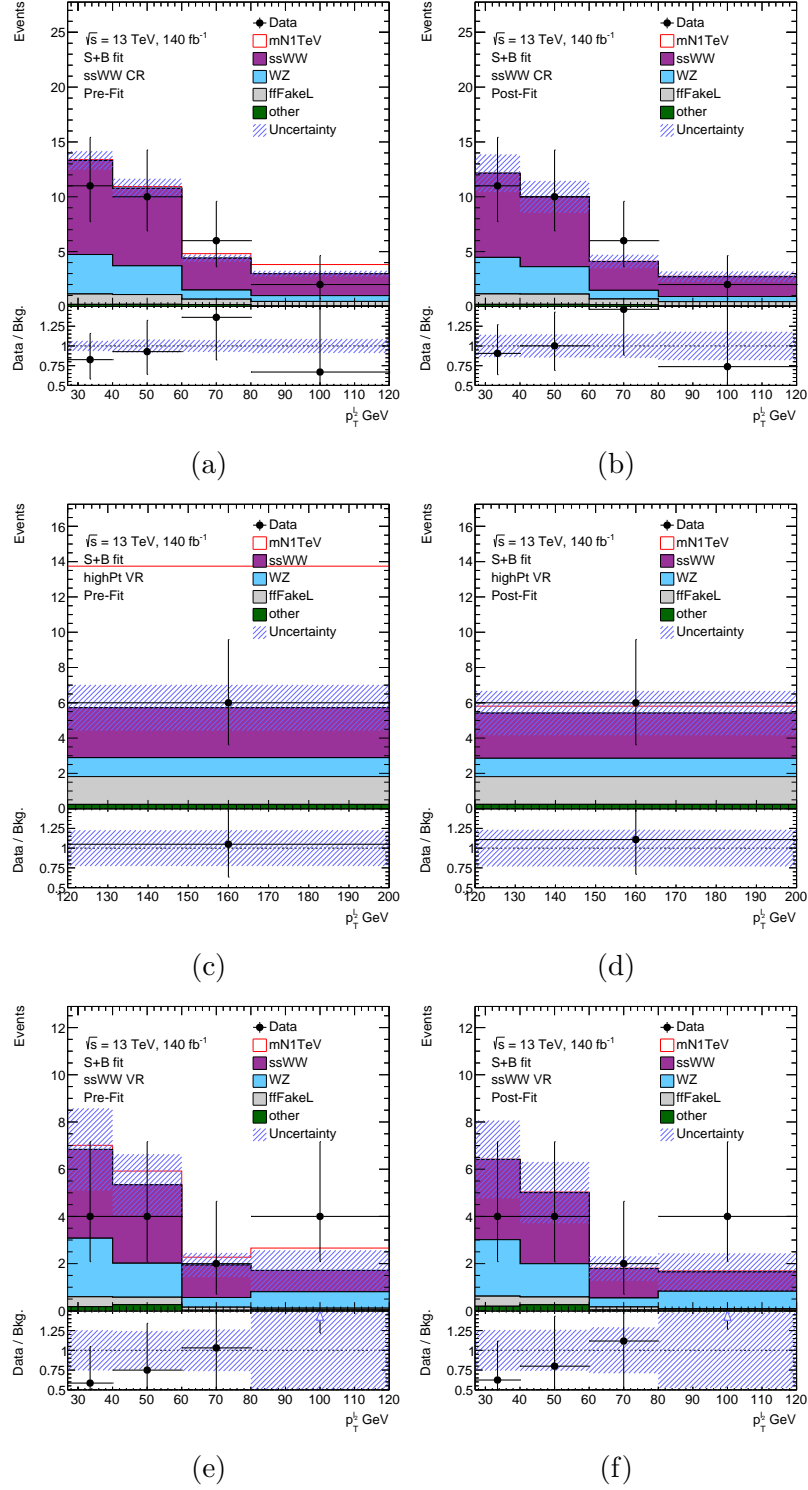
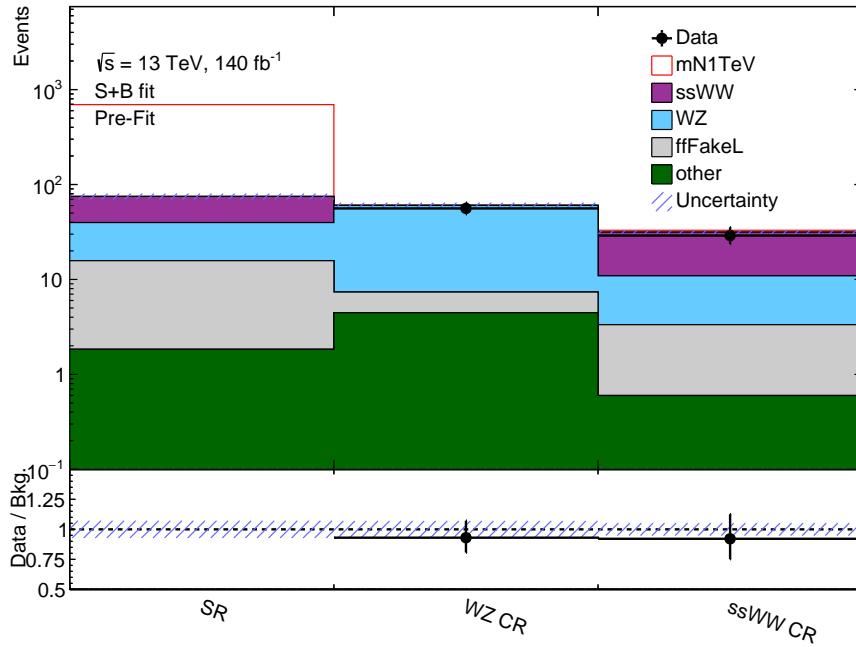
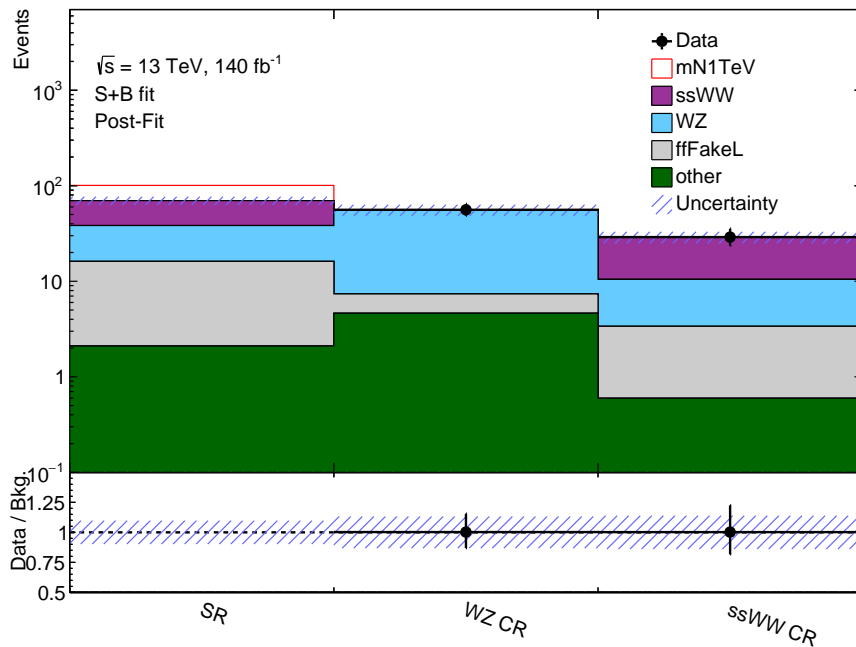


Figure 5.13: Pre-(a,c,e), and post-fit(b,f,d) distributions in the ssWW control(a,b) and validation regions (c,d,e,f) for the fit to the  $m_N = 1$  TeV mass point.



(a) Pre-Fit



(b) Post-Fit

Figure 5.14: Summary plot of the regions before (a) and after (b) the  $m_N = 1$  TeV fit.

### 5.5.4 Systematic Uncertainties

Several pragmatic steps must be taken to propagate systematic uncertainties to our final results. Due to the sheer number of potential variations in different nuisance parameters, doing a complete analysis cutflow profiling these parameters would be far too computationally expensive. Resultantly, a finite number of systematic variations for all the relevant samples are propagated through the analysis software. Each of these then provides bin-by-bin nominal and  $\pm 1\sigma$  variations ( $I^0, I^\pm$  as multiplicative factors) to the fitting software to smoothen, interpolate and extrapolate accordingly for profile likelihood purposes. Notably, the interpolations here are an estimation and are purely to roughly quantify the uncertainty in signal and background estimations. The assumptions made in interpolating and quantifying mismeasurement are rarely true and exact.

The prescription to interpolate systematic variations is provided by HistFactory. For this, a piecewise exponential function is used for  $\theta < 1$  and otherwise fitted with a polynomial (giving  $a_i$ ) between the nominal, up and down multiplicative variations (equation (5.6)). This gives variations that allow the likelihood to be smooth for numerical optimisation [101].

$$I_{\text{poly} \mid \text{exp.}}(\theta; I^0, I^+, I^-) = \begin{cases} (I^+/I^0)^\theta & \theta \geq 1 \\ 1 + \sum_{i=1}^6 a_i \theta^i & |\theta| < 1 \\ (I^-/I^0)^{-\theta} & \theta \leq -1 \end{cases} \quad (5.6)$$

The ATLAS-generated theory and experimental nuisance parameters used in the fit are discussed in appendix C. Here, we provide various post-fit visualisations of the impacts of our nuisance parameters.

Alongside this, some systematic variations from the data-driven background estimates are used. These are outlined further in chapter 6. Some systematic variations with small effects on our exclusions have large statistical fluctuations and are smoothed

so as not to be under-constrained in our fit. This is discussed in section 5.5.4.1.

All systematic variations are further split into their shape and normalisation. Nuisance parameters that have an effect of less than 0.5% on shape or normalisation are pruned (figure 5.15). This provides a significant reduction in computation time. The leading systematic variations are shown in figure 5.19.

These nuisance parameters are profiled for their correlations (figure 5.17) pulls (figure 5.18), and impacts on the fitted  $\mu$  (figure 5.19). Formally, a pull is the measured  $\hat{\theta}_j$  with its post-fit profiled standard deviation  $\Delta\hat{\theta}_j$ . The impact is simply the fitted value of the parameter of interest ( $\mu$ ) with the chosen fitted nuisance parameter fixed at  $\hat{\theta}_j \pm \Delta\hat{\theta}_j$ . A correlation between two systematic variations is the post-fit measured covariance divided the product of the standard deviations (normalising the value between -100% and 100%).

A large source of our uncertainty in the background is the normalisation of the ssWW and WZ control regions. To avoid having a lot of systematic variations having large correlations with  $\mu_{WZ}$  and  $\mu_{ssWW}$  and hence counter-intuitively large looking impacts on our fitted  $\mu$  values, we drop the normalisation across all regions for our ssWW and WZ inputs to the fit. This simply means renormalising the up-down variations of the WZ and ssWW samples such that the integral is the same as the nominal sample summed across all regions. The variations that normalisation would cause re-emerge in the normalisation uncertainty in the fit. This can be seen as a ‘re-diagonalisation’ of our shape and normalisation uncertainties.

The MC statistical nuisance parameters (*Gammas*) are shown in figure 5.16. The gamma nuisance parameters show uncertainties below 15% for all bins (a rough target for ATLAS exotics analyses) and the normalisation factors are compatible with unity.

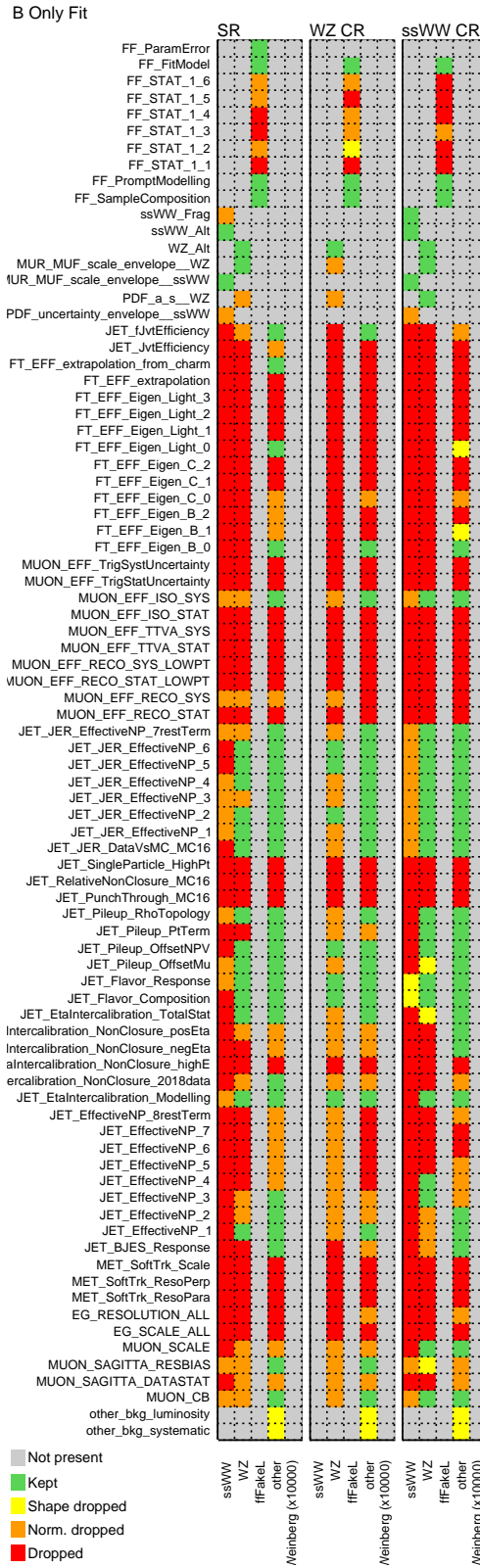


Figure 5.15: Pruning plot for the blinded background-only fit. This shows which of the systematic variations are used in the profiled likelihood as they have quantifiably large impact on bin-by-bin event counts. This keeps the numerical minimisation of the likelihood stable. The individual systematic variations are outlined in chapter 6 and appendix C.

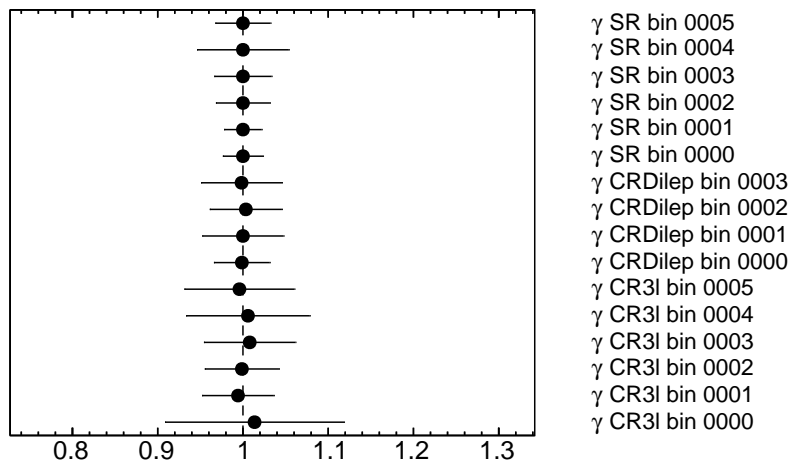


Figure 5.16: Gammas in the background-only fit.

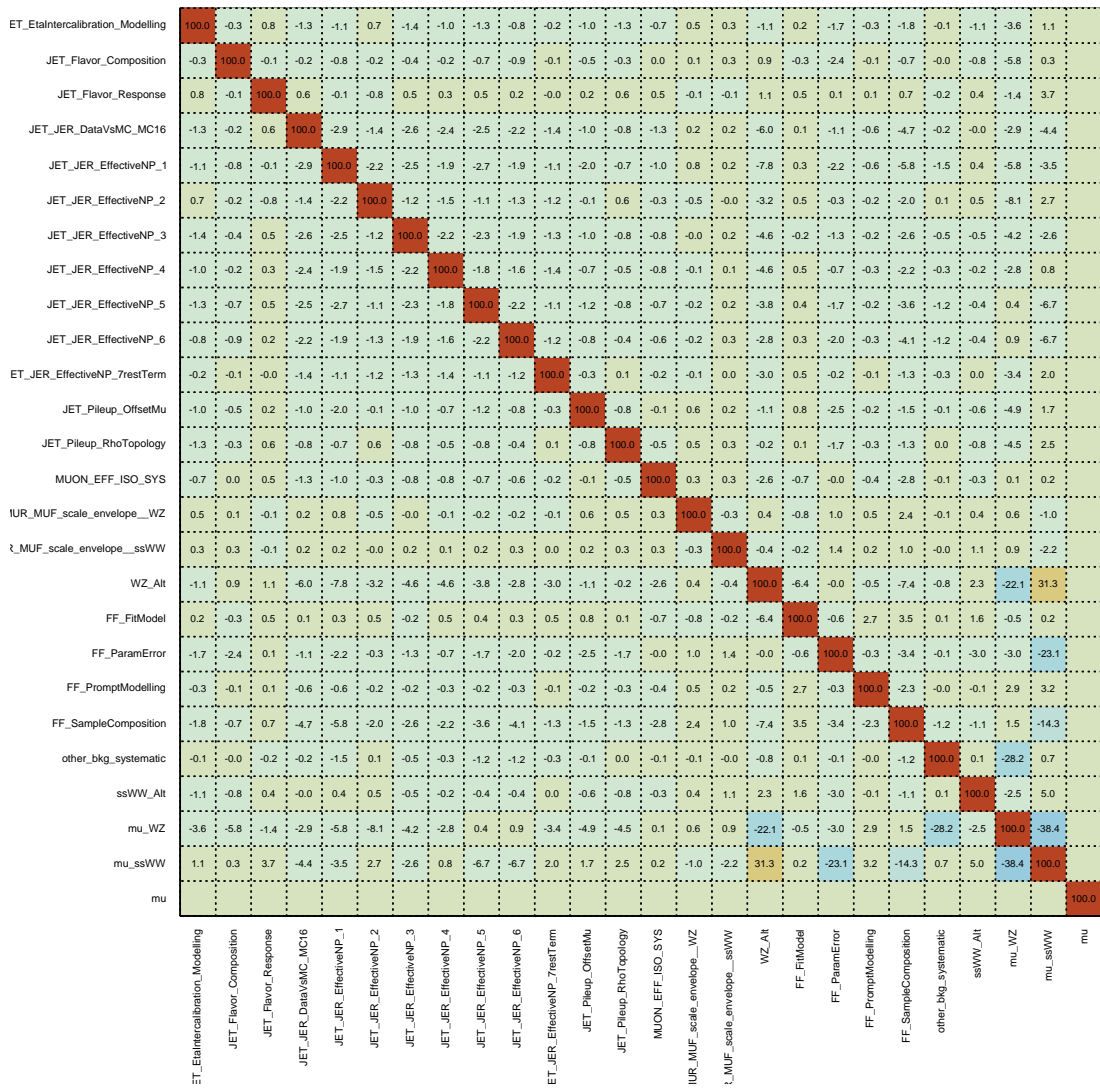


Figure 5.17: Correlation matrix for the background-only fit, correlations smaller than 2% are not shown.

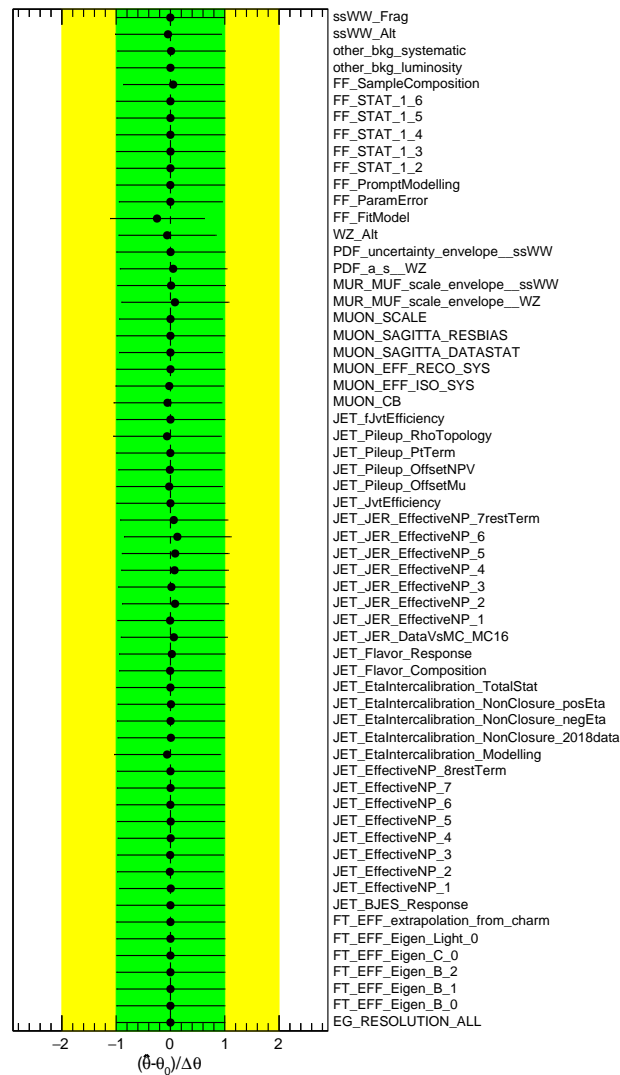
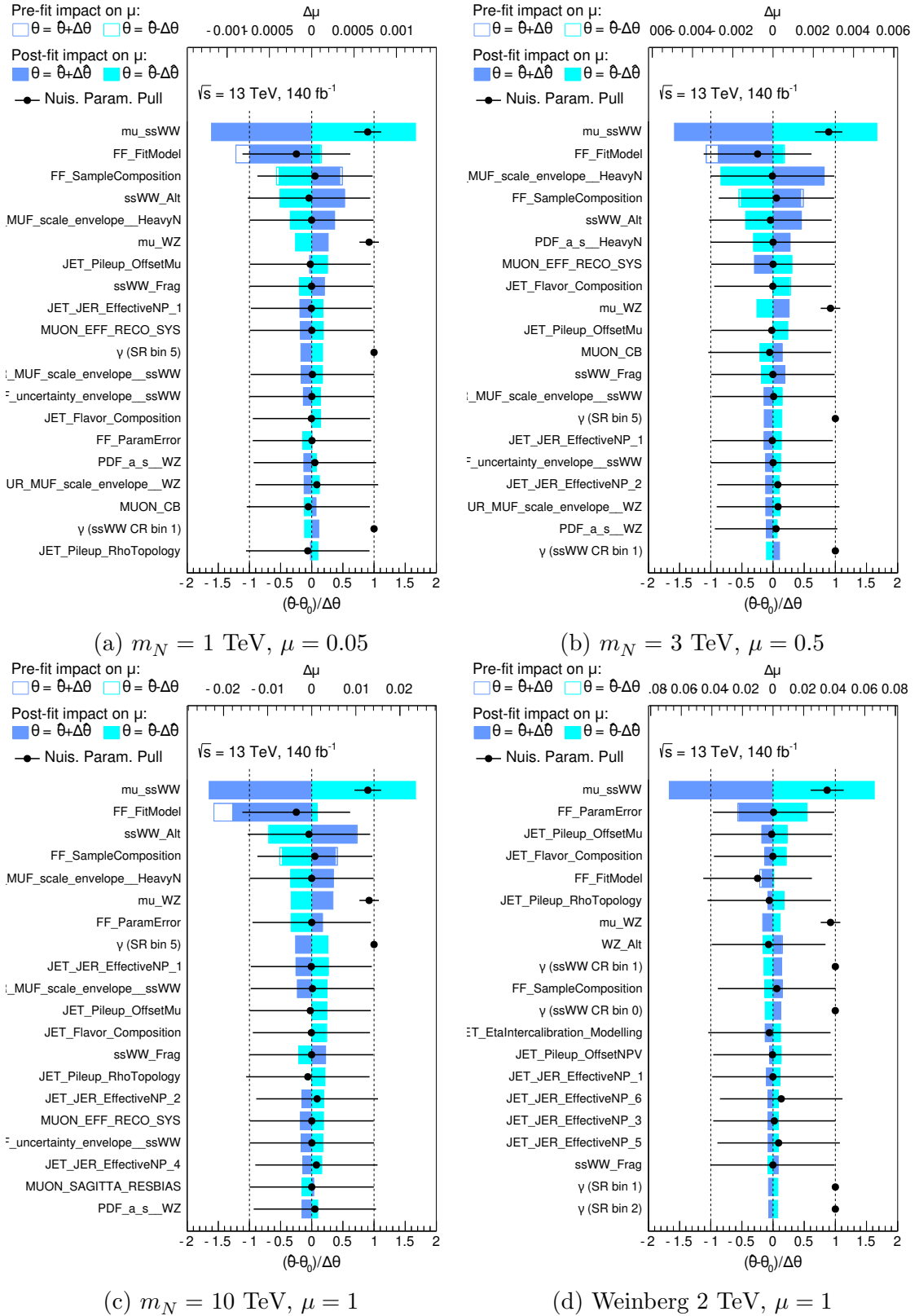


Figure 5.18: Pull plot of all nuisance parameters considered in the background-only fit with Asimov signal data. The theory nuisance are evaluated separately for ssWW and WZ, as indicated by the suffix of the nuisance parameter name.


 Figure 5.19: The ranking of the systematic impacts on the fitted  $\mu$ .

#### 5.5.4.1 Under-Constraints and Smoothing

When the S+B (section 5.5.3) fit was initially run with the raw systematic uncertainty inputs and signal samples with a mixing parameter of one, about a third of the systematic uncertainties were under-constrained. This is when the data given to the fitting methodology makes the nuisance parameter less constrained than the original constraints in the profile likelihood given by  $C_j(\theta_j)$ . This potentially points to fit instability and does not represent anything physical. The causes of this within the analysis can be classified into two categories:

1. The up-down variations are significantly statistically limited. With the form of  $L$  used by ATLAS analysis (equation (5.5)), this phenomenon is not taken into account. To mitigate this, variations are smoothed. This should be done with caution, especially if this is a major cause of uncertainty in a measurement (figure 5.20).
2. For specific combinations of data disagreeing with Monte Carlo and both the up and down variations being in the same direction, it is possible to form an under constraint. Figure 5.21 shows this more visually.

For the latter, a significant amount of time was spent working out where and how the issue was arising. To help identify the issue, the following steps were made:

1. The systematic variations that were initially under constrained were artificially decorrelated. This is where each of the variation's nuisance parameters are split and allowed to float separately for each region and sample.
2. After this the following trends were seen in the under constraints.
  - The under constraint would always include the high- $p_T$  CR variations.
  - The signal sample's experimental systematic variations would usually be under constrained.

- The under constraints were more common in the low mass samples which had higher event counts and higher signal contamination in the high  $p_T$  CR due to the larger event count.
- Examining the systematic variations in the high  $p_T$  region we see that the under constraints only occur when the variation is one-sided in that bin.

With these observations and the second mechanism for under constraint in mind, it can be deduced that the origin of these issues is due to fitting  $\mu$  on mostly MC Asimov data in the SR but a large signal contamination in high  $p_T$  CR, causing the under constraining pulls. The phenomenon goes away with the unblinded data (chapter 7). This issue is mitigated by forcing the Asimov dataset to take more realistic non-contaminating values indicated in table 5.15.

## 5.6 Conclusions

As can be seen in this chapter, generating a SR that is optimised with well-modelled orthogonal control regions is a lengthy process. Alongside this, generating a fitting methodology with a large set of custom systematic uncertainties uncovers nuances in the statistical framework. Profiling the likelihood and understanding correlations and pulls is an important step in any ATLAS analysis.

In the next chapter, we discuss non-prompt backgrounds in more depth, how ‘ffFakeL’ events are derived, and quantify other rarer background processes that were not needed for the fit. After this, the unblinded signal region results are discussed.

Prior to this analysis, the only result to probe this high mass HNL parameter space was an equivalent CMS run 2 analysis [104]. This can be in the context of the whole search space. At the lower mass scales, searches for rare decays in high statistics productions of  $K$  and  $D$  mesons producing on shell  $N$  [54]. The leading limits for these decays are NA62 and the CHARM experiment, respectively [105, 106, 107].

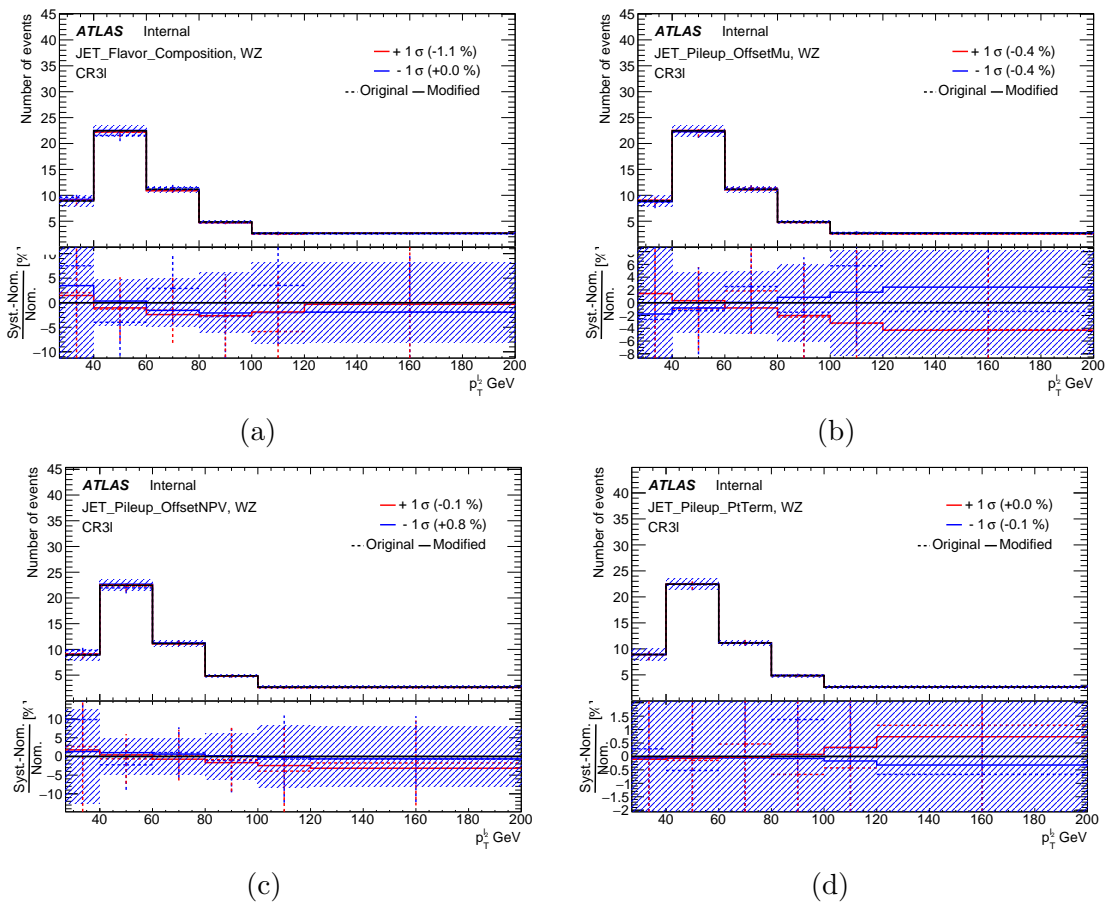


Figure 5.20: The four under constrained fitting parameters that became stable after t-channel smoothing [103]. It can be seen that solid post-smoothing lines have much clearer up-down variations than the previously statistically fluctuating variations (dotted). This is shown with the WZ (labeled CR3l) histogram as the effect is most visible.

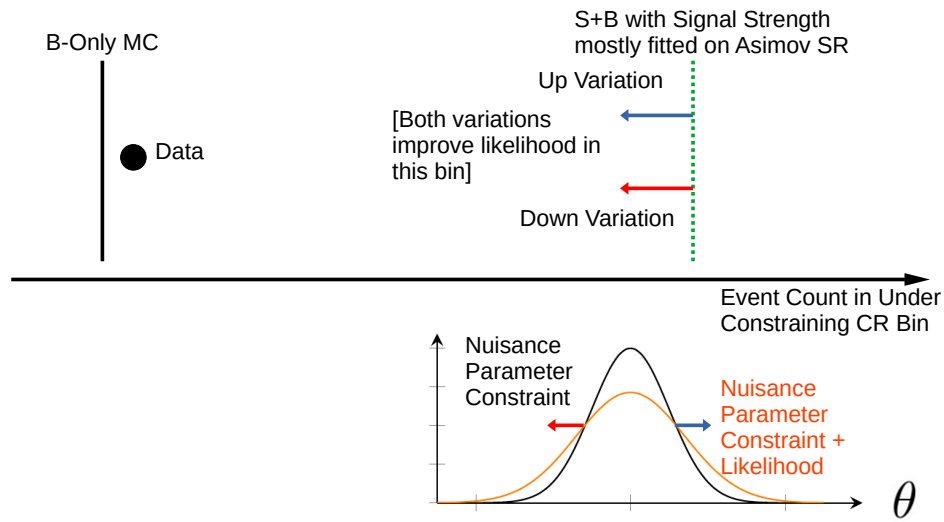


Figure 5.21: An Illustration Of Azimov-data discrepancy leads to under constrained pulls. Both variations in the Monte Carlo are far away from the data in the same direction and the data is significantly far from the expected value. The signal strength  $\mu$  is mostly derived from the rest of the fit (in a very large signal region). This leads to  $\theta$  having a broader convoluted likelihood with data included.

In the intermediate range between this analysis ( $m_D \lesssim m_N \lesssim m_W$ ), the most powerful limits are set by ATLAS and CMS through displaced and prompt decays [55, 60, 108, 109].

## CHAPTER 6

---

### Rare Background Estimation Studies for HNLs at ATLAS

---

In this chapter, we deal with the treatment of background estimation from sources anticipated to be poorly modelled in Monte Carlo (MC). These are primarily events with heavy-flavour hadronic activity alongside a single prompt muon.

Firstly, we roughly classify and quantify the sources of background by using the stored truth information from MC. We then remove MC events from some of these sources through a truth record filter and instead derive fake hadronic counts using adjacent orthogonal regions from data by propagating fake factors from a di-jet enriched sample.

Finally, we show three more studies of background sources that were not necessary to include in our final fit due to deduced negligible effects. These are photons faking muons, charge flip and co-incidentally produced W bosons in the same recorded event (i.e. two uncorrelated W bosons and double-parton scattering).

IFF Class	Description
1	'knownUnknown' suspected here to be mostly $\gamma^* \rightarrow \mu\mu$
2	prompt $e$
4	prompt $\mu$
5	photon fake to $e$
6	$e$ from $\mu$ decay
7	$\tau$ decays
8	b-jets
9	c-jets
10	light flavour (u,d,s) jets

Table 6.1: Breakdown off IFF Classifier codes.

## 6.1 Monte-Carlo Truth Studies

As a preliminary check for an ATLAS analysis, the simulated MC origin (referred to as 'truth') of muons defined by the object selections is inspected. For this process and throughout this chapter, the origin of our leptons is classified into two categories. Real or prompt leptons are used interchangeably in this context to mean leptons from the targeted EW W and Z boson decay processes this analysis is built to probe. The term fake or non-prompt is used to describe leptons that are from other processes. For an analysis with high- $p_T$  muons, this is primarily from c- and b-quark decays. This definition, also in principle, includes any background from other decays, other non-EW sources and misidentification that will be discussed in this chapter.

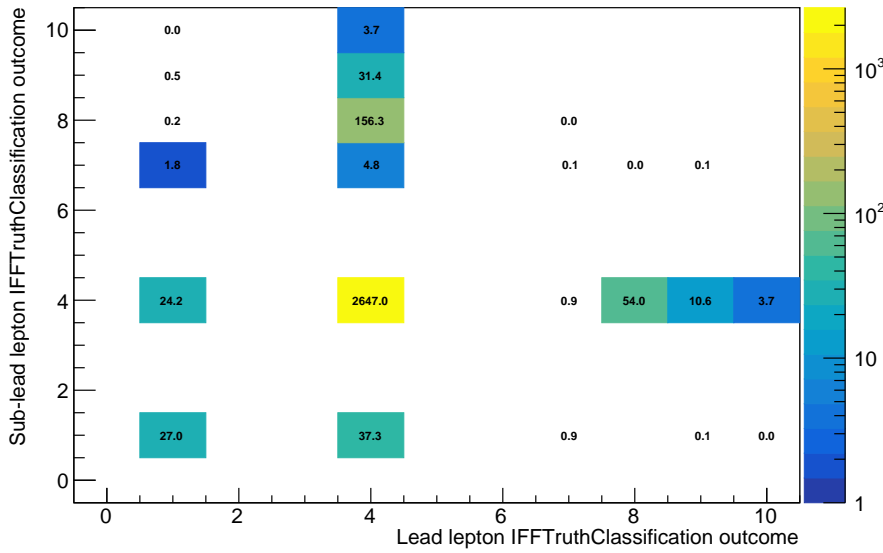
To classify these phenomena, ATLAS uses the IFFTruth Classifier, which examines the truth record output from the various generators and gives a single-value numerical output. These are listed in table 6.1. A priori, before applying our improved estimation techniques for selected IFFclasses, we check the signal region and preselection data's IFFclasses. This allows us to see what types of fakes enter our selections.

To visualise the output of this classifier, figures 6.1a and 6.1b show the number of events as a function of the classification outcome for the leading and sub-leading lepton at pre-selection and in our signal region. This is then projected into a sub-leading truth distribution to show the relative contribution for different Monte

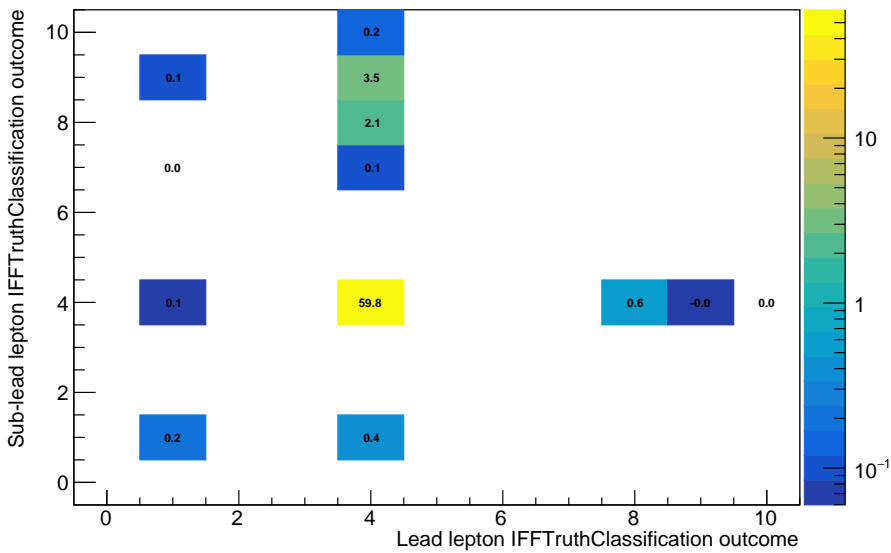
Carlo background samples (figures 6.2a and 6.2b). As can be seen, our non-prompt backgrounds can be roughly broken down as follows:

1. Most ( $\sim 95\%$ ) of our Signal Region and preselection muons are prompt muons.
2. Around  $\sim 5\%$  of the reconstructed muons come from hadronic background sources, primarily from  $c$ - and  $b$ -quarks. These are discussed in detail in section 6.2, including how the ‘ffFakeL’ estimate is derived. Any double non-prompt contribution is negligible.
3. A further sub-leading effect is muons tagged as knownUnknown. This category is chosen if the algorithm cannot determine the source of the reconstructed muon. This is notoriously hard to identify. After the studies described in section 6.3, it is determined that this is likely due to virtual photons converting to a muon pair. This effect is found to have negligible impact on our analysis as only around one event is found in the SR.

Some other backgrounds that would not be present in our simulated backgrounds are estimated (sections 6.4 and 6.5) in an attempt to be exhaustive. These are all also found to be negligible.

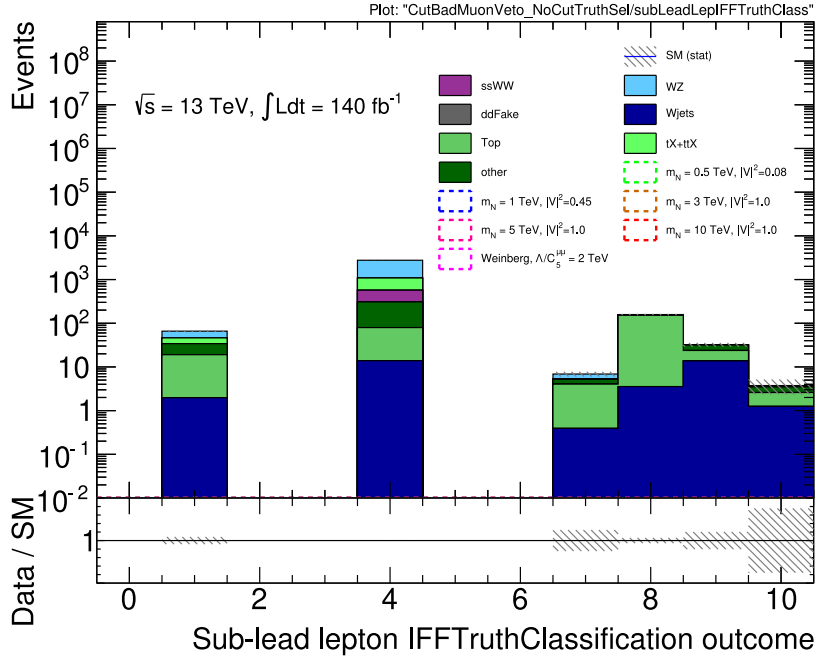


(a) Pre-Selection muon truth scores event counts

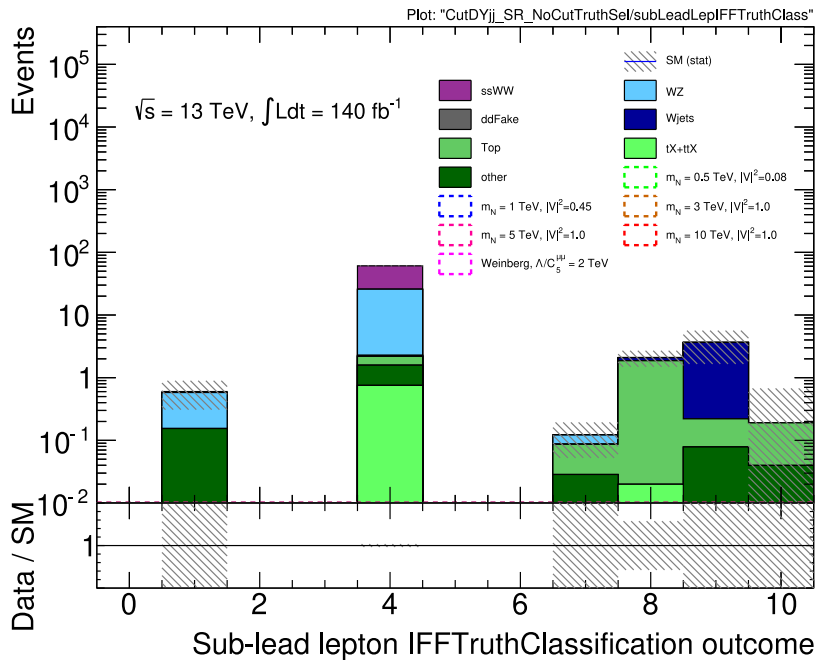


(b) Signal Region muon truth scores event counts

Figure 6.1: The background sample IFF Classification Scores (table 6.1) of the lepton pairs at pre-selection and in the Signal Region, this show that most of our non prompt background is from heavy hadronic sources.



(a) Pre-Selection Projection



(b) Signal Region Projection

Figure 6.2: Projections of figure 6.1 by sub-leading lepton.

## 6.2 Hadronic Fake Estimates

The previous section shows that the non-prompt background mainly arises from heavy flavour ‘hadronic fakes’ (b-quark decays). This predominately originates from  $W$ +jets. To probe this further, the estimation tools from the same-sign WW (ssWW) analysis are exploited [110]. These use the common technique of defining a more loosely defined set of identified leptons that fail our signal definition. These are denoted anti-ID or Bad leptons (as opposed to ID or Good) (see section 5.2 and table 5.5). For muons, this implies failing `FixedCutPflowTight` but passing `FixedCutPflowLoose` (section 5.2.2), failing hadronic isolation BDT selection or that  $3 < d_0/\sigma(d_0) < 10$  (similar to that a b-tagged event). This is combined with a larger-statistics, fake-enriched dataset that is then used to derive a ‘fake factor’. Subsequently, this fake factor is used to derive a more accurate version of the non-prompt background.

As the target data is a rare high-energy signal, the amount of data to estimate fakes, especially in the EW sector, is limited. As a result, the strategy targets commoner QCD di-jet events with the corresponding topology. Such events are selected in the data, requiring only a single muon trigger as preselection. To have adequate statistics to encapsulate as wide a range of  $p_T$  as possible for fitting an extrapolated smooth distribution, a high- $p_T$  and low- $p_T$  trigger are meshed together. This allows avoidance of pre-scaling at high- $p_T$ . Specifically, the pre-scaled `HLT_mu14` and un-prescaled `HLT_mu50` trigger chains are used.

To select this event topology, a reasonably simple selection is conceived (table 6.2). Di-jet events should have transverse momentum conservation due to no invisible neutrino production. Resultantly, we pick events with a baseline muon and signal jet with back-to-back topology ( $\Delta\phi > 2.8$  between the muon candidate and the additional jet). In addition, to reduce further background from  $W$ +jets events, a sum of  $E_T^{\text{miss}}$  and the  $E_T^{\text{miss}}$ -muon combined transverse mass<sup>1</sup> is cut at less than 50 GeV. This rejects events containing  $W$  bosons, which decayed into a high- $p_T$  neutrino

---

<sup>1</sup> $m_T$  mass using only  $E$  and  $p_T$  components of the combined system.

Observable	Requirement	Motivation
Number of baseline muons	=1	Collections to pick fakes
Number of signal jets	> 1	—
$\Delta\phi(\text{jet}, \mu)$	> 2.8	Back-to-back topology di-jet target
$E_T^{\text{miss}} + m_T(E_T^{\text{miss}} + \mu)$	< 50 GeV	If either term is large, indicates a W decay
IFFClass (simulation)	=4	Only select prompt Monte Carlo for equation (6.1)

Table 6.2: Cutflow for the di-jet enriched hadronic fake control region after preselection, with the motivations.

or muon-jet pair with a combined system mass consistent with a W decay. These selections are not perfect, and the remaining prompt contamination can be mitigated. Distributions of this di-jet CR are shown in figure 6.3. The MC samples filtered to be only from prompt processes (IFFclass 4) are used to subtract these processes from data. The fake factor is then derived using this CR with equation (6.1).  $N$  is the number of events.

$$f = \frac{N_{\text{ID}}^{\text{Data}} - N_{\text{ID}}^{\text{Monte Carlo}}}{N_{\text{anti-ID}}^{\text{Data}} - N_{\text{anti-ID}}^{\text{Monte Carlo}}} \quad [\text{Binned in } p_T] \quad (6.1)$$

To then obtain the application properties of  $f$  to our fitting regions, we first define the following notation:  $N_{ab}^{ij}$  is the count/distribution with  $i, j$  the *Real/Fake* and  $a, b$  the *Good/Bad* tag of the leading/subleading muon.  $f_1 f_2$  indicates the fake factor being applied to both leptons by  $p_T$ .

$$\begin{aligned}
 N_{GG}^{RF+FR+FF} = & f \underbrace{(N_{GB} - N_{GB}^{RR})}_{\text{'excess' of GB in data}} + f \underbrace{(N_{BG} - N_{BG}^{RR})}_{\text{'excess' of BG in data}} \\
 & - f \underbrace{(N_{GB}^{FR} + N_{BG}^{RF})}_{\text{cross terms}} - f_1 f_2 \underbrace{(N_{BB} - N_{BB}^{RR+RF+FR})}_{\text{double counting correction}} \quad (6.2)
 \end{aligned}$$

Here two assumptions are made:

1. The only significant source of prompt contamination in  $GB$  or  $BG$  is from processes involving 2 real leptons. Due to the limited MC statistics, the last two terms are neglected, which results in a conservative estimate.

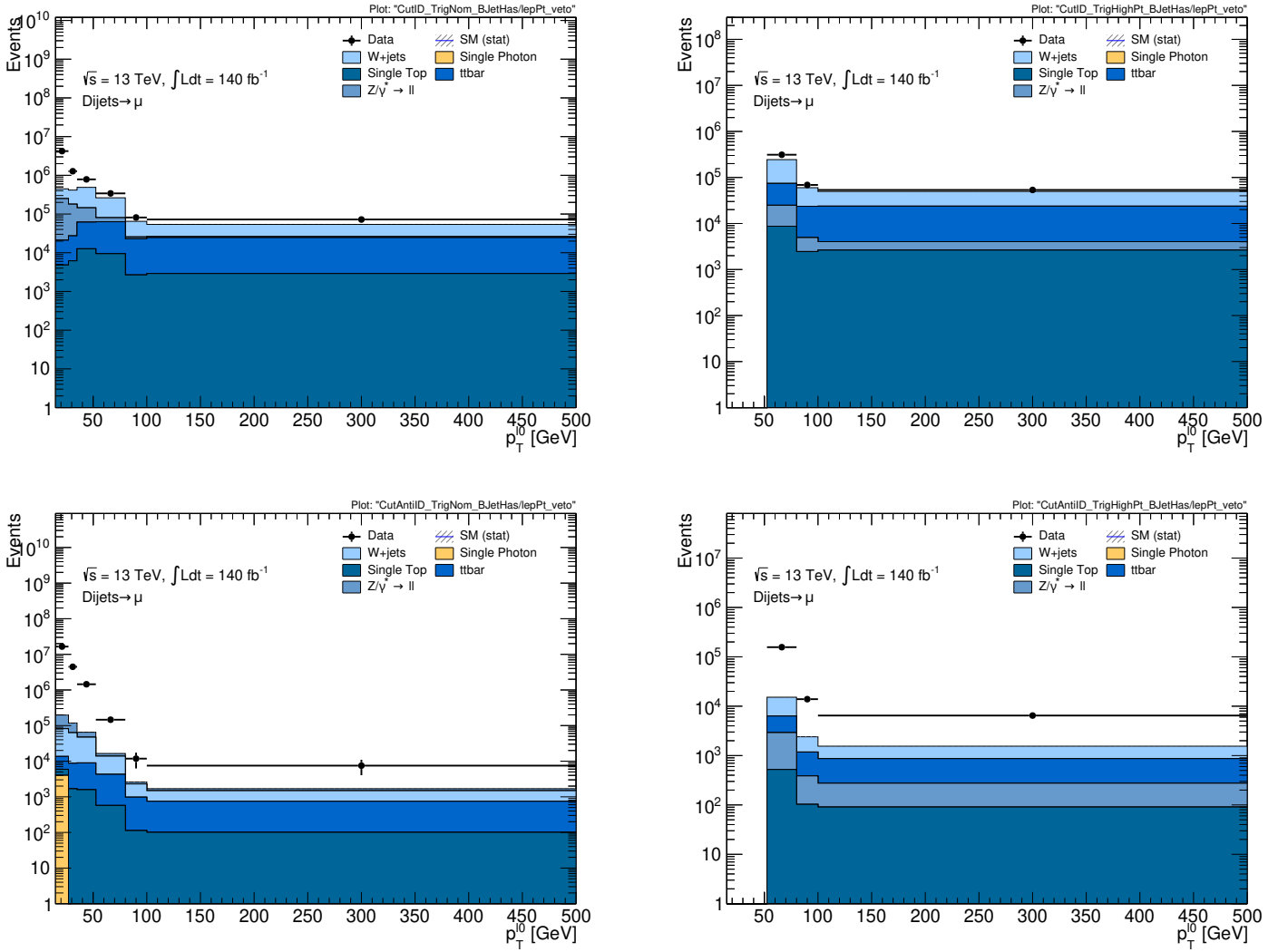


Figure 6.3: Distributions of the ID (top) and Anti-ID (bottom) lepton  $p_T$  for HLT\_mu14 (left) and HLT\_mu50 (right) in events with  $n(b\text{-jet}) > 0$ . By taking the excesses of data in these distributions, we derive a fake factor.

2. The relative transfer factors of the fake factor remain the same between the signal region and the di-jet control region. This is known not to be entirely correct because to match the SR, it was noted a requirement of at least one b-tag to match the truth distributions was needed. This requirement is not used in the SR. Consequently, the lack of confidence in this assumption remains a systematic variation used in the fitting procedure (**FF\_SampleComposition**). The change in the fake factor is shown in figure 6.4.

Applying equation (6.1) to figure 6.3 gives the fake factor  $f$  plotted in figure 6.4. However, using the same  $p_T$  binning as the SR, it is found that this leads to bumpy distributions once applied to our SR and CRs. To mitigate this, the event count per GeV using various functional forms are fitted. These are shown in figure 6.5. This is also done separately for all the CRs discussed in chapter 5. The results of these methods can be seen throughout chapters 5 and 7. The bumpier ‘ddfakes’ labelled histograms were the preliminary unsmoothed histograms used in earlier studies. ‘ffFakeL’ or ‘Non-prompt  $\mu$ ’ used in the statistical fit uses these functional forms.

To encapsulate our systematic uncertainty in this methodology involves introducing several nuisance parameters.

**Compositional difference between the signal and control region:** To estimate differences between the ‘true’ origin of the non-prompt leptons the b-tag requirement applied is flipped (1 to 0). The one-sided nature for this systematic is symmetrised (**FF\_SampleComposition**).

**Alternative Monte Carlo for background subtraction:** To compensate for prompt modelling with MC in this method, in a region where the Monte Carlo simulation is not trusted, we use a different Monte Carlo generator for W+jets (see section 5.3) and symmetrise again (**FF\_PromptModelling**).

**The fake factor statistical uncertainty:** The MC statistical uncertainty of this

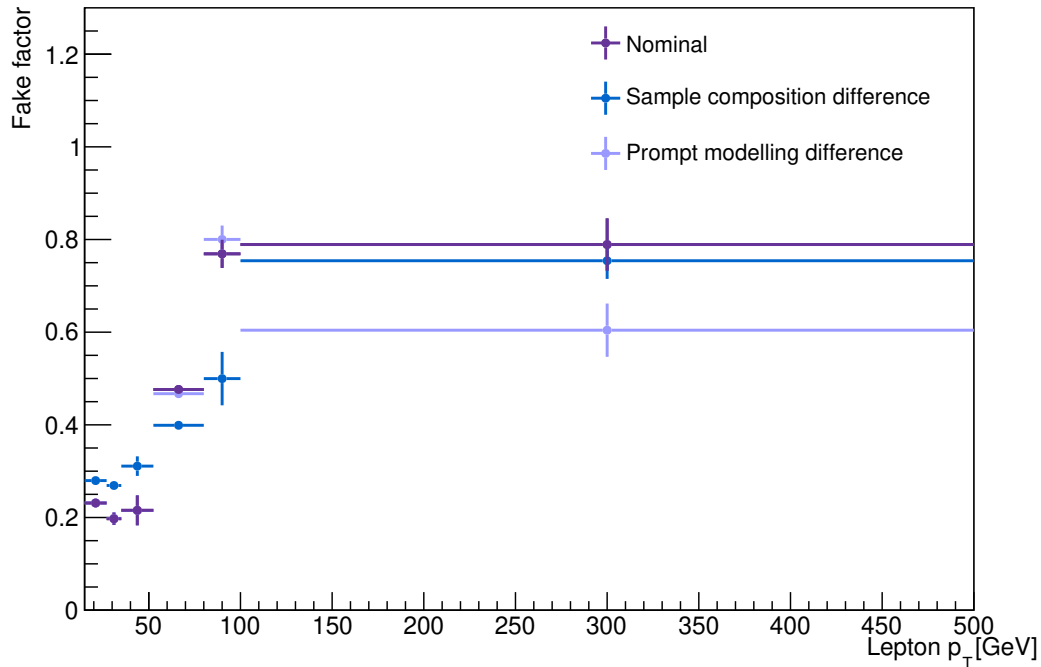
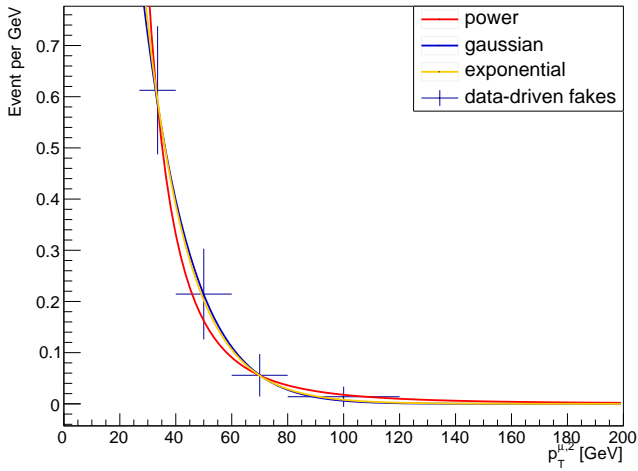


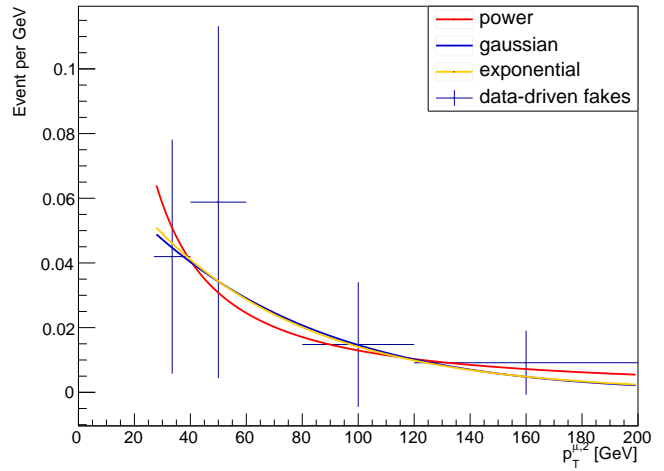
Figure 6.4: The derived fake factor with binning such the distributions from various systematic variations can be compared.

estimate is encapsulated by a systematic variation in each of six bins in the SR (**FF\_STAT\_1\_X** for bin **X**).

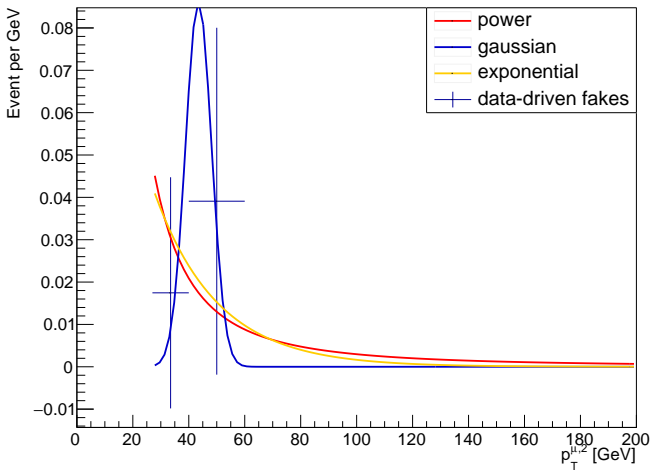
**Functional form choice and error from likelihood functional form fit:** Finally, various functional forms can be used to smoothen the fake estimate's  $p_T$  spectra in the SR and CRs. A power law instead of an exponential is used in the fit, and the difference is used as a systematic variation. These fits are shown in figure 6.5. As our signal is high- $p_T$  and this form is used to extrapolate, this ends up being one of the larger but still small systematic variations (**FF\_FitModel**). Finally, the  $1\sigma$  uncertainties in the fitting parameters are added (**FF\_ParamError**).



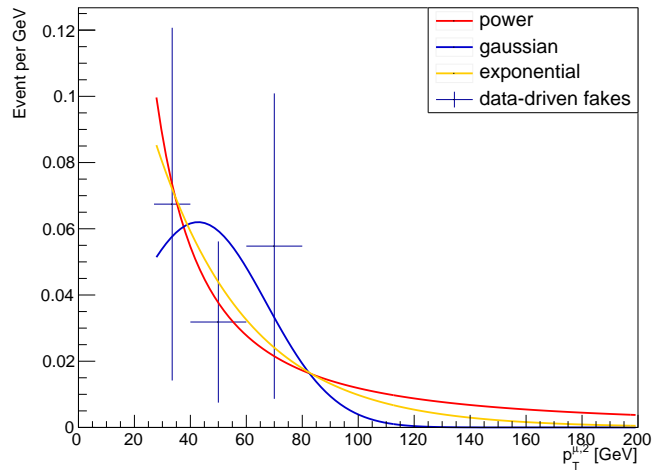
(a) SR



(b) WZ CR



(c) ssWW VR



(d) ssWW CR

Figure 6.5: Visualisation of functional form fits for smoothing hadronic fake estimates [68]. The event density (‘data-driven fakes’) is fitted with sensible, simple functions (power law, gaussian and exponential decay) before the fitted density is used for the event count. The Gaussian does not provide a good fit, so it is not used. The systematic variation **FF\_FitModel** is derived using the 2-point difference between a power law and an exponential decay.

## 6.3 Photon Fake Estimates

A VR is defined to investigate the potential mismodelling of photons faking muons in the signal/control regions. This fake component may be present in our regions according to MC-based estimates shown earlier, although in a small amount; see section 6.1. The region chosen to study photons faking an electron or muon ( $e/\mu$ ) targets  $Z + \gamma$  events where the photon is radiated from the Z decay products and happens to be reconstructed as  $e/\mu$ .

This style of control region is a common feature of an ATLAS analysis for  $\gamma \rightarrow e$ , while this background is usually assumed to be negligible for muons. In this analysis, though, the presence of ‘knownUnknown’ IFF Class muons after preselection (IFF Class 1) was noticed. As these could arise from  $\gamma^* \rightarrow \mu$ , it was proposed to check this hypothesis using a VR. Given the low background expected in the SR, it was believed this was a necessary check.

To construct this region, a selection is detailed below, where the differences with respect to the main analysis preselection<sup>2</sup> (see section 5.4.1) are highlighted in bold. This extends an ssWW analysis procedure to select  $\gamma \rightarrow e$ , and hence, the electron fake selections are retained for comparison.

1. As a limitation of our analysis framework, the first two leading leptons must pass the preselection requirements described in section 5.4.1 **apart from the same-sign requirement**, and in particular must have the same flavour ( $ee$  or  $\mu\mu$ ). Therefore, some potentially interesting events such as  $e\mu e$  or  $\mu e \mu$  cannot be selected. The jet requirements are loosened to improve the statistics.
2. A three-signal lepton selection is applied such that an opposite sign, the same flavour pair of leptons from a Z boson, can be defined. In the  $ee\mu$  and  $\mu\mu e$  channels, it is assumed that the first two leptons are from a Z decay pair of leptons, so it requires  $e^\pm e^\mp \mu$  or  $\mu^\pm \mu^\mp e$ . For  $eee$  and  $\mu\mu\mu$ , the closest opposite

---

<sup>2</sup>The currently unpublished ee channel pre-selection is used to improve the statistics here.

charge pair to the Z mass is taken, and the other lepton is taken to be the fake photon. Rearranging the tagged fake leptons, the  $[e^\pm e^\mp \text{ or } \mu^\pm \mu^\mp]$   $\mu$  channels (fake  $\mu$ ) and  $[e^\pm e^\mp \text{ or } \mu^\pm \mu^\mp]$   $e$  channels (fake  $e$ ) are defined.

3. A trileptonic mass ( $75 \text{ GeV} < m_{\ell\ell\ell} < 100 \text{ GeV}$ ) cut is applied to select FSR photons of on-shell Z and to be orthogonal to the WZ CR.
4. A  $E_T^{\text{miss}}$  Significance cut  $< 2$  is applied to reduce the  $t\bar{t}$  contamination.

The background estimate from the pre-fit MC is compared to the data, and then a preliminary, rough scale factor  $\alpha$  is derived through equation (6.3).

$$\alpha = \frac{N_{\text{CR,Data}} - N_{\text{CR,all MC background except targetted processes}}}{N_{\text{CR,Z+jets and Z}\gamma \text{ MC}}} \quad (6.3)$$

The cutflows for the four channels and their relevant scale factors derived from equation (6.3) are given in tables 6.3 and 6.4. The tri-lepton mass distribution is given in figure 6.6. Reasonable data-MC agreement is seen in most channels with a mass peak corresponding to a Z decay. Interestingly, the  $\mu$  fake Z+jet regions appear to peak above the Z boson mass suggesting ISR production. The IFF Classes are shown in figure 6.7.

There is significant di-boson contamination for the muon fake channels, and the Z+jets background MC has a large statistical error. Scale factors lower than unity in both  $\mu\mu\mu$  and  $ee\mu$  channels are found ( $0.31 \pm 0.24$  and  $0.45 \pm 0.20$ ) giving us confidence that this background can be conservatively evaluated when the MC is used in the analysis.

Indeed, as the analysis developed, analysis regions were chosen in which the W+jets/W+ $\gamma$  contributions were minimal, unlike the SM ssWW analysis, which was our starting point. However, there is still a small number of ‘knownUnknown’ events in the signal region according to the MC estimates ( $\sim 1$ ), and this study helps to gain confidence that the origin of this fake component is understood and correctly modelled such

that MC estimates can be used.

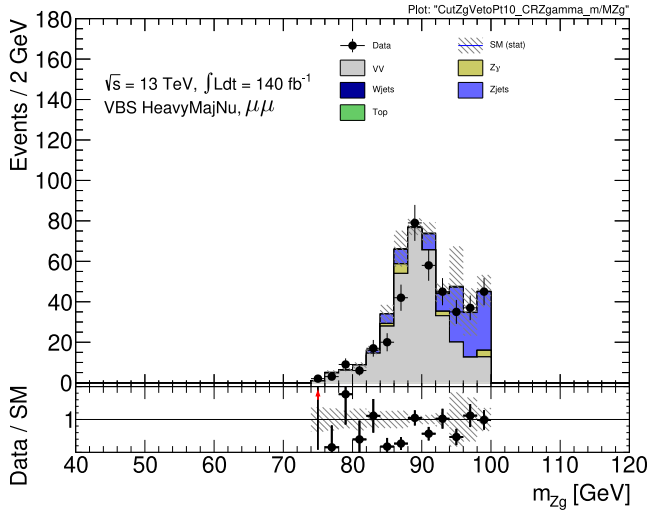
It is also instructive to filter the  $Z\gamma$  control region by IFF Class (to only include the fakes) and plot the tagged fake lepton rapidity. A differing nature in the form of the fakes can be seen, shown in figure 6.8. For the more commonly measured and calculated photon-to-electron fakes, the  $\eta$  distribution is strongly correlated with detector material in a way that is not true for known/unknown muons. This indicates that  $\mu$  fakes originate from off-shell photons, whereas the  $e$  is on shell material conversions. This agrees with the truth study by the ttH group [111].

Table 6.3:  $ee + (e/\mu)$  channel cutflow for the ZGammaCR in section 6.3. The number in each cell represents the number of data events found or the number expected from a process in simulation, after requiring each cut on data.  $\alpha$  is derived using equation (6.3).

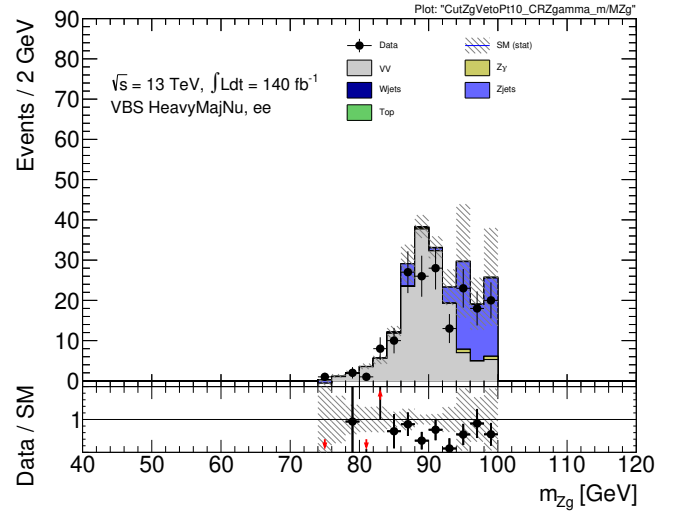
$\sqrt{s} = 137\text{TeV}, \mathcal{L} = 140\text{fb}^{-1}$ (Full Run 2)	VV	$Z\gamma$	Zjets	Top	Data	SF Nom ( $\alpha$ )
Channel Selection	132310 $\pm$ 150	555900 $\pm$ 1100	9603000 $\pm$ 8000	820820 $\pm$ 330	9406605	0.8 $\pm$ 0.0
Identical cuts up to and including lepton pt and eta	44050 $\pm$ 60	92400 $\pm$ 500	2607300 $\pm$ 3500	206060 $\pm$ 170	2783100	0.9 $\pm$ 0.0
exactly one extra signal electron (no extra baseline leptons)	4353 $\pm$ 17	1260 $\pm$ 60	2310 $\pm$ 120	472 $\pm$ 6	8657	0.98 $\pm$ 0.04
Overlap: Vgamma/Vjets	4353 $\pm$ 17	1260 $\pm$ 60	2310 $\pm$ 120	472 $\pm$ 6	8657	0.98 $\pm$ 0.04
OS Lepton pair including l3	4349 $\pm$ 17	1260 $\pm$ 60	2310 $\pm$ 120	472 $\pm$ 6	8647	0.98 $\pm$ 0.04
$75 < m_{ll} < 100$ GeV	281 $\pm$ 7	800 $\pm$ 50	420 $\pm$ 60	29.3 $\pm$ 1.9	1745	1.17 $\pm$ 0.08
$E_T^{\text{miss}}$ significance < 2	189 $\pm$ 6	660 $\pm$ 50	320 $\pm$ 60	4.8 $\pm$ 0.8	1328	1.16 $\pm$ 0.10
exactly one extra signal muon (no extra baseline leptons)	4203 $\pm$ 17	29 $\pm$ 9	1420 $\pm$ 80	465 $\pm$ 5	6131	0.75 $\pm$ 0.07
Overlap: Vgamma/Vjets	4203 $\pm$ 17	29 $\pm$ 9	1420 $\pm$ 80	465 $\pm$ 5	6131	0.75 $\pm$ 0.07
OS Lepton pair including l3	4192 $\pm$ 17	29 $\pm$ 9	1420 $\pm$ 80	427 $\pm$ 5	6066	0.77 $\pm$ 0.07
$75 < m_{ll} < 100$ GeV	225 $\pm$ 6	4.0 $\pm$ 2.7	90 $\pm$ 21	19.3 $\pm$ 1.5	282	0.34 $\pm$ 0.21
$E_T^{\text{miss}}$ significance < 2	154 $\pm$ 6	2.0 $\pm$ 1.1	65 $\pm$ 20	1.7 $\pm$ 0.4	177	0.31 $\pm$ 0.24

Table 6.4:  $\mu\mu + (e/\mu)$  channel cuthrow for the ZGammaCR in section 6.3. The number in each cell represents the number of data events found or the number expected from a process in simulation, after requiring each cut on data.  $\alpha$  is derived using equation (6.3).

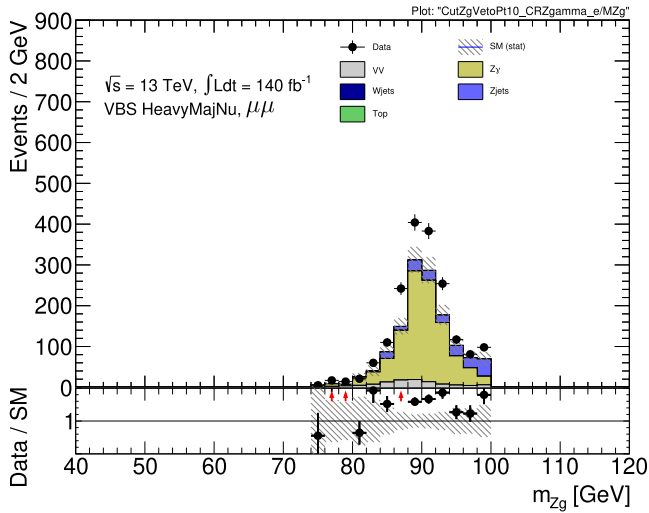
	$\sqrt{s} = 137eV, \mathcal{L} = 140fb^{-1}$ (Full Run 2)		Z $\gamma$		Zjets		Top		Data	SF Nom ( $\alpha$ )
	VV	Z $\gamma$	Z $\gamma$	Zjets	Top	Data	SF Nom ( $\alpha$ )			
Channel Selection	192970 $\pm$ 270	725900 $\pm$ 1300	13592000 $\pm$ 10000	2724700 $\pm$ 600	67055908	4.4 $\pm$ 0.0				
Identical cuts up to and including lepton pt and eta	70130 $\pm$ 70	171800 $\pm$ 700	4999000 $\pm$ 5000	317080 $\pm$ 210	5126085	0.9 $\pm$ 0.0				
exactly one extra signal electron (no extra baseline leptons)	5356 $\pm$ 19	2200 $\pm$ 80	3930 $\pm$ 140	698 $\pm$ 7	12587	0.990 $\pm$ 0.030				
Overlap: Vgamma/Vjets	5356 $\pm$ 19	2200 $\pm$ 80	3930 $\pm$ 140	698 $\pm$ 7	12587	0.990 $\pm$ 0.030				
OS Lepton pair including l3	5343 $\pm$ 19	2200 $\pm$ 80	3930 $\pm$ 140	674 $\pm$ 7	12494	0.990 $\pm$ 0.030				
75 < $m_{ll}$ < 100 GeV	181.4 $\pm$ 3.0	1360 $\pm$ 70	280 $\pm$ 40	45.8 $\pm$ 2.3	2371	1.30 $\pm$ 0.07				
METsig < 2	105.5 $\pm$ 2.1	1050 $\pm$ 60	191 $\pm$ 33	5.6 $\pm$ 0.8	1806	1.37 $\pm$ 0.08				
exactly one extra signal muon (no extra baseline leptons)	9764 $\pm$ 23	53 $\pm$ 11	2400 $\pm$ 110	659 $\pm$ 6	13052	0.83 $\pm$ 0.06				
Overlap: Vgamma/Vjets	9764 $\pm$ 23	53 $\pm$ 11	2400 $\pm$ 110	659 $\pm$ 6	13052	0.83 $\pm$ 0.06				
OS Lepton pair including l3	9764 $\pm$ 23	53 $\pm$ 11	2400 $\pm$ 110	659 $\pm$ 6	13052	0.83 $\pm$ 0.06				
75 < $m_{ll}$ < 100 GeV	519 $\pm$ 8	13 $\pm$ 6	173 $\pm$ 31	33.8 $\pm$ 1.9	668	0.55 $\pm$ 0.17				
$E_T^{\text{miss}}$ significance < 2	338 $\pm$ 7	10 $\pm$ 6	109 $\pm$ 26	3.6 $\pm$ 0.6	398	0.45 $\pm$ 0.20				



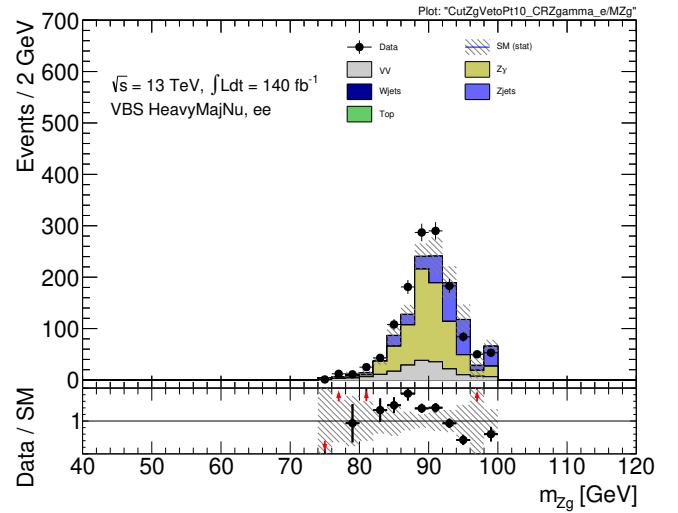
(a)  $\mu\mu\mu$



(b)  $ee\mu$

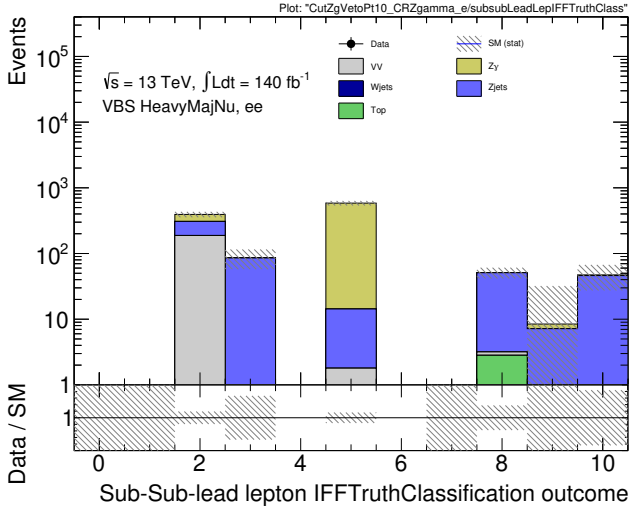


(c)  $\mu\mu e$

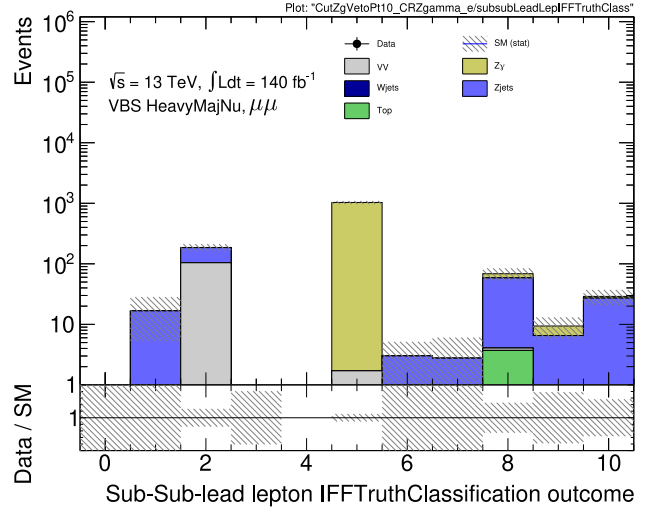


(d)  $eee$

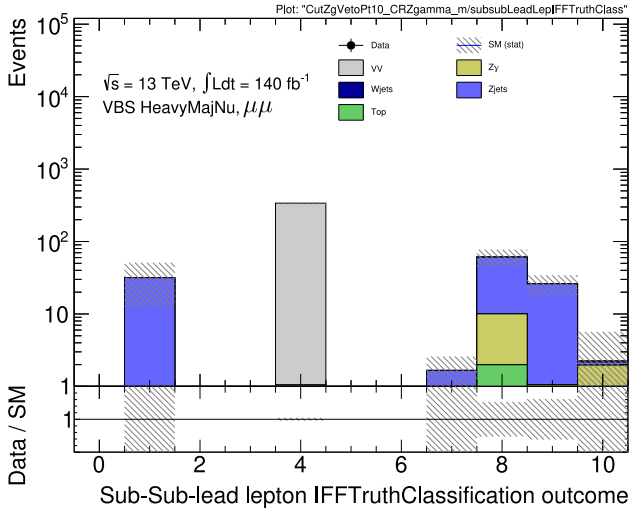
Figure 6.6: The tri-lepton mass distributions ( $m_{Zg}$  or  $m_{\ell\ell\ell}$  in the description) of the 4 validation regions. It can be seen from the peak at 90 GeV in the data we are successfully selecting Zs with mis-reconstructed electrons and muons. The scale factor  $\alpha$  is derived from the mismatch, aiming to rescale the Z+jets/ $\gamma$  MC.



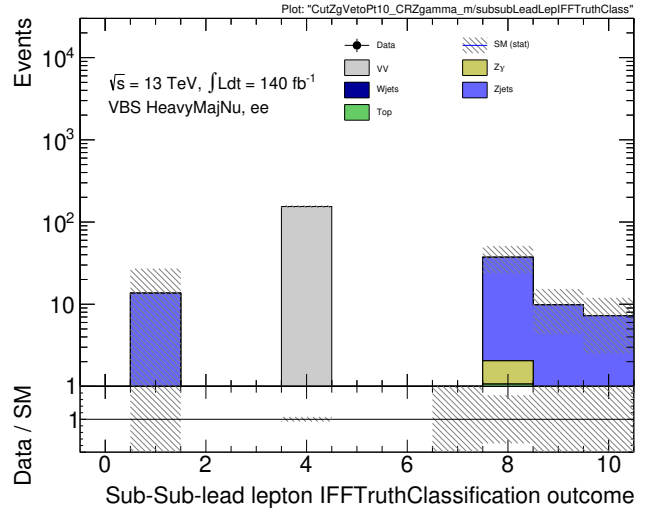
(a)  $eee$  (Target 5)



(b)  $\mu\mu e$  (Target 5)

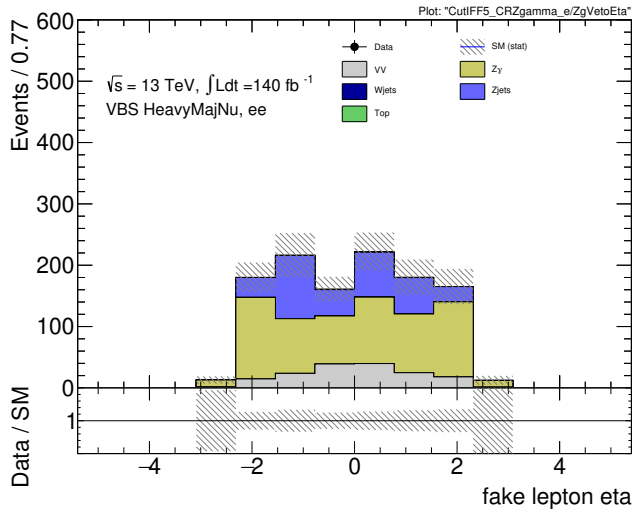


(c)  $\mu\mu\mu$  (Target 1)

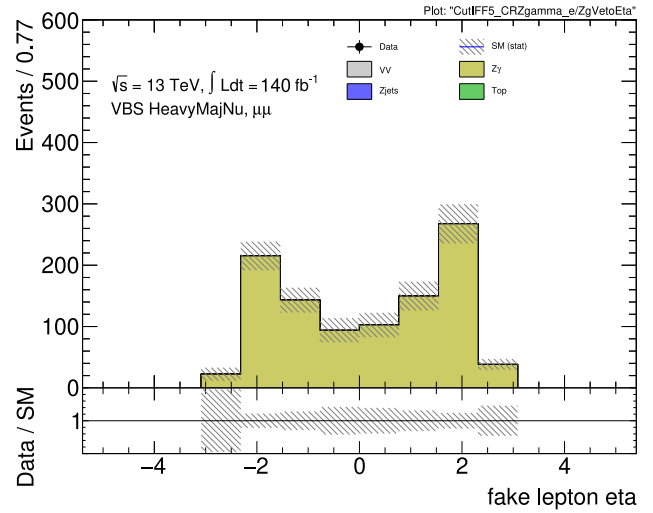


(d)  $ee\mu$  (Target 1)

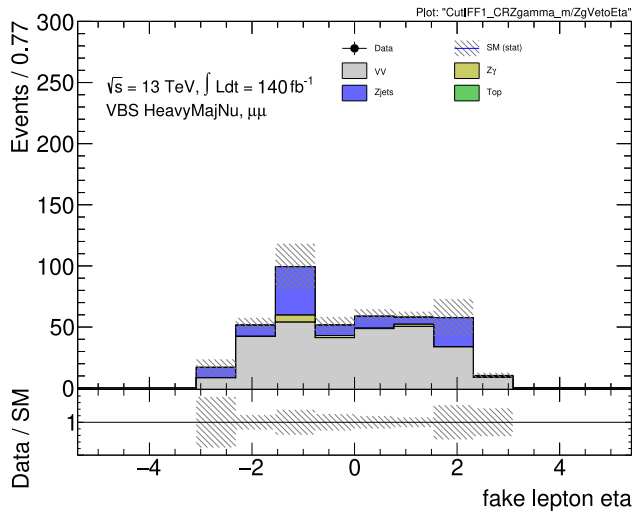
Figure 6.7: IFF Class of third leptons in ZgammaCR, as can be seen it is much more successful at selecting electron fakes than muon fakes. The codes are listed in table 6.1.



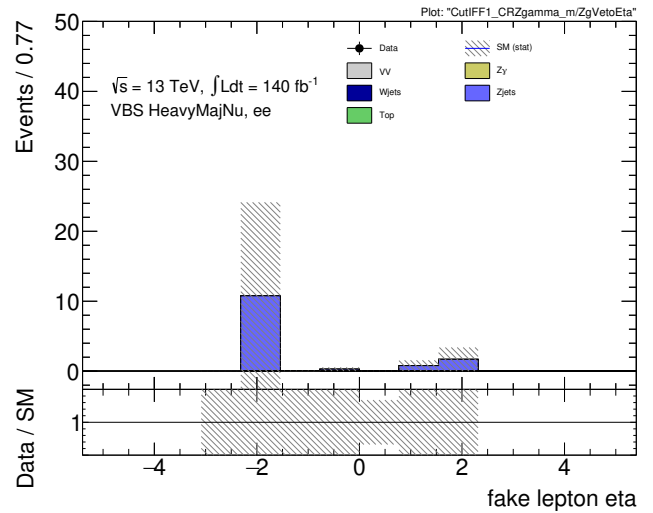
(a)  $eee$



(b)  $\mu\mu e$



(c)  $\mu\mu\mu$



(d)  $ee\mu$

Figure 6.8: Fake lepton  $\eta$  distributions filtered to the desired IFF Class, which demonstrates the difference between  $\gamma \rightarrow e$  and  $\gamma^* \rightarrow \mu$ . The data is not included as we have filtered by the MC truth record which is impossible in data.

## 6.4 Muon Charge Misidentification

Typically, muon charge misidentification (incorrect sign) is taken to be negligible. However, recent work from the muon CP group suggested that charge flip can be significant at very high- $p_T$  ( $> 1$  TeV) where the curvature of the track becomes nearly straight, and miscalibration becomes an issue. A new ‘charge-flip’ IFFTruth classification score is used to study this. However, when this was implemented, no events were found with the code. Some charge-flip events were looked for in the high-statistics Z+jets MC with this method up to a muon  $p_T$  of 200 – 300 GeV, and no such misidentified events are found. If such muons with high- $p_T$  values had been found, further work would have been needed to evaluate their contribution and determine whether the background contribution is negligible. Also, in data (see chapter 7), no such high- $p_T$  muons are found.

## 6.5 Co-Incidental and Double Parton W production

A hypothesised background for this analysis is two pairs of protons in a single bunch crossing, each producing a W boson, contributing to the SRs and CRs. This is called co-incidental W boson production.

To find this contribution, a relatively simple formula is used to estimate its cross-section (equation (6.4)) [68]. This propagates a measured cross-section of single  $W^\pm$  production. It should be noted that here  $\ell$  denotes decay into  $e$  or  $\mu$ . The terms are explained in the next paragraph.

When reconstructing events in ATLAS, the finite size of the beam, together with tracking, is used to reject non-prompt backgrounds and co-incidental events (see section 2.4). This measure is not perfect, and as a result, the overlap probability is estimated. For the estimate, only the longitudinal separation of the tracks ( $\Delta z_0 \sin \theta$  cut in table 5.4) is considered as it is  $10^3$  times larger than transverse beam spot size.

Using this information and the beam shape estimates from the LHC, an estimate for the probability of two proton collisions occupying the same space  $p_c$  is calculated<sup>3</sup>. To make the form valid for two same-flavour leptons within a LHC RF bunch of  $n$  protons,  $p_c$  becomes  $\frac{1}{2}p_c(n-1)$ . Finally, to account for the fraction of scatters being co-incidentally W production,  $\frac{\sigma_{W^+ \rightarrow \ell\nu}}{\sigma_{\text{total pp}}}$  is used.

$$\sigma_{\text{coincidental } W^+} \approx \underbrace{\sigma_{W^+ \rightarrow \ell\nu}}_{\text{single } W^+ \text{ production pp cross-section}} \times \underbrace{\left[ \frac{\sigma_{W^+ \rightarrow \ell\nu}}{\sigma_{\text{total pp}}} \right]}_{\text{fraction of events with } W^+ \rightarrow \ell\nu} \times \underbrace{\frac{1}{2}p_c(n-1)}_{\text{probability of overlap with same flavour } (e,\mu) \text{ in the bunch}} \quad (6.4)$$

This leads to an estimate of 15.3 events. If you take a very pessimistic view of the tracking quality and understanding of bunch shape<sup>4</sup>, this increases to around 80 events. However, to actually get hard jet pairs with back-to-back geometry  $W +$  additional jets are needed alongside further phase space cuts, which will drop this value by at least a factor  $10^{-3}$  per jet. Resultantly, this background is neglected entirely.

Alongside this, producing two  $W$ s from two pairs of incoming partons in the same proton is considered. The theory of this type of production is less trivial, so an effective cross-section  $\sigma_{\text{eff}}$  is used and measured by another analysis [112]. This is defined by equation (6.5).

$$\sigma_{W^\pm \rightarrow l^\pm \nu, W^\pm \rightarrow l^\pm \nu}^{\text{Double Parton W Scatter}} = \frac{1}{4} \frac{\sigma_{W^\pm \rightarrow l^\pm \nu}^2}{\sigma_{\text{eff}}}, \quad (6.5)$$

The ratio of these two investigated cross-sections (equations (6.4) and (6.5)) cancels out the terms in  $\sigma_{W^+ \rightarrow \ell\nu}$ .

---

<sup>3</sup>This is done by roughly integrating across Gaussian beam profiles

<sup>4</sup> $\Delta z_0 \sin \theta$  depends on the rapidity and as the calculation for the overlay is a conservative, estimate an arbitrary choice of rapidity is picked. The conservative case takes  $\eta = 2.5$

$$\frac{\sigma_{W^\pm \rightarrow l^\pm \nu, W^\pm \rightarrow l^\pm \nu}^{\text{DPS}}}{\sigma_{W^+ \rightarrow l \nu}} = \frac{\sigma_{\text{inel}}}{2(n-1)p_c \sigma_{\text{eff}}} \approx \frac{\sigma_{\text{inel}}}{\sigma_{\text{eff}}} \sim 4, \quad (6.6)$$

Resultantly, the contributions from double parton scattering are equally negligible.

## 6.6 Conclusions

This chapter is a testament to how much effort must be put in for a single ATLAS analysis to be comfortable of understanding data beyond comparing provided internal ATLAS simulation MC to data. To be sure backgrounds are well-modelled and that nothing has been overlooked takes a significant proportion of the analysis effort.

---

## Results

---

Here, the unblinded signal region for the analysis is shown alongside a selection of the fit results. As will be seen, no significant excesses are present, and thus exclusion limits are set. The construction of these limits is explained, and some nuances are tested (using asymptotic formulae for limits, asymptotic limits and pulls with real data).

### 7.1 Unblinded Fit

#### 7.1.1 Unblinded Signal Region Data

Before discussing the detailed results of the unblinded fit, it is instructive to inspect the unblinded signal region in figures 7.1a and 7.1b. Broadly strong agreement

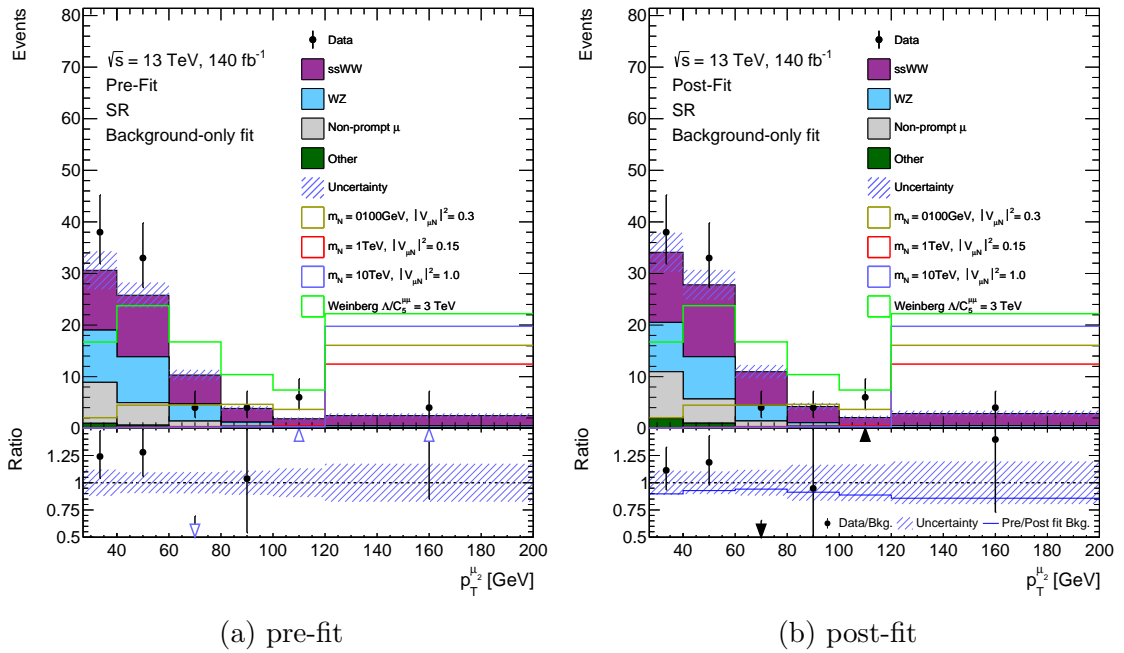


Figure 7.1: The pre- and post-, background-only fit signal region distributions, of which many features of statistical interpretations can be read off by eye. Most notably are the slight excesses in bins 1, 2 and 5.

is found between the Standard Model background estimate and the data in the same manner to the previously unblinded control regions. Obviously, we do not see the clear excess in the final bin in  $p_T$  that would indicate the presence of a signal. Furthermore, the sub-leading high- $p_T$  muons in data do not exceed 200 GeV with our selections. As a check, it is instructive to generate event displays (figures 7.2 and B.1) for signal candidates. Doing so shows events with high  $E_T^{miss} \sim 70$  GeV, which is not especially significant due to how high energy and forward the jets in the event are. These can sensibly be interpreted as our same sign WW events.

The excess in bin 5 is only  $\sim 1.5\sigma$  and does not match the shape of any of the signal samples. In any case, the non-resonant  $W$  boson production analysis has exclusion limits that are much better for this mass range of parameter space [109]. The deficit in bin 3 is also  $\sim 1.5\sigma$  and is certainly not globally significant across all regions or a concern for the background estimate. The slight excesses in the first two bins are pertinent in interpreting the changes in fitting moving from the Asimov dataset in the signal region to the unblinded data. This naturally also slightly weakens the

Sample	SR	ssWW VR	ssWW CR (highpT VR)	WZ CR
ssWW	$34.9 \pm 0.2$	$9.3 \pm 0.1$	$20.4 \pm 0.2$ ( $2.8 \pm 0.1$ )	$< 0.1$
WZ	$23.8 \pm 1.0$	$5.0 \pm 0.5$	$7.5 \pm 0.7$ ( $1.1 \pm 0.1$ )	$52.3 \pm 1.7$
Non-Prompt $\mu$	13.9	0.9	2.8 (1.5)	2.9
other	$1.8 \pm 0.1$	$0.5 \pm 0.1$	$0.6 \pm 0.1$ ( $0.2 \pm 0.1$ )	$4.4 \pm 0.2$
Total SM	$75.1 \pm 2.9$	$15.6 \pm 1.1$	$30.9 \pm 1.4$ ( $4.8 \pm 1.2$ )	$59.4 \pm 2.3$
Data	89	14	29 (6)	56
$m_N = 1$ TeV, $ V_{\mu N} ^2 = 0.45$	$123.8 \pm 1.6$	$0.4 \pm 0.1$	$0.3 \pm 0.1$ ( $1.6 \pm 0.2$ )	$< 0.1$
$m_N = 3$ TeV, $ V_{\mu N} ^2 = 1.00$	$171.7 \pm 2.4$	$0.2 \pm 0.1$	$0.5 \pm 0.1$ ( $3.3 \pm 0.3$ )	$< 0.1$
$m_N = 5$ TeV, $ V_{\mu N} ^2 = 1.00$	$76.1 \pm 1.0$	$< 0.1$	$0.2 \pm 0.1$ ( $1.4 \pm 0.1$ )	$< 0.1$
$m_N = 10$ TeV, $ V_{\mu N} ^2 = 1.00$	$20.7 \pm 0.3$	$< 0.1$	$< 0.1$ ( $0.4 \pm 0.0$ )	$< 0.1$
Weinberg, $\frac{C_5^{\mu\mu}}{\Lambda} = 2$ TeV	$79.6 \pm 1.2$	$0.8 \pm 0.1$	$0.6 \pm 0.1$ ( $0.2 \pm 0.1$ )	$< 0.1$

Table 7.1: The yields in the SR, CRs and VRs compared to unblinded data with statistical uncertainties [68]. Non-prompt muons statistical uncertainties are applied bin-by-bin as a systematic and not combined so are not quoted here.

Weinberg and low mass HNL exclusion limits compared to our blinded expectations. A similar argument can be applied to our same-sign WW normalisations, where we can see a slight increase in  $\mu_{\text{ssWW}}$ , which will improve the SR's agreement with data in bins 1,2 and 4. The pre-fit yield table is shown in table 7.1.

As a final check, some event displays of the signal region data are made in figures 7.2 and B.1. These show sensible looking VBS-style scattering events.

### 7.1.2 Control Regions and Systematic Pulls

With some anticipated results from inspecting the unblinded SR data, looking at the remaining outputs of the fitting methodology is instructive. As we have no significant excesses, the background-only fitting results are shown. Unblinded signal plus background fits used for setting limits are outlined in appendix A.2. The pre- and post-fit CRs and VRs can be seen in figures 7.3 and 7.4 respectively. The data-Monte Carlo agreement between post-fit on an Asimov dataset (section 5.5.2) and the unblinded data is effectively unchanged. The corresponding normalisation factors are visualised in figure 7.5. As can be seen, the upwards pull of  $\mu_{\text{ssWW}}$  by our real data still leaves all background scale factors consistent with 1 and with each other through the various fits.

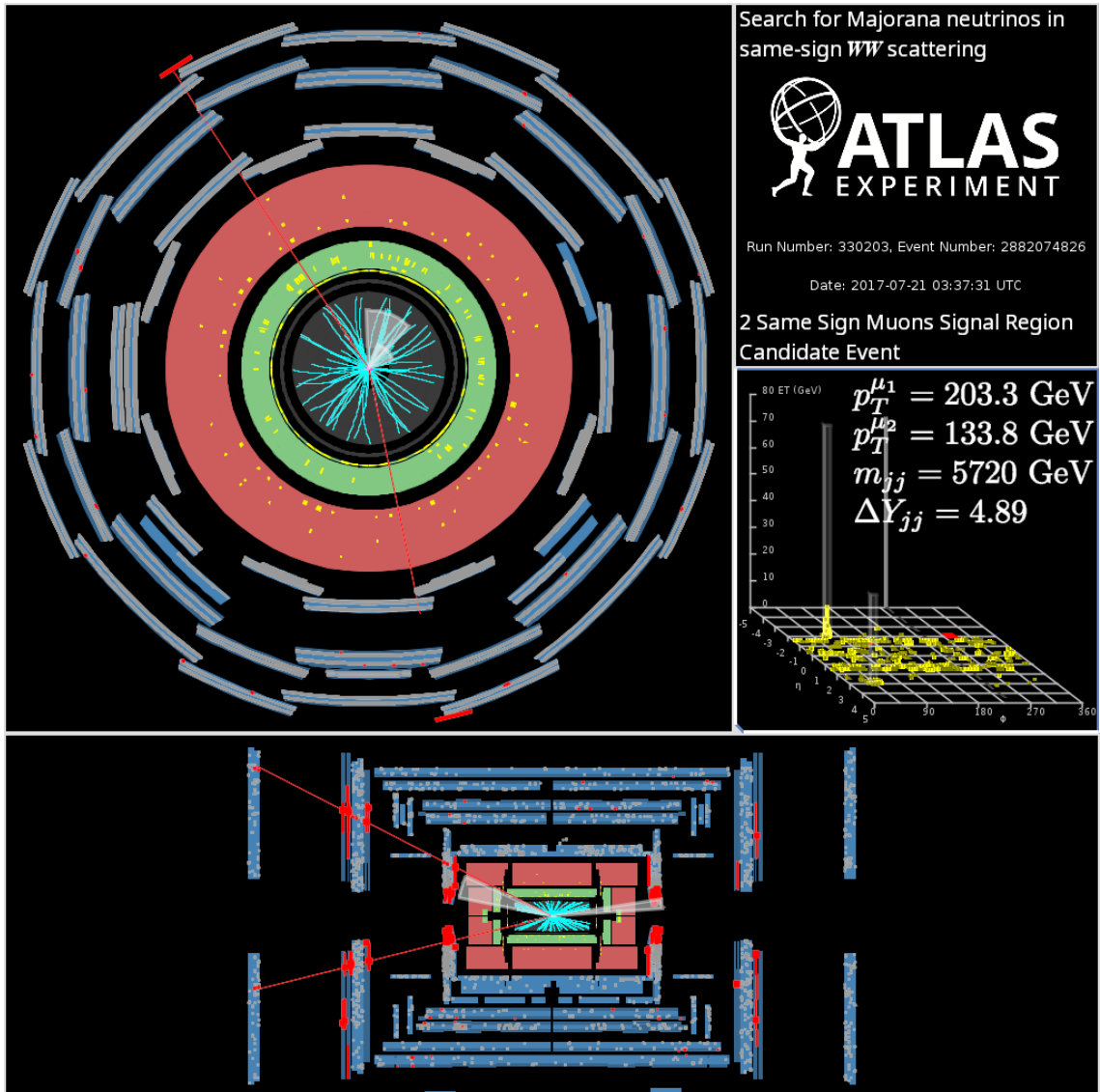


Figure 7.2: An event display of a candidate event in the final (high  $p_T$  and HNL signal-like) bin in the signal region. The missing  $E_T$  is 75 GeV with significance of 1.1. The muons are the long outgoing tracks and the jets are in grey [113].

A complete set of pulls of our systematic uncertainties is given in figure 7.6. This shows that the unblinded data has very little sensitivity to the nuisance parameters, as expected. There are also no large significant pulls in any direction. The only systematic under scrutiny is **FF\_FitModel** derived in section 6.2. This systematic, which was previously constrained, is slightly under-constrained after unblinding. This is very unlikely to have physical or experimental meaning. The  $\pm 1\sigma$  variations in the SR and CRs shown in figure 7.7 help explain the origin of the phenomenon.

What this unconstrained pull means is that, with the real data in the SR, we are less certain of the choice of fitting functions for the fake factor model. Inspecting bins 1 and 2 of the SR (figure 7.7a)<sup>1</sup>, it can be understood why this is happening. The number of events estimated to be from non-prompt muons is largest here, and the total underestimates in both bins<sup>2</sup>; hence, a variation which increases this estimate should be favoured. However, because the variation in bin 1 is opposite to that in bin 2 as function of the nuisance parameter  $\theta$  (red vs blue,  $\theta$  defined in equation (5.5)), this is not possible. This leads to the profiled likelihood being broader in  $\theta$  than with the Gaussian constraint alone. The effect is also small ( $1.2\sigma$  rather than 1). As the final limits presented are also statistically limited, it is safe to neglect<sup>3</sup>.

---

<sup>1</sup>and possibly a sub-leading addition from bin 5 of the SR and final bin the WZ CR.

<sup>2</sup>The ratio plots in figure 7.7 are deceptive in trying to rank relative importance.

<sup>3</sup>Although quite not the same, figure 5.21 can be helpful for visualising this.

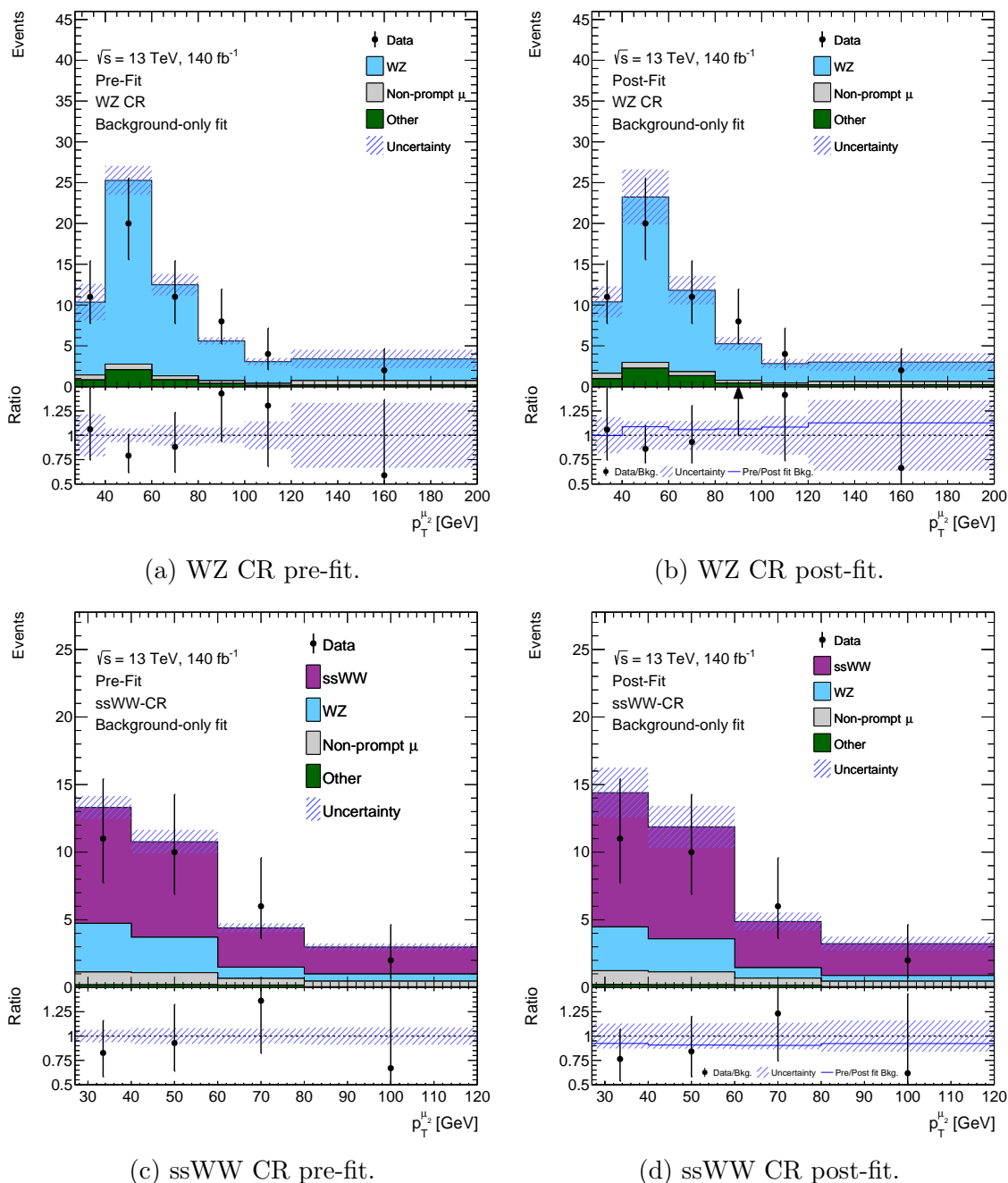


Figure 7.3: Pre- and post-fit Distributions in ssWW and WZ CR. Good data-simulation agreement is seen throughout. The  $\mu_{ssWW}$  shift with real SR data has had no sizeable effect

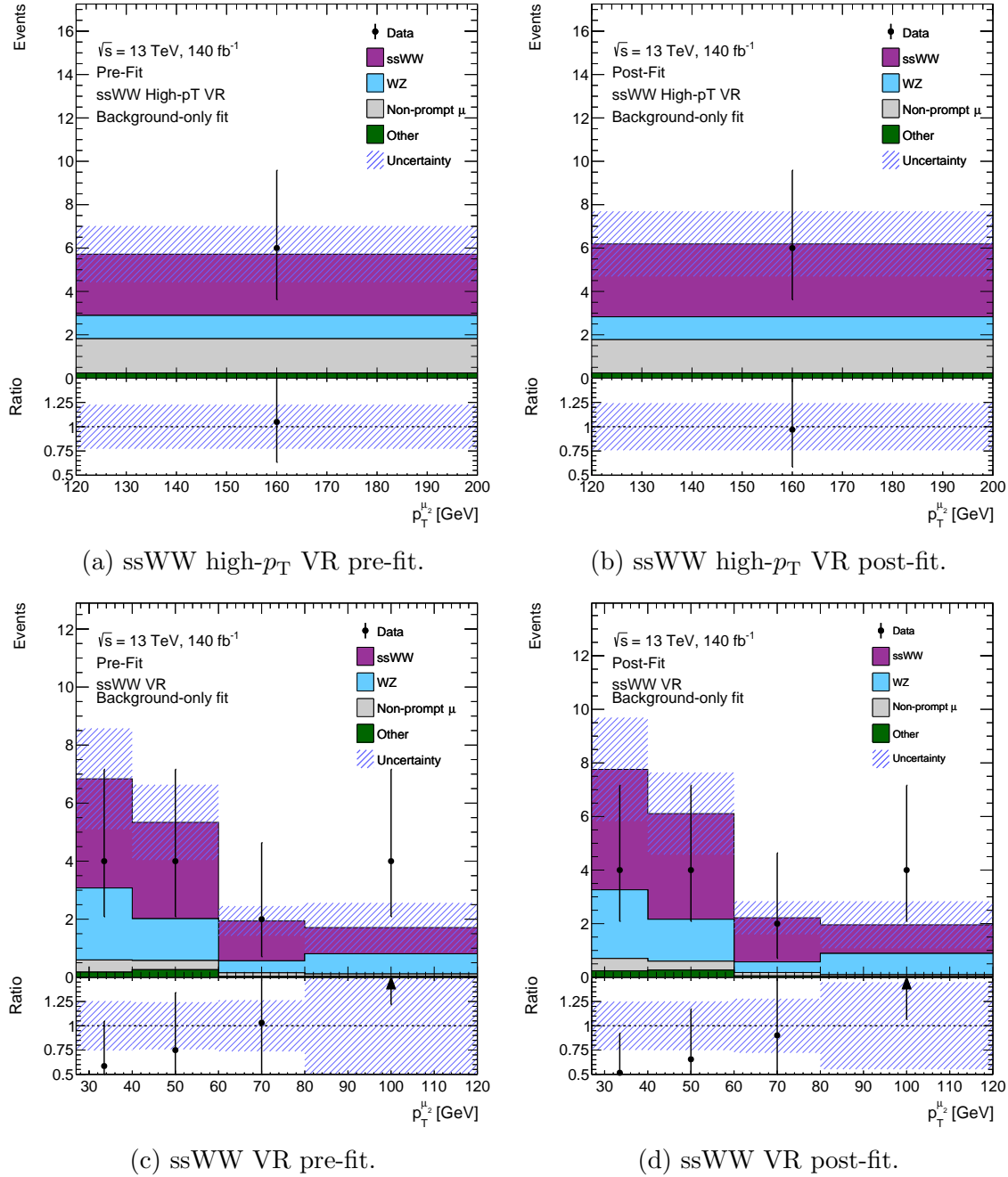


Figure 7.4: The validation regions for the analysis pre- and post- background fit. These are very low statistics and due to the background normalisations being near unity, the agreement does not noticeably change. Including these in the fit only improves the limit by a factor of 0.5%.

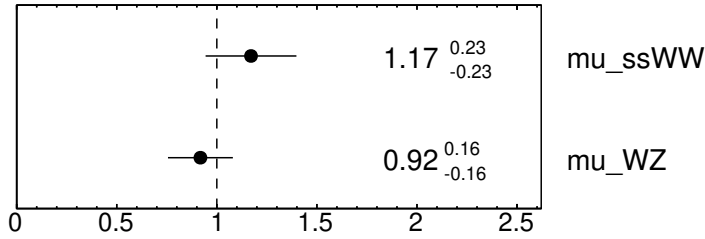


Figure 7.5: The normalisation factors derived ( $\hat{\mu}$ s) in the background-only fit to the unblinded data.

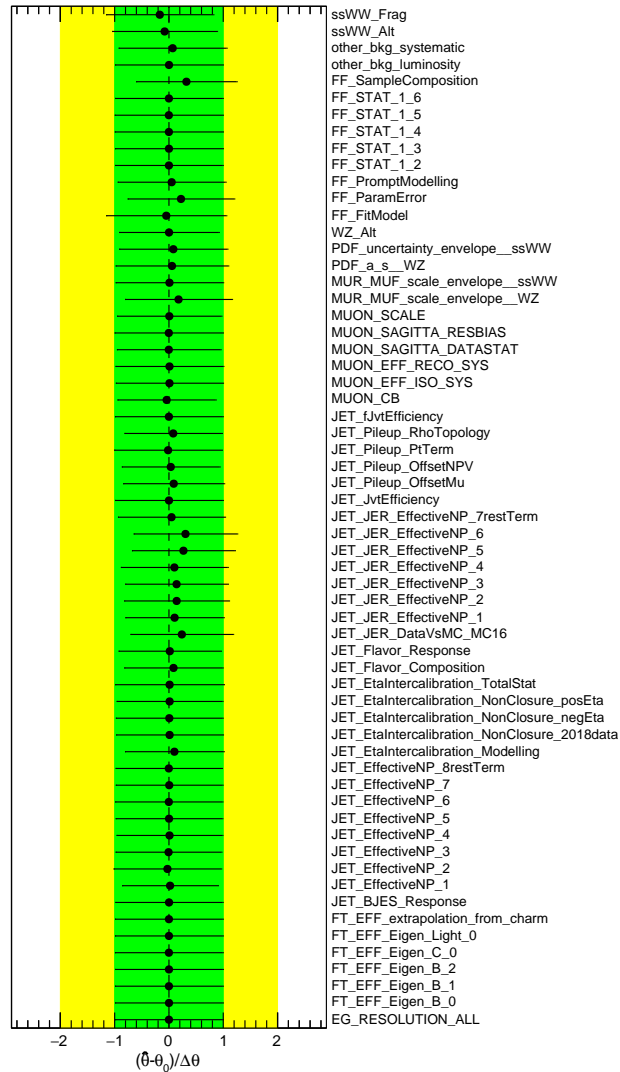
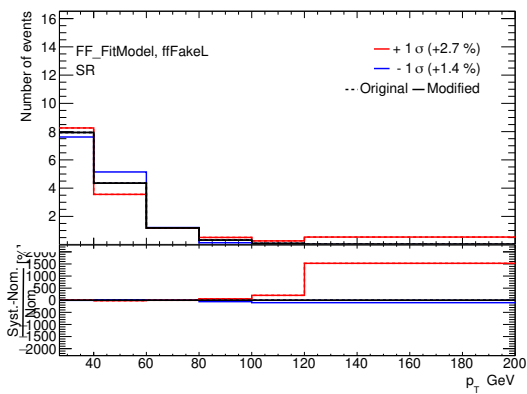
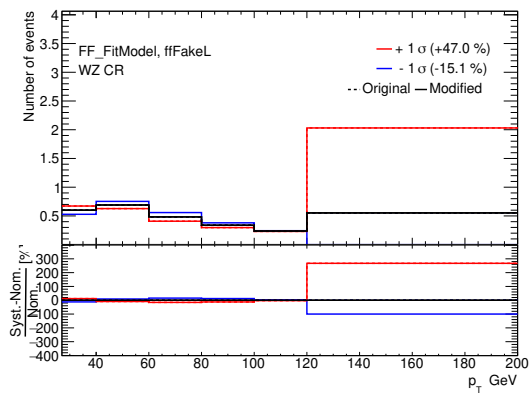


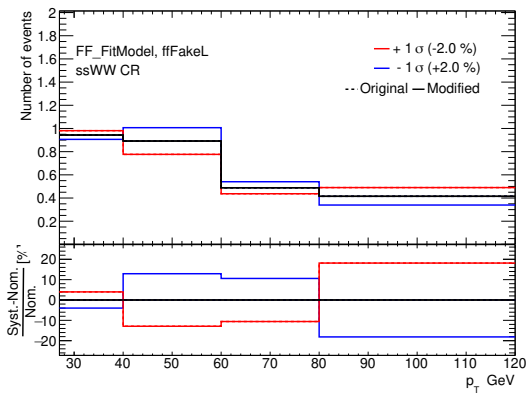
Figure 7.6: The pull plot of all unpruned nuisance parameters considered in the background-only fit.



(a) SR.



(b) WZ CR.



(c) ssWW CR.

Figure 7.7: The  $\pm 1\sigma$  variations in the SR and CRs of FF\_FitModel that lead to an under constraint. The flip in up-down variations in the first two bins in figure 7.7a alongside the underestimate in these bins post-fit is the main cause.

## 7.2 Hypothesis Testing and Confidence Limits

As seen in section 7.1, the fitted values of  $\mu$  are consistent with zero for all signal hypotheses. Hence, the standard particle physics methods are used to set limits. From here, the signal sample becomes the null hypothesis to reject. A limiting value of  $\mu_{\text{lim}}$  is found for each mass hypothesis.

To achieve this, a frequentist test statistic  $q_\mu$  is used. This attempts to discriminate the background and signal + background hypothesis ( $\mu' = 0$ ) for the given signal strength  $\mu$ . This maps any data sample onto  $q_\mu$ . By generating the expected distributions of  $f(q_\mu)$  for a range of  $\mu$ , a  $\mu$  can be found that gives a 5% chance of type-I error<sup>4</sup> of accepting the null hypothesis ( $\mu = \mu_{\text{lim}}$ ) on our injected data [114, 115]. This is called a 95%  $\text{CL}_{S+B}$  limit. This is done by integrating the probability density functions of the test statistic, varying  $\mu$  until a split consistent with our data is obtained.

$$p_q = \int_{q_\mu^{\text{obs}}}^{\infty} f(q_\mu | \mu') dq_\mu (= 0.05 \text{ for } \text{CL}_{S+B}) \quad (7.1)$$

It can be shown through the Neyman-Pearson lemma that the best  $q_\mu$  is the likelihood ratio, which, for computational and mathematical convenience, is written as the profiled log-likelihood ratio (equation (7.2)) [116]. Here  $\mu_{ssWW}$  and  $\mu_{WZ}$  are considered additional nuisance parameters under  $\theta$ .

$$q_\mu = \Lambda(\mu) = -2 \ln \frac{\mathcal{L}(\mu, \hat{\hat{\theta}}(\mu))}{\mathcal{L}(\hat{\mu}, \hat{\theta})}. \quad (7.2)$$

To then evaluate  $f(q_\mu)$  there are two paradigms:

1. Using Monte Carlo ‘toy’ versions of data given the Signal and Signal and Background hypotheses, calculating  $p_q$  as a function of  $\mu$  numerically, and hence, finding  $\mu_{\text{lim}}$ . This becomes very time-consuming if an analysis has a

---

<sup>4</sup>Rejecting a null hypothesis that is in actuality true.

complex signal sample or very high statistics.

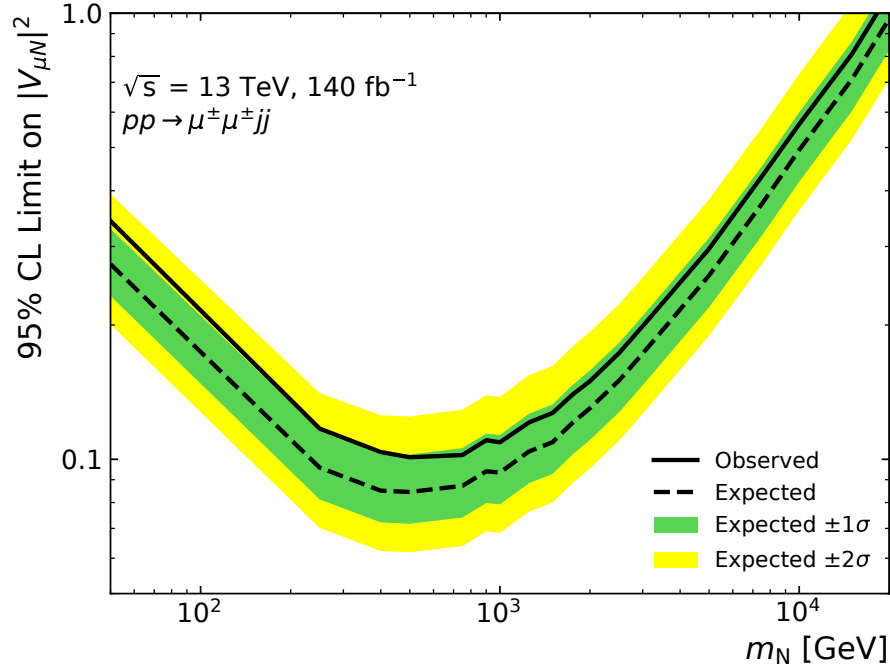
2. As the log-likelihood ratio can be proven to be approximately Gaussian [117], ‘Asymptotic formulae’ can be gained from the fitted  $\mu$  and covariance of the fit [118].

In this analysis, it turns out the procedure with toys is not too computationally expensive. Hence, it is verified the asymptotic formulae prescribed by the ATLAS statistics forum behave perfectly to estimate the final limits [118]. For the expected range of limits, the Asimov data is again used to help encapsulate statistical fluctuations in the data. We can use toys again or extend the asymptotic formulae to derive the  $1\sigma/2\sigma$  bands shown in green/yellow (respectively).

In particle physics, we also normalise our p values from  $CL_{S+B}$  to  $CL_S$  to compensate for spurious signal [119]. For example, in our  $CL_{S+B}$  construction, we could expect to reject the background-only hypothesis even with no signal sensitivity in the analysis. This can be visualised as the hypothesis probability distributions overlapping as  $\mu \rightarrow 0$ . Hence, we use equation (7.3) to define  $CL_S$ .

$$p'_q = \frac{\int_{q_\mu^{\text{obs}}}^{\infty} f(q_\mu | \mu') dq_\mu}{\int_{q_\mu^{\text{obs}}}^{\infty} f(q_\mu | \mu' = 0) dq_\mu} (= 0.05 \text{ for } 95\% CL_S) \quad (7.3)$$

This methodology is encapsulated within TRExFitter as a set of expected and observed limits for each of our mass point fits. The resulting confidence limits extracted from the fits given in appendix A.2 are shown in figure 7.8. To convert to a  $|V|^2$  limit, we simply use that our samples were generated with  $V = 1$  so the limits are given by  $|V| = \sqrt{\mu_{\text{lim}}}$ . A limit above one is not shown because this would break unitarity and hence is not meaningful. It can be that due to the excesses at high- $p_T$  and low- $p_T$ , there are weaker limits than expected but well within statistical fluctuations. The lower mass samples generate a higher number of lower  $p_T$  events,

Figure 7.8: The  $CL_S$  limits for the analysis

leading to slightly weaker limits at low  $m_N$ . The expected limits are between 15% and 20% better than the previously published CMS results [104].

Because the vast majority of our interesting sensitivity is in the final  $p_T$  bin which contains three events, the limits we quote here are extremely statistically limited. The difference between calculating the limits with and without systematic effects is beyond parts per thousand and they are practically invisible on the plots, so are not shown or quoted.

The Weinberg limit is purely a limit of a one-dimensional scale factor, which is based on a baseline sample of  $\frac{\Lambda}{C_5^{\mu\mu}} = 2$  TeV. Hence our  $CL_S$  95 % limit in  $|\frac{\Lambda}{C_5^{\mu\mu}}|$  is given by  $\frac{2}{\sqrt{\mu_{\text{lim}}}}$  TeV. Using this prescription on the data gives an observed (expected) 95% CL lower limit on the  $d = 5$  Weinberg operator  $|\Lambda/C_5^{\mu\mu}|$  at 3.635 ( $4.61_{-0.79}^{+0.82}$ ) TeV. This corresponds to an upper limit on the effective  $\mu\mu$  Majorana neutrino mass of  $m_{\mu\mu}$  16.7 (13.1) GeV.

## 7.3 Conclusions

Sadly, the search for new physics continues. However, for the first time ever HNLs have been excluded up to 20 TeV.<sup>5</sup> This is an achievement for the LHC and its detectors that we are able to exclude such particles up to such high masses at all.

---

<sup>5</sup>This is where the mixing angle limit begins to exceed unity. Any value larger than this would lead to oscillation probabilities greater than one. Hence the model would be non-physical.

---

### Conclusions

---

This thesis draws the author's varied contributions to the ATLAS experiment into a narrative. This takes a reader from fundamental instrumentation and physics principles and connects to a varied array of tasks. These sizeably contributed to the scientific development of the acquisition of ATLAS data and its interpretations for fundamental physics. These make up a small part of the rich tapestry of physics results at the LHC.

The technical trigger work that takes up the first half of the thesis tries to bridge the gap between a physics goal and how this must be implemented in digital electronics. This involves a significant quantity of detailed motivation to understand what and why work needs to take place. The need for a more sophisticated L1Calo system in ATLAS is described. Then, many critical tasks to the goals of the L1Calo group are outlined, from software infrastructure to physical installation. The fruits of the project's labour are then shown in early run 3 LHC data through efficiency turn-on

curves and reduced latency in the  $e/\gamma$  trigger menu items.

In the second half of this thesis, the vastness of an ATLAS physics analysis is broken down. Many optimised object definitions are briefly discussed, often in themselves are many theses, technical reports and performance papers published in the last decade or so. This instrumentation expertise is combined to search for an extension to the neutrino sector into energy scales, which was impossible before ATLAS and LHC run 2. This requires dedicated studies into previously unconsidered rare backgrounds in the data. No hints of new physics are found up to HNL masses up to 20 TeV.

This is not the end of HNL searches at the LHC. Searches of this style are mostly statistically limited in nature, so the HL-LHC will naturally provide better deductive power to exotic extensions to the Standard Model. At the time of writing, equivalent  $ee$  and  $e\mu$  mixing analysis work is ongoing, which will provide further model limits (or discovery) of HNLs in different lepton generations at high masses. The  $\tau$  mixing channels are also of particular interest to theorists as these are the least constrained experimentally.

Also, in the near future, long-lived particle detectors at the LHC such as MATHUSLA, FASER and ANUBIS could provide complimentary sensitivity of long lifetime HNLs alongside conventional detector searches [120, 121, 122]. Higher energy and luminosity electron/proton beams from the Future Circular Collider could provide intuitively larger sensitivity to HNL models [54].

This thesis, as a whole, gives an insight into the deep inner workings of a complex experimental collaboration at the forefront of probing fundamental physics. Without many of these academic efforts of individuals, our understanding of the Standard Model would stagnate.



---

## REFERENCES

---

- [1] D. Binosi, L. Theußl, Jaxodraw: A graphical user interface for drawing feynman diagrams, *Computer Physics Communications* 161 (1) (2004) 76–86. doi:<https://doi.org/10.1016/j.cpc.2004.05.001>.  
URL <https://www.sciencedirect.com/science/article/pii/S0010465504002115>
- [2] E. Rutherford, LXXIX. The scattering of  $\alpha$  and  $\beta$  particles by matter and the structure of the atom, *The London, Edinburgh, and Dublin Philosophical Magazine and Journal of Science* 21 (125) (1911) 669–688. arXiv:<https://doi.org/10.1080/14786440508637080>, doi:10.1080/14786440508637080.
- [3] L. Evans, P. Bryant, LHC Machine, *JINST* 3 (2008) S08001. doi:10.1088/1748-0221/3/08/S08001.
- [4] A. Seryi, *Unifying physics of accelerators, lasers and plasma*, CRC Press, 2015.
- [5] E. Mobs, *The CERN accelerator complex - 2019. Complexe des accélérateurs du CERN - 2019 General Photo* (Jul 2019).  
URL <https://cds.cern.ch/record/2684277>
- [6] R. J. Steinhagen, *Tune and chromaticity diagnostics* (2009). doi:10.5170/CERN-2009-005.317.  
URL <https://cds.cern.ch/record/1213281>
- [7] S. White, *Luminosity Scans at the LHC. Luminosity Scans at LHC* (2011).  
URL <https://cds.cern.ch/record/1357865>
- [8] O. Aberle, et al., *High-Luminosity Large Hadron Collider (HL-LHC): Technical design report*, CERN Yellow Reports: Monographs, CERN, Geneva, 2020.

- doi:10.23731/CYRM-2020-0010.  
URL <https://cds.cern.ch/record/2749422>
- [9] ATLAS Collaboration, The ATLAS Experiment at the CERN Large Hadron Collider, JINST 3 (2008) S08003. doi:10.1088/1748-0221/3/08/S08003.
- [10] CMS Collaboration, The CMS Experiment at the CERN LHC, JINST 3 (2008) S08004. doi:10.1088/1748-0221/3/08/S08004.
- [11] ATLAS Collaboration, A Particle Consistent with the Higgs Boson Observed with the ATLAS Detector at the Large Hadron Collider, Science 338 (2012) 1576. doi:10.1126/science.1232005.
- [12] CMS Collaboration, A New Boson with a Mass of 125 GeV Observed with the CMS Experiment at the Large Hadron Collider, Science 338 (2012) 1569–1575. doi:10.1126/science.1230816.
- [13] LHCb: letter of intent, Tech. Rep. CERN-LHCC-95-5. LHCC-I-8, CERN, Geneva (1995).  
URL <https://cds.cern.ch/record/290868>
- [14] ALICE collaboration, ALICE high-momentum particle identification: Technical Design Report (1998).  
URL <https://cds.cern.ch/record/381431>
- [15] J. Pequenaio, P. Schaffner, How ATLAS detects particles: diagram of particle paths in the detector (Jan 2013).  
URL <https://cds.cern.ch/record/1505342>
- [16] ATLAS inner detector: Technical Design Report, 1, Technical Design Report ATLAS, CERN, Geneva, 1997.  
URL <https://cds.cern.ch/record/331063>
- [17] M. Thomson, Modern particle physics, Cambridge University Press, 2013.
- [18] G. Barr, R. Devenish, R. Walczak, T. Weidberg, Particle physics in the LHC era, Oxford University Press, 2016.
- [19] Vertex Reconstruction Performance of the ATLAS Detector at  $\sqrt{s} = 13$  TeV, Tech. rep., CERN, Geneva, all figures including auxiliary figures are available at <https://atlas.web.cern.ch/Atlas/GROUPS/PHYSICS/PUBNOTES/ATL-PHYS-PUB-2015-026> (2015).  
URL <https://cds.cern.ch/record/2037717>
- [20] ATLAS Collaboration, ATLAS flavour-tagging algorithms for the LHC Run 2  $pp$  collision dataset, Eur. Phys. J. C 83 (2023) 681. arXiv:2211.16345, doi:10.1140/epjc/s10052-023-11699-1.

- [21] A. Vogel, ATLAS Transition Radiation Tracker (TRT): Straw Tube Gaseous Detectors at High Rates, Tech. Rep. ATL-INDET-PROC-2013-005, CERN, Geneva (Apr 2013).  
URL <https://cds.cern.ch/record/1537991>
- [22] R. Wigmans, New developments in calorimetric particle detection, Progress in Particle and Nuclear Physics 103 (2018) 109–161. doi:10.1016/j.pnpnp.2018.07.003.  
URL <https://www.sciencedirect.com/science/article/pii/S014664101830070X>
- [23] ATLAS Collaboration, ATLAS Liquid Argon Calorimeter Phase-I Upgrade Technical Design Report, Tech. Rep. CERN-LHCC-2013-017. ATLAS-TDR-022, final version presented to December 2013 LHCC. (Sep 2013).  
URL <https://cds.cern.ch/record/1602230>
- [24] ATLAS collaboration, ATLAS muon spectrometer: Technical Design Report, Technical design report. ATLAS, CERN, Geneva, 1997.  
URL <https://cds.cern.ch/record/331068>
- [25] J. Pequeno, Computer generated image of the ATLAS Muons subsystem (2008).  
URL <https://cds.cern.ch/record/1095929>
- [26] ATLAS Collaboration, Muon reconstruction and identification efficiency in ATLAS using the full Run 2  $pp$  collision data set at  $\sqrt{s} = 13$  TeV, Eur. Phys. J. C 81 (2021) 578. arXiv:2012.00578, doi:10.1140/epjc/s10052-021-09233-2.
- [27] J. Illingworth, J. Kittler, A survey of the hough transform, Computer Vision, Graphics, and Image Processing 44 (1) (1988) 87–116. doi:[https://doi.org/10.1016/S0734-189X\(88\)80033-1](https://doi.org/10.1016/S0734-189X(88)80033-1).  
URL <https://www.sciencedirect.com/science/article/pii/S0734189X88800331>
- [28] ATLAS Collaboration, New techniques for jet calibration with the ATLAS detector, Eur. Phys. J. C 83 (2023) 761. arXiv:2303.17312, doi:10.1140/epjc/s10052-023-11837-9.
- [29] O. Villalobos-Baillie, MPAGS Lectures in Trigger for Particle Physics (2021).  
URL <https://warwick.ac.uk/fac/sci/physics/mpags/modules/particle/trigger>
- [30] ATLAS Collaboration, Technical Design Report for the Phase-I Upgrade of the ATLAS TDAQ System, Tech. Rep. CERN-LHCC-2013-018. ATLAS-TDR-023, final version presented to December 2013 LHCC. (Sep 2013).  
URL <https://cds.cern.ch/record/1602235>
- [31] I. Brawn, Private Communication (May 14 2020).

- 
- [32] ATLAS level-1 trigger: Technical Design Report, Technical design report. ATLAS, CERN, Geneva, 1998.  
URL <http://cds.cern.ch/record/381429>
- [33] Technical Design Report for the Phase-II Upgrade of the ATLAS TDAQ System, Tech. Rep. CERN-LHCC-2017-020. ATLAS-TDR-029, CERN, Geneva (Sep 2017).  
URL <https://cds.cern.ch/record/2285584>
- [34] G. A. Bird. et al, Commissioning of L1Calo Phase I Upgrade at ATLAS: development and testing of eFEX and FTM modules, Tech. Rep. ATL-COM-DAQ-2020-036, CERN, Geneva, 26th May 2020 (May 2020).  
URL <https://cds.cern.ch/record/2718106>
- [35] U. Blumenschein, J. Montejo Berlingen, B. Kortman, B. Carlson, M. Marinescu, O. Lavoryk, T. Hrynova, Expected performance of the ATLAS Level-1 calorimeter trigger in Run 3, Tech. rep., CERN, Geneva, public plots to be shown at LHCP 2022 (2022).  
URL <https://cds.cern.ch/record/2807728>
- [36] Y. Enari, The Phase-1 Trigger Readout Electronics Upgrade of the ATLAS Liquid Argon Calorimeter, Journal of Physics: Conference Series 1162 (2019) 012041. doi:10.1088/1742-6596/1162/1/012041.
- [37] A. Elliot, A. Watson, A. Costa, et al., private L1Calo communications (May 2021).
- [38] IEEE Standard for VHDL Language Reference Manual, IEEE Std 1076-2019 (2019).
- [39] ATLAS Collaboration, eFEX EDMS (2023).  
URL <https://edms.cern.ch/document/1419789/1>
- [40] N. A. Gorasia, private communication (April 2, 2019).
- [41] Gelmo96 (Wikimedia), DHCP session image, [https://commons.wikimedia.org/wiki/File:DHCP\\_session.svg](https://commons.wikimedia.org/wiki/File:DHCP_session.svg).  
URL [https://commons.wikimedia.org/wiki/File:DHCP\\_session.svg](https://commons.wikimedia.org/wiki/File:DHCP_session.svg)
- [42] T. S. Williams, IPbus A flexible Ethernet-based control system for xTCA hardware, Tech. Rep. CMS-CR-2014-334, CERN, Geneva (Oct 2014).  
URL <https://cds.cern.ch/record/2020872>
- [43] R. Braden, D. Borman, C. Partridge, Computing the Internet checksum, RFC 1071 (Sep. 1988). doi:10.17487/RFC1071.  
URL <https://www.rfc-editor.org/info/rfc1071>
- [44] R. Droms, Dynamic Host Configuration Protocol, RFC 1541 (Oct. 1993). doi:10.17487/RFC1541.  
URL <https://www.rfc-editor.org/info/rfc1541>

- [45] ATLAS Collaboration, ATLAS Level-1 calorimeter trigger performance in early 2023 data taking (2023).  
URL <https://twiki.cern.ch/twiki/bin/view/AtlasPublic/L1CaloTriggerPublicResults>
- [46] M. Drewes, The Phenomenology of Right Handed Neutrinos, *Int. J. Mod. Phys. E* 22 (2013) 1330019. [arXiv:1303.6912](https://arxiv.org/abs/1303.6912), [doi:10.1142/S0218301313300191](https://doi.org/10.1142/S0218301313300191).
- [47] Wikimedia Commons, File:standard model of elementary particles.svg — wikimedia commons, the free media repository, [Online; accessed 9-September-2020] (2020).  
URL [https://commons.wikimedia.org/w/index.php?title=File:Standard\\_Model\\_of\\_Elementary\\_Particles.svg&oldid=430960007](https://commons.wikimedia.org/w/index.php?title=File:Standard_Model_of_Elementary_Particles.svg&oldid=430960007)
- [48] T. Yanagida, Horizontal Symmetry and Masses of Neutrinos, *Progress of Theoretical Physics* 64 (3) (1980) 1103–1105. [arXiv:https://academic.oup.com/ptp/article-pdf/64/3/1103/5394376/64-3-1103.pdf](https://arxiv.org/abs/https://academic.oup.com/ptp/article-pdf/64/3/1103/5394376/64-3-1103.pdf), [doi:10.1143/PTP.64.1103](https://doi.org/10.1143/PTP.64.1103).  
URL <https://doi.org/10.1143/PTP.64.1103>
- [49] E. Majorana, Teoria simmetrica dell'elettrone e del positrone, *Nuovo Cim.* 14 (1937) 171–184. [doi:10.1007/BF02961314](https://doi.org/10.1007/BF02961314).
- [50] J.-L. Tastet, I. Timiryasov, Dirac vs. Majorana HNLs (and their oscillations) at SHiP, *JHEP* 04 (2020) 005. [arXiv:1912.05520](https://arxiv.org/abs/1912.05520), [doi:10.1007/JHEP04\(2020\)005](https://doi.org/10.1007/JHEP04(2020)005).
- [51] J.-L. Tastet, Searching for Heavy Neutral Leptons at CERN, Ph.D. thesis, Københavns Universitet, Faculty of Science, Niels Bohr Institute, Københavns Universitet, Faculty of Science, SCIENCE Faculty Office, Bohr Inst. (2021).
- [52] B. Fuks, J. Neundorf, K. Peters, R. Ruiz, M. Saimpert, Probing the Weinberg operator at colliders, *Physical Review D* 103 (11) (jun 2021). [doi:10.1103/PhysRevD.103.115014](https://doi.org/10.1103/PhysRevD.103.115014).  
URL <https://doi.org/10.1103/PhysRevD.103.115014>
- [53] B. Fuks, J. Neundorf, K. Peters, R. Ruiz, M. Saimpert, Majorana neutrinos in same-sign  $W^\pm W^\pm$  scattering at the lhc: Breaking the tev barrier, *Phys. Rev. D* 103 (2021) 055005. [doi:10.1103/PhysRevD.103.055005](https://doi.org/10.1103/PhysRevD.103.055005).  
URL <https://link.aps.org/doi/10.1103/PhysRevD.103.055005>
- [54] F. F. Deppisch, P. S. B. Dev, A. Pilaftsis, Neutrinos and collider physics, *New Journal of Physics* 17 (7) (2015) 075019. [doi:10.1088/1367-2630/17/7/075019](https://doi.org/10.1088/1367-2630/17/7/075019).  
URL <https://dx.doi.org/10.1088/1367-2630/17/7/075019>
- [55] ATLAS Collaboration, Search for Heavy Neutral Leptons in Decays of  $W$  Bosons Using a Dilepton Displaced Vertex in  $\sqrt{s} = 13$  TeV  $pp$  Collisions with the ATLAS Detector, *Phys. Rev. Lett.* 131 (2023) 061803. [arXiv:2204.11988](https://arxiv.org/abs/2204.11988), [doi:10.1103/PhysRevLett.131.061803](https://doi.org/10.1103/PhysRevLett.131.061803).

- 
- [56] T. Asaka, M. Shaposhnikov, The  $\nu$ MSM, dark matter and baryon asymmetry of the universe, *Physics Letters B* 620 (1) (2005) 17–26. doi:<https://doi.org/10.1016/j.physletb.2005.06.020>.  
URL <https://www.sciencedirect.com/science/article/pii/S0370269305008087>
- [57] P. Higgs, Broken symmetries, massless particles and gauge fields, *Physics letters* 12 (2) (1964) 132–133. doi:[10.1016/0031-9163\(64\)91136-9](https://doi.org/10.1016/0031-9163(64)91136-9).
- [58] A. Pich, Effective field theory (1998). arXiv:[hep-ph/9806303](https://arxiv.org/abs/hep-ph/9806303).
- [59] S. Weinberg, Baryon- and lepton-nonconserving processes, *Phys. Rev. Lett.* 43 (1979) 1566–1570. doi:[10.1103/PhysRevLett.43.1566](https://doi.org/10.1103/PhysRevLett.43.1566).  
URL <https://link.aps.org/doi/10.1103/PhysRevLett.43.1566>
- [60] ATLAS Collaboration, Search for heavy neutral leptons in decays of  $W$  bosons produced in 13 TeV  $pp$  collisions using prompt and displaced signatures with the ATLAS detector, *JHEP* 10 (2019) 265. arXiv:[1905.09787](https://arxiv.org/abs/1905.09787), doi:[10.1007/JHEP10\(2019\)265](https://doi.org/10.1007/JHEP10(2019)265).
- [61] J.-L. Tastet, O. Ruchayskiy, I. Timiryasov, Reinterpreting the ATLAS bounds on heavy neutral leptons in a realistic neutrino oscillation model, *JHEP* 2021 (12) (dec 2021). doi:[10.1007/jhep12\(2021\)182](https://doi.org/10.1007/jhep12(2021)182).  
URL <https://doi.org/10.1007%2Fjhep12%282021%29182>
- [62] A. Aste, A Direct Road to Majorana Fields, *Symmetry* 2 (4) (2010) 1776–1809. doi:[10.3390/sym2041776](https://doi.org/10.3390/sym2041776).  
URL <http://dx.doi.org/10.3390/sym2041776>
- [63] P. D. Bolton, F. F. Deppisch, P. B. Dev, Neutrinoless double beta decay versus other probes of heavy sterile neutrinos, arXiv preprint arXiv:[1912.03058](https://arxiv.org/abs/1912.03058) (2020). doi:[10.1007/JHEP03\(2020\)17](https://doi.org/10.1007/JHEP03(2020)17).
- [64] ATLAS Collaboration, Measurement and interpretation of same-sign  $W$  boson pair production in association with two jets in  $pp$  collisions at  $\sqrt{s} = 13$  TeV with the ATLAS detector (2023). arXiv:[2312.00420](https://arxiv.org/abs/2312.00420), doi:[10.48550/arXiv.2312.00420](https://doi.org/10.48550/arXiv.2312.00420).
- [65] CMS Collaboration, Measurements of production cross sections of  $WZ$  and same-sign  $WW$  boson pairs in association with two jets in proton–proton collisions at  $\sqrt{s} = 13$  TeV, *Phys. Lett. B* 809 (2020) 135710. arXiv:[2005.01173](https://arxiv.org/abs/2005.01173), doi:[10.1016/j.physletb.2020.135710](https://doi.org/10.1016/j.physletb.2020.135710).
- [66] P. Pigard, Electron studies and search for vector boson scattering in events with four leptons and two jets with the CMS detector at the LHC. , presented 2017 (2017).  
URL <https://cds.cern.ch/record/2290139>

- [67] ATLAS Collaboration, Electron and photon performance measurements with the ATLAS detector using the 2015–2017 LHC proton-proton collision data, JINST 14 (12) (2019) P12006. [arXiv:1908.00005](https://arxiv.org/abs/1908.00005), [doi:10.1088/1748-0221/14/12/P12006](https://doi.org/10.1088/1748-0221/14/12/P12006).
- [68] M. Queitsch-Maitland et al., VBS Heavy Majorana Neutrino Search - INT note of EXOT-2020-06, Tech. rep., CERN, Geneva (2020).  
URL <https://cds.cern.ch/record/2715929>
- [69] G. Aad, et al., Muon reconstruction and identification efficiency in ATLAS using the full Run 2  $pp$  collision data set at  $\sqrt{s} = 13$  TeV, Eur. Phys. J. C 81 (7) (2021) 578. [arXiv:2012.00578](https://arxiv.org/abs/2012.00578), [doi:10.1140/epjc/s10052-021-09233-2](https://doi.org/10.1140/epjc/s10052-021-09233-2).
- [70] M. Cacciari, G. P. Salam, G. Soyez, The anti- $k_t$  jet clustering algorithm, JHEP 2008 (04) (2008) 063–063. [doi:10.1088/1126-6708/2008/04/063](https://doi.org/10.1088/1126-6708/2008/04/063).  
URL <https://doi.org/10.1088/1126-6708/2008/04/063>
- [71] ATLAS Collaboration, Properties of Jets and Inputs to Jet Reconstruction and Calibration with the ATLAS Detector Using Proton-Proton Collisions at  $\sqrt{s} = 13$  TeV, Tech. rep., CERN, Geneva, all figures including auxiliary figures are available at <https://atlas.web.cern.ch/Atlas/GROUPS/PHYSICS/PUBNOTES/ATL-PHYS-PUB-2015-036> (2015).  
URL <http://cds.cern.ch/record/2044564>
- [72] ATLAS Collaboration, Jet reconstruction and performance using particle flow with the ATLAS Detector, Eur. Phys. J. C 77 (2017) 466. [arXiv:1703.10485](https://arxiv.org/abs/1703.10485), [doi:10.1140/epjc/s10052-017-5031-2](https://doi.org/10.1140/epjc/s10052-017-5031-2).
- [73] ATLAS Collaboration, Performance of pile-up mitigation techniques for jets in  $pp$  collisions at  $\sqrt{s} = 8$  TeV using the ATLAS detector, Eur. Phys. J. C 76 (2016) 581. [arXiv:1510.03823](https://arxiv.org/abs/1510.03823), [doi:10.1140/epjc/s10052-016-4395-z](https://doi.org/10.1140/epjc/s10052-016-4395-z).
- [74] ATLAS Collaboration, Forward jet vertex tagging using the particle flow algorithm, ATL-PHYS-PUB-2019-026 (2019).  
URL <https://cds.cern.ch/record/2683100>
- [75] ATLAS Collaboration,  $E_T^{\text{miss}}$  performance in the ATLAS detector using 2015-2016 LHC p-p collisions, Tech. rep., CERN, Geneva, all figures including auxiliary figures are available at <https://atlas.web.cern.ch/Atlas/GROUPS/PHYSICS/CONFNOTES/ATLAS-CONF-2018-023> (2018).  
URL <https://cds.cern.ch/record/2625233>
- [76] ATLAS Collaboration, Object-based missing transverse momentum significance in the ATLAS detector, Tech. rep., CERN, Geneva, all figures including auxiliary figures are available at <https://atlas.web.cern.ch/Atlas/GROUPS/PHYSICS/CONFNOTES/ATLAS-CONF-2018-038> (2018).  
URL <http://cds.cern.ch/record/2630948>

- 
- [77] ATLAS collaboration, ATLAS flavour-tagging algorithms for the LHC Run 2  $pp$  collision dataset, Tech. rep., CERN, Geneva (2022). [arXiv:2211.16345](https://arxiv.org/abs/2211.16345).  
URL <https://cds.cern.ch/record/2842028>
- [78] ATLAS Collaboration, Measurement of  $b$ -tagging efficiency of  $c$ -jets in  $t\bar{t}$  events using a likelihood approach with the ATLAS detector, ATLAS-CONF-2018-001 (2018).  
URL <https://cds.cern.ch/record/2306649>
- [79] ATLAS Collaboration, Calibration of light-flavour  $b$ -jet mistagging rates using ATLAS proton–proton collision data at  $\sqrt{s} = 13$  TeV, ATLAS-CONF-2018-006 (2018).  
URL <https://cds.cern.ch/record/2314418>
- [80] ATLAS Collaboration, Flavor Tagging with Track Jets in Boosted Topologies with the ATLAS Detector, Tech. rep., CERN, Geneva, all figures including auxiliary figures are available at <https://atlas.web.cern.ch/Atlas/GROUPS/PHYSICS/PUBNOTES/ATL-PHYS-PUB-2014-013> (2014).  
URL <https://cds.cern.ch/record/1750681>
- [81] ATLAS Collaboration, Fast simulation of the ATLAS calorimeter system with Generative Adversarial Networks, ATL-SOFT-PUB-2020-006 (2020).  
URL <https://cds.cern.ch/record/2746032>
- [82] S. Agostinelli, et al., Geant4 - a simulation toolkit, Nuclear Instruments and Methods in Physics Research Section A: Accelerators, Spectrometers, Detectors and Associated Equipment 506 (3) (2003) 250–303. doi:10.1016/S0168-9002(03)01368-8.
- [83] J. Catmore et al. on behalf of the ATLAS experiment, A new petabyte-scale data derivation framework for ATLAS, Journal of Physics: Conference Series 664 (7) (2015) 072007. doi:10.1088/1742-6596/664/7/072007.  
URL <https://dx.doi.org/10.1088/1742-6596/664/7/072007>
- [84] ATLAS Collaboration, Luminosity determination in  $pp$  collisions at  $\sqrt{s} = 13$  TeV using the ATLAS detector at the LHC, Eur. Phys. J. C 83 (2023) 982. [arXiv:2212.09379](https://arxiv.org/abs/2212.09379), doi:10.1140/epjc/s10052-023-11747-w.
- [85] ATLAS Collaboration, Observation of Electroweak Production of a Same-Sign W Boson Pair in Association with Two Jets in  $pp$  Collisions at  $\sqrt{s} = 13$  TeV with the ATLAS Detector, Phys. Rev. Lett. 123 (2019) 161801. [arXiv:1906.03203](https://arxiv.org/abs/1906.03203), doi:10.1103/PhysRevLett.123.161801.
- [86] D. J. Gross, F. Wilczek, Ultraviolet behavior of non-abelian gauge theories, Phys. Rev. Lett. 30 (1973) 1343–1346. doi:10.1103/PhysRevLett.30.1343.  
URL <https://link.aps.org/doi/10.1103/PhysRevLett.30.1343>
- [87] R. D. Ball, et al., Parton distributions for the LHC run II, JHEP 04 (2015) 040. [arXiv:1410.8849](https://arxiv.org/abs/1410.8849), doi:10.1007/JHEP04(2015)040.

- [88] T. Sjöstrand, et al., An introduction to PYTHIA 8.2, *Comput. Phys. Commun.* 191 (2015) 159. [arXiv:1410.3012](https://arxiv.org/abs/1410.3012), [doi:10.1016/j.cpc.2015.01.024](https://doi.org/10.1016/j.cpc.2015.01.024).
- [89] D. J. Lange, The EvtGen particle decay simulation package, *Nucl. Instrum. Meth. A* 462 (2001) 152. [doi:10.1016/S0168-9002\(01\)00089-4](https://doi.org/10.1016/S0168-9002(01)00089-4).
- [90] Alwall, J. et al, The automated computation of tree-level and next-to-leading order differential cross sections, and their matching to parton shower simulations, *JHEP* 07 (2014) 079. [arXiv:1405.0301](https://arxiv.org/abs/1405.0301), [doi:10.1007/JHEP07\(2014\)079](https://doi.org/10.1007/JHEP07(2014)079).
- [91] ATLAS Collaboration, ATLAS Pythia 8 tunes to 7 TeV data, ATL-PHYS-PUB-2014-021 (2014).  
URL <https://cds.cern.ch/record/1966419>
- [92] E. Bothmann, et al., Event generation with Sherpa 2.2, *SciPost Phys.* 7 (3) (2019) 034. [arXiv:1905.09127](https://arxiv.org/abs/1905.09127), [doi:10.21468/SciPostPhys.7.3.034](https://doi.org/10.21468/SciPostPhys.7.3.034).
- [93] R. Frederix, E. Re, P. Torrielli, Single-top  $t$ -channel hadroproduction in the four-flavour scheme with POWHEG and aMC@NLO, *JHEP* 09 (2012) 130. [arXiv:1207.5391](https://arxiv.org/abs/1207.5391), [doi:10.1007/JHEP09\(2012\)130](https://doi.org/10.1007/JHEP09(2012)130).
- [94] P. Nason, A new method for combining NLO QCD with shower Monte Carlo algorithms, *JHEP* 11 (2004) 040. [arXiv:hep-ph/0409146](https://arxiv.org/abs/hep-ph/0409146), [doi:10.1088/1126-6708/2004/11/040](https://doi.org/10.1088/1126-6708/2004/11/040).
- [95] S. Frixione, P. Nason, C. Oleari, Matching NLO QCD computations with parton shower simulations: the POWHEG method, *JHEP* 11 (2007) 070. [arXiv:0709.2092](https://arxiv.org/abs/0709.2092), [doi:10.1088/1126-6708/2007/11/070](https://doi.org/10.1088/1126-6708/2007/11/070).
- [96] S. Alioli, P. Nason, C. Oleari, E. Re, A general framework for implementing NLO calculations in shower Monte Carlo programs: the POWHEG BOX, *JHEP* 06 (2010) 043. [arXiv:1002.2581](https://arxiv.org/abs/1002.2581), [doi:10.1007/JHEP06\(2010\)043](https://doi.org/10.1007/JHEP06(2010)043).
- [97] ATLAS Collaboration, Search for Majorana neutrinos in same-sign  $WW$  scattering events from  $pp$  collisions at  $\sqrt{s} = 13$  TeV, *Eur. Phys. J. C* 83 (9) (2023) 824, all figures including auxiliary figures are available at <https://atlas.web.cern.ch/Atlas/GROUPS/PHYSICS/PAPERS/EXOT-2020-06/>. [arXiv:2305.14931](https://arxiv.org/abs/2305.14931), [doi:10.1140/epjc/s10052-023-11915-y](https://doi.org/10.1140/epjc/s10052-023-11915-y).  
URL <https://cds.cern.ch/record/2859645>
- [98] Formulae for Estimating Significance, Tech. rep., CERN, Geneva, all figures including auxiliary figures are available at <https://atlas.web.cern.ch/Atlas/GROUPS/PHYSICS/PUBNOTES/ATL-PHYS-PUB-2020-025> (Sep 2020).  
URL <https://cds.cern.ch/record/2736148>
- [99] K. Cranmer, G. Lewis, L. Moneta, A. Shibata, W. Verkerke, HistFactory: A tool for creating statistical models for use with RooFit and RooStats, Tech. rep., New York U., New York (2012).  
URL <http://cds.cern.ch/record/1456844>

- 
- [100] T. Adye, W. Buttinger, Hands-on statistics (June 2021).  
URL <https://indico.stfc.ac.uk/event/299/contributions/1841/attachments/611/1060/adye-stats.pdf>
- [101] K. Cranmer, G. Lewis, L. Moneta, A. Shibata, W. Verkerke, HistFactory: A tool for creating statistical models for use with RooFit and RooStats, Tech. rep., New York U., New York (2012).  
URL <http://cds.cern.ch/record/1456844>
- [102] L. Moneta, et al., The RooStats Project, PoS ACAT2010 (2010) 057. arXiv:1009.1003, doi:10.22323/1.093.0057.
- [103] CERN ATLAS internal gitlab: CommonSystSmoothingTool.  
URL [https://gitlab.cern.ch/atlas-phys/exot/CommonSystSmoothingTool/-/blob/master/doc/algorithm\\_description.md](https://gitlab.cern.ch/atlas-phys/exot/CommonSystSmoothingTool/-/blob/master/doc/algorithm_description.md)
- [104] CMS Collaboration, Probing heavy Majorana neutrinos and the Weinberg operator through vector boson fusion in proton–proton collisions at  $\sqrt{s} = 13$  TeV (2022). arXiv:2206.08956.
- [105] NA62 Collaboration, Search for heavy neutral lepton production in  $k^+$  decays to positrons, Physics Letters B 807 (2020) 135599. doi:<https://doi.org/10.1016/j.physletb.2020.135599>.  
URL <https://www.sciencedirect.com/science/article/pii/S0370269320304032>
- [106] CHARM Collaboration, A search for decays of heavy neutrinos, Physics Letters B 128 (5) (1983) 361–366. doi:[https://doi.org/10.1016/0370-2693\(83\)90275-7](https://doi.org/10.1016/0370-2693(83)90275-7).  
URL <https://www.sciencedirect.com/science/article/pii/S0370269383902757>
- [107] CHARM Collaboration, A search for decays of heavy neutrinos in the mass range 0.5–2.8 GeV, Physics Letters B 166 (4) (1986) 473–478. doi:[https://doi.org/10.1016/0370-2693\(86\)91601-1](https://doi.org/10.1016/0370-2693(86)91601-1).  
URL <https://www.sciencedirect.com/science/article/pii/S0370269386916011>
- [108] Search for long-lived heavy neutral leptons with displaced vertices in proton–proton collisions at  $\sqrt{s} = 13$  TeV, JHEP 2207 (2022) 081. arXiv:2201.05578, doi:10.1007/JHEP07(2022)081.  
URL <https://cds.cern.ch/record/2799658>
- [109] CMS Collaboration, Search for Heavy Neutral Leptons in Events with Three Charged Leptons in Proton–Proton Collisions at  $\sqrt{s} = 13$  TeV, Phys. Rev. Lett. 120 (2018) 221801. arXiv:1802.02965, doi:10.1103/PhysRevLett.120.221801.

- [110] C. Bittrich, et al., Support note for measurement of electroweak  $W^\pm W^\pm jj$  production at  $\sqrt{s} = 13$  TeV, Tech. rep., CERN, Geneva (2018).  
URL <https://cds.cern.ch/record/2309552>
- [111] ATLAS Collaboration, Search for the Associated Production of a Higgs Boson and a Top Quark Pair in multilepton final states in  $80 \text{ fb}^{-1}$   $pp$  Collisions at  $\sqrt{s} = 13$  TeV with the ATLAS Detector, Tech. rep., CERN, Geneva (2018).  
URL <https://cds.cern.ch/record/2314122>
- [112] CMS Collaboration, Evidence for  $WW$  production from double-parton interactions in proton–proton collisions at  $\sqrt{s} = 13$  TeV, Eur. Phys. J. C 80 (2020) 41. arXiv:1909.06265, doi:10.1140/epjc/s10052-019-7541-6.
- [113] N. Konstantinidis, et al., The Atlantis event visualisation program for the ATLAS experiment (2005). doi:10.5170/CERN-2005-002.361.  
URL <http://cds.cern.ch/record/865603>
- [114] G. Cowan, Statistical data analysis, Oxford science publications, Clarendon Press, Oxford, 1998.
- [115] W. Buttinger, ZZ Production and Limits on Anomalous Triple Gauge Couplings with the ATLAS experiment at the LHC, presented 21 Nov 2013 (2013).  
URL <http://cds.cern.ch/record/1662921>
- [116] J. Neyman, E. S. Pearson, On the problem of the most efficient tests of statistical hypotheses, Philosophical Transactions of the Royal Society of London. Series A, Containing Papers of a Mathematical or Physical Character 231 (1933) 289–337. doi:10.1098/rsta.1933.0009.  
URL <http://www.jstor.org/stable/91247>
- [117] A. Wald, Tests of statistical hypotheses concerning several parameters when the number of observations is large, Transactions of the American Mathematical Society 54 (3) (1943) 426–482. doi:10.2307/1990256.  
URL <http://www.jstor.org/stable/1990256>
- [118] G. Cowan, K. Cranmer, E. Gross, O. Vitells, Asymptotic formulae for likelihood-based tests of new physics, The European Physical Journal C 71 (2) (feb 2011). doi:10.1140/epjc/s10052-011-1554-0.  
URL <https://doi.org/10.1140%2Fepjc%2Fs10052-011-1554-0>
- [119] A. L. Read, Presentation of search results: the  $CL_S$  technique, J. Phys. G 28 (2002) 2693. doi:10.1088/0954-3899/28/10/313.
- [120] MATHUSLA Collaboration, Long-lived particles at the energy frontier: the MATHUSLA physics case, Reports on Progress in Physics 82 (11) (2019) 116201. doi:10.1088/1361-6633/ab28d6.  
URL <https://dx.doi.org/10.1088/1361-6633/ab28d6>

- [121] F. Kling, S. Trojanowski, Heavy neutral leptons at FASER, Phys. Rev. D 97 (2018) 095016. doi:10.1103/PhysRevD.97.095016.  
URL <https://link.aps.org/doi/10.1103/PhysRevD.97.095016>
- [122] M. Hirsch, Z. S. Wang, Heavy neutral leptons at ANUBIS, Phys. Rev. D 101 (2020) 055034. doi:10.1103/PhysRevD.101.055034.  
URL <https://link.aps.org/doi/10.1103/PhysRevD.101.055034>

## APPENDIX A

---

### Supplementary Statistical Modelling Plots

---

This section provides some additional images showing the behaviour of a signal and background-only fit after unblinding, a signal fit and the blinded Weinberg fit.

#### A.1 Extra Unblinded Background-Only Fit Plots

This section shows the systematic variation responses of the background only fit once unblinded for completeness. Figures A.1 to A.3 show nearly identical behaviour with real data.

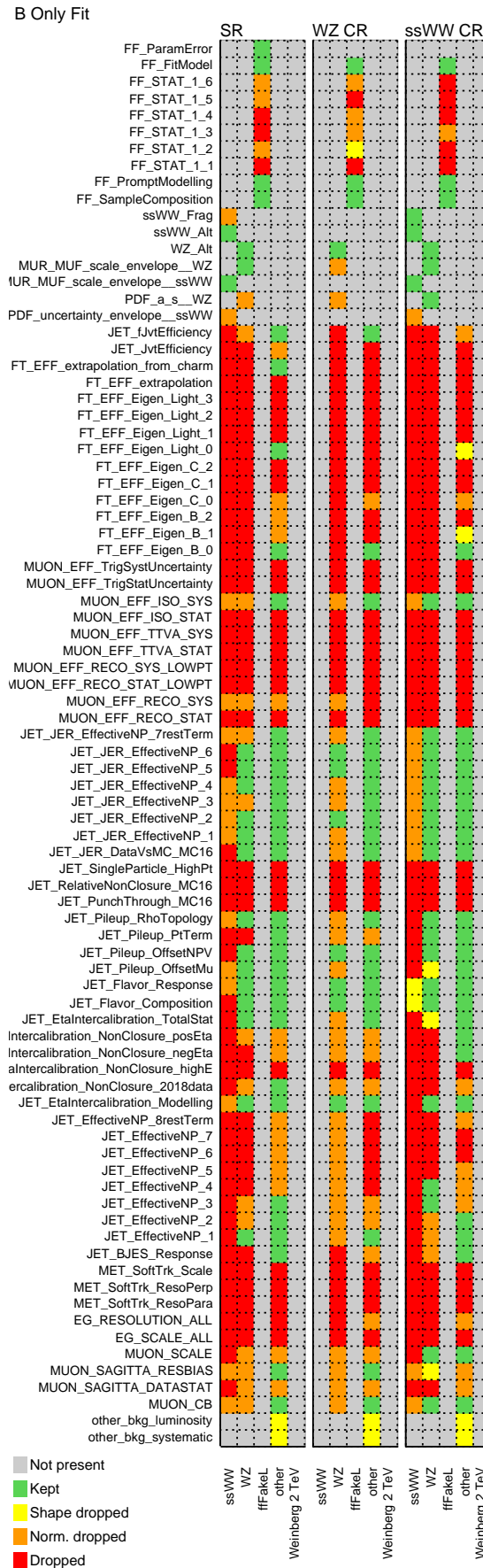


Figure A.1: Pruning plot for the unblinded background-only fit.

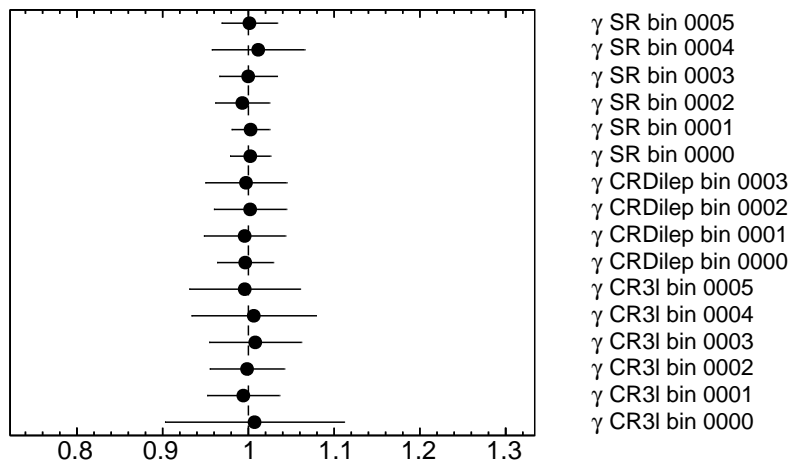


Figure A.2: Gammas in the unblinded background-only fit.

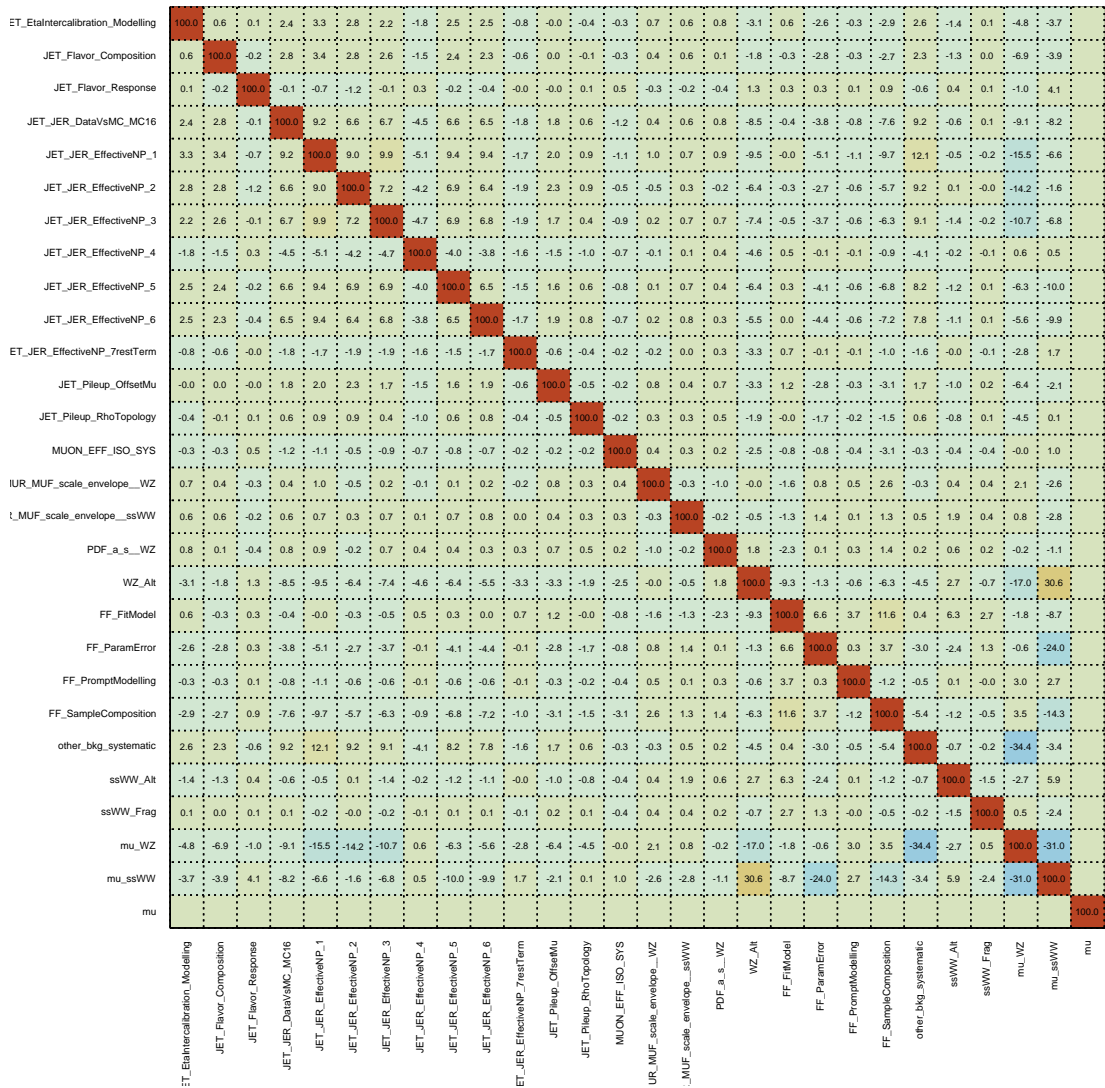
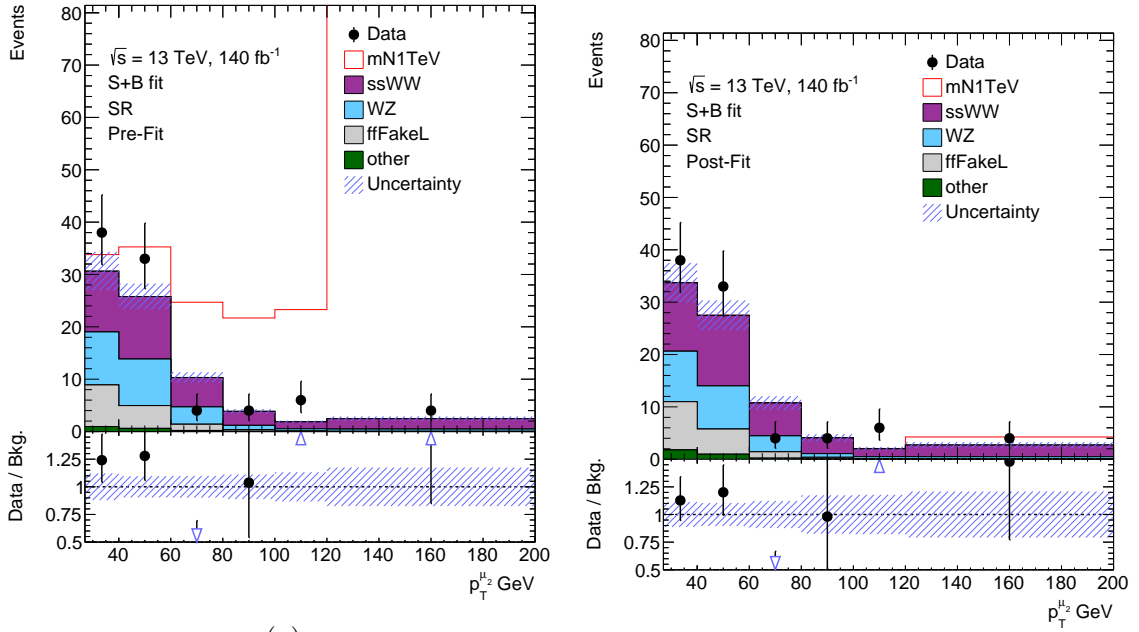


Figure A.3: Correlation matrix for the unblinded background-only fit.

## A.2 Signal Fit on Unblinded Data

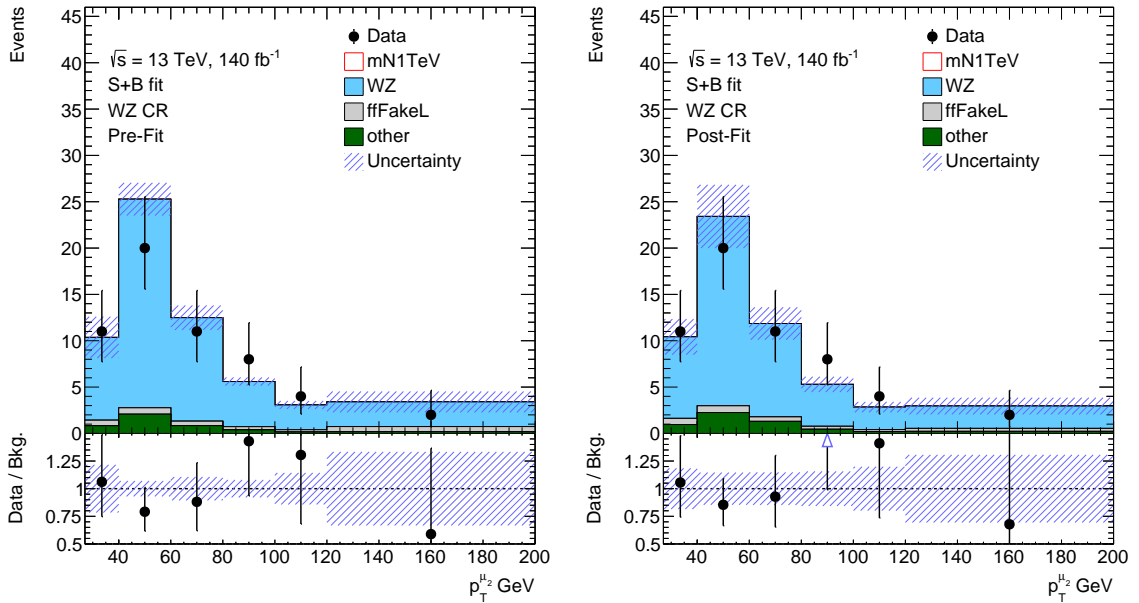
This section provides figures A.4 to A.6, showing the stable fitting of  $m_N = 1$  TeV signal sample pointing to no discovery.



(a)

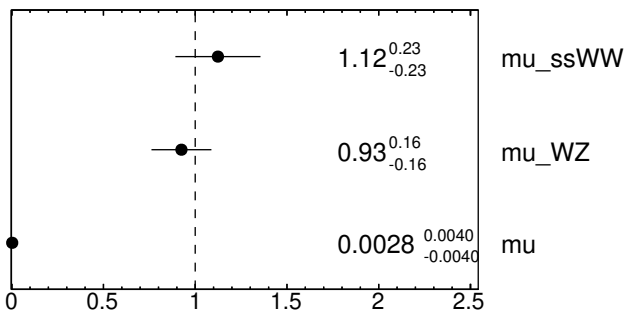
(b)

launch



(c)

(d)



(e)  $\mu$ s derived in the unblinded  $m_N = 1$  TeV fit.

Figure A.4: Pre- (a, c) and postfit (b, d) distributions in the signal region (a, b) and WZ control region (c, d)

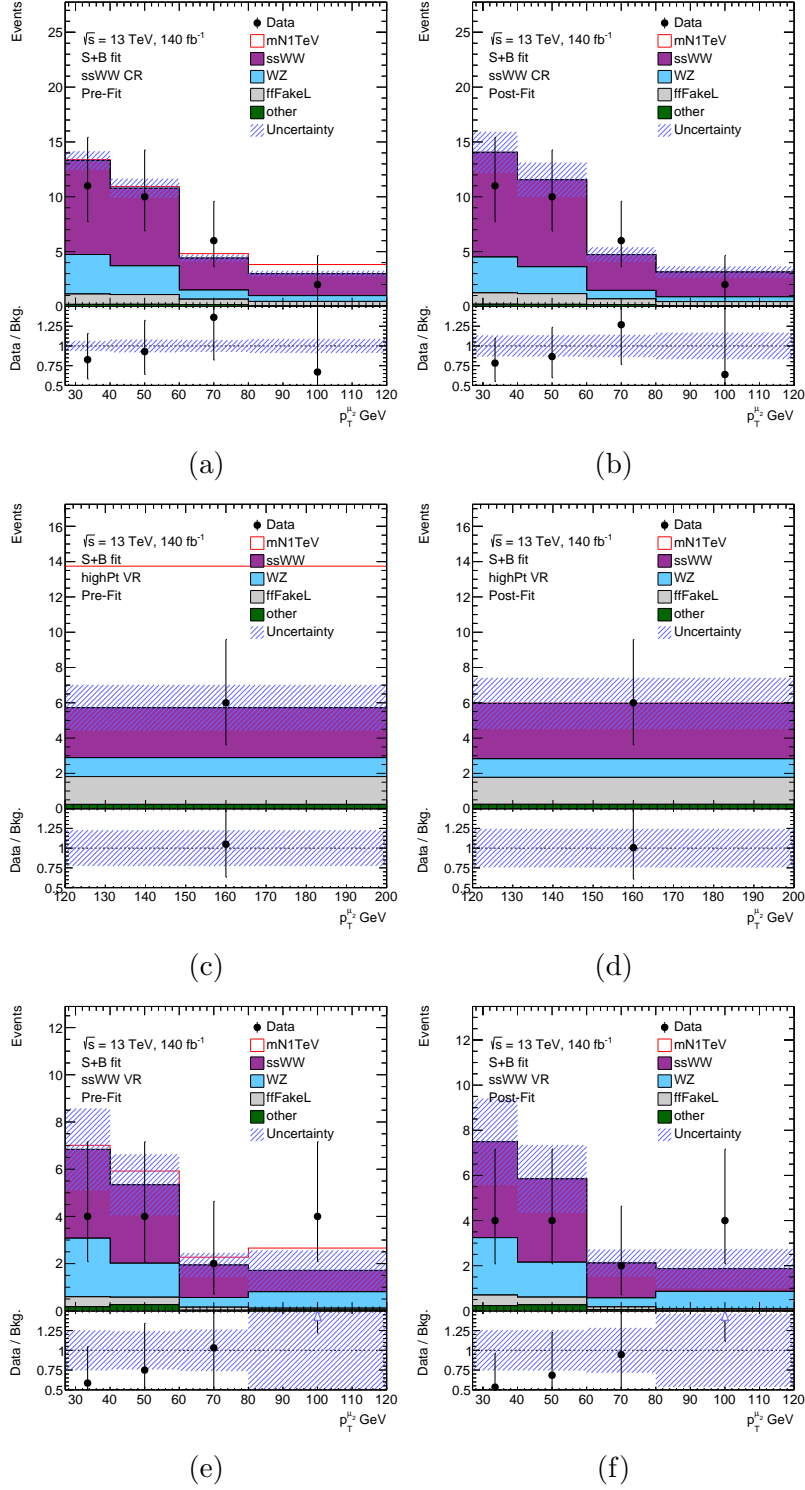
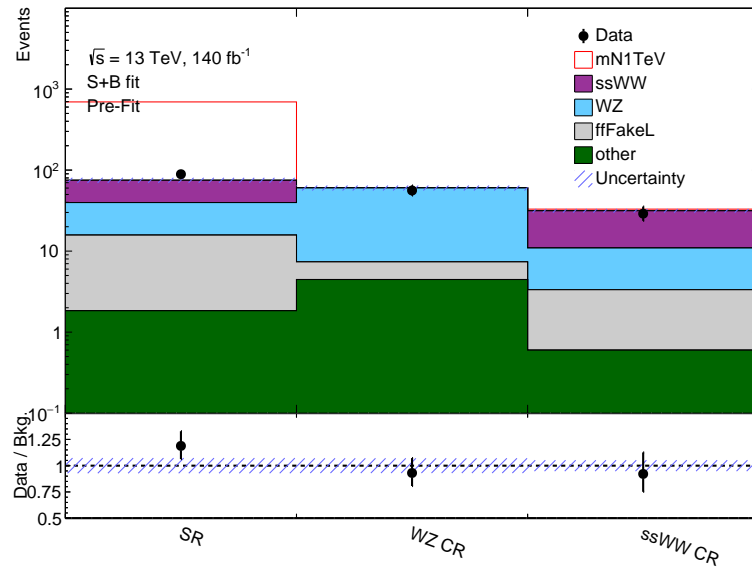
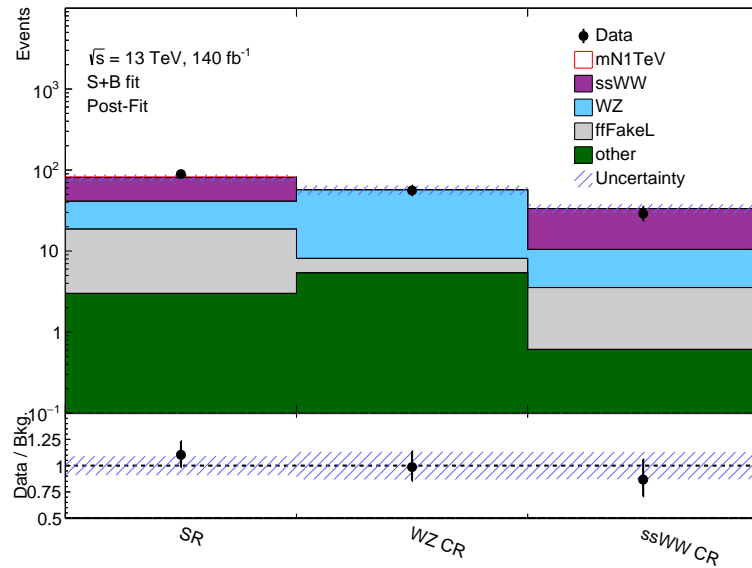


Figure A.5: Pre- (a, c, e), and postfit (b, f, d) distributions in the ssWW CR (a, b) and VRs (c, d, e, f) in the unblinded  $m_N = 1$  TeV fit.



(a) Pre-Fit

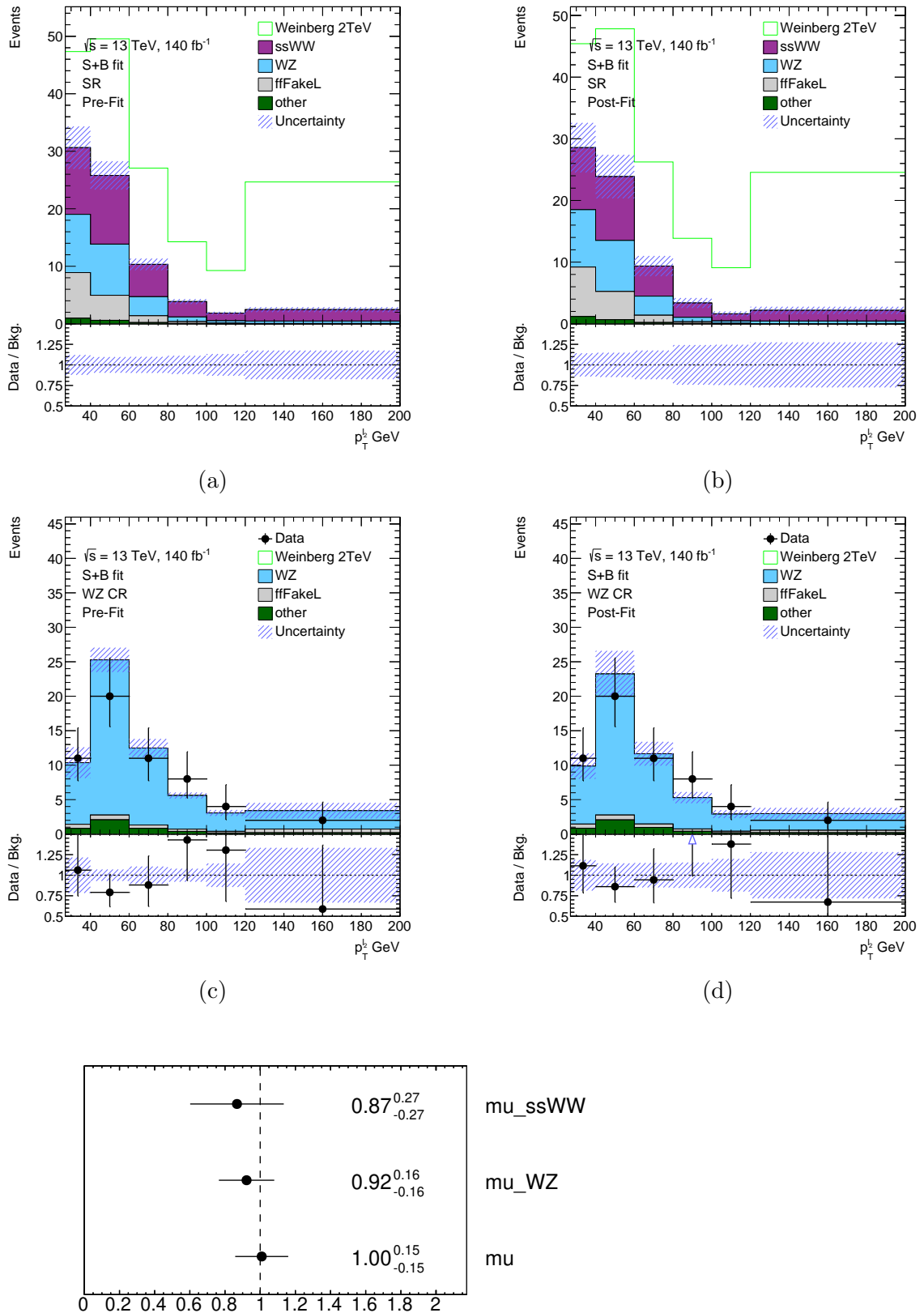


(b) Post-Fit

Figure A.6: Summary plot of the regions Pre-Fit (a) and Post-Fit (b) the  $m_N = 1$  TeV fit.

### A.3 Blinded Weinberg Fit

The blinded Weinberg model fit is shown in this to demonstrate the fit converges and behaves as expected in figures A.7 to A.9.



(e)  $\mu$ s derived in the blinded Weinberg fit.

Figure A.7: Pre- (a, c) and postfit (b, d) distributions in the SR (a, b) and WZ control region (c, d) alongside the fitted normalisation factors (e) for the blinded Weinberg fit

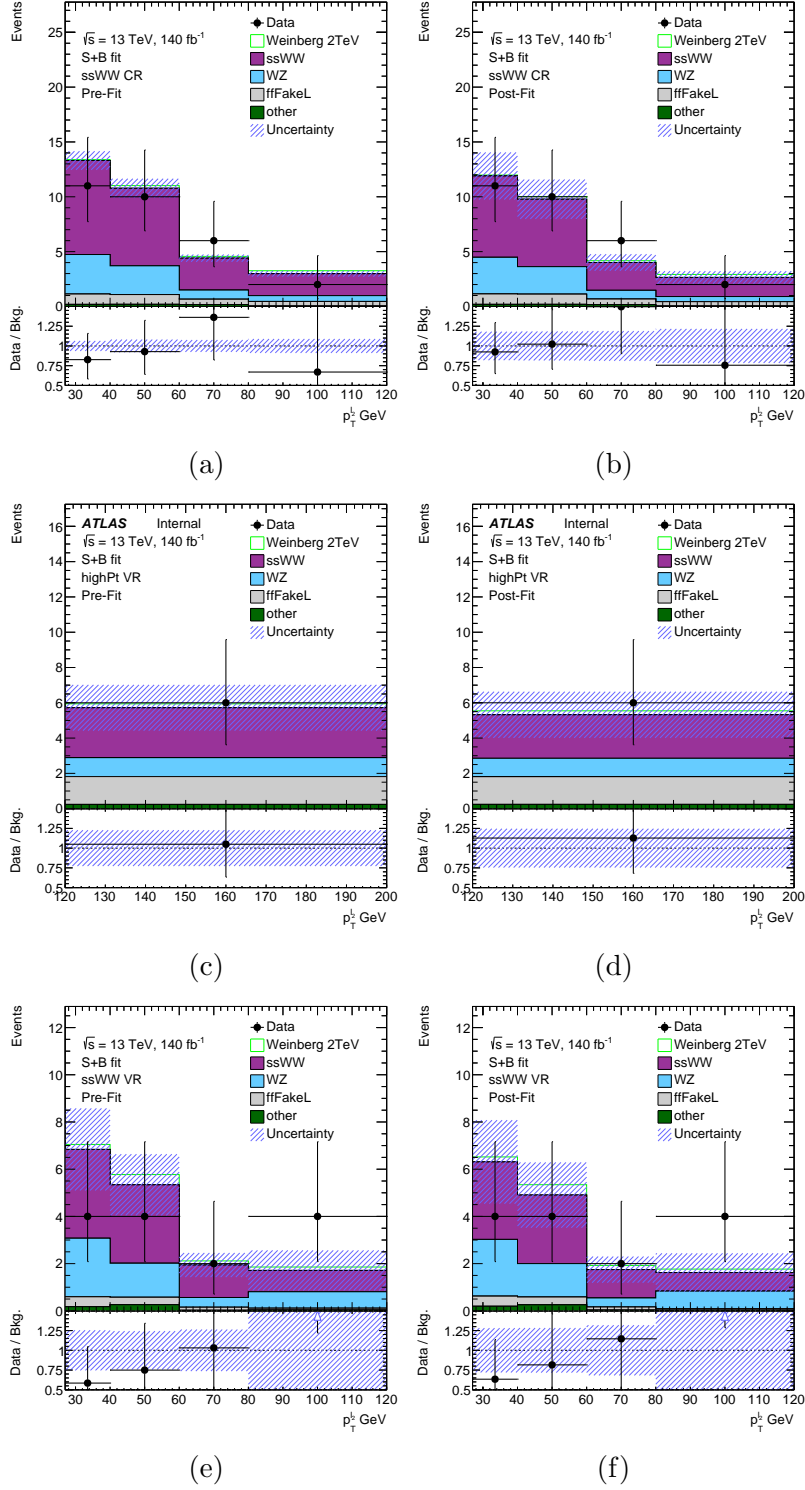
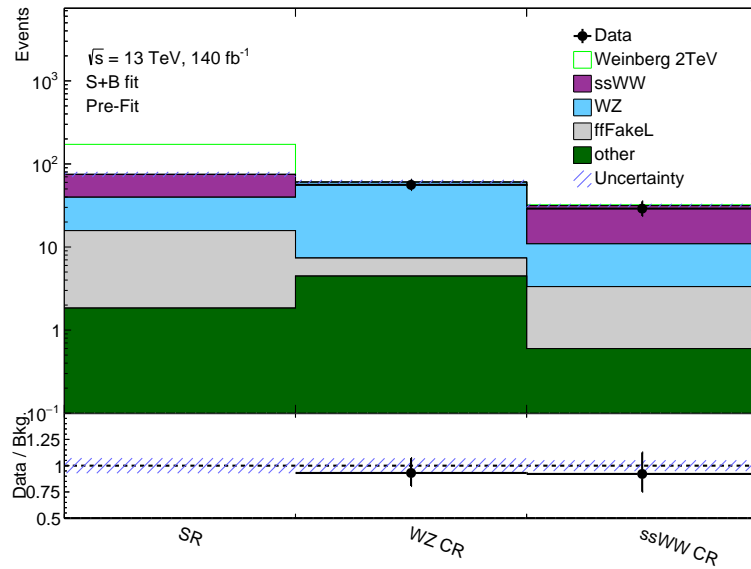
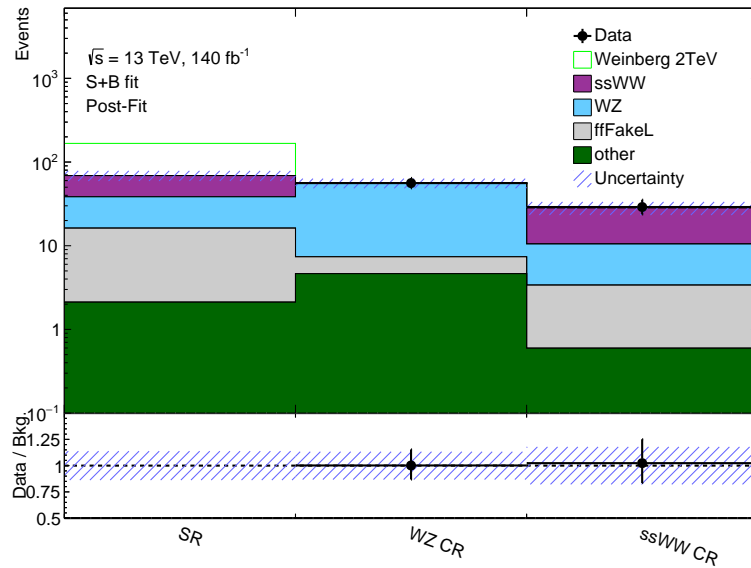


Figure A.8: Pre- (a, c, e), and postfit (b, d, f) distributions in the ssWW CR (a, b) and VRs (c, d, e, f) in the Weinberg model fit.



(a) Pre-Fit



(b) Post-Fit

Figure A.9: Summary plot of the regions pre-fit (a) and post-fit (b) for the blinded Weinberg fit.

## APPENDIX B

---

### Supplementary Images

---

This section provides a secondary event display of sub-leading bin of the signal region in figure B.1.

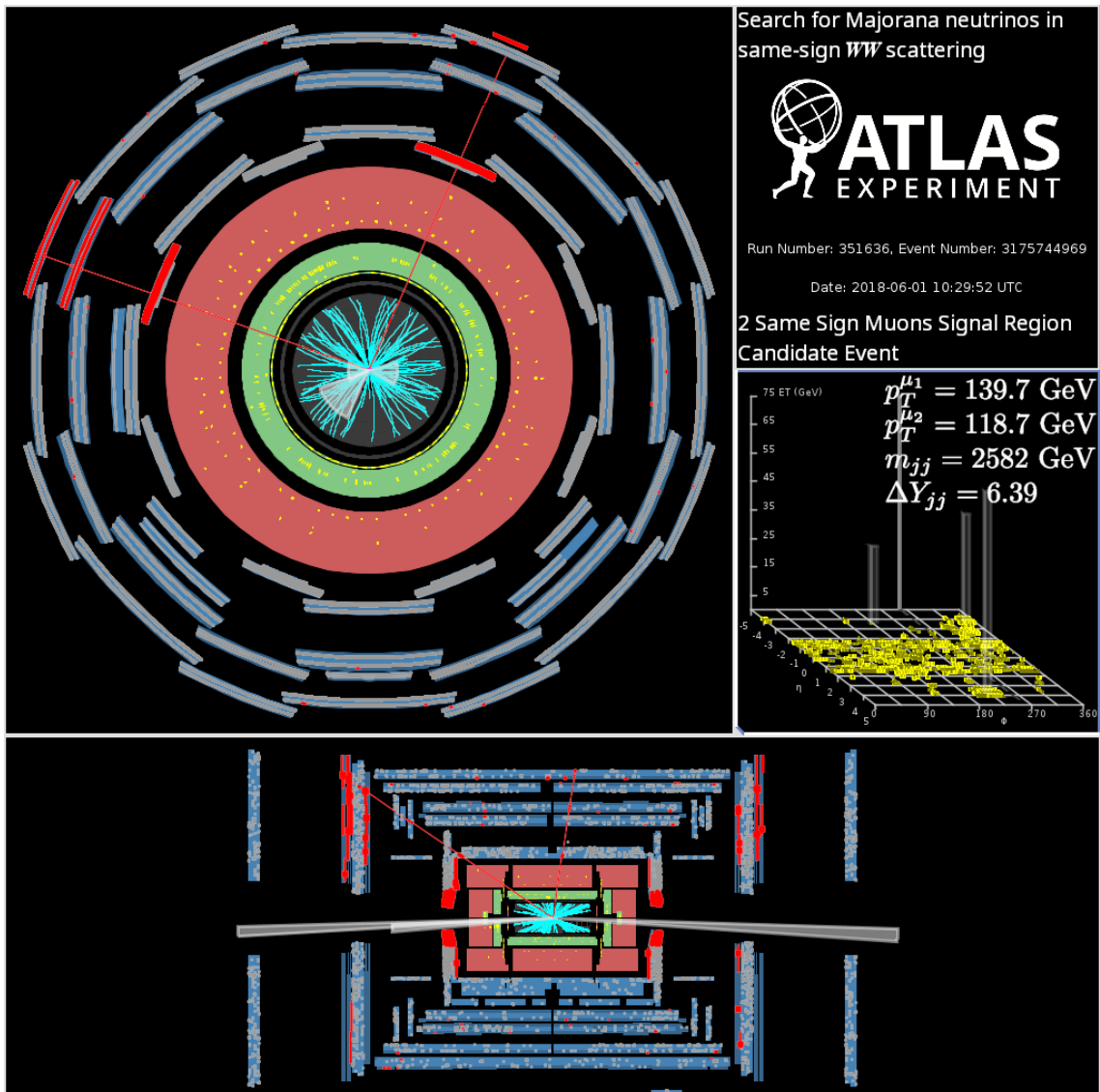


Figure B.1: Candidate event in the penultimate bin ( $p_T^{\mu_2}$  between 100 and 120 GeV) in the signal region

---

## Systematics Quantification Summary

---

The systematics for this analyses mostly uses the common tools for all ATLAS analysis provided by the CP groups. These arise from two major sources.

1. The uncertainties due to the experimental reconstruction of objects
2. The modelling uncertainties in the theoretical background and signal generator estimations (these are strongly correlated to previous measurements of the standard model).

For completeness in this appendix we outline both of these. All of these listed systematic variations change our expected and observed limits negligibly.

### C.1 Experimental Systematics

Alongside a global uncertainty on the number of events from the luminosity measurement, the fit uses a common set of provided systematic variations for jets, muons and jets. Electron energy systematic variations are also considered as due to the analysis rejecting baseline electrons. These are summarised in full with the corresponding systematic variations in table C.1.

For the muon objects, the systematic variations are driven by the uncertainties in track reconstruction efficiency alongside isolation qualities.

The jet systematic variations are more complex and relate to pile-up and detector response variations. These include treatment of detector response at high rapidity. Some of these are leading systematic variations as we are working with high rapidity separation jets. These modify our event yields and signal regions shapes indirectly through what is accepted in our cutflow as function of  $\theta_j$ . Various systematic variations are also in place as data-MC mismatch correction uncertainties. The calibrated energy deposit measurement is split into its absolute scale error (Jet Energy Scale) and determined resolution (Jet Energy Resolution).

The MET resolution is reduced to a much simpler form already by the Combined Performance (CP) group.

## C.2 Theoretical Systematic Variations

The theoretical systematic variations are only considered for the MC generation of the ssWW, WZ and signal (HNL or Weinberg) samples, otherwise a negligible 50% error is applied as systematic to the sample. These pertain to the measurements of fundamental quantities from previous analysis (i.e. masses of fundamental particles, the PDF fits on proton scattering data or  $\alpha_s$  measurements).

For this analysis the main sources of theoretical uncertainty are the  $Q^2$  cut-off scales for factorisation  $\mu_f$  (equation (5.3)) and renormalisation  $\mu_r$  (the process's matrix element),  $\alpha_s$  and PDF uncertainties and differences with alternative MC generators (denoted **scale\_envelope**, **PDF\_a\_s** and **\_Alt** respectively).

Scale uncertainties encapsulate higher order correction terms in the Feynman diagram expansion by varying these scale cut-offs from their nominal values (which are based on reconstructed  $Q^2$  of the process).

The modelling and measurement of PDF and  $\alpha_s$  is combined together in quadrature.

For background generator uncertainties we use an alternative showering model for ssWW (Herwig) and an alternative generator via Sherpa. For the WZ samples we use POWHEG+pythia instead of Sherpa. To generate smooth systematic  $1\sigma$  histograms for the fit from these 2-point variations we take the nominal sample as the central valued bin and the bin-by-bin difference as the  $\sigma$  value.

Systematic uncertainty Label	Short description
<b>Event</b>	
Luminosity	uncertainty in the total integrated luminosity (0.83% used, final luminosity measurement)
<b>Electrons</b>	
EG_SCALE_ALL	energy scale uncertainty
EG_RESOLUTION_ALL	energy resolution uncertainty
<b>Muons</b>	
MUON_EFF_RECO_STAT	reconstruction and ID SF uncertainty for $p_T > 15$ GeV
MUON_EFF_RECO_SYS	
MUON_EFF_RECO_STAT_LOWPT	reconstruction and ID efficiency SF uncertainty for $p_T < 15$ GeV
MUON_EFF_RECO_SYS_LOWPT	
MUON_ISO_STAT	isolation efficiency SF uncertainty
MUON_ISO_SYS	
MUON_TTVA_STAT	track-to-vertex association efficiency SF uncertainty
MUON_TTVA_SYS	
MUONS_SCALE	energy scale uncertainty
MUON_CB	combined track resolution uncertainty
MUON_SAGITTA_DATASTAT	statistical uncertainty in the charge dependent corrections
MUON_SAGITTA_RESBIAS	momentum scale uncertainty based on residual charge-dependent bias and data/MC non-closure
MUON_EFF_ISO_STAT	statistical/systematic uncertainty in muon efficiency scale factors
MUON_EFF_ISO_SYS	
MUON_EFF_TrigStatUncertainty	trigger efficiency SF uncertainty
MUON_EFF_TrigSystUncertainty	
<b>Small-R Jets</b>	
JET_EffectiveNP_1-7	jet energy scale (JES) uncertainty
JET_BJES_Response	b-jet energy scale uncertainty
JET_EtaIntercalibration_Modelling	$\eta$ intercalibration uncertainty of forward JES
JET_EtaIntercalibration_NonClosure_2018data	
JET_EtaIntercalibration_NonClosure_highE	
JET_EtaIntercalibration_NonClosure_negEta	
JET_EtaIntercalibration_NonClosure_posEta	
JET_EtaIntercalibration_TotalStat	
JET_Flavor_Composition	JES uncertainty due do different responses between quark and gluon jets
JET_Flavor_Response	
JET_Pileup_OffsetMu	JES uncertainty due to pileup
JET_Pileup_OffsetNPV	
JET_Pileup_PtTerm	
JET_Pileup_RhoTopology	
JET_PunchThrough_MC16	
JET_RelativeNonClosure_MC16	
JET_SingleParticle_HighPt	JES punch-through uncertainty due to muons in close proximity of jets
JET_JER_EffectiveNP_1-6	JES data-MC non-closure uncertainty
JET_JER_EffectiveNP_7restTerm	JES uncertainty from calibration used for very high-pT jets
JET_JER_DataVsMC_MC16	uncertainty in jet energy resolution (JER)
FT_EFF_EIGEN_B_0-2	uncertainty accounting for differences between the nominal MC and data JER
FT_EFF_EIGEN_C_0-2	b-tagging efficiency uncertainties for b-jets
FT_EFF_EIGEN_Light_0-3	c-mistagging efficiency uncertainties
FT_EFF_EIGEN_extrapolation	light jet mistagging efficiency uncertainties
FT_EFF_EIGEN_extrapolation_from_charm	b-tagging efficiency uncertainty on the extrapolation on high $p_T$ -jets
JET_JvtEfficiency	mistagging efficiency uncertainty on $\tau$ -jets
JET_fJvtEfficiency	jet-vertex-tagger (JVT) efficiency SF uncertainty
	forward jet-vertex-tagger (fJVT) efficiency SF uncertainty
<b><math>E_T^{\text{miss}}</math>-Terms</b>	
MET_SoftTrk_ResoPerp	track-based soft term uncertainty related to transversal resolution
MET_SoftTrk_ResoPara	track-based soft term uncertainty related to longitudinal resolution
MET_SoftTrk_Scale	track-based soft term uncertainty related to longitudinal scale

Table C.1: Summary of the experimental systematic uncertainties considered in the analysis [68].